Advanced Thermometry Studies of Superconducting Radio-Frequency Cavities

A Dissertation

Presented to the Faculty of the Graduate School

of Cornell University

in Partial Fulfillment of the Requirements for the Degree of

Doctor of Philosophy

by

Jens Knobloch

August 1997

Advanced Thermometry Studies of Superconducting Radio-Frequency Cavities

Jens Knobloch, Ph.D.
Cornell University 1997

Superconducting niobium radiofrequency (rf) cavities for e^+e^- accelerators presently are limited to accelerating gradients of 25 MV/m — far less than their theoretical capability of 50 MV/m. Power dissipation by *field emission* electrons presents the main impediment to higher gradients. Other mechanisms, including *thermal breakdown* and *multipacting* also contribute to anomalous losses.

To improve our understanding of cavity losses, we constructed a new system to map the temperature distribution of 1.5 GHz cavities during operation in superfluid helium. Based on existing devices, our system represents significant improvements in both resolution and acquisition speed. Hence, previously undetected losses and transient effects could be studied. Furthermore, a procedure was developed to examine the cavity interior in an electron microscope and an x-ray analysis (EDX) system, thereby permitting the correlation of thermometry data with the physical appearance of defects, as well as the identification of foreign elements.

The powerful combination of thermometry and microscopy was used for extensive field emission studies. Our results show that emission occurs predominantly from conducting particles. Their emission strength, however, is influenced by the adsorption of gases released during otherwise unrelated cavity events, such as thermal breakdown.

Of particular interest for improved cavity performance are emitters that explode ("process") when they are heated by the emission current. Thermometry data suggests that processing occurs when both the current density and the total current exceed thresholds. Microscopy demonstrates that the ionization of gases from the emitter is crucial to the initiation of the explosion. This fact is underscored by results obtained from the examination of emitters processed with intentionally administered helium gas.

To obtain more quantitative results, we performed numerical simulations of rf processing, including the ionization of gases by the field emission current. These simulations illustrate the conditions required for emitter explosion, and they confirm the importance of a plasma during such events.

Numerous other performance degrading mechanisms were studied as well, leading to our discovery of flux trapping during cavity breakdown and the detection of two point multipacting. Other observed losses, arising from hydride precipitation and titanium in grain boundaries, were a direct result of standard cavity preparation procedures and are avoidable with appropriate precautions.

To my wife:

The soul that can speak through the eyes can also kiss with a gaze.

—Gustavo Adolfo Bécquer

Acknowledgments

The contributions of many people, both at a scientific level and at the personal level, have been crucial to the completion of this dissertation.

I would like to extend a huge thank you to my advisor and committee chair, Hasan Padamsee, whose constant guidance, encouragement, and confidence in my abilities has helped me through many a trying period. Similarly, I thank my other committee members, past and present: Barbara Cooper, Malvin Kalos, David Rubin, and Maury Tigner.

Cries for help were always answered by current and past members of the Superconducting Radio Frequency Group — Sergey Belomestnykh, Phil Barnes, Eric Chojnacki, Curtis Crawford, Joel Graber, Walter Hartung, Tom Hays, Joe Kirchgessner, Don Metzger, David Moffat, Henry Muller, Richard Noer, Michael Pekeler, Peter Quigley, James Sears, Alexis Trebendis, and Vadim Veshcherevich. Discussions with all of them have always been of tremendous help. In particular I'd like to thank Walter for having run the multipacting trajectory calculations discussed in this dissertation.

The construction of the test stand would not have been possible without the efforts of the Newman Lab machinists: Chuck Firenze, Henry Hansteen, Gerhardt Hellmann, Phil Hutchings, John Kaminsky, Seth Marks, Randy Miller, Tom Reitz, and Roger Seely. Thanks for always accepting my rush jobs with a smile! The same counts for the other technical staff at Newman Lab who helped on many occasions: Holly Conklin, Bill Edwards, Terri Gruber, Ron Proudy, Neil Sherwood, and Mike Stevens.

In the same vein, I want to thank all the undergraduate researchers in the SRF group who have worked on some part of the experiment, in particular Nicholas Black, Daniel Kapner, Gautam Parthasarathy, Chris Roat, and Karen Stachowsky. Without their help I would still be in the basement of Newman Laboratory trying to get the experiments to run.

The collaborative work with Adam Drobot and David Chernin (both from SAIC[1]), who helped with extensive modifications of the computer code MASK, was pivotal to my ability to perform the field emission simulations. This dissertation would be incomplete without their contributions. Cavities given to the SRF group by Peter Kneisel from CEBAF were also gratefully accepted, since we had exhausted our own reserves. I also wish to thank Claire Antoine and the Laboratoire de Süe, who carried out PIXE analyses of our titanium contaminated cavities.

The Newman Lab support staff — Pam Morehouse, Monika Norris, Chuck Lyons,

[1]Science Applications International Corporation

Mary Wright, Lois Billups — and the drafting department — Don Miller, Dawn Sears, Tom Kobela, Dick Mitstifer, Jim Lacey, and Tim O'Connell — were always willing to help, or simply to chat to brighten the day. Thanks especially to Pam for her endless supply of coffee and cookies. They helped a starving grad student survive.

This work was funded by the National Science Foundation, with supplementary support from the U.S.-Japan Collaboration.

On a more personal level, I'd like to thank my Mom, Dad, and Sis for always supporting me, for placing such importance on my education and for giving me a wonderful home, filled with love, to grow up in. A special thank you to my Father for having kindled in me the love of Science.

A big thank you and hug also goes out to Grandma and Grandpa, and Oma and Opa, for the root beer floats, the evenings on the porch, the candy drawer, the Skat games, wonderful Christmases ..., and for having raised two great families whom I am immensely proud to be a part of.

I am indebted to my Aunt Colette and Uncle Fred for many a pep talk over the phone, and to Aunt Monika and Uncle Paul for giving me a second home away from home on my numerous visits to Washington D.C.

I would also like to extend my gratitude to my parents-in-law, René and Marie-Louise, for all their support, the Foie Gras, the wine and, most importantly, for the pride they take in my work.

Finally I'd like to thank my best friend and wife Véronique, for all the late night dinners brought to the lab when I had to run experiments, and the help in mounting countless thermometers on weekends. Without your tremendous patience, support and love, this work would not have been completed.

Table of contents

List of figures

List of tables

List of abbreviations

ADC	Analog to Digital Converter.
BCP	Buffered Chemical Polish (HNO_3 + H_3PO_4 + HF).
BCS	Bardeen-Cooper-Schrieffer (theory).
cw	Continuous Wave.
DIXE	Deuterium Induced X-ray Emission.
dc	Direct Current.
EDX	Energy Dispersive X-ray (analysis).
FWHM	Full-Width-at-Half-Maximum.
IDC	Insulation Displacement Connector.
MIM	Metal–Insulator–Metal (interface).
MIV	Metal–Insulator–Vacuum (interface).
MP	MultiPacting.
PCB	Printed Circuit Board.
PIXE	Proton Induced X-ray Emission.
RRR	Residual Resistance Ratio.
rf	Radio-Frequency.
SEC	Secondary (electron) Emission Coefficient.
SEM	Scanning Electron Microscope.
TE	Transverse Electric (cavity mode).
TM	Transverse Magnetic (cavity mode).

List of symbols

a^2	Area of a grain boundary.
A_{ab}	Cable attenuation (in dB).
A_{bc}	Cable attenuation (in dB).
A_{ae}	Cable attenuation (in dB).
A_{FN}	Effective field emission area.
A_{d}	Effective defect area exposed to the rf field.
A_{M}	Field emission parameter in MASK.
A_n	Area closest to thermometer n.
α	≈ 1.76.
α_{r}	Recombination rate coefficient.
α_{T}	First Towsend coefficient.
B_{M}	Field emission parameter in MASK.
β	External coupling strength of the input coupler.
β_{FN}	Field enhancement factor.
c	Speed of light.
c_{d}	Temperature correction factor, based on the distance between a defect and the nearest thermometer.
C_{R}	Richardson constant for thermionic emission.
χ	Electron affinity of an insulator.
d	Width of the MASK simulation region.
D_T	Thermal diffusion constant of niobium.
D_{Ti}	Diffusion constant of titanium in niobium.
δ	RF field penetration depth in a grain boundary.
Δ	Superconductor energy gap.
e	Positron charge.
E_{acc}	Average accelerating gradient.
E_{em}	Electric field at a field emission site.

E_{pk}	Peak surface electric field in the cavity.
E_{s}	Electric field in a plasma sheath.
E_0	Electric field applied to a defect.
ϵ_0	Permittivity of free space.
ϵ_T	Temperature signal per watt due to a point defect.
η_T	Thermometer efficiency.
f_q	Charge "neutralization" factor.
F	Effusion flux of neutral particles in MASK.
Δf	Cavity bandwidth.
G	Cavity geometry factor.
γ_q	Space charge limit parameter in MASK.
h	Planck's constant.
$\hbar$	Planck's constant/2π.
H_{c}	Thermodynamic critical magnetic field of a superconductor.
H_{c1}	Lower critical magnetic field of a superconductor.
H_{c2}	Upper critical magnetic field of a superconductor.
H_{ext}	Externally applied dc field.
H_{pk}	Peak surface magnetic field in the cavity.
H_{sh}	Superheating magnetic field of a superconductor.
H_{tb}	Threshold magnetic field for thermal breakdown.
H_0	RF magnetic field applied to a defect.
I_{FN}	Fowler-Nordheim emission current.
I_{min}	Minimum current needed for rf processing.
$I_{\mathrm{pk},l}$	Peak emission current up to time step l.
$I_{\mathrm{pk}}^{\mathrm{th}}$	Theoretical peak emission current in MASK.
j_{FN}	Fowler-Nordheim emission current density.
j_{max}	Critical current of a Josephson junction.
j_{min}	Minimum current density needed for rf processing.
j_T	Electric current density due to a thermal gradient.
k_{b}	Boltzmann constant.
K_0	Electron emission energy.
K_E	$= E_{\mathrm{pk}}/\sqrt{P_{\mathrm{t}}}$.
K_T	Average thermometer response to a uniform power flux.
K_U	$= U/P_{\mathrm{t}}$.
κ_T	Thermal conductivity of niobium.
κ_U	$= E_{\mathrm{pk}}/\sqrt{U}$.

ℓ	Distance traversed by the field emission current in bulk material.
λ	Mean free path of electrons in a gas.
λ_D	Debye length.
λ_L	London penetration depth.
m_e	Electron mass.
m_n	Neutral particle mass.
M_i	Ion mass.
μ_0	Permeability of free space.
n	Multipacting order.
n_e	Electron density.
n_i	Ion density.
n_n	Neutral particle density.
n_s	Cooper pair density.
$\nu_{\mathrm{i},l}$	Partial ionization rate per volume.
ν_i	Total ionization rate per volume.
ν_r	Recombination rate per volume.
ω	Angular frequency.
ω_0	Angular frequency of the TM_{010} cavity mode.
p	Gas pressure.
P_FN	Joule losses of the field emission current.
P_d	RF power dissipated in the cavity alone.
$P_\mathrm{d}^\mathrm{cal}$	RF power dissipated in the cavity, as determined by thermometry.
P_e	RF power dissipated into the input coupler.
$P_\mathrm{e}^\mathrm{inst}$	RF power emitted into the input coupler instantaneously after P_f is switched off.
P_f	Incident rf power.
$P_\mathrm{f,d}$	Incident rf power measured at the directional coupler.
P_r	Reflected rf power.
$P_\mathrm{r,d}$	Reflected rf power measured at the directional coupler.
P_total	Total rf power dissipated in the cavity and into the coupler ($= P_\mathrm{d} + P_\mathrm{e}$).
P_t	Transmitted rf power.
$\hat{P}$	RF power measured at the oscilloscope.
ϕ	Angular coordinate in a cylindrical system.
ϕ_0	ϕ-coordinate of a field emitter.
φ_n	Electron impact phase during multipacting.
Φ_0	Magnetic flux quantum.
Φ	Work function of a metal.

q	Electric charge.
$q_{\max}$	Maximum charge that can be emitted per simulation time step.
$\dot{Q}$	Power dissipated in a defect.
Q_0	Unloaded cavity quality.
Q_{e}	External quality of the input coupler.
Q_{L}	Loaded cavity quality.
r_{d}	Defect radius.
r_{em}	Emitter radius.
r_{m}	Radius of field emitter melt zone.
R	Radius of the MASK simulation region.
R	Thermometer resistance.
$\mathcal{R}$	Thermal contact resistance.
R_{BCS}	BCS surface resistance.
R_{d}	Defect surface resistance.
R_{In}	Surface resistance of superconducting indium.
R_{g}	Normal state resistance of a grain boundary.
R_{n}	Normal conducting surface resistance.
R_{s}	Total superconducting surface resistance.
$R_{\mathrm{s}}^{\mathrm{high}}$	High field surface resistance of a lattice of Josephson junctions.
$R_{\mathrm{s}}^{\mathrm{low}}$	Low field surface resistance of a lattice of Josephson junctions.
R_0	Superconducting residual surface resistance.
$\bar{R}_0$	Mean superconducting residual surface resistance.
R_F	Ratio of the magnetic force to the electric force.
R_Φ	Superconducting surface resistance due to trapped flux.
ρ	Radial coordinate in a cylindrical system.
ρ	Resistivity of a field emitter.
ρ_d	Droplet radius.
S	Coordinate along the cavity contour.
S_0	S-coordinate of the field emitter location.
S_T	Thermopower coefficient (Seeback effect).
σ_{l+}	Partial ionization cross-section.
σ_{t}	Total ionization cross-section.
Σ_q	Charge density per area.
dt	Time step used in MASK.
t_{expl}	Time it takes for a microemitter to explode (after melting).
t_{gas}	Time it takes gas from a microemitter to move to the region of dominant ionization.
t_{heat}	Time it takes the emission current to melt a microemitter.
ΔT	Temperature rise recorded by a thermometer.
T_{b}	Helium bath temperature.

T_c	Critical temperature of a superconductor.
T_d	Temperature of a particulate defect.
T_e	Electron temperature.
T_m	Melting temperature of a metal.
T_λ	Lambda temperature of helium.
τ	Loaded cavity decay time.
U	Energy stored in the cavity.
v_e	Electron velocity.
V_a	Peak applied voltage in MASK simulations.
V_s	Potential drop in a plasma sheath.
w_s	Weight of a macroparticle of species s.
$\mathbf{x}_n$	Electron impact site during multipacting.
ξ_0	Superconductor coherence length.
z	z-coordinate in a cylindrical system.

Chapter 1

Introduction

1.1 Motivation for cavity research

1.1.1 The need for particle accelerators

In the early days of this century, three "elementary" particles had been identified — the electron, the proton, and the neutron. All matter known at the time could be explained in terms of these constituents. However, the simple picture offered by these particles was already shattered within a few decades. By the 1960's a myriad of new "elementary" particles were discovered that threatened to be very confusing. Being driven by a desire to find an underlying simplicity, researchers expended much effort to explain the multitude of particles in terms of even more fundamental "building blocks." This endeavor culminated in the development of the "Standard Model." According to this model, there are a total of 24 fundamental particles: six "flavors" of quarks arranged in three generations of two, six leptons (also in three generations) and an equal number of antiparticles. By combining quarks of different flavors, all mesons and baryons known to date can be explained.

Parallel to the development of the elementary particle picture, the large number of different forces observed in nature was not understood. But, beginning with the unification of the electric and magnetic forces, all forces were eventually shown to be different manifestations of four fundamental ones — the electromagnetic force, the weak force, the strong force and gravity. These forces are transmitted by bosonic particles, of which 13 are believed to exist. Salam, Weinberg and Glashow in the 1970's then developed the theoretical framework for the unification of the electromagnetic and the weak forces by a single *electroweak* force. Only below energies of 1 TeV does it manifest itself as two seemingly separate forces. Three fundamental forces remain. However, it is postulated that these three are also unified at much higher energies. (The strong and electroweak forces at $\geq 10^{12}$ GeV and gravity at $\geq 10^{19}$ GeV.)

Past and current particle accelerators have proved pivotal in providing the experimental evidence that vindicates the Standard Model, which now is accepted as one of this century's great successes. For example, in 1983, researchers at CERN proved the existence of the W^+, W^- and Z^0 particles, three of the four carriers of the electroweak force.[1] And only as recently as 1995 was the postulated sixth quark (the "top") discov-

[1] The photon is the fourth carrier.

ered at Fermilab, to complete the three generations of quarks.

Nevertheless, mysteries remain. Why do quarks have mass? Why are they so much heavier than leptons? Why is there a preponderance of matter over antimatter in the universe? Why are there three generations of quarks and leptons, when only the first generation is sufficient to describe the tangible universe? ...[2] Answers to some of these and other questions, it is hoped, will be provided by future generations of particle accelerators.

1.1.2 Frontier accelerators

Accelerator research is rapidly progressing on two main frontiers: Pushing the beam energy and increasing the beam current/luminosity. For example, in the last 12 years the beam energy has increased by a factor of 10.

Currently, the highest energy accelerators are the $p\bar{p}$ Fermilab Tevatron (1 TeV in the center of mass) and the LEP e^+e^- accelerator at CERN (165 GeV in the center of mass). The two are roughly complementary.[3] The luminosity record, on the other hand, is currently held by the Cornell Electron Storage Ring (CESR) at 3×10^{32} cm^{-2}s^{-1}, operating at a modest 10.6 GeV in the center of mass (CM).

To be able to probe new physics, the next generation of accelerators has to be an order of magnitude higher in energy and about two orders of magnitude higher in luminosity.

The energy frontier has to be extended to 1 TeV (for e^+e^- accelerators) or more to be able to search for the Higgs particle which, it is hoped, will distinguish between a number of different theories of electroweak symmetry breaking. The theories attempt to explain matters such as the mass of quarks and the dramatically different behavior of the weak and electromagnetic forces. Because the (non-resonant) cross-section of interesting events reduces quadratically with increasing energy, the luminosity also has to be increased with the square of the beam energy.

Two machines proposed to push the energy frontier are the Large Hadron collider at CERN (pp, 14 TeV CM) and the TeV superconducting linear collider TESLA at DESY (e^+e^-, 1 TeV CM).[4] Both require luminosities of $1 - 2 \times 10^{34}$ cm^{-2}s^{-1}.

The current/luminosity frontier is also being advanced at lower energies to enable researchers to observe rare events such as the decay of B and $\bar{B}$ mesons. These decays are believed to violate charge-parity (CP) symmetry, which may explain why matter is much more abundant in the universe than antimatter. However, CP violation is an extremely rare event, and over 10^7 $B\bar{B}$ pairs need to be produced annually for effective studies. Luminosities in excess of 10^{34} cm^{-2}s^{-1} are needed.

High current, high luminosity storage rings to produce copious numbers of $B\bar{B}$'s ("B-factories") for CP violation studies are planned (and now being constructed) at KEK in Japan and at SLAC. These accelerators are not pushing the energy frontier, but rather are increasing the stored current to new levels. One to two amperes will be stored in the KEK B-factory to reach a luminosity[5] of 3×10^{33} cm^{-2}s^{-1}.

[2] For an in depth discussion of many outstanding questions, see Reference [1].

[3] Because protons and antiprotons are each made of three quarks, the collision energy is shared among the six constituents involved. According to conventional wisdom, a $p\bar{p}$ accelerator has to be roughly six to ten times as energetic as an e^+e^- accelerator to probe the same physics.

[4] Linear colliders based on normal conducting cavities have also been proposed (e.g., the NLC).

[5] The KEK B-factory will be operating with asymmetric beam energies so that lower luminosities than

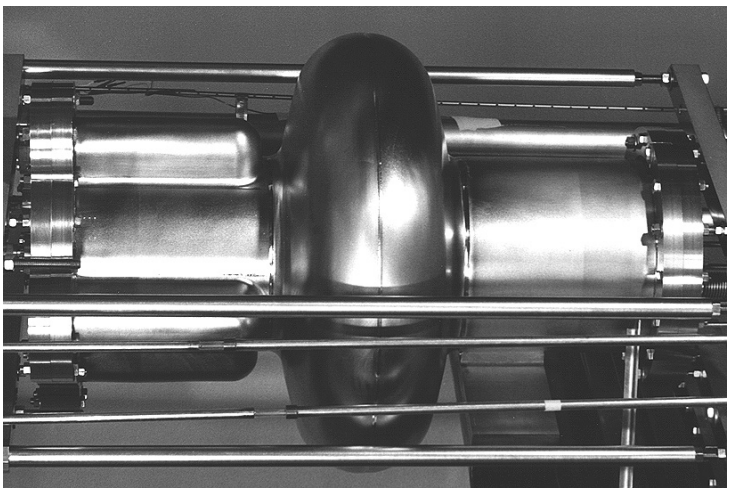

Figure 1.1: An example of a superconducting cavity to be used in the phase III upgrade of the CESR storage ring. The cavity length is about 80 cm.

Omitted in this discussion entirely, but equally important, are new accelerator facilities designed not for particle physics but for other applied research. They include light sources (e.g., SOLEIL in France), tritium production for defense and potential fusion applications (e.g., the ATP at Los Alamos), neutron sources for materials research (e.g., the ANS) and the accelerator based transmutation of nuclear waste products (ATW). In many cases they also push accelerator technology to new levels. [2]

1.1.3 Superconducting cavities

It is the devices used to provide energy to the particles that are crucial to an accelerator. Most commonly used are radio frequency (rf) cavities, an example of which is shown in Figure 1.1.

In the past, copper cavities were used for acceleration (e.g., at SLAC). However, superconducting niobium and lead[6] technology has proven itself over the last ten years as a promising alternative, being used in machines such as HERA (Hamburg, Germany) and TJNAF (Newport News, VA). Continuous wave (cw) accelerating gradients of 10 MV/m have been achieved, exceeding levels that are possible with copper cavities. Many of the future projects (among them TESLA, LEP-II, the KEK B-factory, and the LHC) are relying on superconducting cavities to achieve their design goals. Thus, superconductors will play a pioneering role at both the energy frontier and the high current frontier. In some very imaginative and novel designs (for example multi-TeV $\mu^+\mu^-$ colliders), superconducting rf is completely indispensable, illustrating that this technology holds the key for the next generation of particle accelerators and perhaps even beyond. Extensive research has therefore been performed to understand the performance limitations of superconducting cavities and to improve upon the achieved accelerating gradients. The work presented here is similarly motivated.

10^{34} $\mathrm{cm}^{-2}\mathrm{s}^{-1}$ are sufficient.

[6] Our discussion of superconducting cavities applies primarily to niobium cavities.

1.1.3.1 Advantages of superconducting cavities

Although not completely loss free above $T = 0$ K, as in the dc case, superconducting cavities dissipate orders of magnitude less power than normal conducting cavities. Niobium cavities, like those installed at TJNAF, routinely achieve quality (Q_0) factors 10^5 to 10^6 times that of copper cavities.[7] The dramatically reduced resistivity translates into a number of very important advantages. They include:[8]

1. *Operating cost savings* Even when taking into account the cost of refrigerating superconducting cavities, their power demand in cw applications is more than two orders of magnitude less than that of equivalent copper cavities.

2. *Capital cost savings* The reduced power requirements translate into capital cost savings, since fewer (and sometimes simpler) klystrons are needed.

3. *High gradient* The reduced power consumption also enables superconducting cavities to operate at high cw gradients.

4. *Reduced impedance* The aperture of superconducting cavities is large, thereby minimizing disruptive interactions of the cavity with the beam (characterized by the impedance). Higher currents can therefore be accelerated.[9] This fact is the main motivation for using superconducting rf technology in high current machines such as CESR.

1.1.3.2 Cavity performance limitations

A limit on the maximum accelerating gradient of superconducting cavities is imposed by the superheating magnetic field.[10] At no point of the cavity surface may the magnetic field exceed the superheating field, otherwise the superconductor goes normal conducting ("quenches"). Niobium cavities of the shape used in our test are therefore limited to an accelerating gradient of about 50 MV/m.

For a number of reasons, though, such high accelerating gradients are never achieved in practical cavities. The most common limiting mechanisms are *field emission*, *thermal breakdown*, and, at times, *multipacting*. These are discussed in detail in Chapter 3.

Field emission is the primary mechanism that limits present day cavities to accelerating gradients below 25 MV/m. In the presence of a high surface electric field, rf power is lost to electrons that tunnel out of the cavity wall at very localized points. The emitted electrons are accelerated by the electromagnetic fields and, upon impact, heat the cavity wall and produce x-rays. Field emission scales exponentially with the electric field and is capable of consuming inordinate amounts of power.

Thermal breakdown generally results when a highly resistive defect on the rf surface causes a large fraction of the cavity to quench. An abrupt reduction of the cavity quality

[7] The cavity quality Q_0 is defined as 2π times the number of oscillations it takes the cavity to dissipate an energy equal to that stored in its fields. The higher the Q_0 the lower the cavity's power dissipation.

[8] See Reference [2] for more details.

[9] Cavities are the main source of impedance in an accelerator.

[10] A fundamental electric field limit is neither predicted by the theory of superconductivity nor has one been observed experimentally up to 210 MV/m. [3]

results. Thermal breakdown can also be initiated by the heat from bombarding field emission electrons.

Multipacting is a resonant process, in which a large number of electrons build up an avalanche by repeated impact with the cavity walls. Again, the heat deposited by these impacts can lead to thermal breakdown. In the absence of thermal breakdown, the absorption of rf power by multipacting electrons can still make it impossible to raise the cavity fields.

Even at low field levels (below an accelerating gradient of a few MV/m) all cavities display losses higher than theoretically expected. The anomalous losses are attributed to a temperature independent *residual resistance*. The dominant sources for this resistance are impurities on the rf surface, adsorbed gases, and residual magnetic flux that is trapped in the superconductor as it is cooled through the transition temperature.[11] In some cases the precipitation of niobium hydride at the rf surface due to hydrogen stored in the wall may also contribute to the residual resistance. This phenomenon is known as the "Q-virus", and it can be avoided by driving out the hydrogen during a vacuum bake of the cavity at 900 °C.

1.2 Studying loss mechanisms

As we have seen, the key to increasing accelerator performance needed for future applications lies with our ability to improve the rf cavities. Even current proposals such as TESLA are pushing state of the art superconducting technology to the limit. It is therefore imperative, both out of fundamental interest and for the important forthcoming applications, that we gain a better understanding of the anomalous losses in cavities.

1.2.1 Experimental approach

1.2.1.1 Thermometry

One extremely successful scheme in the study of cavity losses has been thermometry. Its strength lies in the fact that ultimately each loss mechanism produces heat in the cavity wall. Thermometry thus can be used for the study of *all* types of losses.

The generic setup consists of an array of thermometers placed on the exterior surface of the cavity. The thermometers typically are carbon resistors specially prepared to insulate them from the cryogen (helium), yet allowing them to be in thermal contact with the cavity surface. Below 4.2 K the exponential increase of the thermometers' resistance with decreasing temperature allows for sensitive measurements at the millikelvin level.

The effectiveness of temperature mapping was first demonstrated by Lyneis in 1972. [4] Since then, thermometry has been used as a powerful diagnostic tool by numerous laboratories. [5–14] Its power has been proven repeatedly. For example, it has been possible to locate thermal breakdown sites and field emitters. It is these and other successes that gave the impetus for the construction of a new system used for the studies reported on here.

[11] Mu-metal is used to shield cavities from the earth's magnetic field, but residual fields always remain in the cryostat.

This newly developed system (for 1.5 GHz cavities) improves significantly on previous designs in two important categories: speed and sensitivity. The fastest system to date for comparable cavities required about 15 s for the acquisition of a temperature map. [5, 15] The resolution of this system was limited to temperature signals above 5 mK, so that many low level losses went undetected. A high sensitivity system, using a lock-in amplifier, was developed as well, which could resolve microkelvin temperature signals. [6, 7] However, map acquisition times up to 50 minutes were needed and transient effects (such as the activation and deactivation of field emitters) could not be studied.

In contrast, our new system is able to acquire temperature maps in less than 0.2 s while still resolving signals at the 150 μK level. Both of these features have been critical in our study of low level losses and transient behavior. An increased resolution of 30 μK is even possible if the acquisition time is lengthened to 2.5 s.

1.2.1.2 Microscopy

Past studies with 3 GHz cavities have shown that thermometry data can be used successfully to locate anomalous losses (especially field emission), whose source may subsequently be studied in an electron microscope. [16, 17]

With this success in mind, we developed a system to cleanly dissect cavities following their rf tests, for further analysis in an electron microscope and an energy dispersive x-ray system. The latter is used for the elemental analysis of defects.

Our improved thermometry system, combined with a second setup to measure the cavity quality (described in Chapter 4), and our ability to examine the rf surface in a microscope provided us with a very powerful set of tools to study loss mechanisms. A measurement of the cavity quality sums the power dissipation of all active loss mechanisms. For detailed studies we then use thermometry to localize the sources of these losses. Due to the system's improved resolution, new losses, that previously have gone undetected, can now be observed. Temporal changes in power dissipation, that often provide vital information on the mechanisms involved, can now also be recorded because of the higher speed of the thermometry system. Finally, the microscopy enables us to correlate the temperature data with the physical properties of lossy sites — an important step that was lacking in many previous cavity studies.

1.2.2 Experimental objectives

Armed with this new setup, we set out to systematically study both low and high field losses. In particular, we hoped to find active emission sites, since these dominate the behavior of present day cavities.

To learn to control the impact of emission, we need to fill in the gaps in our understanding of emitter behavior. What are the questions that beg to be answered?

A quantum mechanical analysis of field emission (the Fowler-Nordheim theory) predicts that the current should *not* be significant below 1 GV/m. [18] But then, why is field emission so prevalent in rf cavities? In previous dc field emission studies, micron size metallic particles with jagged features were found to be a prolific source of emitters. Is the same true of field emission in rf cavities? Until this study, active emitters in rf cavities had never been located and examined with surface analytic instruments. Our experiments demonstrate that indeed metal particles, sometimes jagged, are often found

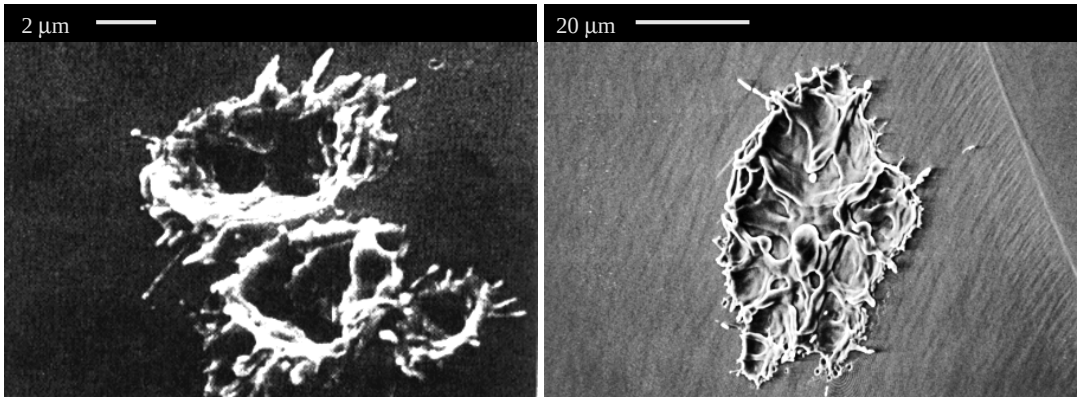

(a) (b)

Figure 1.2: Examples of emission sites. (a) Craters found on the cathode of a dc gap [22] after voltage breakdown. (b) Emission site found in a 3 GHz cavity. (It is suspected that the emitter rf processed, but thermometry data is not available to confirm this assumption.)

to cause emission in cavities. This (often qualitative) observation fits with the traditional view, that the geometric enhancement of the electric field facilitates field emission. However, it is hard pressed to account for field enhancement of more than 10 – 100, as is frequently observed. We also found, on occasion, that smooth particles and even flat sites can emit. A more sophisticated model is therefore required to explain the enhanced emission.

Field emission in both dc studies and rf cavities is frequently found to be unstable. When the electric field is increased for the first time, emission will switch on, and it continues even if the electric field is lowered to values where no emission was previously recorded. We observed such events frequently during our studies. But what is the cause of activation? We have shown that on some occasions the arrival of particles is a simple cause.

There have been several studies that suggest condensation of gas can also activate emitters. [19, 20] Does this take place at particle sites as well? Our results confirm gas activation in many cases. In particular, we identified a particulate emitter that showed reproducible increases in emission with experimental conditions that promoted the condensation of gases on the particles. Decreases of emission consistent with gas removal were also observed.

Occasionally emitters also switch off abruptly, this being known as *processing* or *conditioning*. Here more is already known. DC high voltage studies with niobium and copper electrodes have shown that field emission is almost always a pre-cursor to voltage breakdown, and that the breakdown event destroys the emitter (e.g., [21–23]) The breakdown event is associated with a discharge and its accompanying plasma. Frequently multiple (micron size) craters are found at the site of the discharge (see Figure 1.2(a)).

Yet, there are outstanding issues about emitter processing by discharge. Is the mechanism in rf cavities the same as that for dc gaps? What is the chain of events that take place between emission and voltage breakdown? What are the factors that govern the conditions for the formation of the discharge? For example, where does the gas for the

discharge come from? Does the gas play any role in the field emission process before breakdown? Certain emitters will process at a given field, while others will not. What determines whether an emitter is processable? The experimental part of our work was designed to address many of these questions.

Prior to these experiments, we assumed that the heating by the field emission current alone is responsible for initiating the explosion. Our experiments, though, proved this hypothesis to be wrong. Microscopy revealed new features of emission sites that help us to draw a more complete picture of how field emission progresses to discharge. The evidence suggests that a plasma can coexist with rf emission before the onset of the discharge, and that gases play an important role in the progression of an emitter from steady state emission to its explosion. At first, parts of the emitter (microtips) melt due to Joule heating from the emission current. The vapor that evolves from the melting tip provides the initial source of gas that ultimately is responsible for initiating discharge.

What is puzzling about the geometric field enhancement model of emission is the observation that large areas of the rf surface, many tens of microns across, can melt during the processing of an emitter (see Figure 1.2(b)), even though steady state emission is from sub-micron regions. In many instances such regions are also surrounded by small "satellite" craters. How does field emission continue after the microtip of the emitter melts? What produces the satellite craters? Again, we found that the plasma present during the discharge can explain such features.

When the field level and the accompanying emission current is not sufficient to initiate a discharge spontaneously, it is possible to deactivate emitters by the intentional addition of helium gas in the superconducting cavity (known as *helium processing*). How does helium processing work? A number of helium processing mechanisms have been identified. We were able to demonstrate, for the first time, that one important mechanism involves discharge. This discovery also emphasizes the important role played by gas during the transition from steady state field emission to discharge.

Guided by such experimental findings, we developed numerical simulations to model the electron impact ionization of gases evolving from hot emitters. The simulations reveal some of the mechanisms underlying the discharge. Newly created ions bombard the emitter and can lead to further gas evolution. Once a sufficiently dense gas builds up and large numbers of ions accumulate near the emitter, considerable electric field enhancement results that leads to an instability in the emission current. A discharge is then created.

The improved understanding can account for certain characteristic features of discharge events, such as the occurrence of satellite craters at emission sites. The simulations also provide the basis for an understanding of the conditions required for processing. For example, both the current density and total current drawn from an emission site need to exceed threshold values. Furthermore, our simulations set a time scale for the formation of discharge conditions.

We also intended to use the advanced thermometry to gain insights into other important aspects superconducting cavity behavior. We were able to advance our understanding of thermal breakdown, multipacting and residual surface resistance mechanisms. We have identified an interaction between thermal breakdown and the activation of field emission via the gases released during the breakdown. The advanced thermometry system also enabled us to recognize weak and short lived multipacting, and we found inter-

esting examples of the activation of field emission by gases released during multipacting. Gas discharge events initiated by multipacting were documented as well, and we showed that the discharge can reduce the residual surface resistance. We also identified new sources of residual losses, due to foreign particles as well as magnetic flux generated and trapped during thermal breakdown or multipacting events.

1.3 Organization of the dissertation

The following chapter (Chapter 2) gives a brief outline of the electrodynamics of cavities. It is designed to explain the terms used throughout this report. In a second part we introduce some qualitative features of rf superconductivity needed to understand intrinsic cavity characteristics such as the finite surface resistance. We also explain the fundamental magnetic field limitation of superconducting cavities.

Chapter 3 expands upon the various anomalous cavity losses touched on in this introduction, and it summarizes the present understanding of the mechanisms. The chapter is divided into three sections. The first concentrates on losses that only occur at high fields and are the main limitation of rf cavities at present. The second section is devoted to low field losses responsible for the residual resistance. The final part then covers some of the experimental techniques used to study loss mechanisms. It also serves to explain thermometry in more detail and to put its power in context.

Chapter 4 provides an in depth description of the new thermometry and cavity quality measurement systems we built to study anomalous losses. The two are designed to complement each other. The chapter also covers the measurement techniques we used to analyze cavity behavior, and it explains the procedure we adopted to examine cavities in the electron microscope.

The remainder of the dissertation covers the results obtained with the thermometry/quality factor measurement system and from our microscopic examination of cavities.

Chapters 5 and 6 are devoted entirely to our studies of field emitters. First we discuss the data that yields information on the mechanisms responsible for enhanced field emission. We show examples of field emission from metallic particles, consistent with the idea of geometric field enhancement, and we demonstrate that in some cases the arrival of such particles can lead to the activation of field emission. However, we also present evidence here, that emission cannot be explained solely by geometric field enhancement by sharp projections. Other mechanisms, such as the adsorption of gases on the rf surface, are shown to play an important role in governing the intensity of field emitters. In particular, we present examples of emission activation due to the adsorption of gases, and the deactivation of emitters following thermal cycling.

We then turn to the important realization that the evolution of gas from hot field emitters and its ionization by the emission current is pivotal to rf processing. We will present microscopy data which demonstrates that such processing events can result in the explosion of the emission site. It is the production of a plasma that expedites the explosion by augmenting the dissipated power in the emitter.

We also describe the unprecedented microscopic examination of helium processed field emitters and the identification of two distinct types of helium processing. One class proceeds by sputtering the rf surface with helium ions (or by some similar mechanism),

resulting only in superficial changes to the emitter. The other class processes by the same mechanism as explosive rf processing and provides confirmation of the importance of plasma activity to rf processing. This fact is at odds with our previous assumption, that the field emission current alone is responsible for the explosion.

Our results with rf and helium processed emitters hence allow us to formulate a revised theory of the evolution of field emitters from steady state emission to the processing stage. Based on this theory, predictions on the processability of field emitters can be made. The description of the revised model also provides the introduction to Chapter 6.

Numerical simulations of field emission and the early stages of rf processing with a specially modified version of the program MASK are discussed in Chapter 6. We will show that these simulations confirm the important role played by the plasma, which is critical to rf processing and for the creation of such features as satellite craters. We also discuss some of the criteria that need to be met for rf processing to occur.

New information on two further high field loss mechanisms, thermal breakdown and multipacting, are covered in Chapter 7. Each is discussed in a separate section.

Several interesting observations on thermal breakdown are described. Among them are the fact that:

1. Defects at or near the equator weld of the cavity appear to be the most common cause for thermal breakdown.

2. Particles falling into the cavity during its preparation are a potential source of thermal breakdown.

3. Thermal breakdown is responsible for generating and trapping magnetic flux that results in significant increases of the residual surface resistance in the breakdown area.

Thanks to our high speed thermometry system we were also able to identify multipacting events in our cavities. Several new discoveries are described, including:

1. The direct observation of two-point multipacting in progress in elliptical cavities. These cavities were believed to be multipacting free.

2. The fact that multipacting, similar to thermal breakdown, produces and traps magnetic flux that increases the residual surface resistance.

3. The observation that multipacting can initiate a discharge which removes gas adsorbates on the rf surface, resulting in significant improvements of the residual surface resistance.

4. Evidence that multipacting may precipitate thermal breakdown, thereby limiting cavity performance.

Chapter 8 then covers our results from studies of the residual resistance of niobium. Some of these results were only made possible by the high sensitivity of the thermometry system. We found that:

1. Niobium-hydride precipitation (Q-virus) occurs preferentially along the equator weld, resulting in abnormally high rf losses in this region.

2. Titanium, used as a high temperature solid state getter to improve the purity of niobium, diffuses along niobium grain boundaries much faster than in the bulk. Above 1500 – 1600 °C diffusion over macroscopic distances is possible, and the titanium may even impregnate the entire cavity wall. A dramatic reduction of the cavity quality is subsequently observed.

The unprecedented observation of particle arrival on the rf surface during cavity operation is also discussed in this chapter. In some cases, such particles were responsible for the activation of field emission, as is discussed in Chapter 5.

Finally, we conclude with Chapter 9 with a summary.

Chapter 2

Cavity fundamentals

2.1 Introduction

In this chapter we give an overview of the basics of superconducting cavities. We start by discussing the electrodynamics of radiofrequency (rf) cavities, the accelerating mode and the general expressions used to describe power dissipation. Although later we focus exclusively on superconducting cavities, this section applies equally well to both normal and superconducting cavities.

In the second part, we introduce the rudiments of superconductivity. In particular, we will illustrate why superconducting cavities dissipate a small, but finite amount of power despite the fact that superconductors carry dc currents without losses. We will also explain the fundamental magnetic field limitation of superconducting cavities. Practical field limitations will be discussed in the next chapter.

This chapter is not designed to give an in depth overview of the theory of cavities. Rather, we will emphasize the aspects needed to understand this report. For further information the reader is referred to numerous texts that give an excellent review of the subject (see, for example, [2, 8, 24, 25]).

2.2 Electrodynamics

2.2.1 RF fields in cavities

2.2.1.1 Cavity modes

The rf fields in cavities are derived from the eigenvalue equation

$$\left(\nabla^2 - \frac{1}{c^2}\frac{\partial^2}{\partial t^2}\right)\left\{\begin{array}{c}\mathbf{E}\\ \mathbf{H}\end{array}\right\} = 0, \tag{2.1}$$

which is obtained by combining Maxwell's equations. [24] It is subject to the boundary conditions

$$\hat{n}\times\mathbf{E} = 0 \quad \text{and} \quad \hat{n}\cdot\mathbf{H} = 0 \tag{2.2}$$

at the cavity walls. Here $\hat{n}$ is the unit normal to the rf surface, c is the speed of light and $\mathbf{E}$ and $\mathbf{H}$ are the electric and magnetic field respectively.

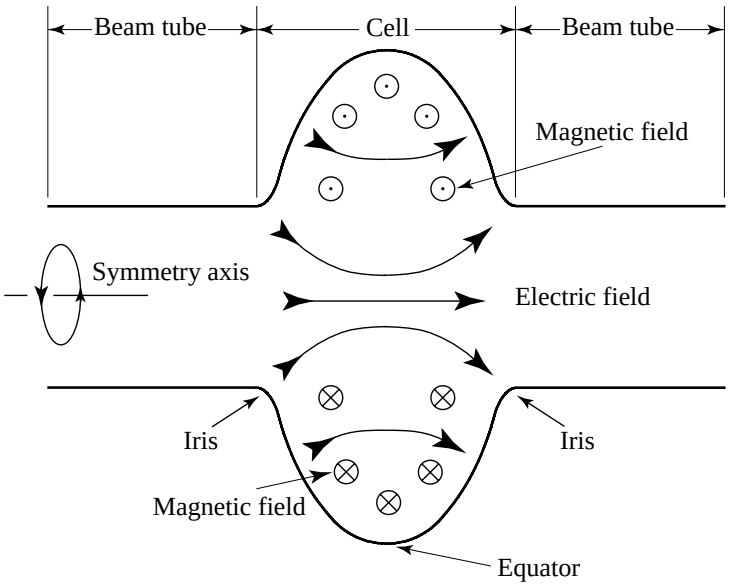

Figure 2.1: Schematic of a generic speed-of-light cavity. The electric field is strongest near the symmetric axis, while the magnetic field is concentrated in the equator region.

In cylindrically symmetric cavities, such as the pillbox shape, the discrete mode spectrum given by (2.1) splits into two groups, transverse magnetic (TM) modes and transverse electric (TE) modes.[1] For TM modes the magnetic field is transverse to the cavity symmetry axis whereas for TE modes it is the electric that is transverse. For accelerating cavities, therefore, only TM modes are useful.[2]

Modes are classified as TM_{mnp}, where the integers m, n, and p count the number of sign changes of E_z in the ϕ, ρ, and z directions respectively.[3] Only TM_{0np} ($n = 1, 2, 3\ldots$, $p = 0, 1, 2\ldots$) modes have a nonvanishing longitudinal electric field on axis, and the TM_{010} mode is used for acceleration in most cavities.

For practical reasons, a simple pillbox shape is not used for speed of light cavities. [2] Instead, a deformed version as shown in Figure 2.1 is preferred. The electric field of the TM_{010} mode is greatest at the irises and near the symmetry axis, while the magnetic field is concentrated in the equator region. The geometry of the cell and the addition of beam tubes makes it very difficult to calculate the fields analytically, and one reverts to numerical simulations with codes such as SUPERFISH [26] or SUPERLANS [27,28] to obtain the field profiles. Although TM modes acquire a finite H_z due to the perturbative effect of the beam tubes, the main characteristics of the TM modes are preserved, and one still uses the TM_{mnp} classification scheme to identify modes.

[1] Strictly, this statement is only true if there are no beam tube openings.
[2] The symmetry axis usually is chosen to coincide with the beam line.
[3] TE modes are classified in a similar manner.

2.2.1.2 The accelerating field

The accelerating voltage ($V_{\rm acc}$) of a cavity is determined by considering the motion of a charged particle along the beam axis. For a charge q, by definition,

$$V_{\rm acc} = \left| \frac{1}{q} \times \text{maximum energy gain possible during transit} \right|. \tag{2.3}$$

We used speed-of-light structures in our tests, and the accelerating voltage is therefore given by

$$V_{\rm acc} = \left| \int_{z=0}^{z=d} E_z(\rho = 0, z) e^{i\omega_0 z/c} dz \right|, \tag{2.4}$$

where d is the length of the cavity and ω_0 is the eigenfrequency of the cavity mode under consideration. Frequently, one quotes the accelerating field $E_{\rm acc}$ rather than $V_{\rm acc}$. The two are related by

$$E_{\rm acc} = \frac{V_{\rm acc}}{d}. \tag{2.5}$$

With single cell cavities, the choice of d is somewhat ambiguous, since the beam tubes can be made arbitrarily long. Hence $E_{\rm acc}$ is not uniquely defined. Frequently one therefore calculates $E_{\rm acc}$ for an equivalent infinite periodic structure and quotes its $E_{\rm acc}$ for the single cell.

2.2.1.3 Peak surface fields

When considering the practical limitations of superconducting cavities, two fields are of particular importance — the peak electric surface field ($E_{\rm pk}$) and the peak magnetic surface field ($H_{\rm pk}$). As will be discussed in Section 2.3.3, 3.2.1, and 3.2.2, in most cases these fields determine the maximum achievable accelerating gradient in cavities. Figure 2.2 shows the surface electric and surface magnetic field in the cavities we tested. The surface electric field peaks near the irises, and the surface magnetic field is at its maximum near the equator.

To maximize the potential cavity performance, it is important that the ratios of $E_{\rm pk}/E_{\rm acc}$ and $H_{\rm pk}/E_{\rm acc}$ be minimized. In an ideal pillbox cavity, the ratios are given by

$$\frac{E_{\rm pk}}{E_{\rm acc}} = \frac{\pi}{2} = 1.6 \tag{2.6}$$

$$\frac{H_{\rm pk}}{E_{\rm acc}} = 30.5 \ \frac{\rm Oe}{\rm MV/m}. \tag{2.7}$$

The addition of beam tubes increases these values. For example, the ratios of the cavities discussed in this report are

$$\frac{E_{\rm pk}}{E_{\rm acc}} = 1.83 \tag{2.8}$$

$$\frac{H_{\rm pk}}{E_{\rm acc}} = 45 \ \frac{\rm Oe}{\rm MV/m}. \tag{2.9}$$

These values were obtained by solving for the fields in the TM_{010} mode numerically with the code SUPERFISH. [26]

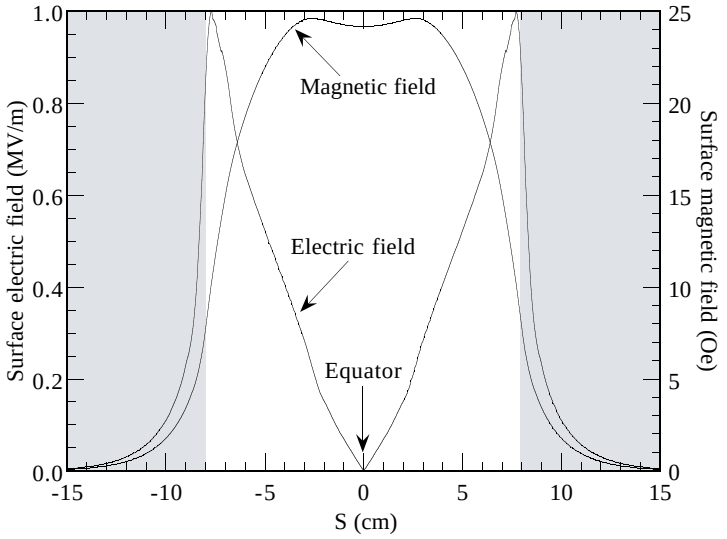

Figure 2.2: Surface electric and magnetic fields as a function of distance from the cavity equator in the elliptical cavity shape used in tests. In both cases $E_{\rm pk} = 1$ MV/m. The light area delimits the cell region of the cavity.

2.2.2 RF power dissipation and cavity quality

To support the electromagnetic fields in the cavity, currents flow in the cavity walls at the surface. If the walls are resistive, the currents dissipate power. The resistivity of the walls is characterized by the material dependent surface resistance $R_{\rm s}$ which is defined via the power $P_{\rm d}$ dissipated per unit area:

$$\frac{dP_{\rm d}}{da} = \frac{1}{2}R_{\rm s}|\mathbf{H}|^2. \tag{2.10}$$

In this case, H is the local surface magnetic field. In Section 2.3 we will show that superconductors are not completely lossless at rf frequencies, so that (2.10) applies equally to normal conductors and superconductors.

Directly related to the power dissipation is an important figure of merit called the cavity quality (Q_0). It is defined as

$$Q_0 = \frac{\omega_0 U}{P_{\rm d}}, \tag{2.11}$$

U being the energy stored in the cavity. The Q_0 is just 2π times the number of rf cycles it takes to dissipate an energy equal to that stored in the cavity.

For all cavity modes, the time averaged energy in the electric field equals that in the magnetic field, so the total energy in the cavity is given by

$$U = \frac{1}{2}\mu_0\int_{\rm V}|\mathbf{H}|^2\,dv = \frac{1}{2}\epsilon_0\int_{\rm V}|\mathbf{E}|^2\,dv, \tag{2.12}$$

where the integral is taken over the volume of the cavity. Equation 2.10 yields the dissipated power

$$P_{\rm d} = \frac{1}{2}\int_{\rm S}R_{\rm s}|\mathbf{H}|^2\,ds, \tag{2.13}$$

where the integration is taken over the interior cavity surface. (By keeping R_s in the integral we have allowed for a variation of the surface resistance with position.) Thus one finds for Q_0:

$$Q_0 = \frac{\omega_0 \mu_0 \int_V |\mathbf{H}|^2 \, dv}{\int_S R_s |\mathbf{H}|^2 \, ds}. \tag{2.14}$$

The Q_0 is frequently written as

$$Q_0 = \frac{G}{\bar{R}_s}, \tag{2.15}$$

where

$$G = \frac{\omega_0 \mu_0 \int_V |\mathbf{H}|^2 \, dv}{\int_S |\mathbf{H}|^2 \, ds} \tag{2.16}$$

is known as the *geometry constant*, and

$$\bar{R}_s = \frac{\int_S R_s |\mathbf{H}|^2 \, ds}{\int_S |\mathbf{H}|^2 \, ds} \tag{2.17}$$

is the mean surface resistance (weighted by H^2). For the 1.5 GHz cavities we studied $G = 270\ \Omega$. The (mean) surface resistance of well prepared niobium at 1.6 K can be as low as 5 nΩ.[4] Hence Q_0 values on the order of 5×10^{10} are possible. In rare cases even greater Q_0 values have been achieved experimentally.

2.3 Superconductivity

The discussion so far applies equally well to both normal and superconducting cavities. However, to understand the behavior of superconducting cavities some knowledge of superconductivity[5] is required. Numerous texts have been written about this subject as applied to superconducting rf cavities [2,8] and the *Proceedings of the Workshops on RF Superconductivity* [29–35] are a valuable resource as well. We will therefore concentrate on the salient aspects that pertain to the experimental results reported here.

2.3.1 Theory of superconductivity

It is well known that superconductors lose their *dc* resistivity completely below a critical temperature T_c. Of all the elements, niobium has the highest critical temperature with $T_c = 9.22$ K. The mechanism responsible for this fascinating behavior is complex but was successfully explained by Bardeen, Cooper, and Schrieffer (BCS) in 1957. [36]

According to the BCS theory, it is energetically favorable for electrons in superconductors to pair off as so-called "Cooper pairs" to yield a bosonic pseudo-particle. This pairing process is assisted by phonons. Each pair consists of two electrons of opposite momentum and spin. The temperature dependent pairing energy $\Delta(T)$ (per electron) is responsible for creating an energy gap in the electronic spectrum between the bosonic ground state and the energy levels of the unpaired fermionic electrons. $\Delta(T = 0)$ is fairly small, on the order of a few meV.

[4] The value of 5 nΩ should be contrasted with a surface resistance of 2 mΩ for copper at cryogenic temperatures.

[5] Our discussion applies to classic, low temperature superconductors.

Although the paired state is energetically favorable below T_c, not all electrons are in the bosonic ground state when $0 < T < T_c$, because there is a finite probability that some pairs are split by thermal excitations. The probability is governed by the Boltzmann factor $\exp(-\Delta(T)/k_b T)$, k_b being the Boltzmann constant. Below $T = T_c/2$ the Cooper pair density $n_s(T)$ is close to $n_s(T = 0)$, and the number of unpaired electrons is given by

$$n_e \approx 2n_s(T = 0) \exp\left(-\frac{\Delta(T)}{k_b T}\right) \qquad \left(T < \frac{T_c}{2}\right). \tag{2.18}$$

In this temperature range the energy gap $\Delta(T)$ is also close to its zero temperature value. The BCS theory predicts that $\Delta(T = 0) = \alpha k_b T_c$, $\alpha \approx 1.76$. Hence,

$$n_e \approx 2n_s(T = 0) \exp\left(-\alpha \frac{T_c}{T}\right). \tag{2.19}$$

2.3.2 Superconductor surface resistance

Although superconductors do not exhibit any dc resistivity, there are small losses for rf currents. This fact can be explained by a model of interpenetrating normal conducting electrons and superconducting Cooper pairs when $T > 0$ (*two fluid model*). Collisions between Cooper pairs and lattice defects, impurities, or phonons are insufficient to split the pairs and scatter them out of the ground state. Hence, any current carried by these pairs flows without resistance. On the other hand, the unpaired electrons can be scattered and dissipate energy. Nevertheless, the dc resistivity of a superconductor is zero because the lossless Cooper pair current "shorts out" any fields in the superconductor. The normal conducting electrons never see an electric field and do not contribute to the current flow.

In the rf case the situation is different. Although Cooper pairs cannot be scattered, they do possess inertia. At microwave frequencies, they no longer screen externally applied fields completely and normal conducting electrons are accelerated. This component of the electron fluid then causes power dissipation. By (2.19) the number of unpaired electrons declines exponentially with temperature and one observes a corresponding decline in the surface resistance of the superconductor.

A simple application of the two fluid model yields a surface resistance

$$R_s \propto \omega^2 \exp\left(-\alpha \frac{T_c}{T}\right) \qquad \left(T \leq \frac{T_c}{2}\right) \tag{2.20}$$

that drops exponentially to zero at $T = 0$. [2] Measurements on real superconductors show that the surface resistance is in fact given by

$$R_s = A_s \frac{\omega^2}{T} \exp\left(-\alpha \frac{T_c}{T}\right) + R_0 = R_{BCS}(T) + R_0 \qquad \left(T \leq \frac{T_c}{2}\right). \tag{2.21}$$

Here A_s is a material dependent constant. The first term is the BCS resistance, which is similar to that given by (2.20). The second term in (2.21) is a temperature independent *residual resistance*. Its nature is not completely understood, but it has been established that it is affected by, for example, impurities, trapped flux, adsorbed gases, and microscopic particles. We will discuss these in Chapter 3.

The R_0 term always dominates R_s at low temperatures. For well prepared niobium $R_0 = 5$ nΩ is possible. It is therefore pointless to cool superconducting cavities to temperatures for which $R_{BCS} \ll R_0$. At 1.5 GHz, for example, the residual resistance of niobium begins to dominate at $T < 1.8$ K.

2.3.3 Critical magnetic field

One of the unique characteristics of superconductors is that they expel any externally applied dc magnetic field H_{ext} provided that H_{ext} is less than a critical field. This phenomenon is called the *Meissner effect* (see, for example, [37,38]). Two classes of (low temperature) superconductors exist, known as type I and type II. The superconducting mechanism is the same in both cases, but the surface energy for normal conducting–superconducting boundaries differs for the two types. As a result, type I and type II superconductors behave differently in a magnetic field.

In the case of type I superconductors, the surface energy is positive. This class remains in the perfect Meissner state in applied dc fields up to a temperature dependent critical field H_c. However, by expelling the applied field the superconductor raises its energy. When $H_{ext} > H_c$ the magnetic energy exceeds the energy gained by producing Cooper pairs, and the sample goes normal conducting ("quenches"). The temperature dependence of H_c is given by [37]

$$H_c(T) = H_c(0)\left[1 - \left(\frac{T}{T_c}\right)^2\right]. \tag{2.22}$$

Type II superconductors (such as niobium [39] and Nb_3Sn) are different because the surface energy of a superconducting–normal conducting interface is negative, so that the creation of interfaces can be energetically favorable. Similar to type I materials, they too expel a dc magnetic field completely up to a lower critical field H_{c1}. Rather than quenching above this value, though, they enter what is known as the mixed state, where normal conducting cores of radius ξ_0 form in the superconductor.[6] Each core carries a magnetic flux quantum $\Phi_0 = hc/2e$. The density of these flux tubes, or "fluxoids", increases with H_{ext} until the entire sample becomes normal conducting at an upper critical field H_{c2}.

Based on these observations with dc fields, one might believe that rf cavities can only operate effectively up to a field $H_{pk} = H_{c1}$ for type II or H_c for type I materials. However, in the rf case the situation is relaxed with respect to dc fields.

It takes a normal conducting region a finite amount of time to nucleate in a superconductor when H_{ext} exceeds H_c (H_{c1} in type II materials). The nucleation time is on the order of 10^{-6} s [40] which is long compared to an rf period at microwave frequencies. Theory predicts, that the complete Meissner state persists up to a superheating critical field H_{sh} where $H_{sh} > H_c$ (type I), $H_{sh} > H_{c1}$ (type II). [41] For niobium, the superheating critical field expected from theory is approximately 2200 – 2400 Oe. [8] The corresponding peak electric field for a typical cavity shape is about $E_{pk} = 100$ MV/m. An exact value of H_{sh} still needs to be measured, but experiments have indeed confirmed that niobium cavities can operate at $H_{pk} > H_{c1}$. [42]

[6] ξ_0 is known as the *coherence length* and is a measure of the distance over which the material can revert from the superconducting state to the normal conducting state.

In fact, real cavities of the type used in our test rarely exceed fields of $E_{\mathrm{pk}} = 60$ MV/m because of a number of mechanisms not fundamental to superconductivity. It is these mechanisms, that we set out to study. An overview is given in the next chapter.

Chapter 3

Cavity loss mechanisms

3.1 Introduction

In this chapter we will briefly discuss the various anomalous loss mechanisms that are encountered in a typical cavity, as well as the techniques that have been developed in the past to study them. The losses are called "anomalous" because they are not predicted by the BCS theory of superconductivity.

The chapter is divided into three sections. The first is dedicated to losses that only manifest themselves at high electric or magnetic fields and limit the cavity performance — field emission, thermal breakdown, and multipacting. Especially the first two often prevent present day cavities from achieving their full potential. Much work has gone into understanding and eliminating them. The second section covers some of the low field loss mechanisms that govern the residual resistance R_0 — flux trapping, adsorbed gases, and resistive particles. The last section then describes some of the common techniques used to identify and to measure cavity loss mechanisms.

For an in depth discussion of these and related loss mechanism References [2,8] among others are recommended for further reading.

3.2 High field loss mechanisms

The loss mechanisms we are about to discuss usually only manifest themselves when cavity fields exceed $E_{\mathrm{pk}} \approx 10$ MV/m. Losses tend to increase drastically with E_{pk} and hence it is not appropriate to include them in the R_0 term in Equation 2.21. Because of the rapid growth of the power dissipation with field, these mechanisms limit the maximum accelerating gradient that can be attained. Hence many experiments have been adopted to understand and subsequently eliminate these loss mechanisms. For the same reason, the main emphasis of our experiments was to gain new information on high field loss mechanisms.

3.2.1 Field emission

The most frequently encountered limitation in superconducting cavities is electron field emission. Although the basic principle of field emission is understood, a detailed and quantitative theory of the mechanisms involved is still lacking. It is known that field

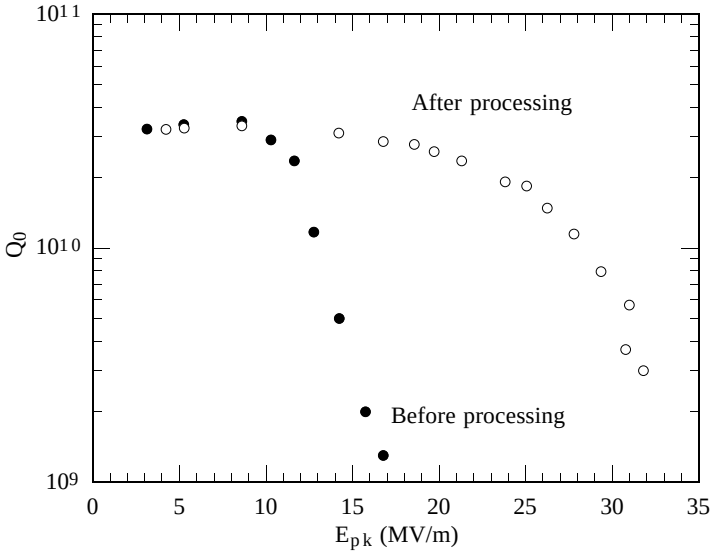

Figure 3.1: Q_0 versus $E_{\rm pk}$ curve of a cavity that was heavily loaded by field emission. The left curve was obtained before the emitter ceased to emit and the right curve was obtained afterwards. Although the original emitter no longer was active in the latter case, other emission sites started up at higher fields and limited the maximum achievable field.

emission is a quantum mechanical process whereby electrons tunnel out of the cavity wall from microscopic defects, assisted by the cavity's electric field.

A good discussion of field emission is given in Reference [43]. Nevertheless, we will provide a short overview of the field, because a significant fraction of our studies was devoted to gaining a better understanding of field emission.

3.2.1.1 Observation of field emission

Field emission is characterized by an exponential drop in the Q_0 versus $E_{\rm pk}$ curve as shown in Figure 3.1. At the same time x-ray detectors placed near the cryostat detect energetic (0.1 – 1 MeV) x-rays when field emission is active.

In accelerating the emission charges, the electromagnetic fields dissipate power, leading to the rapid decline of the Q_0. The accelerated current impacts the cavity walls producing heat that can be detected by thermometry, and bremsstrahlung x-rays that can be observed with x-ray detectors. The increased temperature of the cavity surface in the bombarded region also raises the power dissipation. Ultimately a quench of the superconductive state may result (see Section 3.2.2).

As will be discussed shortly, the field emission current increases exponentially with the electric field. Hence, once field emission activates, it becomes difficult to raise the fields much further due to the high rf power demand on the microwave generator as well as the power dissipation in the helium bath. Occasionally, an emitter abruptly extinguishes ("processes") and the Q_0 recovers, so that the electric field can be increased further (Figure 3.1). The processing mechanism is not completely understood and thus was addressed by our studies to gain a clearer picture. Despite the benefits gained from processing, other emitters become active at higher fields and again limit the maximum

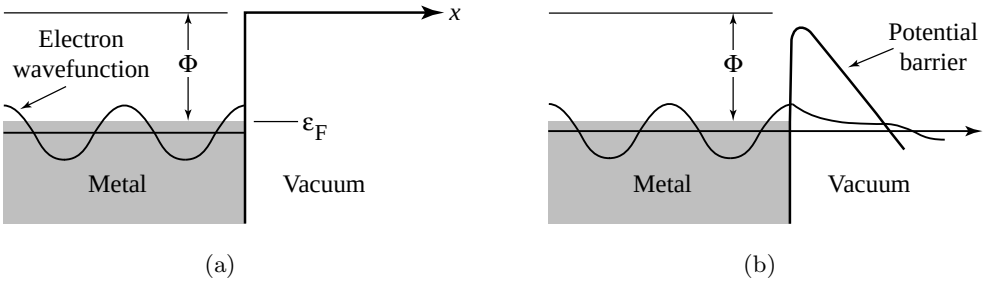

Figure 3.2: Electrostatic potential of the metal–vacuum interface. (a) No electric field applied, (b) with an electric field applied.

attainable E_{pk}. Not only does the power dissipated by a single emitter rise with E_{pk}, but also the total number of active emitters increases with field. Field emission therefore is the chief limitation of present day cavities.

3.2.1.2 Theory of field emission

The original theory of field emission was developed by Fowler and Nordheim in 1928 for a metal–vacuum interface as shown in Figure 3.2. [18] Ordinarily electrons are confined to the cavity walls by the potential barrier at the interface because electron energies are less than the work function Φ required for them to escape (Figure 3.2(a)). In the presence of an electric field, however, the originally infinitely thick barrier is deformed into a triangular, finite-thickness barrier. Energetic electrons can now tunnel through the barrier (Figure 3.2(b)). The triangular barrier is further lowered and rounded at its tip due to the attractive force generated between emitted electrons and the conducting surface (image charge effect). The shape of the potential barrier due to both the image charge and the applied field (E) is given by

$$V(x) = -\frac{e^2}{16\pi\epsilon_0 x} - eEx. \tag{3.1}$$

The first term results from the image charge effect.

Fowler and Nordheim found that the tunneling current I_{FN} for the potential in (3.1) is given by

$$I_{\mathrm{FN}} = j_{\mathrm{FN}} A_{\mathrm{FN}} = A_{\mathrm{FN}} \frac{e^3 E^2}{8\pi h \Phi t^2(y)} \exp\left(-\frac{8\pi\sqrt{2m_{\mathrm{e}}\Phi^3}\, v(y)}{3heE}\right). \tag{3.2}$$

The exponential nature of I_{FN} is characteristic of the quantum mechanical tunneling process. Here j_{FN} is the current density, h is Planck's constant, m_{e} and e are the positron mass and charge respectively, $y = \sqrt{e^3E/4\pi\epsilon_0\Phi^2}$ and $v(y)$ and $t(y)$ are tabulated functions [44] that account for the image charge effect. If the image charge is ignored, these functions are unity. Even for reasonable values of E they are on the order of unity and slowly varying. Hence, a plot of $\ln(I_{\mathrm{FN}}/E^2)$ versus $1/E$ yields a straight line (known as a Fowler-Nordheim plot).

For niobium ($\Phi \approx 4$ eV) Equation 3.2 predicts that field levels on the order of 3 GV/m are required to achieve microampere emission currents (assuming $A_{\mathrm{FN}} \approx 0.01\ \mu\mathrm{m}^2$). In

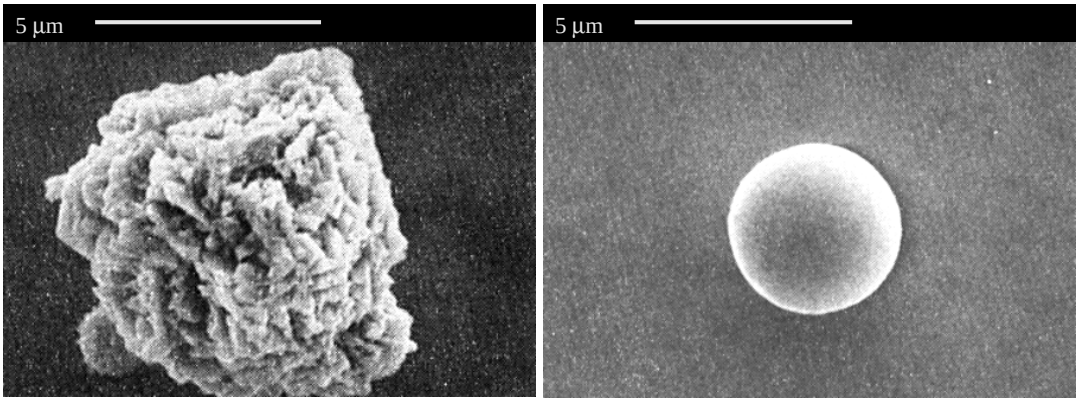

(a) (b)

Figure 3.3: (a) DC field emitting nickel particle. Emission was recorded at fields as low as 20 MV/m. (b) Spherical nickel particle found not to emit up to 120 MV/m in the same experiments. [47]

fact, field emission currents on the order of microamperes are routinely encountered in superconducting cavities at fields below 40 MV/m. Nevertheless the observed emission current follows the Fowler-Nordheim law in (3.2), provided one makes the substitution $E \to \beta_{\mathrm{FN}} E$ for all occurrences of E [45], so that

$$I_{\mathrm{FN}} = j_{\mathrm{FN}} A_{\mathrm{FN}} = A_{\mathrm{FN}} \frac{e^3 (\beta_{\mathrm{FN}} E)^2}{8\pi h \Phi t^2(y)} \exp\left(-\frac{8\pi\sqrt{2m_{\mathrm{e}}\Phi^3}\, v(y)}{3he\beta_{\mathrm{FN}} E} \right) \tag{3.3}$$

$$y = \sqrt{\frac{e^3 \beta_{\mathrm{FN}} E}{4\pi\epsilon_0 \Phi^2}}. \tag{3.4}$$

Generally, β_{FN} values in the range $50 < \beta_{\mathrm{FN}} < 1000$ and A_{FN} values in the range of 10^{-18} m^2 $< A_{\mathrm{FN}} < 10^{-9}$ m^2 have been observed in superconducting cavities. More careful dc studies carried out at Wuppertal even revealed that A_{FN} values as low as 10^{-22} m^2 and as high as 10^{-4} m^2 are possible. [46]

Geometric field enhancement Originally, it was believed that electric field enhancement due to sharp whiskers or similar geometric structures at the emission site is responsible for β_{FN}. In fact, most emission sites found in dc gaps are conducting particles such as iron, chromium, nickel, copper, and carbon. One example of such an emitting particle is shown in Figure 3.3(a). Its jagged appearance indeed conforms with the theory of emission by field enhancement. Hence, it comes as little surprise that the smooth particle in Figure 3.3(b) did not emit.

The field enhancement factors calculated for simple structures are typically $\beta_{\mathrm{FN}} \leq 10$. [47–50] However, values of β_{FN} for emitters found in dc studies as well as in rf studies range from $\beta_{\mathrm{FN}} = 100$ – 1000. [51] Rarely could geometric structures with aspect ratios required for β_{FN} values up to 1000 be identified in cavities or dc gaps.

Higher β_{FN} values can be obtained with geometric structures with moderate aspect ratios if a small whisker is present on the tip of a larger one (see Figure 3.4). We will

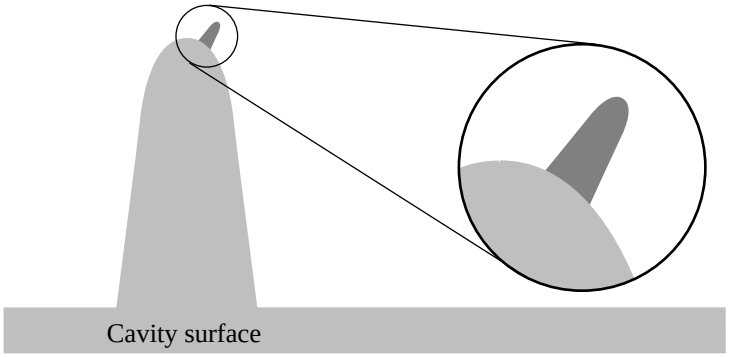

Figure 3.4: Substantial field enhancement up to several hundred can be achieved if a small whisker sits on a large one (tip-on-tip model).

show several examples of such field emitters found in cavities with our thermometry system. According to this "tip-on-tip" model the β_{FN} values of each structure roughly multiply to give the overall enhancement factor. [47] If each whisker has a β_{FN} value of 10, then the total enhancement factor is close to 100. Studies at Saclay have indeed shown that artificially introduced particles with jagged edges and also scratches emitted with β_{FN} values given by the tip-on-tip model, whereas smooth spheres did not emit. (The particles shown in Figure 3.3 are from this study.) Still, the tip-on-tip model is hard pressed to account for the frequently observed β_{FN} values in excess of 100.

Many observations remain inconsistent with the simple geometric explanation of electron field emission, beginning with the unphysical values for A_{FN} found at Wuppertal. Values of $A_{\mathrm{FN}} = 10^{-4}$ m^2 are many orders of magnitude larger than the largest emission sites found, and $A_{\mathrm{FN}} = 10^{-22}$ m^2 is equally unphysical because the emission region would have to be subatomic in size. Furthermore, it was found in dc experiments that despite their similar geometric appearance only a small fraction (5 – 10 %) of all particles present on a niobium surface field emit. [52, 53]

There are also other observations that cannot be explained by geometric field enhancement. For example, field emitters have been shown to suddenly activate irreversibly. Such events can be precipitated by administering gases, like oxygen, to the cavity. [19] Subsequent cycling to room temperature and retesting has shown that often the emitters are deactivated again. However, further admission of gases to the cavity may reactivate the same emitters. Even if gases are not artificially added to the cavity, activation of emitters has been observed and we studied such events extensively. We will show that in some cases the activation of emitters can be correlated with other events in the cavity (such as thermal breakdown), which are a likely source of gases.

Another observation inconsistent with geometric field enhancement is the fact that field emission from niobium surfaces can be deactivated by vacuum baking the sample to 1400 °C. [46,52,53] One might believe that geometric defects become less acute due to the heat treatment. However, subsequent heating to 200 – 600 °C activates many emitters, thereby ruling out that hypothesis. Instead it is believed that the interface between the emitting particles and the niobium surface plays an important role in governing field emission. Heat treatment is responsible for changing this interface layer.

There are many qualitative, and perhaps somewhat speculative, models for field

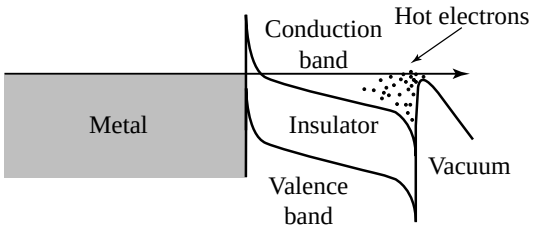

Figure 3.5: Band diagram of a metal–insulator–vacuum interface as it applies to the MIV model.

emission enhancement which have therefore been developed. They are chiefly based on the fact that contaminants and defects on the rf surface affect the electronic band structure of the system. The following are short descriptions of the main models.

MIV model An example is the metal–insulator–vacuum (MIV) model [54] which assumes that an insulator is present on the metallic rf surface. Since most metals, including niobium, possess a natural oxide layer, this model may apply to niobium rf cavities. For niobium the oxide is about 50 Å thick.

The blocking contact at the metal–insulator interface under zero field conditions prevents the injection of electrons into the insulator. However, when an electric field is applied it penetrates the insulator, and at sufficiently high fields electrons can be injected into the conduction band of the insulator. In the insulator region, the electrons gain energy (are heated) by the electric field and are emitted thermionically into the vacuum at the second interface (see Figure 3.5). Emission therefore follows the Richardson-Dushman law of thermionic emission:

$$j_{\mathrm{R}} = C_{\mathrm{R}} T_{\mathrm{e}}^2 \exp\left(-\frac{\chi}{k_{\mathrm{b}} T_{\mathrm{e}}}\right) \tag{3.5}$$

where χ is the electron affinity of the insulator, T_{e} is the electron temperature and C_{R} is a constant. According to the MIV model, T_{e} to first order is proportional to the macroscopically applied field, so that

$$j_{\mathrm{R}} \propto E^2 \exp\left(-\frac{A}{E}\right) \tag{3.6}$$

which has the form of the Fowler-Nordheim equation (A is a constant).

MIM model The metal–insulator–metal (MIM) model was developed as an extension to the MIV model. In addition to the metal–insulator interface a metal flake sits on top of the insulator. [54] The basic emission mechanism is the same as with the MIV model. However, because the flake is not grounded it "probes" the electric field nearby and adopts the potential close to the equipotential at the flake's highest point. [54, 55] The potential at this point is thereby "transmitted" to the particle–insulator interface. If the flake height is h and the insulator thickness is d then the externally applied field is enhanced by a factor on the order of h/d in the insulator region.

The MIM model appears to very applicable to field emission in rf cavities, since past studies have shown that emission almost always occurs from sites where conducting particles are found.

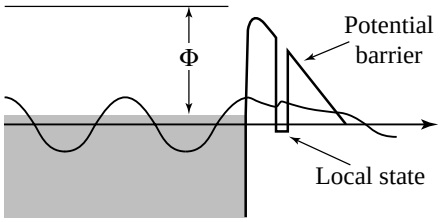

Figure 3.6: Band diagram used in Reference [56] for a metal–vacuum interface with a local energy level due to an adatom. The tunneling of electrons with energies close to the local state is greatly enhanced.

Resonant tunneling To account for enhanced emission from gas condensation, another model assumes that adatoms are responsible for creating localized energy levels near the metal surface as is schematically shown in Figure 3.6. One dimensional calculations [56] show that the tunneling process of electrons with energies close to the localized states can be resonantly enhanced (see Figure 3.6). Halbritter [57], for example, suggests that adsorbed water with its strong dipole moment is crucial to enhanced electron field emission. Water is certainly one of the main adsorbates on the cavity walls, especially if the cavity is not baked following assembly, as is customary.

The one dimensional current calculations predict that tunneling is enhanced by up to a factor of 10^4 for adsorbates less than a single monolayer thick. Although this mechanism alone is still insufficient to turn a β_{FN} value of 10 due to a geometric enhancement into a β_{FN} value of 100, it may, in conjunction with other mechanisms, explain the observation that adsorbed oxygen enhances field emission as discussed in Reference [19]. We, too, will provide experimental evidence of field emission enhancement by small amounts of gas.

In light of the present knowledge and level of understanding, it now is believed that field emission enhancement is due to a combination of geometric field enhancement and some other model (or models), and therefore depends on both foreign particulates as well as the interface or condensed gases. Whatever the complete explanation may be, it is clear that the values for β_{FN} and A_{FN} cannot be deduced from the physical geometry of the field emitters alone. Nevertheless the Fowler-Nordheim parameters provide a valuable means of characterizing the emission current.

3.2.1.3 Avoiding field emission

Much effort has been expended in reducing field emission in rf cavities. Of paramount importance is cleanliness throughout the preparation stage of the cavities. All cleaning and mounting is carried out with high purity solvents/water and in clean rooms. Prior to assembly, cavities are routinely chemically etched to remove several micrometers of surface material. Other treatments, such as high pressure rinsing [58] and heat treatment [59–61] have also been developed to avoid contaminants or at least to deactivate them. A more detailed discussion of the preparation procedure used at Cornell is given in Section 4.6.1.

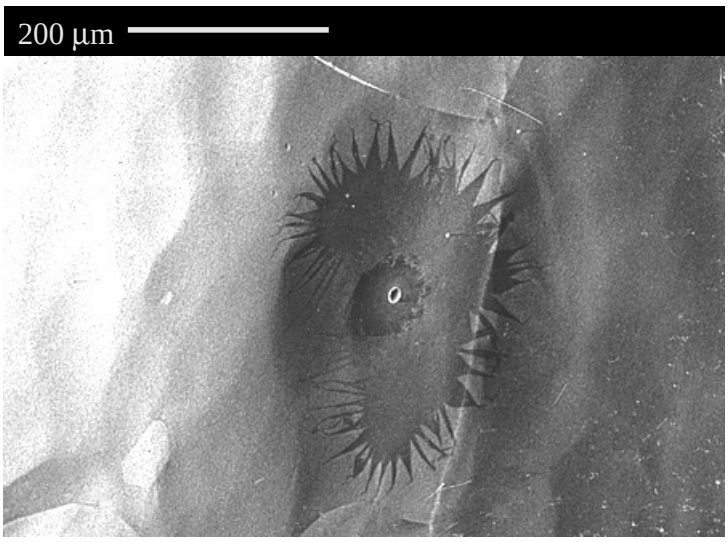

Figure 3.7: RF processed field emitter found in a 3 GHz cavity.

3.2.1.4 RF processing

Despite all precautions, some particulates do make it to the cavity surface and cause field emission. In this case one can perform in situ high power processing, whereby the cavity is pulsed with high power pulses (up to 1 MW for as long as 1 ms). [17,62] Higher electric fields are attained during the pulses, driving up the emission current. Frequently the deactivation of emitters results (rf processing). Such events may also occur in continuous wave (cw) operation at low power.

Microscopic examinations of processed emitters located by thermometry in 3 GHz cavities have demonstrated, that in many cases rf processing is the result of an explosion of the emitter. [16] An example of such an exploded site is shown in Figure 3.7. Low power (cw) experiments with 5.8 GHz "mushroom" cavities, specially designed for examination in an SEM, also revealed such exploded sites[1] (see Figure 3.8). [63]

Molten craters and molten debris are found at the center of these sites, surrounded by a larger dark region called a "starburst." Until recently, it was assumed in the superconducting rf community that the emission current density at high fields was so great, that the current's Joule losses melted any particles originally at the center of the starburst and caused them to explode (see, for example, [17, 63]). RF processing thus takes place once the emitted current density (and hence the product $\beta_{\mathrm{FN}} E_{\mathrm{pk}}$) exceeds a critical value. It is thought that the explosive event also creates the starburst.

Starbursts are a common feature of many processed emitters and, since they are visible at low magnification, serve as a useful guide for locating emitters in the SEM. However, they are known to fade within an hour when exposed to air, so field emission samples have to be stored under vacuum or in a nitrogen atmosphere to preserve starbursts. Experiments carried out at Cornell [63] and Saclay [64] also confirmed that starbursts are created when arcing is initiated by dc field emitters. Sensitive Auger studies in the past have shown that the starburst region is characterized by the *absence* of

[1] However, no thermometry data is available on the prior activity of the emitter.

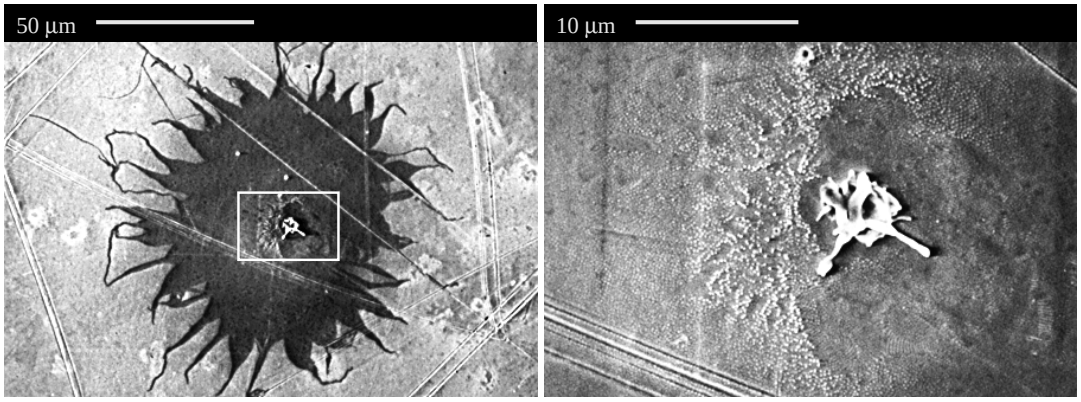

(a) (b)

Figure 3.8: Exploded emitter found in a 5.8 GHz "mushroom" cavity. (a) Low magnification picture, (b) magnified view of the framed region.

a thin layer of fluorine (thickness $\geq$ 50 Å) that is present everywhere else on the cavity surface. [65] Most likely, the fluorine is a remnant from the chemical polishing (described in Section 4.6.1). The current hypothesis is that an extended plasma, produced by a discharge during the explosion of the emitter, removes such surface contaminants. This extended plasma is thought to be merely a revealing side effect of the processing event. The cleaned region appears dark in the SEM because of the reduction of the secondary electron emission coefficient. Starbursts are not seen at visible wavelengths. [65]

As we will show in Chapter 5, important questions regarding the processing mechanism remain. In particular, we find that the Joule heating by the field emission current is insufficient to create molten structures such as those in Figure 3.8(b). It is not clear what mechanism is responsible for the explosion and what determines whether an emitter processes or not. Our work supports the emerging view that other mechanisms are responsible for melting the emitter, such as the bombardment of the rf surface by ions. These ions are created by the field emission current as it passes through a cloud of gas evolving from the emission site. [66,67] The plasma that develops can also create an electric field on the order of GV/m at its interface with the conducting wall. Theories that attribute an important role to plasma formation by dc field emitters during discharges have been developed (e.g. [22, 68–70]), but a study of field emission and processing in rf cavities is lacking. We will show in Chapter 5, that the microscopy results of field emitters are consistent with the theory that a plasma also plays an important role in melting rf field emitters. Numerical simulations carried out for the first time also confirm these results. The simulations are described in Chapter 6.

Apart from the explosive processing events leaving remnants as in Figures 3.7 and 3.8, we observed that many emitters extinguished without a dramatic explosion. Frequently such sites could be reactivated following a thermal cycle or by admitting gases to the cavity. Another thrust of our studies was therefore to gain a better understanding of the activation and deactivation of emitters.

3.2.1.5 Helium processing

Often the admission of small amounts of helium to the cavity (about 0.1 – 1 mtorr, measured at room temperature) while applying rf power can precipitate the extinction of emitters ("helium processing"). [45, 71] Several mechanisms have been proposed to explain this observation. They include the erosion and blunting of emission tips by sputtering [45], an alteration of the surface composition due to the implantation of ions [72], and the desorption of gases by impacting helium ions [45, 57]. However, the actual mechanism has never been fully resolved and our experiments were also designed to shed more light on the processes involved.

3.2.2 Thermal breakdown

The onset of thermal breakdown is characterized by a sudden quench of the cavity's stored energy. The time constant for the quench to run its course is on the order of a few milliseconds. [73] Once the stored energy is dissipated, the cavity recovers its original high Q_0 state and begins to fill again. Thermal breakdown therefore is a self-pulsing mechanism. It usually occurs without any precursor such as x-rays, an unusually large power dissipation, or a noticeably declining Q_0.

In many cases thermal breakdown presents an absolute maximum to the achievable field and cannot be surmounted by techniques such as rf processing. Efforts to understand and eliminate thermal breakdown, in parallel with the study of field emission, are vital to improve cavity performance.

3.2.2.1 Thermal breakdown models

Two models have been proposed to elucidate the nature of thermal breakdown. In one model it is assumed that a small superconducting region (called a defect) has a critical magnetic field lower than that of niobium and becomes normal conducting prematurely. Although in the dc case, superconducting currents flow around the defect, rf currents are driven through it due to the reactive component of the rf impedance. The increased power dissipation at the defect drives the neighboring superconducting material into the normal conducting state. As a result, the normal conducting region grows rapidly, leading to a quench of the entire cavity surface or a large fraction of it.

The competing model assumes that a small, resistive defect is always present on the rf surface. In the steady state a power $\dot{Q}$ ($\propto H^2$) is dissipated in the defect due to ohmic losses in the presence of the magnetic field. The power $\dot{Q}$ has to be conducted to the helium bath by the surrounding superconducting niobium. At high fields the low thermal conductivity of superconducting niobium is not sufficient to carry away the dissipated power. The temperature of the superconducting region surrounding the defect rises and exceeds $T_c = 9.22$ K. The additional resistive area present results in even more power dissipation. This situation is unstable and similar to that encountered in the other model. The normal conducting region expands rapidly, leading to a quench of a large fraction of the cavity's surface.

The models differ in that thermal breakdown occurs when H^2 (i.e. $\dot{Q}$) exceeds a threshold value in the latter case. In the former case thermal breakdown is triggered when H exceeds the superheating field of the defect. This difference was exploited in experiments which showed that the second model is operative for the thermal breakdown

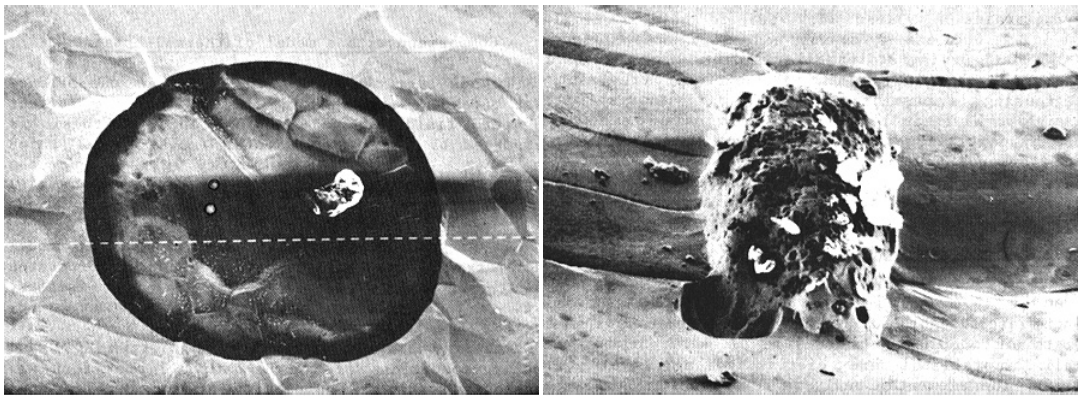

(a) (b)

Figure 3.9: Defects observed by thermometry to cause thermal breakdown. (a) A drying stain (440 μm in diameter) with a crystal containing potassium, chlorine and phosphorous, and (b) a 360 μm tungsten inclusion in a TIG weld. [75] Note that TIG welds are no longer used to manufacture cavities.

sites that were studied. [74] However, defects that cause thermal breakdown by the first model may exist as well.

3.2.2.2 Types of thermal breakdown

Thermal breakdown can be triggered by defects, field emission, multipacting or by the BCS surface resistance.

Defect related Thermal breakdown discussed so far is triggered by a defect present at the rf surface. Discussed in Section 3.4.2 are diagnostic techniques that have been used to locate such thermal breakdown sites among other features that delineate the behavior of superconducting cavities. An examination of cavities in a microscope often revealed defects at the location of thermal breakdown sites, such as those in Figure 3.9. Occasionally the defects found in the past were associated with foreign particulates introduced during the TIG welding of the cavity or beads introduced during electron beam welding. Improvements in welding techniques, especially the use of smooth full penetration electron beam welding, has reduced the occurrence of such defects. TIG welding is no longer used.

In Chapter 7 we will show that thermal breakdown can also be caused by loose particles falling into the cavity during assembly. In fact, their heating in the magnetic field can become so severe, that they partially melt and adhere very strongly to the rf surface.

Field emission related Field emission can also trigger a quench.[2] The power dissipated by impacting field emission electrons raises the wall temperature along the azimuth of the emission site (see Section 4.8). In many cases the temperature distribution has

[2]Multipacting, to be discussed in the next section, can trigger a breakdown by the same mechanism.

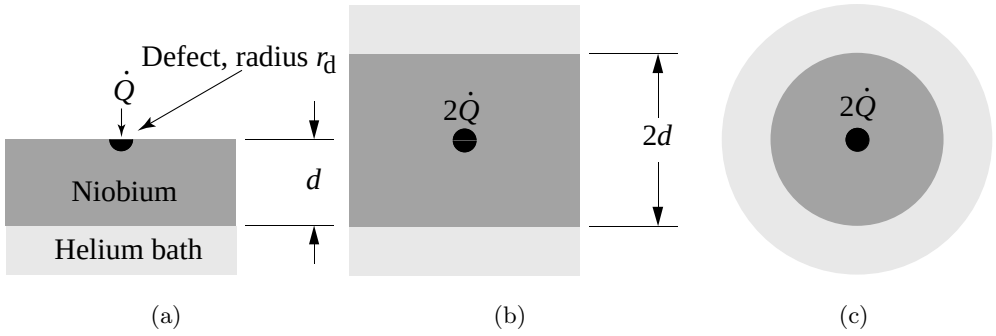

Figure 3.10: Geometry used to determine the thermal breakdown field due to a defect.

a fairly narrow peak. The BCS surface resistance rises exponentially with temperature, so that the ohmic losses in the bombarded region are also augmented. Eventually T_c is exceeded. The region affected by the emission current is normally large compared to ohmic heating at particulate defects so that the total dissipated power is large. If the surrounding cavity material has low thermal conductivity, thermal breakdown results. This breakdown mechanism is yet another reason why a better understanding of field emission is so important.

Global thermal instability A similar situation can also occur in the absence of field emission or a defect. Even a defect free cavity dissipates power due to the finite superconducting R_s, thereby raising the rf surface temperature. At sufficiently high bath temperatures the BCS resistance constitutes a significant part of the total R_s. Since it rises exponentially with temperature, a thermal instability may result at a high magnetic field. Such an instability is not defect related — it occurs throughout the entire high magnetic field region and hence is known as a *global thermal instability*. [17] It is particularly important at high bath temperatures and at high rf frequencies.

3.2.2.3 Estimating the thermal breakdown field

One can make a simple estimate of the breakdown field for a defect. Defects are typically at most a few hundred micrometers in size. On this scale, the cavity wall is equivalent to an infinite plane, thickness d, with a defect on one side and the helium bath on the other side (see Figure 3.10(a)). We model the defect itself as a hemisphere, radius r_d, embedded in the infinite plane. By symmetry this situation is equivalent to the sandwich in Figure 3.10(b) provided we let $\dot{Q} \to 2\dot{Q}$. If the temperature of the niobium on the helium side is close to the bath temperature T_b, one can simplify the analysis one step further by using the spherical arrangement in Figure 3.10(c) (provided $r_d \ll d$).

In the steady state, the temperature profile in the niobium bulk must satisfy

$$\boldsymbol{\nabla} D_T \boldsymbol{\nabla} T = 0. \tag{3.7}$$

Here D_T is the temperature dependent thermal diffusion coefficient. The boundary conditions that need to be satisfied at the defect radius r_d and at the helium interface

are:

$$2\dot{Q} = -4\pi r_{\rm d}^2 \kappa_T \boldsymbol{\nabla} T(r_{\rm d}) \tag{3.8}$$

$$T(d) \approx T_{\rm b}, \tag{3.9}$$

where κ_T is the thermal conductivity of niobium. Equation 3.7 has to be integrated, subject to the boundary conditions above, to yield the temperature profile in the niobium bulk. The integration is complicated by the fact that the differential equation is non-linear on account of the temperature dependent D_T and κ_T.

To simplify, we assume that D_T is temperature independent. In that case, (3.7) reduces to $\nabla^2 T = 0$ and the solution is

$$T(r) = T_{\rm b} + \frac{2\dot{Q}}{4\pi\kappa_T}\left(\frac{1}{r} - \frac{1}{d}\right) \qquad (r \geq r_{\rm d}). \tag{3.10}$$

We are only interested in the temperature near the defect, where $r \ll d$, so that

$$T(r) = T_{\rm b} + \frac{\dot{Q}}{2\pi\kappa_T r} \qquad (r_{\rm d} \leq r \ll d). \tag{3.11}$$

We now need an estimate of $\dot{Q}$. If an area $A_{\rm d}$ ($\approx \pi r_{\rm d}^2$) of the particle is exposed to the magnetic field, then

$$\dot{Q} \approx \frac{1}{2}\pi r_{\rm d}^2 R_{\rm d} H^2, \tag{3.12}$$

where $R_{\rm d}$ is the surface resistance of the defect and H is the local magnetic field. Thus

$$T(r) = T_{\rm b} + \frac{r_{\rm d}^2 R_{\rm d} H^2}{4\kappa_T r}. \tag{3.13}$$

Solving for H, one finds

$$H = \sqrt{\frac{4\kappa_T r[T(r) - T_{\rm b}]}{r_{\rm d}^2 R_{\rm d}}}. \tag{3.14}$$

If we assume that a quench takes place when $T(r_{\rm d})$ reaches the critical temperature $T_{\rm c}$, then the thermal breakdown field $H_{\rm tb}$ is

$$H_{\rm tb} = \sqrt{\frac{4\kappa_T (T_{\rm c} - T_{\rm b})}{r_{\rm d} R_{\rm d}}}. \tag{3.15}$$

Consider, for example, a 70 μm diameter defect with a surface resistance of 8 mΩ embedded in the rf surface. A typical thermal conductivity of RRR = 300 niobium[3] at a few Kelvin is 50 $\mathrm{Wm^{-1}K^{-1}}$. [76] If the bath temperature is $T_{\rm b} = 1.6$ K we expect a quench at $H_{\rm tb} \approx 930$ Oe $= 7.4 \times 10^4$ A/m. In our cavity geometry the corresponding peak electric field is about 38 MV/m.

Besides ignoring the temperature dependence of the thermal conductivity, many other oversimplifications were made, including our somewhat arbitrary choice of the defect surface resistance, and the fact that the defect topography was ignored. For example,

[3]The RRR (residual resistance ratio) is the ratio of the resistivity at room temperature to that at 4.2 K, *in the normal conducting state*. The purity, and hence the thermal conductivity, of niobium is directly related to the RRR.

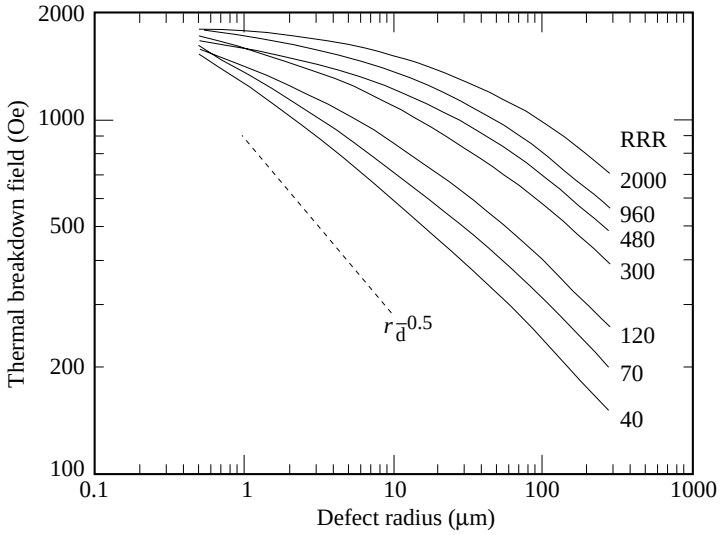

Figure 3.11: Simulated breakdown field $H_{\rm tb}$ as a function of defect radius. $R_{\rm d} = 8$ mΩ, $d = 2$ mm, and $f = 3$ GHz. [79]

consider a conducting hemisphere on the rf surface sitting in a uniform externally applied field H_0. In this case the field at the surface of the hemisphere is given by [24]

$$H = \frac{3H_0}{2}\cos\theta, \tag{3.16}$$

θ being the angle to the normal of the rf surface. The applied field is augmented by a factor of 3/2 at the top of the hemisphere, whereas the field vanishes altogether where the hemisphere and the rf surface meet. In other geometries matters are somewhat different. For example, the peak field near an infinitely long cylinder perpendicular to the applied field is $2H_0$. [38]

By integrating over the surface of the hemisphere, on finds that the average magnetic field squared is

$$\bar{H}^2 = \frac{3}{4}H_0^2, \tag{3.17}$$

which is actually slightly less than the applied field. The surface area of the defect increases by a factor of two, so that overall $\dot{Q}$ increases by 50 %. However, since the real shapes of the defects vary, and the uncertainty in $R_{\rm d}$, κ_T, and $r_{\rm d}$ is also substantially larger than 50 %, there is little point in including the relatively minor effect of the particle geometry.

To improve over the simple estimate for $H_{\rm tb}$, Equation 3.7 needs to be integrated numerically. Such calculations were performed, for example, at CERN [77] and, more recently, at Wuppertal for 3 GHz cavities. [78,79] The breakdown fields for various defect sizes and niobium purities are shown in Figure 3.11 for $R_{\rm d} = 8$ mΩ and $d = 2$ mm. Most of our cavities were of RRR = 300 niobium, and a breakdown field of 800 Oe is predicted if $r_{\rm d} = 70$ μm. At this field $E_{\rm pk} = 32.5$ MV/m. This value constitutes good agreement with the breakdown field given by (3.15).

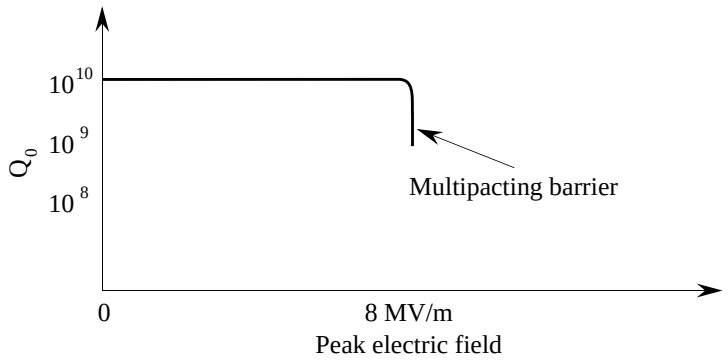

Figure 3.12: Q_0 versus $E_{\rm pk}$ curve of a superconducting cavity when multipacting is encountered.

Equation 3.15 and the simulations illustrate that the threshold field for thermal breakdown depends critically on the thermal conductivity of the bulk cavity material. The key to raising the average accelerating gradients achieved in niobium cavities has therefore been the improvement of the thermal conductivity. One approach is to post purify a cavity by solid state gettering with titanium or yttrium. [80–82] The thermal conductivity is directly related to the RRR of the material and one finds that the average quench field increases as the square root of the RRR. [83] However, the introduction of this additional step in cavity preparation can also impact the surface resistance in ways that need to be understood. Our studies showed, for example, that the diffusion of titanium over long distances in grain boundaries can cause substantial rf losses (see Chapter 8).

3.2.3 Multipacting

Multipacting in rf structures is a resonant process, in which a large number of electrons build up an avalanche, absorbing rf power so that it becomes impossible to increase the cavity fields by raising the incident power. The electrons collide with structure walls, leading to a large temperature rise and eventually to thermal breakdown. In most cases, multipacting can be avoided by selecting a spherical or elliptical cavity shape. Nevertheless, we did observe mild cases of multipacting in our elliptical cavities (see Chapter 7). Although, not serious in its own right, we discovered that the multipacting induced quenches can create and trap magnetic flux which increases the low field losses.[4] Hence multipacting should not be ignored completely.

3.2.3.1 Past observation of multipacting in cavities

Before the invention of spherically (and elliptically) shaped cavities, the onset of multipacting was usually recognized when the field level in the cavity remained fixed, as if a barrier were present, even as more rf power was supplied. In effect, the Q_0 of the cavity abruptly reduced at the multipacting threshold, as shown in Figure 3.12. The behavior of the stored energy as multipacting is encountered following the application of rf power, is depicted in Figure 3.13.

[4]Such effects were also observed as a result of thermal breakdown.

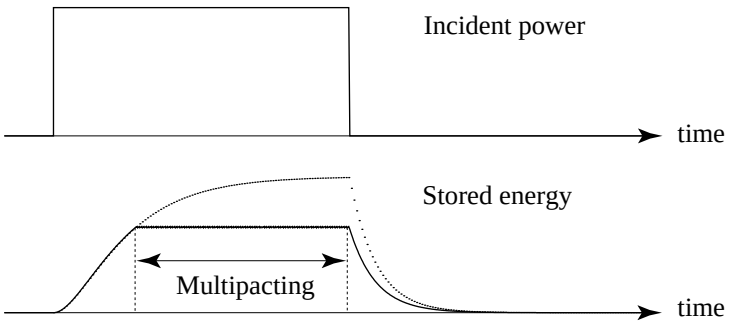

Figure 3.13: Stored energy of a cavity subject to multipacting. The cavity is driven by a square power pulse, longer than the natural decay time of the cavity. The dotted curve indicates the levels that would be achieved if multipacting were not active.

In many cases, it is found that such a multipacting barrier can be surmounted by "processing." This is done by allowing multipacting to progress for several minutes, while slowly raising the rf power. Eventually, and sometimes abruptly, the Q_0 improves and the multipacting ceases. Often, further multipacting barriers appear at higher fields; they may process as well. Barriers which can be processed are called *soft* barriers, whereas others, which persist, are known as *hard* barriers. In general, once soft barriers have been processed, they do not reappear, provided the cavity is kept under vacuum. However a soft barrier may reappear after the cavity is exposed to air, which indicates that multipacting is strongly dependent on the condition of the first few monolayers of the rf surface. Surface adsorbates can also strongly affect the multipacting behavior.

3.2.3.2 Theory of multipacting

The accepted mechanism for multipacting is as follows: an electron is ejected from some point $\mathbf{x}_0$ on one of the cavity's surfaces at a phase φ_0 of the rf field. This may be precipitated by a cosmic ray, photoemission or an impacting field emission electron. The emitted electron is accelerated by the rf fields and eventually impacts a wall again at point $\mathbf{x}_1$ and phase φ_1, thereby producing secondary electrons. The number of secondary electrons is given by the secondary emission coefficient (SEC) that depends on the surface characteristics and on the impact energy of the primary. In turn, the secondaries are accelerated and, upon impact, produce another generation of electrons. The process then repeats. The electron current increases exponentially if the number of emitted electrons exceeds the number of impacting ones, and if the trajectories satisfy specific resonance conditions. The increase in current is limited only by the available rf power and by space charge effects. (See Reference [2] for more details.)

3.2.3.3 Secondary electron emission

For most materials the SEC exceeds unity in a range from a few ten eV to a few thousand eV. Relativistic effects therefore have little influence on multipacting. The magnitude of the SEC in this range varies significantly from material to material. Nevertheless, the

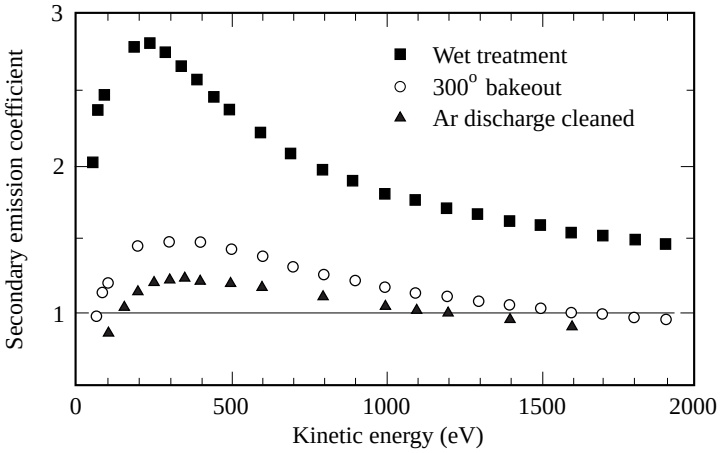

Figure 3.14: Secondary emission coefficient of niobium following various treatments. [8] Accurate measurements at very low impact energies have not been performed to our knowledge.

general form of the SEC for most materials is similar to that shown in Figure 3.14. The shape of the curves is explained by the fact that only secondary electrons created by the impacting charge within a small distance of the surface are able to escape the bulk. [2,84]

Since the emission of electrons occurs at the surface, sample preparation is critical in determining the SEC. This is illustrated in Figure 3.14, which shows the SEC for niobium following several different treatments. One finds that wet treatment (similar to our cavity preparation techniques) results in large secondary emission over the entire measured range of impact energies. Argon discharge cleaning or a bakeout, which both remove surface adsorbates, are very effective in reducing the SEC.

Adsorbates that can enhance secondary emission include hydrocarbons (from pump oil vapors) and lubricants used in polyethylene. [85, 86] For example, polyethylene bags are therefore inappropriate for storage of rf components susceptible to multipacting.

Since many of the adsorbates are only a few monolayers thick, they can be desorbed by electrons impacting the surface. In many cases, continuous multipacting serves to lower the SEC, which explains why some multipacting barriers are soft.

3.2.3.4 Common multipacting scenarios

Many different, and sometimes very exotic, multipacting trajectories are possible in rf structures. The most common types are known as *one point* and *two point* multipacting.

One-point multipacting In the case of one point multipacting, the electrons are forced by the magnetic field along quasi-cyclotron orbits that loop back on themselves, so that the electrons impact the cavity wall at, or very near, the emission site. The impact phase φ_1 is the same as the emission phase φ_0 (i.e., the rf period must be an integer multiple of the cyclotron period). The number of rf periods required by the electrons to return to the point of origin denotes the multipacting *order*. Furthermore, the requirement that the SEC be greater than one must be fulfilled for the impact energy. To satisfy this condition, multipacting orbits are usually well-localized compared to the overall cavity size.

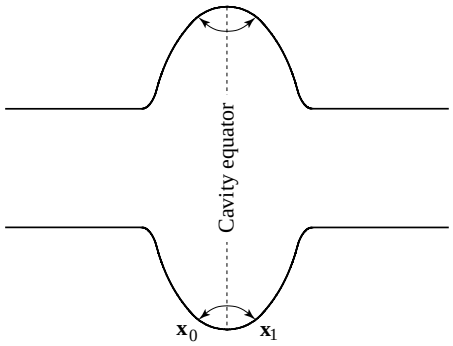

Figure 3.15: Two-point multipacting trajectories in an elliptical superconducting cavity.

Assuming the charges follow cyclotron-like orbits, then the magnetic fields at which multipacting occurs are given by [2]

$$H_n = c_{\mathrm{m}} \frac{m_{\mathrm{e}} \omega_0}{\mu_0 e n}, \quad (n = \text{integer}), \tag{3.18}$$

provided the SEC exceeds 1. In (3.18) n is the multipacting order, and c_{m} is a constant on the order of unity.

Several solutions to the one-point multipacting problem were explored. [74, 87, 88] By far the most successful solution was to round the cavity walls to make a "spherical" cavity. [89] In this shape there are no stable electron trajectories, as electrons drift to the equator within a few generations. At the equator the electric field vanishes, so that the secondaries do not gain any energy and the avalanche is arrested. Elliptical cavities, as used in our tests, were shown to be equally free of one-point multipacting.

Two-point multipacting Two-point multipacting occurs when the electron trajectories include two impact sites, $\mathbf{x}_0$ and $\mathbf{x}_1$, which usually are two points opposite a symmetry plane. The resonance condition requires, that the time between impacts is a half integer ($[2n-1]/2$) multiple of the rf period. The integer n again denotes the order of multipacting. If $\mathbf{x}_0$ and $\mathbf{x}_1$ are on opposite points of a symmetry plane, the newly emitted electrons at $\mathbf{x}_1$ will return to $\mathbf{x}_0$ along an orbit which mirrors the trajectory of the primaries.

In general, two-point multipacting in spherical or elliptical cavities is rare, because for most trajectories the impact energy is too large for the SEC to be greater than 1. The only place in this type of cavity where two-point multipacting has been observed is between opposite points near the equator, as shown in Figure 3.15. [71] Indeed, somewhat surprisingly, we too found this type of multipacting in our cavities, and we will discuss its effects on the cavity behavior in Chapter 7.

3.3 Low field loss mechanisms

We now turn to cavity loss mechanisms that are active even at very low fields. In Section 2.3.2 we showed that a superconductor intrinsically is resistive at rf frequencies, although R_{s} values are many orders of magnitude lower than those for normal conducting cavities (see Equation 2.21).

The BCS component in (2.21) can be made arbitrarily small by cooling the superconductor. However, the R_0 term is temperature independent[5] and eventually dominates the total R_s. It is not explained by the BCS theory. Although not fully understood, several loss mechanisms have been identified in the past.

3.3.1 Flux trapping

A well understood loss mechanism results from the trapping of dc magnetic flux in the cavity wall during cooldown through T_c. Even the terrestrial magnetic field is sufficient to cause low Q_0's, and cavities have to be shielded with μ-metal.

When a perfect superconductor is cooled in a magnetic field through T_c, the field is expelled from its interior. However, imperfect specimens have defects and impurities (pinning centers) that can prevent flux from escaping the superconductor. Normal conducting regions, each of radius ξ_0 and carrying one quantum of magnetic flux $\Phi_0 = hc/2e$ are left behind in the bulk after the superconducting transition is made. The distance ξ_0 is the coherence length over which the normal conducting state changes to the superconducting state. The "fluxoids" perform oscillations in the rf fields and, due to induced eddy currents, dissipate power.

Experiments have shown that even high purity niobium samples cooled in low magnetic fields (up to 3 Oe) trap all the flux. [90] Theoretical treatments [91–93] of this situation show that the surface resistance (R_Φ) due to trapped flux is proportional to the normal conducting resistance R_n, where

$$R_\Phi = R_n \frac{H_{ext}}{H_{c2}}. \tag{3.19}$$

$H_{c2} \approx 3000$ for high purity niobium niobium. [78] If $H_{ext} = 1$ Oe and $R_n \approx 2$ mΩ (at 1.5 GHz) then we expect a surface resistance of $R_\Phi = 670$ nΩ due to flux trapping. Experiments show that $R_\Phi = 350$ nΩ [90] in this case. To achieve Q_0 values of 10^{10} ($R_0 = 27$ nΩ) with our cavities, the magnetic field therefore may not exceed about 80 mOe (we are assuming that $R_{BCS} \ll 27$ nΩ).

However, external magnetic fields are not the only source of trapped flux. As we will show in Chapters 7 and 8, we discovered that magnetic flux can also be generated by thermocurrents during a cavity quench (either due to thermal breakdown or multipacting). Subsequent trapping of this flux leads to additional losses as well.

3.3.2 Adsorbed gases

Gases adsorbed on the cavity surface during cooldown are also known to have a detrimental effect on the surface resistance. Studies at CEBAF have shown that a Q_0 degradation is observed if the cavity is not evacuated completely prior to cooldown. [94] Hydrogen, carbon-dioxide, carbon-monoxide and water are the most common constituents of the residual gas in cavities. [95] Furthermore, throughout our experiments we found that field emission is also affected by gases (see Chapter 5). The role of these adsorbates must not be ignored.

[5] In many cases R_0 is field independent as well.

3.3.3 Hydrogen contamination

Cavities are subjected to extensive cleaning procedures prior to assembly in the cryostat (see Section 4.6.1). Included in these steps is chemical polishing with a mixture of nitric, phosphoric and hydrofluoric acid (BCP). Other laboratories use electropolishing as an alternative.

Studies [96–98] have shown that extensive chemical and electro-chemical polishing at temperatures exceeding 15 °C can result in a reduction of the cavity Q_0 at low field and a further drop as $E_{\rm pk}$ is raised. Due to historical reasons, this situation has been termed the "Q-virus" or the "Q-disease." The Q_0 drop is exacerbated if the cavity is "parked" during cooldown in a temperature range between 60 and 150 K for a period of one hour or more. Q_0 reductions by more than two orders of magnitude have been observed. High purity niobium (with a RRR exceeding 100) is known to be specially sensitive to these effects.

The accepted mechanism for the Q degradation is hydride formation. Depth profiles of chemically etched niobium have shown that up to 5 at. % (0.054 wt. %) of hydrogen is stored in the niobium bulk near the surface during the etch. [97] The longer the etch and the warmer the acid, the more hydrogen is absorbed. In addition, typically 1 wt. ppm of hydrogen is already present in delivered commercial niobium. A study of niobium's phase diagram [99] reveals that niobium hydride precipitates and undergoes several phase transitions between 220 and 130 K. It is believed that these hydride phases have a lower critical temperature $T_{\rm c}$ and critical field $H_{\rm c}$ and a higher surface resistance. Significant quantities of hydride are formed if the original hydrogen concentration exceeds 2 wt. ppm. However, between 100 K and 200 K the formation time for large areas of hydride phase is long enough due to the slow diffusion of hydrogen, so that a rapid cooldown through this temperature range prevents the manifestation of the Q-disease.

Correspondingly, one frequently (but not always) finds that the original Q_0 of an afflicted cavity can be recovered by thermally cycling it to room temperature and cooling down rapidly to 4.2 K. The danger zone between 150 K and 60 K should be crossed in less than about 1/2 – 1 hour to avoid renewed Q_0 degradation.

The Q-disease can be avoided altogether by vacuum baking the cavity at temperatures exceeding 900 °C for several hours. The high temperature drives out most of the hydrogen from the niobium bulk. The equilibrium hydrogen concentration $c_{\rm H}$ of a sample heat treated at temperature T in an atmosphere with partial hydrogen pressure $p_{\rm H_2}$ is given by [100]

$$c_{\rm H} = 0.153\sqrt{p_{\rm H_2}}e^{4766.4/T} \qquad (420\ {\rm K} < T < 1770\ {\rm K}), \tag{3.20}$$

where $c_{\rm H}$ is in wt. ppm, T is in Kelvin and $p_{\rm H_2}$ is in torr. For typical furnace pressures of 10^{-6} torr achieved by us, $c_{\rm H} \approx 0.01$ wt. ppm at 900 °C, much less than the hydride precipitation limit of 2 wt. ppm. Following the furnace treatment, an etch is required to clean the surface once again, but provided it is short and the acid temperature is kept below 15 °C the Q-disease does not re-establish itself.

Similarly, it is believed that low RRR cavities are not afflicted by the Q-disease because defects and impurities trap the hydrogen [97, 101] and prevent hydride precipitation.

Despite the progress made in understanding the Q-virus, questions still remain. For example, what is the maximum acid temperature that can be used to etch cavities

Table 3.1: Sizes of particles found on 80 cm^2 silicon wavers cleaned in the same manner as cavities. The average particle density was 128 cm^{-2}.

Size range	Number of particles
0.3 – 1.2 μm	5825
1.2 – 2.0 μm	405
2.0 – 3.0 μm	2720
3.0 μm and above	1069

without the danger of hydride precipitation? Can the Q-virus always be cured by a fast cooldown? Is the RRR the only factor that influences the hydride precipitation? In Chapter 8 we will show, that the Q-disease may manifest itself to some extent even if all etching is performed at acid temperatures below the established 15 °C cutoff, and that the equator weld is especially susceptible to hydride precipitation. These losses, we will see, cannot always be eliminated completely by a rapid cooldown.

3.3.4 Particulates and impurities

As mentioned in Section 2.2.2 a measurement of the cavity Q_0 only yields the average surface resistance given by

$$\bar{R}_s = \bar{R}_{BCS} + \bar{R}_0 = \frac{G}{Q_0}. \tag{3.21}$$

Included in the $\bar{R}_0$ term are losses due to local defects or inclusions and even particles adhering to the surface. Sub-millimeter sized particles can dominate the $\bar{R}_0$ term because their surface resistance may be more than 10^7 times greater than that of superconducting niobium.

Studies at KEK [102] have shown that over 100 particles/cm^2 are present on silicon surfaces chemically treated and rinsed with deionized water in the same manner as cavities. As shown in Table 3.1, most of these particles are only on the order of 0.3 – 1 μm in size.

Similar studies at Cornell [103] using niobium (RRR = 250) rather than silicon wafers also revealed particle densities on the order of 100 – 1000 particles/cm^2. Again most particles were micron sized. The main impurities were hafnium, stainless steel, silicon and carbon. Inclusions incorporated at the niobium manufacturing site during the rolling process are a likely source of the hafnium.[6] The density of hafnium particles reduced significantly when large amounts of niobium were etched away.

High purity Russian niobium (RRR = 500) was also treated and examined in the same manner, and the particle density was found to be up to an order of magnitude lower. This result indicates that many of the particles in the RRR = 250 material originally were inclusions that were exposed by the etching process.

As will be discussed in Chapter 8, our cavity tests also observed (for the first time) the motion of microscopic particles during rf tests. Not only do these particulates affect the residual resistance, but they can also cause field emission and other high field losses.

[6]The manufacturer of the niobium (Teledyne-Wah Chang) also processed hafnium and we assume that the same machines were used to roll both niobium and hafnium sheets.

If we consider the KEK results typical for rf cavities, then the contribution of particles to the mean rf surface resistance is as much as 30 nΩ provided we assume a surface resistance of the 5 mΩ for each particle.[7] The real value may differ significantly because not all particles are conducting, and we do not know the actual surface resistance of those that are conducting. Nevertheless, our simple estimate is comparable to typical results obtained for $\bar{R}_0$ in good rf cavities.

3.4 Studying loss mechanisms

When evaluating a cavity's performance, it is important that loss mechanisms are correctly identified and characterized. Numerous methods for studying cavity losses have been developed over the years and many of these techniques complement each other. They can be divided into two groups: global methods and local methods. Several of these were used in our experiments.

3.4.1 Global diagnostic techniques

Global techniques are incapable of identifying the location of excessive power dissipation. Instead they measure an average for the entire cavity. Nevertheless, they are extremely useful in identifying the dominant form of power dissipation. The following is a sampling of the techniques used in the past.

3.4.1.1 Cavity quality factor measurement

Discussed in Section 2.2.2 is the cavity quality factor Q_0. Standard cavity measurements invariably always include the measurement of Q_0 versus $E_{\rm pk}$ (or $E_{\rm acc}$). Measurements of the power used to drive the cavity, the power reflected at the cavity–input coupler interface and the decay time of the cavity fields when the input power is switched off are used to calculate the Q_0. This technique is explained in more detail in the description of our experiment (Section 4.4).

The cavity quality is very useful, because it measures the sum of *all* cavity losses. The measurement of Q_0 thus was one of the main diagnostic techniques used in our studies. The shape of the Q_0 versus $E_{\rm pk}$ can be used to identify the dominant loss mechanism. For example, if the Q_0 drops rapidly, as in Figure 3.1, field emission is the likely culprit. On the other hand, if the curve is flat and a quench occurs, then defect related thermal breakdown is probably at fault.

If a single field emitter dominates the power dissipation in the cavity, one can even extract an estimate of the emitter's $\beta_{\rm FN}$ from a Fowler-Nordheim plot of the dissipated power.

3.4.1.2 Current measurements

Many field emitted electrons are intercepted by the cavity walls in the cell region. Nevertheless, for most emitter locations, a sizable number of electrons enter the beam tubes. A biased pickup probe in the beam tube can be used to collect these electrons. The collected current is a direct measure of the field emission activity in the cavity. Provided

[7] 5 – 10 mΩ is a reasonable value for normal conducting metallic particles at cryogenic temperatures.

one emitter is dominant, a Fowler-Nordheim plot can be used to estimate β_{FN}. This value is independent of that obtained from Q_0 versus E_{pk} measurements.

3.4.1.3 X-ray detection

Closely related to the current measurements is the use of an x-ray detector located outside the cavity cryostat. The detector measures the amount of bremsstrahlung produced by field emission electrons as they impact the cavity walls. We therefore used x-ray detection to observe the onset of field emission in our experiments.

Once again, Fowler-Nordheim plots may be used to determine β_{FN} of the dominant emitter. [45] Note, though that the x-rays tend to be very directional, so that a large spatial variation of the intensity is common.

3.4.2 Local diagnostic techniques

To be able to pinpoint defects such as field emitters, mapping techniques are required. Many different types have been developed in this category as well, and we will only give a short overview.

3.4.2.1 X-ray detection

Rather than placing an x-ray detector outside the cryostat, an array of small scintillators can be mounted near the cavity surface to yield an x-ray map. [104, 105] Normally, the x-ray intensity is peaked near the main electron impact sites. However, spurious signals result from x-ray reflections and scattering, so that at times the evaluation of the x-ray maps can be challenging. Since most, if not all, the information gained from x-ray maps is just as readily obtained by temperature mapping (described below), we decided to forego the use of the x-ray mapping.

3.4.2.2 Light detection

Electron field emission (and possibly magnetic heating) raise the defect temperature to very high levels. Light emission in the visible range is therefore to be expected. As we will see later, field emission is also associated with plasma activity resulting in light emission. A specially designed cavity was developed at Saclay to study the intensity and spectra of field emitters. [106, 107] Not only is one able to localize the emission sites, but one can also gain valuable information on the nature of field emission from the light spectra.

For accelerating cavity geometries light detection is of lesser use, because large areas of the cavity cannot be viewed from an optical port which has to be located in the beam tubes. We therefore decided not to use light detection.

3.4.2.3 Thermometry

Ultimately most of the power dissipated by the various cavity loss mechanisms is transferred as heat to the cavity wall. Thus, an ideal system for studying all types of loss mechanisms is an array of temperature sensors on the cavity wall.

The utility of temperature mapping was first demonstrated by Lyneis in 1972 when he used thermometry to locate a thermal instability. [4] Since then, temperature mapping has successfully been employed by numerous laboratories far more extensively than any other local technique. The main advantage of thermometry over the other systems lies in the fact that it can be used to study *all* loss mechanisms in a cavity. If the thermometers are calibrated, the cavity Q_0 can be extracted directly from temperature maps (see Section 4.5.4). Furthermore, the temperature signals are recorded at the site of the power dissipation, and the temperature maps can readily distinguish between the various loss mechanisms. Because of this universal applicability of temperature mapping, we chose thermometry as our main diagnostic tool.

Excellent reviews of thermometry have been given in several references (e.g., [108, 109]). Since thermometry plays the central role in our investigation we will give a brief outline of the different types of systems in existence.

Common to all systems are the temperature sensing elements — usually Allen-Bradley carbon resistors, nominally 100 Ω. Carbon is a semiconductor and increases its resistance R exponentially with decreasing temperature T. At liquid helium temperatures the gradient dR/dT is several 10 Ω/mK, permitting sensitive temperature measurements. The bakelite casing of the resistor is ground away on one side for good thermal contact to the cavity wall. The remaining sides are encased in epoxy to prevent excessive cooling of the thermometer by the helium bath. To map the cavity, numerous thermometers are attached to the cavity wall, separated by distances of about 1 cm. Two distinct arrangements of the thermometers have been used.

Rotating thermometry systems To minimize the number of thermometers required (and the cavity preparation time), about 20 thermometers are mounted on a rotating arm that matches the cavity contour. The arm presses the exposed side of the sensing elements against the cavity wall (see Figure 3.16). A computer system measures the resistance of each thermometer and converts the values to temperatures. The temperature profile along one azimuth of the cavity thereby is obtained in a single scan. The arm is then moved by a motor to a new position. In this manner the surface temperature of the entire cavity is obtained. Systems of this type have been used at CERN [8, 9], DESY [10, 11] and Wuppertal [13] among others.

The main drawback of this system is the long acquisition time of a complete temperature map. Because of the need for a complete rotation of the arm, acquisition times as long as 1/2 hour are normal. As a result, only stable losses can be monitored in the steady state. Processing events or thermal breakdown can only be observed if they are at the azimuth of the rotating arm.

Another disadvantage lies in the fact that the sensitivity of rotating systems diminishes significantly if they are operated below the lambda-point of helium ($T_\lambda = 2.2$ K). The reason is explained later. In the past rotating systems were therefore almost exclusively used for studies above T_λ. In turn, this meant that only low frequency cavities ($f < 1$ GHz), for which R_{BCS} is not significant at T_λ, could be studied effectively.

Fixed thermometry systems Many of the problems associated with rotating systems are solved by using a fixed array of thermometers to cover the entire cavity surface (see Figure 4.8 in the next chapter). For this reason, we opted to use a fixed thermometry

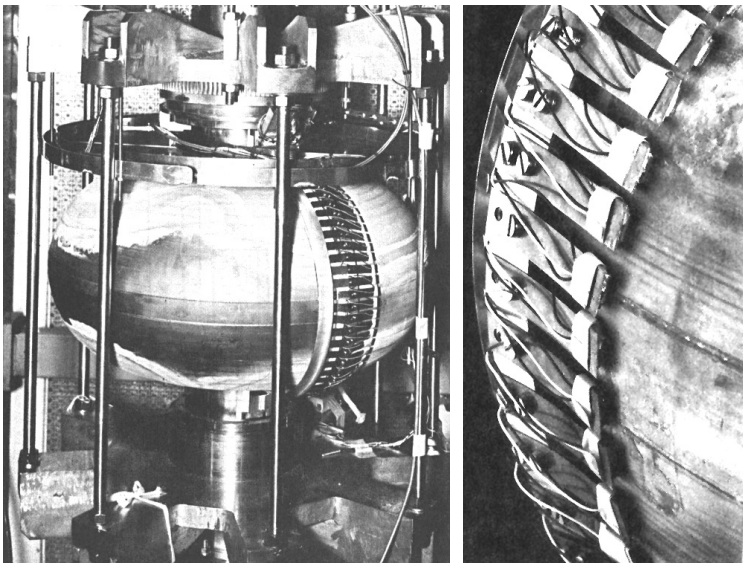

(a) (b)

Figure 3.16: Rotating thermometry system employed by CERN for temperature mapping of single-cell 500 MHz cavities. [8]

system in our studies. Similar systems are also employed at KEK [14] and DESY [12]. A multiplexing system is able to obtain a fast temperature map, allowing both transient and steady state effects to be studied.

Different multiplexing schemes have been developed to scan the thermometers. For example, an intricate matrix system was used at Cornell for an older thermometry system [5,15] to minimize the number of connections needed between the thermometers and the computer. Such a system reduces the reliance on expensive hardware but makes it more susceptible to wire failures and cross-talk problems. In contrast, the system developed for this dissertation employs a dedicated channel for each thermometer to avoid cross-talk and wire failure problems.

Fixed thermometry is inherently much faster than rotating systems. Temperature maps can be acquired in 15 s with present systems. The new design discussed in Chapter 4 is even faster, requiring less than 0.2 s. Thus, short lived cavity events can be studied and extensive data on the evolution of loss mechanisms with E_{pk} can be obtained.

Another advantage of the new setup described in Chapter 4 and other fixed systems lies in the fact that they can be used in superfluid helium.[8] Older systems, and especially rotating setups, had to operate above the lambda point because of superfluid helium's extreme effectiveness at entering even the finest gaps, thereby cooling the thermometers. Results with nucleate film boiling helium I are also comparable to superfluid helium. [109] Hence, in the past, thermometry could only be carried out effectively in subcooled helium. But subcooled helium carries with it a severe penalty as well. Heat transport in this case is governed by convection, which can be laminar or turbulent. Large variations

[8]Our system, in fact, must operate below 2 K to avoid excessive BCS losses.

in cooling are observed, depending both on the surface orientation and the heat flux from the wall. Above fairly low flux densities of 8 mW/cm^2 nucleate boiling starts, complicating matters further. A careful calibration therefore is required to be able to interpret temperature maps correctly. [108]

All these problems are avoided with our system by using superfluid helium instead. Improvements in thermometer design and the use of grease between the cavity wall and the thermometer, that shields the sensing element from the superfluid helium, permit very efficient sensing of the cavity wall temperature.

The only real drawbacks of fixed thermometry systems, although not severe, are the long times required to prepare the large number of thermometers in the system for tests (about two man-days for a 1.5 GHz cavity) and the reduced spatial resolution (in azimuth) with respect to the rotating systems. The latter is mitigated by the fact that the temperature distribution due to a point heat source on the cavity interior spreads over more than a centimeter at the outside cavity wall. Hence, a sub-centimeter spatial resolution is not essential.

Chapter 4

Experimental setup and technique

4.1 Introduction

In this chapter, we give a detailed discussion of the hardware and software used to test 1.5 GHz cavities. A Q_0 versus E_{pk} measurement system and a thermometry system provide the main diagnostic tools to study cavity loss mechanisms.

We begin by describing the system required to operate a cavity at cryogenic temperatures and to determine the cavity quality Q_0. We also give an overview of the mathematical expressions needed for these Q_0 measurements.

In Section 4.5 we then describe the centerpiece of our experiments — the thermometry system. [110] It uses a fixed thermometer array and is designed to operate in 1.6 K liquid helium, well below the lambda point. The thermometers can detect sub-millikelvin temperature rises in the cavity wall and thus provide an ideal means of studying cavity loss mechanisms.

To offer a more complete picture of our experiments, a discussion of a typical cavity test follows. This section explains in more detail the Q_0 and thermometry measurements as well as other testing techniques.

Finally, we complete this chapter by describing the steps involved in the microscopic examination of the dissected cavities and how to coordinate the investigation with information provided by the temperature maps. In particular, our ability to locate field emitters using thermometry data requires straight forward but fairly extensive computer simulations.

4.2 LE1 cavity shapes

All cavities we tested were single cell, cylindrically symmetric, elliptical cavities. The eigenfrequency of the TM_{010} mode is just below 1.5 GHz (L-band) — hence the cavities are designated LE1. The residual resistance ratio (RRR) of the niobium was about 250 – 300 in all cases.

Single cell cavities were made using available dies for multicell cavities. Three different shapes, termed Mark II (center cell), Mark III (end cell) and Mark I (early design no longer used for multicell cavities), were used. Nominally, the shapes of all our LE1 cavities are the same. However, there are subtle differences (on the order of millimeters). The shape parameters are given in Figure 4.1 and Table 4.1. The difference between

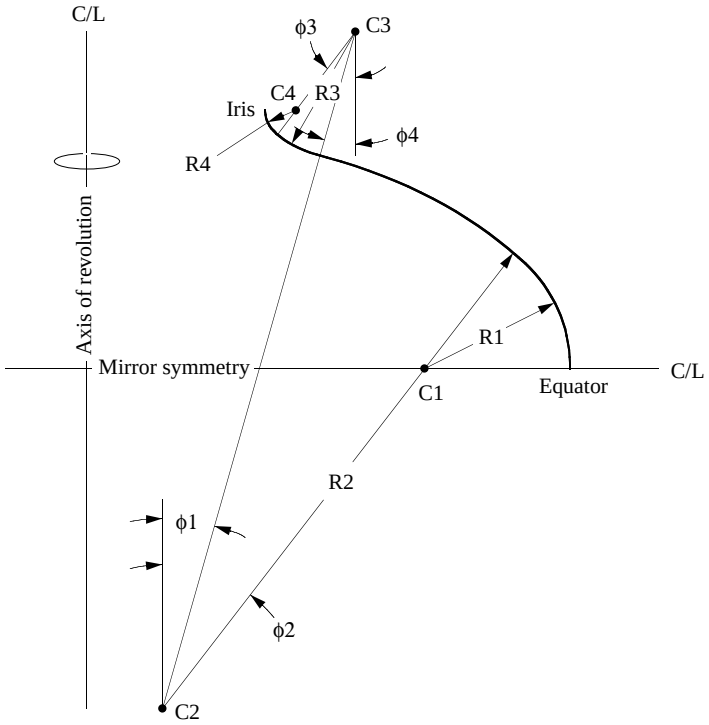

Figure 4.1: Contour of a quarter segment of the LE1 cavities used in rf tests. The parameters are given in Table 4.1.

Table 4.1: Parameters for the shape of Mark I, Mark II and Mark III LE1 cavities in Figure 4.1.

Parameter	Mark I	Mark II	Mark III
R1	2.963	2.828	2.892
C1X	6.239	6.575	6.422
C1Y	0.000	0.000	0.000
R2	10.108	11.122	10.646
C2X	1.812	1.516	1.658
C2Y	−5.610	−6.572	−6.118
R3	2.492	2.498	2.498
C3X	5.241	5.249	5.249
C3Y	6.515	6.526	6.526
R4	0.591	0.590	0.590
C4X	4.091	4.095	4.095
C4Y	5.001	5.006	5.006
$\phi 1$	15.75°	15.89°	15.89°
$\phi 2$	38.29°	37.58°	37.58°
$\phi 3$	37.24°	37.22°	37.22°
$\phi 4$	15.97°	15.97°	15.97°

Mark II and Mark III cavities is not very large, but significant differences do exist with respect to the Mark I cavities. The following is a list of all cavities tested, sorted by cavity shape:

Mark I LE1-17, LE1-21*, LE1-Heraeus*

Mark II LE1-20*, LE1-23*, LE1-27

Mark III LE1-31, LE1-32, LE1-33, LE1-34, LE1-CEBAF

All cavities were nominally either $1/8''$ (0.32 cm) or $1/16''$ (0.16 cm) thick. Cavity half cells were deep drawn and then electron beam welded at the equator. Iris welds were used to attach beam tubes. For more details on the manufacturing of cavities see Reference [2]. Cavities marked by a $\star$ were previously heat treated [60, 80, 82, 111] with titanium for other experiments.

4.3 Description of the test stand

The test stand described here serves dual purposes. It is designed to measure the Q_0 as a function of $E_{\rm pk}$, thereby yielding information on the global behavior of the cavity. To complement these measurements, an array of 756 thermometers attached to the outside surface of the cavity monitors the temperature distribution. As discussed in Section 3.4.2 the temperature data provides valuable information on local loss mechanisms in the cavity.

The schematic and picture in Figure 4.2 depict the complete test stand. The cavity is mounted vertically on a bellows arrangement which serves dual purposes as an adjustable input coupler (to be discussed later) and to evacuate the cavity. 1.5 mm superconducting indium wire is used as a seal between the cavity flange and the stainless steel flange of the bellows arrangement. The top of the cavity is capped off with a niobium endplate with a monitor probe at its center (to be discussed later). Again 1.5 mm indium wire is used as a seal. Thermometers are mounted on the cavity exterior for temperature mapping in superfluid helium. They are discussed in Section 4.5.

The cavity is evacuated via the bellows leading into the "viking" horn and the stainless steel tubing that connects to the top plate. Only one of the two legs is used for pumping purposes; the other solely provides mechanical stability. When first evacuating the cavity, a roughing pump/turbo pump combination is used to reduce the pressure to about 2×10^{-6} torr. Care is taken, that the pumpdown rate does not exceed about 5 torr/s, to avoid turbulence that may allow dust from the vacuum line to enter the cavity.[1] Water condensation and accompanying droplet formation is also prevented by a slow pumpdown rate. [112] Once a pressure of 2×10^{-6} torr is achieved the system is switched over to a 30 l/s ion pump mounted on the top plate, which further reduces the pressure to about 2×10^{-8} torr. The final pumpdown takes a couple of days if the system has not been baked, which provides ample time to mount the thermometer array (discussed later).

Apart from the ion pump, the top plate accommodates high vacuum plumbing and valves, that permit the isolation of various parts of the system. A cold cathode gauge

[1] The same precautions are also taken when the cavity is being bled up to room pressure.

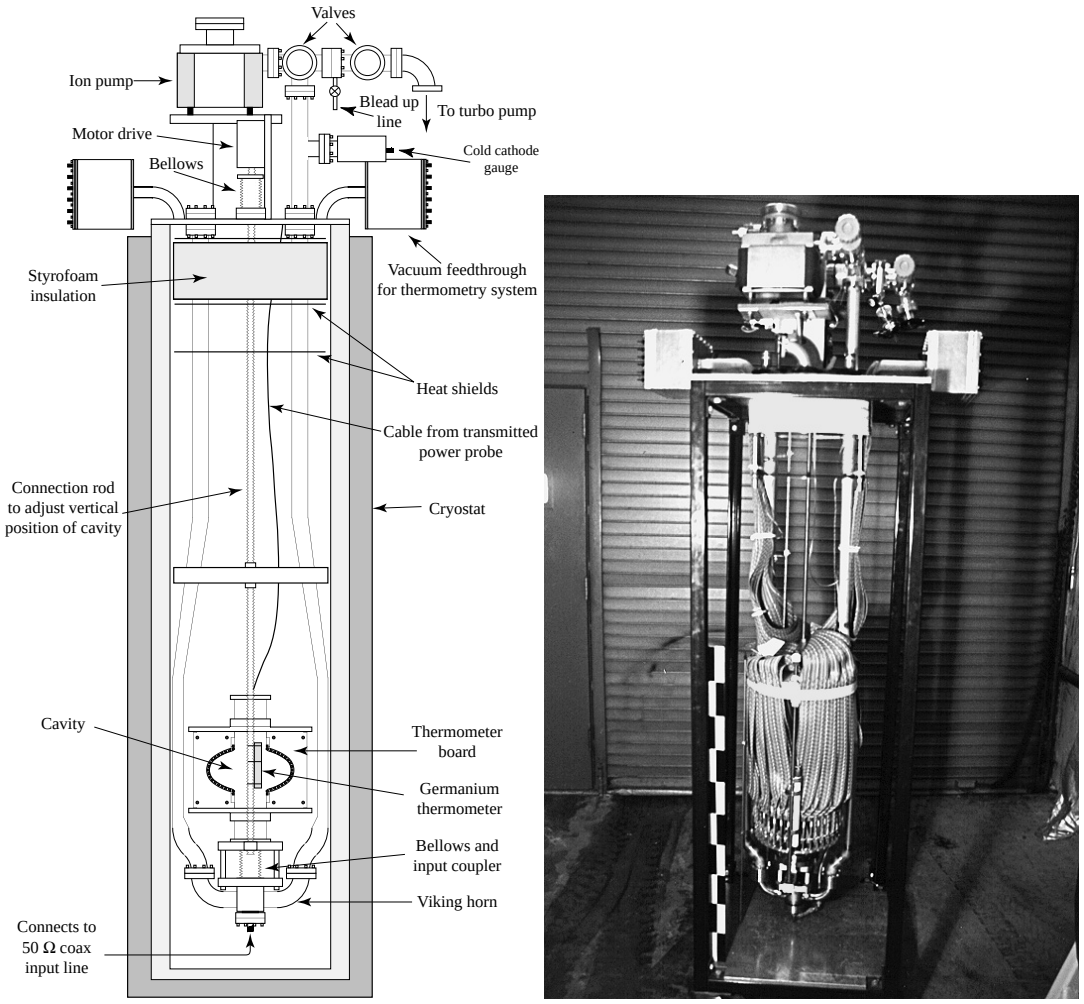

Figure 4.2: Schematic and picture of the test stand used to test LE1 cavities.

monitors the pressure in the vacuum line to the cavity. A 0.3 μm filter is attached to the vacuum system via a break-out line. The filter is used to cleanly bleed up the test stand to atmospheric pressure at the end of a test. Alternatively, it can be used to administer small quantities of gas to the cavity during a test.

A motor on the top plate facilitates the vertical motion of the cavity over the coaxial input coupler housed in the bellows at the bottom of the test stand. The coupling adjustment technique is discussed in the next section. Several feedthroughs are also incorporated in the top plate for electrical connections to the thermometry system and other diagnostic tools.

Up to 250 W of rf power from a solid state amplifier is available to excite the cavity. A feedback loop (described later) is used to stabilize the rf frequency. RF power is carried to the cavity via a 50 Ω coaxial line. High voltage connectors are needed to make the connection between the feedthrough at the top plate and the coax below. This precaution is necessary to avoid arcing in subatmospheric ($\approx$ 6 torr) helium gas present

in this region during cavity tests. Above the top plate the coax is connected to two directional couplers (shown later in Figure 4.5). These divert −20 dB of the forward traveling and reflected power to a power meter. The signals are used for determining the cavity quality and will be discussed later. A circulator and load between them prevents power being reflected to the amplifier to protect the microwave electronics.

The test stand is inserted in a 38 cm diameter, 183 cm deep cryostat. The outer jacket of the cryostat is filled with liquid nitrogen to minimize the heat leak to the interior. The inside is filled with liquid helium and then evacuated to about 6 torr to lower the bath temperature from 4.2 K to 1.6 K. Two 91.4 cm dip sticks (which become superconducting at liquid helium temperatures) are used to monitor the level of the helium bath. It takes approximately 250 l of helium to fill the cryostat, and under normal operating conditions this is sufficient for 12 hours of testing.

The cryostat itself is housed in "cave" with 60 cm thick steel block shielding interleaved with lead sheets. The shielding is needed to absorb x-rays produced by field emission electron bremsstrahlung during cavity tests. An interlock system shuts off rf power to the cavity if radiation levels outside the cave exceed 2 mR/h. This can prove to be an experimental limitation for very heavily field emission loaded cavities.

An x-ray detector within the confines of the cave is used to monitor x-rays. Usually the onset of these can be correlated with a rapid decline of the cavity Q_0 with increasing field.

4.4 Setup for cavity quality measurements

As discussed in Chapter 2, the cavity quality is given by

$$Q_0 = \frac{\omega_0 U}{P_\mathrm{d}}, \tag{4.1}$$

where ω_0 is the eigenfrequency of the cavity mode, U is the energy stored in that mode and P_d is the power dissipated in the cavity. Since $U \propto E_\mathrm{pk}^2$ we see that the Q_0 is constant versus field, provided the cavity losses are quadratic in nature. A measurement of the Q_0 versus E_pk thus provides a means of determining when anomalous (also called non-quadratic) losses, such as field emission, begin to dominate the cavity behavior.

In this section we provide an overview of the technique used to measure Q_0. A Macintosh Quadra 700 controls the setup and performs most measurements automatically via a GPIB interface. The same computer also runs the thermometry system, that will be discussed in the Section 4.5.

4.4.1 Cavity coupling

To match the cavity impedance to the 50 Ω input line, the coupling arrangement in Figure 4.3 is used. The cavity's TM_{010} accelerating mode is excited by electrically coupling to the TEM mode of the coaxial line protruding into the cavity from the bottom. The center conductor extends beyond the limit of the outer conductor, thereby permitting the fields to couple to the TM_{010} mode. The input coupler enters the cavity from the bottom, to avoid unnecessary dust contamination of the cavity.

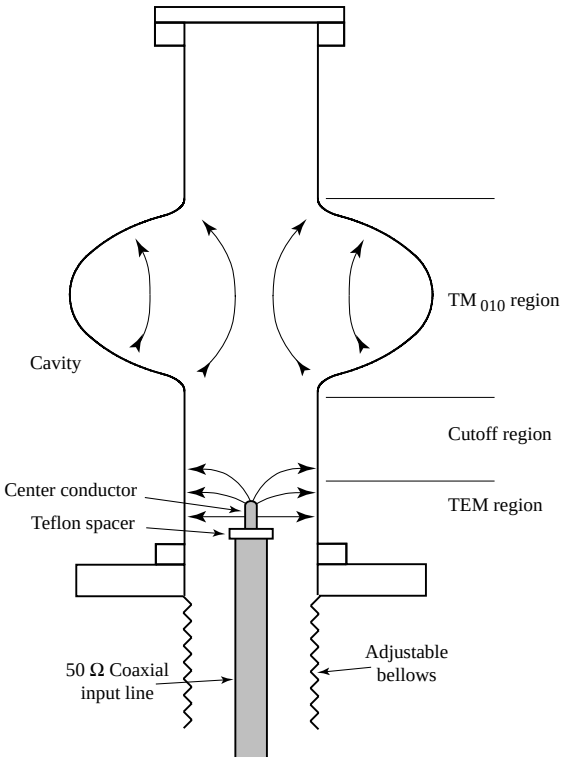

Figure 4.3: Input coupler arrangement used to couple rf power into the cavity.

The *external coupling* ($Q_{\rm e}$) of the input probe is defined as

$$Q_{\rm e} = \frac{\omega_0 U}{P_{\rm e}} = \frac{Q_0}{\beta}, \tag{4.2}$$

where $P_{\rm e}$ is the power dissipated into the coupler if the stored energy is U, and $\beta = P_{\rm e}/P_{\rm d}$ is the *coupling strength*. For impedance matching we need $P_{\rm e} = P_{\rm d}$ or $\beta = 1$.

A typical cavity Q_0 at low field is 2×10^{10}, but at high field it can degrade rapidly to 10^8 due to field emission. Adjustable input coupling is therefore necessary to get power into the cavity at all field levels. The coupling can be changed by moving the cavity up or down with respect to the coax using the motor drive at the top of the test stand. The bellows arrangement around the coupler preserves the cavity vacuum. The movement changes the penetration of the coupler. Since the fields of the TM_{010} mode are below cutoff in the 8.9 cm diameter beam tube, they decay exponentially with distance from the cell. Hence, a cavity motion of 2 cm is sufficient to alter the external coupling by a decade. With a stroke of 4.5 cm we can cover a coupling range from approximately $Q_{\rm e} = 2 \times 10^8$ to $Q_{\rm e} = 4 \times 10^{10}$.

To measure the coupling strength β, the cavity response to steady state and transient input signals is observed. An analysis of an equivalent circuit representing the cavity, the input line, and the generator, shows that the reflected ($P_{\rm r}$) power *in the steady state* is [2, 113]

$$P_{\rm r} = P_{\rm f} \left(\frac{\beta - 1}{\beta + 1} \right)^2, \tag{4.3}$$

where P_f is the input power from the microwave generator. Thus a measurement of P_f and P_r yields the cavity coupling:

$$\beta = \frac{1 \pm \sqrt{\frac{P_\mathrm{r}}{P_\mathrm{f}}}}{1 \mp \sqrt{\frac{P_\mathrm{r}}{P_\mathrm{f}}}}. \tag{4.4}$$

The upper sign applies when $\beta > 1$ and the lower sign applies when $\beta < 1$. For $\beta = 1$ (unity coupling) the reflected power vanishes.

By conservation of energy, the power dissipated in the cavity walls (P_d) in the steady state is given by

$$P_\mathrm{d} = P_\mathrm{f} - P_\mathrm{r} = P_\mathrm{f} \frac{4\beta}{(1+\beta)^2}. \tag{4.5}$$

If the cavity is in the steady state and the input power is abruptly switched off, then the power instantaneously emitted from the cavity into the input line ($P_\mathrm{e}^\mathrm{inst}$) is given by βP_d (see Equation 4.2):

$$P_\mathrm{e}^\mathrm{inst} = \beta P_\mathrm{d} = P_\mathrm{f} \frac{4\beta^2}{(1+\beta)^2}. \tag{4.6}$$

Equation 4.6 thus provides an alternate way to (4.4) of determining the input coupling. One finds that

$$\beta = \frac{1}{2\sqrt{\frac{P_\mathrm{f}}{P_\mathrm{e}^\mathrm{inst}} - 1}}. \tag{4.7}$$

The response of a cavity to a square input pulse is shown in Figure 4.4 for an undercoupled cavity, a unity coupled cavity, and an overcoupled cavity (see References [2,113] for a derivation). In the depicted cases, the length of the pulse is long enough for the cavity to attain a steady state before the power is turned off again. Initially, all power is reflected when the pulse is turned on, so the spike at the beginning equals the full incident power. Once power does leak into the cavity the reflected power rapidly decays to its equilibrium value. Typical decay times at 1.5 GHz are about 1 s. At the instant when the rf power is switched off again, the reflected power jumps to $P_\mathrm{e}^\mathrm{inst}$ before decaying to zero as the stored energy in the cavity is dissipated. (The decay will be discussed further in the next section.)

The reflected power traces suggest a simple way of measuring the cavity coupling, which we adopted. Part of the reflected power is diverted to a crystal detector using a directional coupler. The signal from the former is connected to a digital oscilloscope (Tektronix 5223), that displays the reflected power trace. The computer sends a square power pulse to the cavity and triggers the oscilloscope to begin the acquisition of a trace. Once completed, it is downloaded to the Macintosh via GPIB for extraction of the input power, the steady state reflected power and the instantaneously emitted power. Only ratios of P_f, P_r, and $P_\mathrm{e}^\mathrm{inst}$ appear in the expressions for β, and calibrated values are not required. To avoid confusion with other power measurements discussed later, we will denote the (uncalibrated) powers obtained from the oscilloscope by a hat. Thus $\hat{P}_\mathrm{f}$, $\hat{P}_\mathrm{r}$, and $\hat{P}_\mathrm{e}^\mathrm{inst}$ represent the powers obtained from the oscilloscope, in voltage units. These are used by the computer to calculate β.

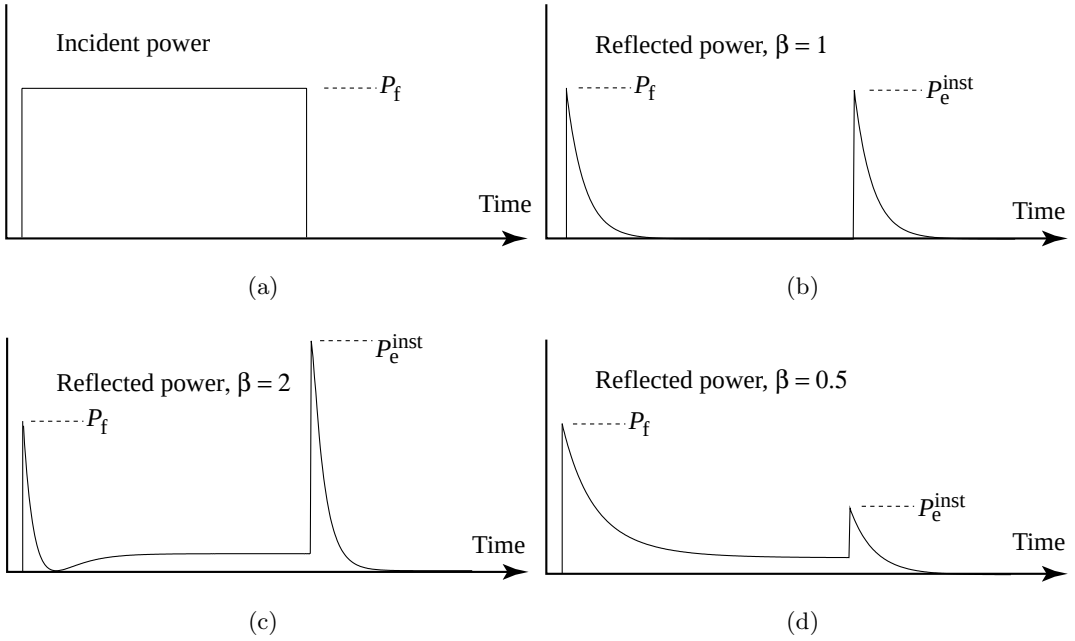

Figure 4.4: Temporal evolution of the power reflected at the input coupler if the cavity excited by a square input pulse.

4.4.2 Low field cavity quality

We know from Equations 4.1 and 4.2 that the total power P_{total}, dissipated by the cavity when the input power is switched off, is given by:

$$\begin{aligned} P_{\text{total}} &= \frac{dU}{dt} = P_{\text{d}} + P_{\text{e}} \\ &= \omega_0 U \left(\frac{1}{Q_0} + \frac{1}{Q_e} \right) \\ &= \frac{(1+\beta)\omega_0 U}{Q_0} = \frac{\omega_0 U}{Q_{\text{L}}}, \end{aligned} \tag{4.8}$$

where we have defined the *loaded quality* Q_{L} to be

$$Q_{\text{L}} = \frac{\omega_0 U}{P_{\text{total}}} = \frac{Q_0}{(1+\beta)}. \tag{4.9}$$

Provided no anomalous (non-quadratic) losses are active (i.e., Q_{L} is constant), solving (4.8) for U is simple:

$$U(t) = U_0 e^{-\omega_0 t/Q_{\text{L}}}. \tag{4.10}$$

The quantity U_0 is the stored energy just before the input power is switched off. The decay time of the stored energy is

$$\tau = \frac{Q_{\text{L}}}{\omega_0}. \tag{4.11}$$

The power emitted into the input coupler decays at the same rate as the stored energy because $P_{\text{e}}(t) = \beta P_{\text{d}}(t)$. Note that the emitted and reflected powers are identical, once

the input power is switched off. A measurement of the decay of the reflected power thus directly yields the loaded Q. Once the cavity coupling is determined (by using the method outlined earlier) it is simple to extract the unloaded Q:

$$Q_0 = (1+\beta)Q_{\mathrm{L}} = (1+\beta)\,\omega_0\tau. \tag{4.12}$$

We see that all the information necessary to obtain Q_0 can be obtained by measuring the cavity response to a square input pulse.

4.4.3 Electric field

To determine the peak electric field level in the cavity, we recall that the dissipated power in the steady state is given by (4.5):

$$P_{\mathrm{d}} = P_{\mathrm{f}}\frac{4\beta}{(1+\beta)^2}.$$

Since $P_{\mathrm{d}} = \omega_0 U/Q_0$, the steady state stored energy can be calculated:

$$U = \frac{P_{\mathrm{f}}Q_0}{\omega_0}\frac{4\beta}{(1+\beta)^2}. \tag{4.13}$$

From electrodynamics it is known that the stored energy is related to the peak electric field by

$$E_{\mathrm{pk}}^2 = \kappa_U U, \tag{4.14}$$

where the proportionality constant κ_U is only dependent on the cavity geometry. The constant can be obtained with computer codes such as SUPERFISH [26] and SUPERLANS. [27, 28] For the LE1 cavities we tested, one finds that

$$\kappa_U \approx 16.9\ (\mathrm{MV/m})/\sqrt{\mathrm{J}}. \tag{4.15}$$

Once κ_U is known and U is determined via (4.13) then E_{pk} in the steady state can be calculated. A calibrated measurement of P_{f} in addition to $\hat{P}_{\mathrm{f}}$ is therefore required. Such a measurement is made by the computer with a microwave power meter (Hewlett-Packard 436 A) via GPIB.

4.4.4 High field cavity quality

Equation 4.10 only applies if the dissipated power in the cavity scales quadratically with E_{pk}. This is usually the case at low fields (below a few MV/m). However, at higher fields, losses such as field emission begin to dominate the power dissipation and the decay of U is not governed by a constant τ. It is therefore difficult to extract the cavity Q from the decay of $\hat{P}_{\mathrm{r}}$ (although it can be done [114, 115]).

To circumvent this problem, one adopts a different approach for Q_0 measurements at high fields. In addition to the input power probe, a second (transmitted) power coupler is added to the cavity. In our case the coupler penetrates the top endcap of the cavity. This (fixed) probe is only weakly coupled to the cavity, the external Q being greater than 10^{12}. Very little power is transmitted out of this probe and the various expressions developed in the previous sections still apply.

To begin, Q_0 and $E_{\rm pk}$ are determined at a low electric field as outlined earlier. Care must be taken that no anomalous losses are active. At the same time the power emitted into the transmission probe ($P_{\rm t}$) in the steady state is measured. Same as $P_{\rm e}$, $P_{\rm t}$ is proportional to U. Since $E_{\rm pk}$ and U have just been measured, the following calibrations can be made:

$$K_E = \frac{E_{\rm pk}}{\sqrt{P_{\rm t}}}, \qquad K_U = \frac{U}{P_{\rm t}}. \tag{4.16}$$

These two quantities only dependent on the external coupling of the transmission probe, not $E_{\rm pk}$. Once known, K_E and K_U enable us to determine the stored energy and peak electric field in the cavity at any time, by simply measuring $P_{\rm t}$. Furthermore, a measurement of β, using the methods outlined earlier, directly yields $P_{\rm d}$ via (4.5). In turn, the dissipated power and stored energy give the cavity Q_0 by (4.1).

The technique just described is powerful because the Q_0 measurement at high fields does not require the ability to measure the (rapidly changing) decay rate of the reflected power instantaneously after the forward power to the cavity is switched off.

4.4.5 Feedback circuit and power measurements

At 1.5 GHz the unloaded Q_0 of the TM_{010} mode is typically 2×10^{10}. For a unity coupled cavity ($Q_{\rm L} = 10^{10}$) the bandwidth $\Delta f = \omega_0/(2\pi Q_{\rm L})$ of the mode is less than 1 Hz. For resonant excitation of the mode we therefore require a feedback system to stabilize the generator frequency and phase. The signal from the transmission probe can conveniently be used to provide the feedback signal. A schematic of the feedback arrangement used during cavity tests, along with the other components required to measure the forward, reflected and transmitted powers is shown in Figure 4.5.

An oscillator produces a 10 mW, 1.5 GHz signal. The computer controls the amplitude via a modulator and a pin attenuator, allowing the signal to be pulsed. The resulting waveform is boosted by a solid state amplifier (100 W or 250 W) and fed into the cavity through the input coupler at the bottom.

A -20 dB directional coupler at the test stand top plate diverts part of the forward power to a power meter. The meter permits the measurement of $P_{\rm f}$. Another -20 dB directional coupler diverts part of the signal reflected at the cavity input to an rf detector and digital oscilloscope, allowing measurements of $\hat{P}_{\rm r}$, $\hat{P}_{\rm e}$ and $\hat{P}_{\rm f}$. Similarly, part of transmitted signal from the output probe is routed into a power meter for $P_{\rm t}$ measurements. The circulator between the two directional couplers for $P_{\rm f}$ and $\hat{P}_{\rm r}$ is used to absorb all reflected power to protect the microwave amplifier. It also prevents standing waves in the directional couplers that might otherwise affect the couplers' directionality.

The remainder of the transmitted signal is amplified and routed to the "rf" input of a microwave mixer. Part of the original oscillator signal forms the "lo" input for the mixer. A trombone style phase shifter in the line from the oscillator permits the user to adjust the relative phase of the mixer's two inputs.

The mixer's dc output voltage varies linearly with the phase between the two inputs[2] and is transmitted to the frequency control of the oscillator. It ensures frequency and phase stability by keeping the microwave signal in lock with the oscillations in the cavity. The phase shifter in the line between the oscillator and the mixer is required to compensate for a difference in the effective distance traveled by the two input signals to the

[2]Linearity is only guaranteed for small phase differences.

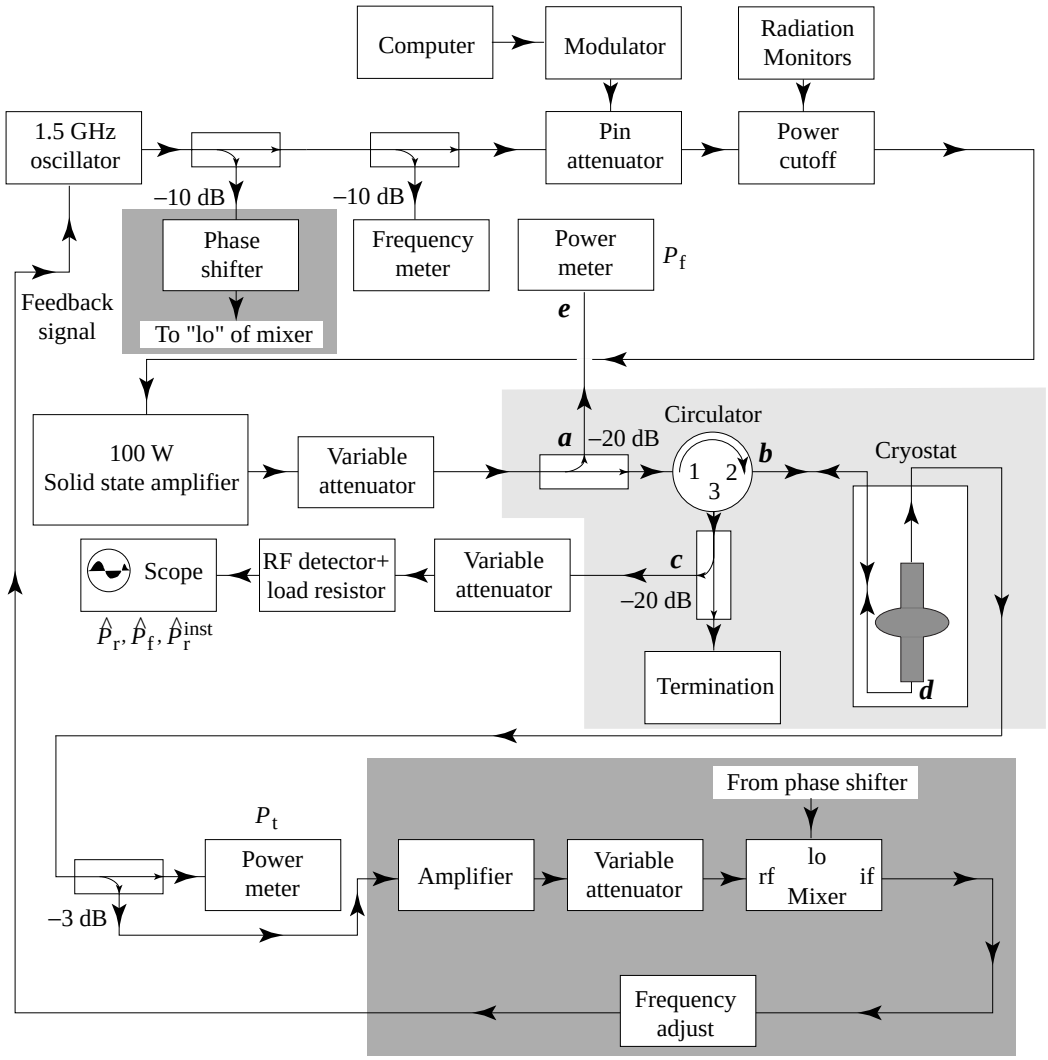

Figure 4.5: Schematic of the cavity testing system. Shown are the components required to measure the forward, reflected and transmitted powers for Q_0 versus E_{pk} measurements, and the feedback circuit. Devices in the light shaded region are in the shielded test area. All other devices are mounted in the operations rack outside the shielding. The dark shaded region denotes the main components of the feedback circuit.

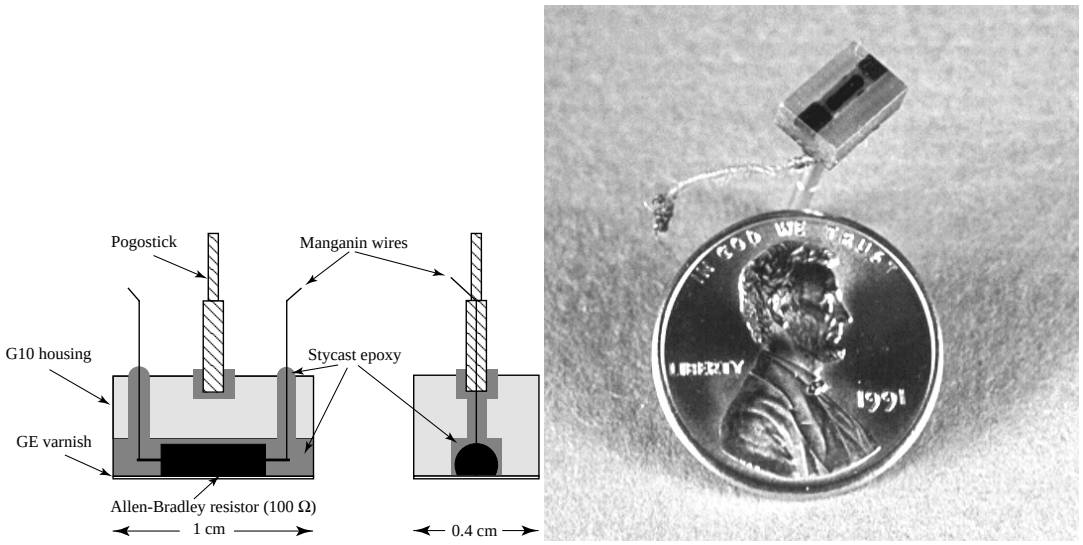

Figure 4.6: (a) Schematic and (b) picture of the thermometers used by the temperature mapping system. The sensing element is a 100 Ω Allen-Bradley carbon resistor.

mixer, and to compensate for any dc offsets the mixer may have. Note that at 1.5 GHz the wavelength in vacuum is 20 cm.

4.5 The thermometry system

The thermometry system discussed here is designed to operate in parallel with the Q_0 versus $E_{\rm pk}$ measurements. Both systems are controlled by the same computer. 756 thermometers, specially designed for high sensitivity in superfluid helium, cover the exterior cavity surface. This fixed thermometer array, in conjunction with a high speed multiplexing system, permits the rapid acquisition of temperature maps. The user therefore is able to acquire extensive calorimetry data and, simultaneously, Q_0 versus $E_{\rm pk}$ data under various cavity operating conditions.

4.5.1 Thermometers

The thermometer design was adopted from a previous thermometry system used at Cornell. [5] The schematic and a picture of a thermometer are shown in Figure 4.6. The temperature sensing element is a 100 Ω carbon Allen-Bradley resistor (5 %, 1/8 W). Because carbon is a semiconductor, its resistance increases exponentially with decreasing temperature. At 1.6 K this effect is very pronounced (≈ 30 Ω/mK) and even millikelvin temperature variations can be detected. However, the resistance of these thermometers changes when they are cycled to room temperature, so that each thermometer needs to be recalibrated for every cavity test. The calibration procedure will be discussed later.

The regular resistor leads (high thermal conductivity wire) are clipped close to the body of the resistor. In their place manganin wires, 0.14 mm in diameter, are spot welded to the remaining resistor contacts. Manganin has a low thermal conductivity

and is used to minimize the cooling of the resistor by liquid helium via the leads. Several such modified resistors are set in a groove made in 3 mm thick G-10 board spaced about 2 cm apart. The manganin leads are passed through small holes at the bottom of the groove. The depth of the groove is slightly greater than the diameter of the resistor body.

The groove then is filled with epoxy (Stycast 2850 FT), thereby encasing the resistors and spot welds. The epoxy–G-10 combination is designed to thermally isolate the carbon resistor from the helium bath it is immersed in. Care needs to be taken to de-air the stycast in a 1 torr vacuum before it cures. This ensures that no gas is trapped in small bubbles, that could cause problems during cryogenic cycling and in the superfluid environment to which the thermometers are exposed.

The top surface of the epoxy–G-10 combination is ground away until the carbon elements of the resistor are exposed. This side will later be attached to the cavity surface. Spring loaded pins ("pogo sticks") are mounted with stycast in recessed holes in the bottom of the G-10 board opposite the resistor bodies. Later, when the thermometers are mounted on the cavity surface, these provide a contact force of about 2 N.

Next, the G-10 board is sectioned to yield the individual thermometers. The top surface of each thermometer is burnished with 600 grit emery cloth for a smooth finish. A thin layer of GE-Varnish (7031), diluted to 50 % with acetone, is applied to insulate the carbon element electrically from the cavity.

To help attach the thermometers to the cavity surface, 72 boards of G-10 material (3.2 mm thick) are machined to match the cavity contour, while leaving a 1 cm gap between the cavity surface and the board. 19 equispaced grooves (1.5 mm deep, 16 mm long) are machined perpendicular to the cavity contour in half of these boards (type A). In each of the remaining 36 boards (type B) only two grooves (near the beam tubes) are machined. Each type A board is then sandwiched together with a type B board to yield 36 completed "thermometer boards." The grooves now effectively are holes into which the pogosticks of thermometers can be inserted. Each thermometer board thus accommodates 21 thermometers which it presses against the cavity wall. The arrangement of 19 grooves in one half of the board and 2 grooves in the other half is needed to avoid interference between the pogosticks of thermometers near the beam tube. A completed thermometer board with thermometers is shown in Figure 4.7.

Four semicircular aluminum plates are attached to the top and bottom beam tubes of the cavity to form two rings. Each ring has 36 radial grooves (6.4 mm wide) into which the thermometer boards slide (Figure 4.8). Once the boards are in place, non-magnetic stainless steel set-screws are inserted into threads at the outer end of the grooves to firmly push the boards against the cavity.

Apeazon N grease is applied to the varnished side of the thermometers prior to inserting the boards in the holders. When the thermometers press against the cavity wall, the grease spreads into any remaining gaps and prevents superfluid helium from cooling the sensing element unnecessarily. Especially the thermometers attached at the top and bottom iris require copious amounts of grease because the curvature of the iris prevents good contact between the cavity and the thermometers. These thermometers are also ground away along the edges more than the others, to permit them to squeeze into the narrow space of the iris. In spite of these measures, their sensing efficiency is diminished with respect to the other thermometers.

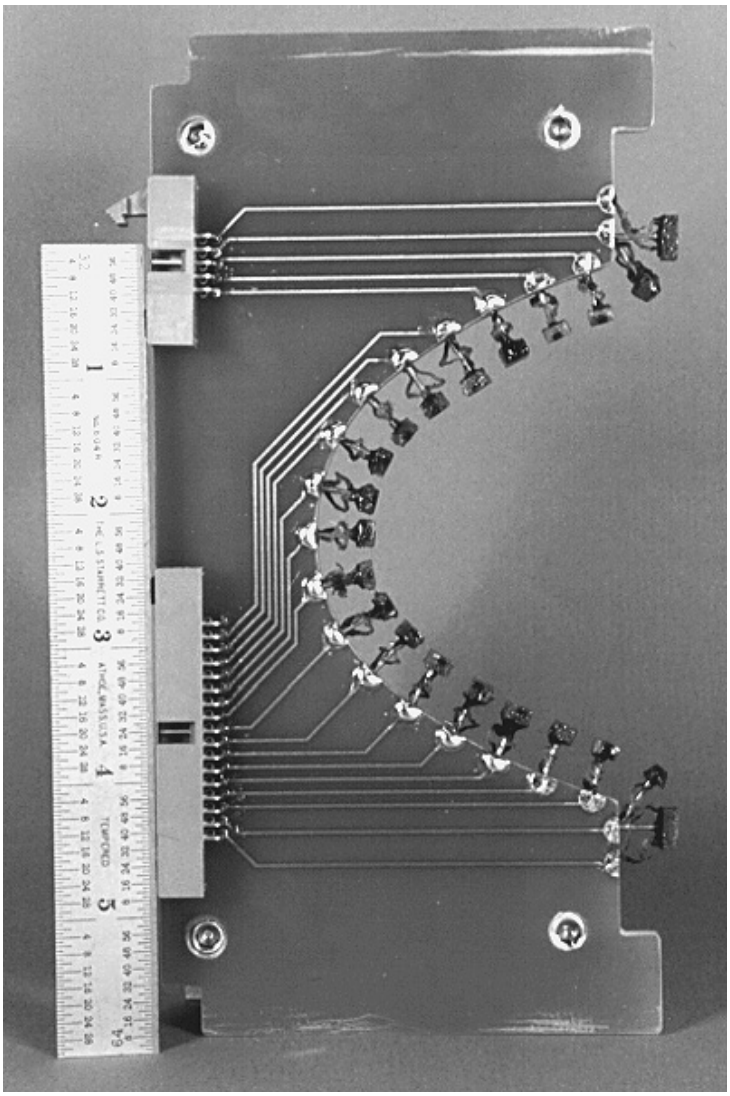

Figure 4.7: A single thermometer board designed to match the contour of LE1 cavities. Each board holds 21 thermometers.

Altogether 36 thermometer boards, spaced by 10°, are used to cover the cavity with a total of 756 thermometers. The spacing between thermometers on neighboring boards varies from about 0.65 cm at the iris, to 1.7 cm at the equator, whereas the spacing along a board is about 0.85 cm. Calculations and experiments have shown that the full width at half maximum (FWHM) of the temperature distribution due to a point heat source on the cavity interior is between 0.5 cm and 1.2 cm at the outer cavity surface. [116] We expect that at least two thermometers should respond to heating on the cavity interior, provided the dissipated power is sufficient.

An additional 8 thermometers are suspended in the helium bath without being in contact with the cavity. These are used to monitor the bath temperature while a map is being acquired, thereby permitting us to compensate for thermal drifts during the acquisition. Hence a total of 764 thermometers needs to be scanned for one temperature

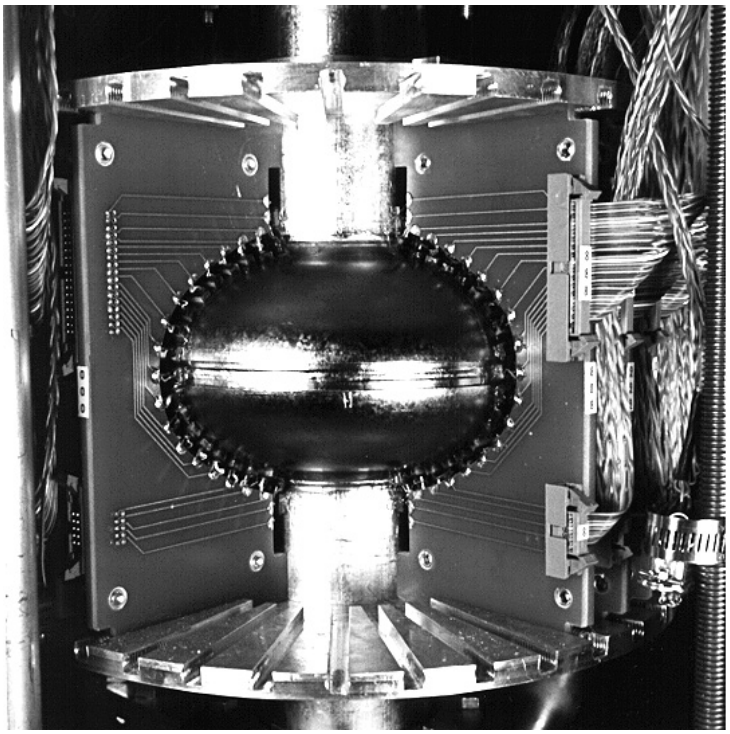

Figure 4.8: Picture of thermometers mounted on a cavity. Seven boards were removed to expose the cavity.

map.

At 1.6 K, which presently is the lowest temperature we can reach with our pumping system, the resistance of the thermometers is typically about 12 kΩ and their sensitivity dR/dT is approximately 33 Ω/mK.

4.5.2 Electronics

Based on past experience, we found it important that each thermometer can be operated independently. In a previous temperature mapping system developed at Cornell the emphasis was on reducing the number of leads. [5, 15] Most leads were shared by several thermometers, and up to 55 thermometers could be affected by a single wire failure, thereby seriously compromising the reliability of the system. Furthermore, cross-talk between thermometers sharing leads proved to be a common problem. In many cases artificial signals in temperature maps complicated the interpretation of thermometry data.

In the system being described here independent leads are used for every thermometer, to ensure that only one thermometer will be affected by a wire failure, and that cross-talk is minimized. However the independence comes at a cost. Using the wiring scheme detailed below, 1528 leads need to be connected from the 6 torr helium space in which the cavity is operated to a multiplexing scheme at room pressure and temperature.

The potential heat leak through the numerous wires into the liquid helium was not a major concern. Tests showed that the heat leak was only 1 – 2 W despite the large

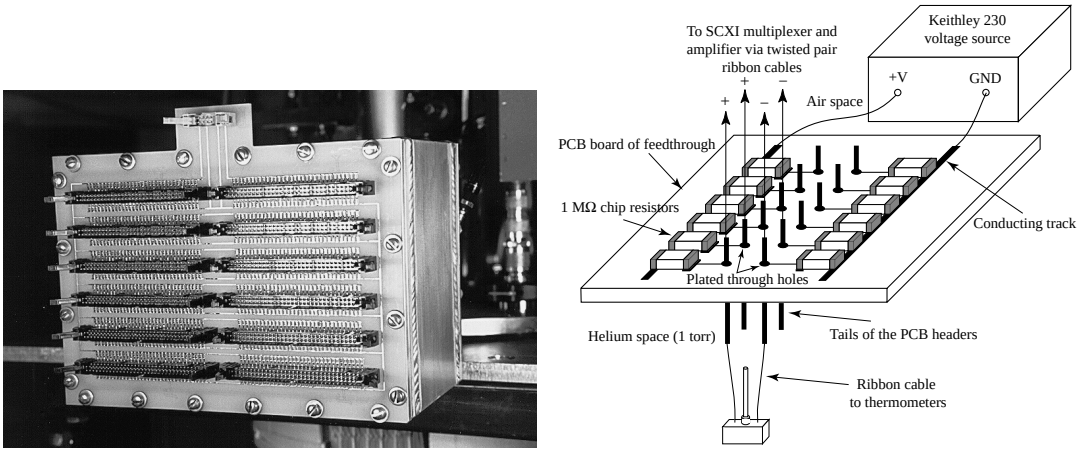

(a) (b)

Figure 4.9: (a) Picture of one of the two feedthrough boxes at the top plate of the test stand. Each feedthrough provides 768 connections and is capable of maintaining a vacuum better than 1 torr. (b) Schematic of the circuit on the front panels of the feedthroughs and the wiring in the cyostat. The 1 MΩ chip resistors, in combination with the Keithley voltage source act as individual current sources for the thermometers.

number of leads. However, we were limited to an operating temperature above 1.6 K. This limit was set by the pumps employed to evacuate the cryostat.

4.5.2.1 Wiring in the cryostat

Printed circuits on the thermometer boards are used to simplify the wiring scheme. The leads from each thermometer are soldered to pads nearby on the thermometer board. Conducting tracks from the pads lead to printed circuit board (PCB) header connectors at the outer edge of the boards. These connect to PVC insulated twisted-pair ribbon cables (28 gauge) via insulation displacement connectors (IDC's). In turn these are connected to two specially developed feedthroughs at the top plate of the test stand (Figure 4.9(a)).

The feedthroughs consist of two $16.5 \times 23.6 \times 12.7$ cm^3 aluminum boxes that are bolted onto flanges leading into the cryostat via rectangular vacuum tubes. Each of the boxes has a demountable brace at the front side, needed to support the room pressure acting on the feedthrough. A demountable 16.5×23.6 cm^2, 0.32 cm thick G-10 board with 768 plated through holes sits on the brace. Twelve 64 pin PCB headers with 1.55 cm long tail pins are inserted in these holes and soldered in place. The headers are on the air side of the feedthrough and their tails protrude into its vacuum space. The solder is sufficient to maintain a vacuum of better than 1 torr. Each of the two G-10 boards also holds the appropriate printed circuits to operate the thermometers in parallel (see Figure 4.9(b)). The key components of these circuits are 768 1 MΩ chip resistors on each feedthrough, of which always two in conjunction with the driving voltage act as a current source for one thermometer. The chip resistors also isolate the thermometers from each other, thereby eliminating ground loop problems. The grids on the feedthroughs are driven by a Keithley 230 voltage source controlled via GPIB by the same Macintosh Quadra 700

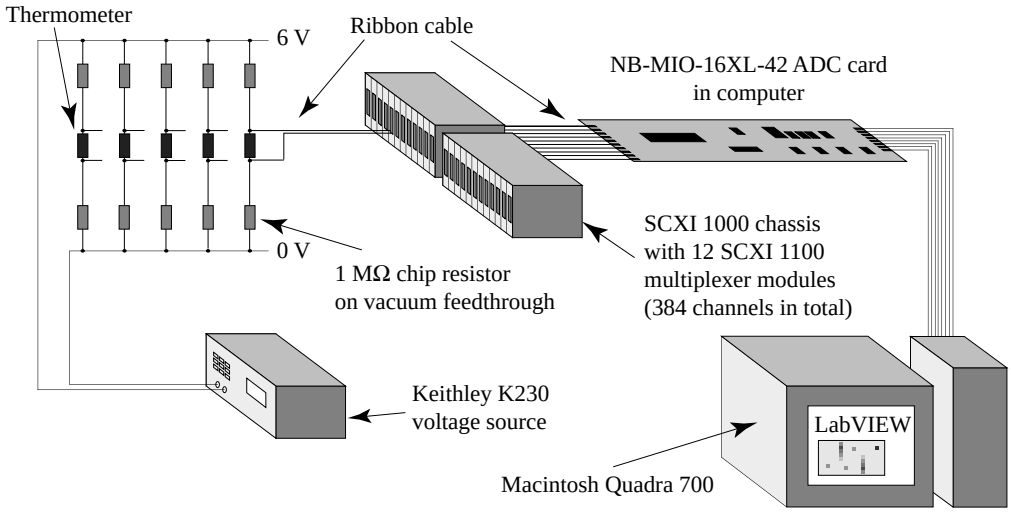

Figure 4.10: Schematic of the multiplexing scheme used to scan the thermometers.

used for Q_0 versus E_{pk} measurements. Typical excitation voltages used are 6 V, so that the voltage drop across a 12 kΩ resistor is about 36 mV.

The twisted-pair ribbon cables from the thermometer boards are routed via the rectangular vacuum pipes into the feedthroughs. There they are attached to the long PCB header tails on the interior using conventional IDC's. Should a cable fail, it is simple to detach it from the feedthrough and to insert a new one.

Initially there was some concern that the IDC's were prone to failure in superfluid helium. Such events, though, were not observed until the system had been cycled for over 30 times. On the few occasions that connections did fail, it was a simple five minute operation to cut off the IDC and replace it with a new one.

The PVC insulation of the twisted-pair ribbon cables was subject to some cracking at cryogenic temperatures. Teflon insulation is more resilient at low temperatures but proved to be too expensive. Despite the occasional cracking of the PVC cables, no short circuits were recorded in more than 40 thermal cycles, because the insulation maintained a physical separation between conductors.

4.5.2.2 Multiplexers

On the air side of the feedthrough, IDC's connect to 2 meter long, shielded, twisted-pair, ribbon cables (sense wires) that lead to the multiplexing system. A schematic of the system is shown in Figure 4.10.

We adopted the SCXI$^{\mathrm{TM}}$ system from National Instruments to scan the voltage signals across the thermometers. Together with a measurement of the excitation current, the thermometer resistance can then be deduced. The heart of the multiplexing system consists of two SXCI 1001 chassis placed outside the radiation shielding of the test area. Both chassis contain twelve SCXI-1100 modules, each of which is capable of multiplexing 32 differential inputs. We therefore are able to scan a total of 768 signals. The modules also amplify the multiplexed signals by gains of 1 – 2000, before they are routed to the Macintosh (about 3.5 meters away) via a 50 conductor shielded twisted-pair ribbon cable.

The signals are digitized at the computer by a National Instruments NB-MIO-16XL-42 16 bit analog to digital converter (ADC). The specified maximum rate of conversions is 24 kHz. A National Instruments direct memory access board (NB-DMA 2800) is used in conjunction with the ADC to write information directly to the computer's memory to free up the main processor for other tasks. The acquisition software was written in the LabVIEW^{TM} programming language.

The connections between the feedthrough and the SCXI chassis are arranged in such a manner that neighboring thermometers are always scanned sequentially in time. This results in a somewhat awkward wiring scheme, however it resolves any cross talk problems that could otherwise occur due to settling times in the amplifiers on the multiplexer cards. The impedance seen by the amplifiers nearly equals the resistance of the thermometers (about 12 kΩ at 1.6 K). We found that for the largest anticipated jumps between sequentially scanned voltages, the amplifiers settle to within 99.995 % of the true value within the scan interval, provided we operate within the specifications of the ADC. In this case settling problems would not become apparent unless temperature resolutions better than 20 μK are required. However, should it become desirable in the future to operate at a bath temperature of 1.4 K, the thermometer resistances would increase to about 40 kΩ and settling times become an issue. Spurious signal could then appear in temperature maps. However, the effect of crosstalk is minimized by scanning neighboring thermometers sequentially, since these are generally affected by the same heat source.

4.5.3 Thermometer calibration and map acquisition

To determine the thermometer resistances, the Macintosh measures the average voltage drop across each thermometer by scanning the resistors several times. It then switches the polarity of the drive source and repeats the process before taking the difference between the two sets of measurements. These values, along with a measurement of the excitation voltage, allow the computer to calculate the resistance of each thermometer. By reversing the polarity and only using the differences between voltages, any contact voltages in the circuits are canceled out. The same is true for amplifier offsets. If the number of scans at each polarity is limited to one, the entire scanning process takes less than 0.14 s, which is about a factor of 100 faster than previous fixed thermometry systems. On the other hand, if we are willing to sacrifice some acquisition speed for an improvement in resolution, we can easily increase the number of scans over which we average.

4.5.3.1 Calibration

A calibrated LakeShore germanium thermometer (GR-200A-250) is also included in the helium bath. It serves as a reference during the calibration of the carbon thermometers when the helium bath is cooled from 4.2 to 1.6 K at the outset of a test. It is excited by a 10 μA current source. The current and voltage drop across the thermometer are measured by a microammeter and voltmeter respectively to yield the thermometer's resistance. Both are connected to the Macintosh via GPIB interfaces.

Calibration points are taken at about 0.1 K intervals, using the scanning scheme outlined above. Once the calibration measurements are completed, the data is approximated

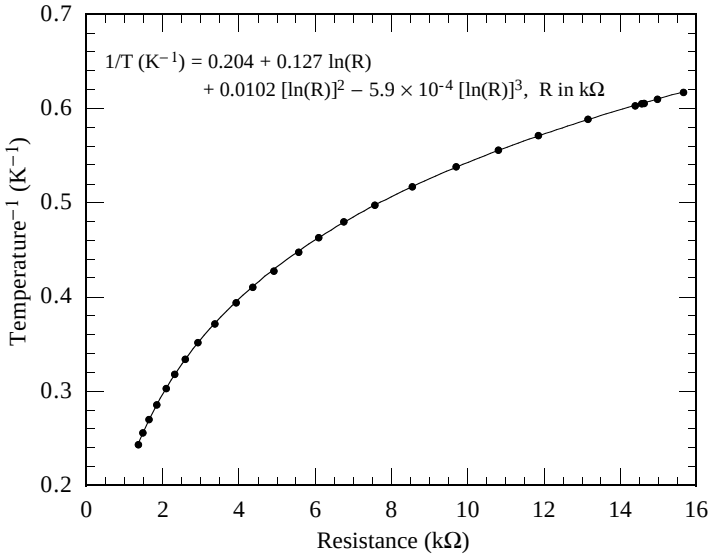

Figure 4.11: Calibration data obtained for one of the 764 thermometers and the appropriate curve fit using Equation 4.17.

by a function of the form,

$$\frac{1}{T} = a_n + bx_n + cx_n^2 + dx_n^3; \qquad x_n = \ln R_n, \tag{4.17}$$

where T is the bath temperature measured by the germanium thermometer, R_n is the resistance of carbon thermometer n, and a_n, b_n, c_n, and d_n are fit parameters. Figure 4.11 shows a typical calibration curve and the fit given by (4.17). For each thermometer the square deviation between the measured data and the fit is computed. Thermometers are deemed faulty if this value exceeds the mean of all thermometers by a factor of ten. Bad thermometers are subsequently ignored during the acquisition of temperature maps. Generally, less than eight thermometers fail during each test. They are replaced between tests.

4.5.3.2 Temperature mapping

Once the calibration is completed the system is ready to map the temperature distribution of the cavity. A complete map is obtained by measuring the resistances of all thermometers as outlined above, once with the rf power to the cavity switched on, and once with it switched off. It is the difference in temperature (ΔT) that the computer then calculates using the thermometer calibration. This procedure cancels out any self heating of the thermometers due to the excitation voltage. The eight carbon thermometers immersed in the helium bath but not attached to the cavity are used to measure the bath temperature drift during the acquisition of a temperature map. These drifts are subsequently subtracted from the measured ΔT's of the thermometers.

If desired, the user can also map the cavity several times in rapid succession to study transients or a sub region of the cavity can be mapped to investigate individual sites of interest.

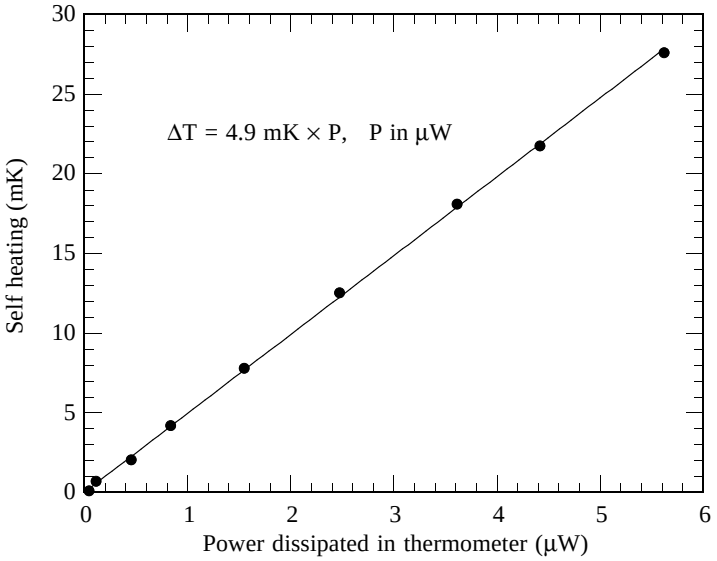

Figure 4.12: Measured self heating of a carbon thermometer as a function of the power dissipated by the excitation voltage.

4.5.4 Test of the thermometry system

To test the precision of the calibration fit using (4.17), bath drift measurements were carried out. These entail taking a temperature map at 1.6 K when no power is applied to the cavity. The bath temperature is then allowed to drift to some intermediate temperature below the lambda point (we stay below the lambda point to avoid temperature gradients) and the thermometers are scanned again. The measured temperature differences are compared with that recorded by the germanium thermometer. Results showed that the Allen-Bradley resistors were accurate to about 1 %.

Extensive studies have been performed on the efficiency of the thermometers. [116] The efficiency η_{T} is defined as the ratio of the measured temperature rise to the theoretical temperature rise (based on heat flow simulations) at the cavity's outer surface. Generally it was found that η_{T} was around 35 % $\pm$ 13 %. The response of the thermometers was found to be linear with the power flux in the range 1 μK to 1 K. [116] The equivalent power flux over the linear range is about 1 μW/cm^2 to 1 W/cm^2.

A study of the self heating of the thermometers as a function of the power dissipated by the excitation current revealed a linear dependence as well. A temperature rise of approximately 1 mK was detected for a power dissipation of 0.2 μW (see Figure 4.12). On the other hand, during our experiments we could easily detect temperature rises of 0.1 mK or less due to external heat sources. Although this is less than the self heating, the latter is easily calibrated out, since all measurements are designed to yield the temperature difference between the cavity in operation (rf power on) and the input power being switched off. However, for self heating greater than the 1 mK level we found that the measured signals were severely swamped, thereby compromising the sensitivity of the system.

Figure 4.13 depicts a temperature map obtained at 17.2 MV/m during a test run of the thermometry system. For convenience the same data is plotted in a flattened view

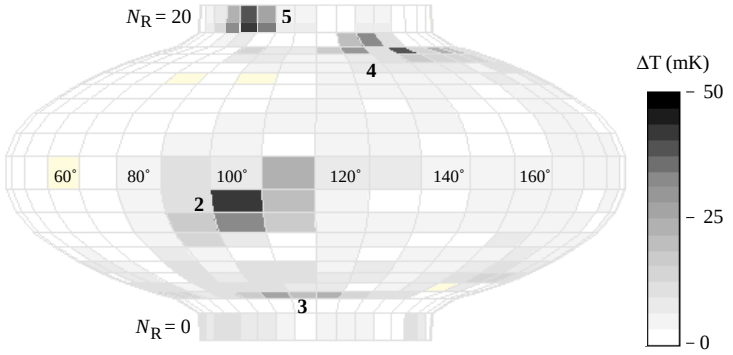

Figure 4.13: Temperature map, superimposed on the cavity shape, obtained during a test of the temperature maping system at 17.2 MV/m.

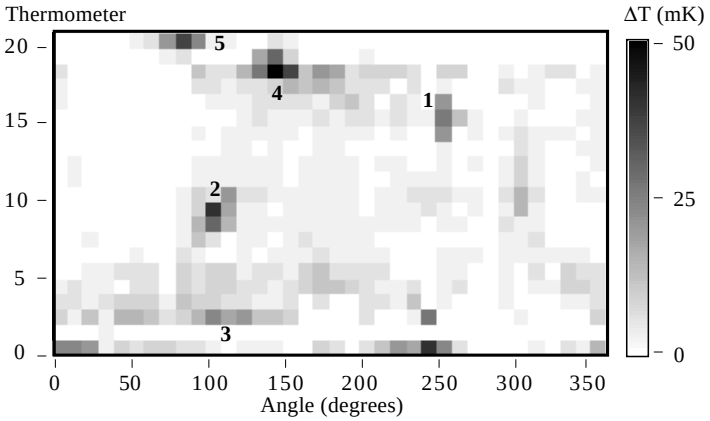

Figure 4.14: Temperature data in Figure 4.13 shown in a flattened view of the cavity. The abscissa represents the angle around the cavity and the ordinate represents the thermometer number (N_R), starting from the bottom iris.

of the cavity in Figure 4.14.

The heating observed at point 1 is due to weak ohmic losses. Figure 4.15 depicts the profile of the heating along the azimuth of point 1 (i.e. along one thermometer board) as a function of the distance from the equator along the cavity contour (S). The peak electric field was 0.7 MV/m. It takes about 2.5 s to acquire a temperature map at this high resolution. We see that the 63 μK peak due to the heat source at point 1 is clearly visible above the mean background signal of $\overline{\Delta T} = 6.7$ μK. The 3σ level of the noise registered by the remaining thermometers is about 33 μK. This resolution is about a factor of 150 times better than existing high speed systems (e.g., [5]) and even approaches the capabilities of the highest resolution system we know of [6, 7] at only a fraction ($\approx 1/1000$) of its map acquisition time. If the scan time is reduced further to about 140 ms, the 3σ level of the noise increases to around 0.2 mK. Even at this resolution we can detect the temperature rise due to a surface resistance of 10 nΩ at $E_{pk} = 10$ MV/m. This value is less than the residual resistance of most cavities we tested.

The thermometry data in a temperature map can be converted to an equivalent

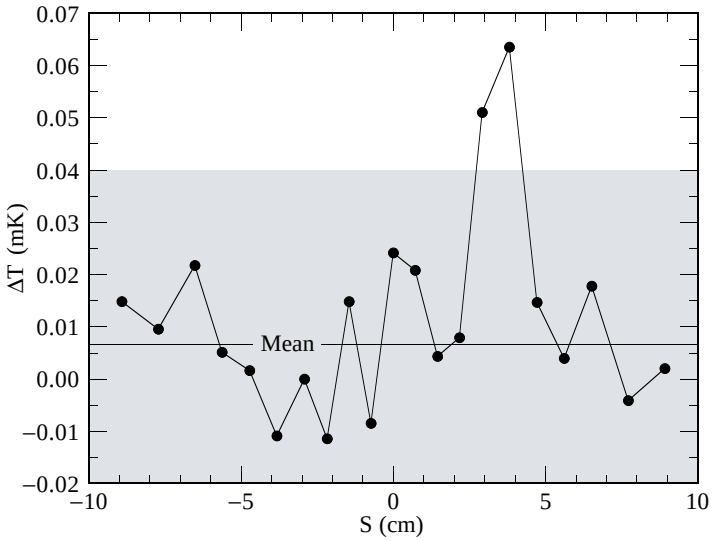

Figure 4.15: Temperature profile along the azimuth of point 1 in Figure 4.14, illustrating the temperature resolution of the thermometry system. The data was obtained at $E_{\rm pk} = 0.7$ MV/m. The gray band delimits $\overline{\Delta T} \pm 3\sigma$.

cavity Q_0. The total power dissipated in the cavity ($P_{\rm d}^{\rm cal}$), as measured by calorimetry, is given by

$$P_{\rm d}^{\rm cal} = \frac{1}{K_T} \sum_{n=1}^{758} \Delta T_n A_n, \tag{4.18}$$

where n runs over all thermometers, A_n is the area of the region closest to thermometer n, ΔT_n is the temperature rise registered by thermometer n and K_T is the temperature response of the thermometers to a unit of uniform power flux. It is assumed that K_T is roughly the same for all thermometers. Using (4.18) the cavity Q_0 as measured by calorimetry is known:

$$Q_0^{\rm cal} = \frac{\omega U}{P_{\rm d}^{\rm cal}}. \tag{4.19}$$

A comparison of $Q_0^{\rm cal}$ with the Q_0 obtained from power measurements is a useful check on how well the thermometers measure cavity losses. Figure 4.16 illustrates one such comparison. The curves match well, provided a value of $K_T = 2.3$ Kcm^{2}W^{-1} is used.[3] At higher field levels we sometimes observed small discrepancies with some cavities. Usually these are associated with field emission activity. Not all emission electrons strike the walls in the region covered by thermometers and the thermometry system may underestimate the dissipated power. Furthermore, not all the energy of field emission electrons is converted into heat upon impact. A small portion is radiated away as bremsstrahlung x-rays.

[3] K_T varies from cavity to cavity because of different surface characteristics and thermometer contact pressure. A calibration at one field level is therefore required. In all cases, though, K_T is on the order of 1 Kcm^{2}W^{-1}.

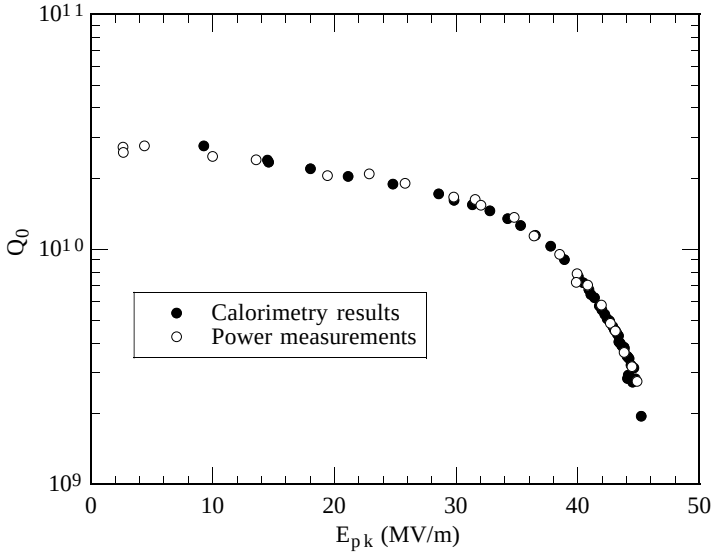

Figure 4.16: Comparison of Q_0 results from the temperature mapping system and from conventional power measurements.

4.6 A typical cavity test

What follows is a description of the typical techniques used to prepare and test a cavity. This section is designed to convey a more complete understanding of the procedures and measurements involved and to illustrate the degree of automation of the testing system.

4.6.1 Cavity preparation

Prior to testing, all cavities have to be thoroughly cleaned to eliminate any particle contamination on the inside surfaces. The following sequence is employed.

1. If the cavity has previously been used in cavity tests, any indium (from seals) remaining on the flanges is removed with copper scrapers. The cavity is then immersed in nitric acid for at least 1 hour to dissolve indium that may have fallen into the cell. This step is required, because the acid mixture described in step 2 does not remove indium sufficiently rapidly.

2. All cavities are etched in a mixture of nitric, hydrofluoric and phosphoric acid (buffered chemical polish or BCP) in a volumetric ratio of 1:1:2. [117] The entire cavity is immersed in this mixture. About 10 μm is removed from the surfaces of previously etched cavities. Newly manufactured cavities are etched longer, to remove up to 100 μm. During all etches, care needs to be taken that the acid temperature does not exceed 15 °C, to avoid hydrogen contamination (see Section 3.3.3). At acid temperatures between 0 °C and 15 °C typical etch rates are 1 to 1.5 μm/min.

3. Following etching and rinsing in high purity deionized water, the cavity is mounted on a continuous flow rinsing apparatus. In this setup, deionized water flows through

the cavity in a closed loop. A filtering system in the loop removes ions and particulates before the water enters the cavity. Rinsing is performed for at least 1 hour. At no time is the cavity exposed to air during this process.

4. Once the rinsing is completed, the cavity is sealed with the water inside and carried into a class 10 clean room. There the water is drained and the cavity is dried by flushing warm, filtered nitrogen gas through it for 1/2 to 1 hour.

5. When the cavity is dry, the endplate with the output probe is mounted on the top flange. The bottom cavity flange is then attached to the coupler/bellows arrangement of the test stand.

6. Slow evacuation of the cavity with a turbo pump follows. Pump down rates exceeding 5 torr/s are avoided to prevent dust contamination and water condensation. Once the pressure is below 2×10^{-6} torr the system is switched over to the ion pump that lowers the pressure to about 2×10^{-8} torr. This step takes a couple of days.

7. During or following the final pumpdown, the thermometers are mounted on the cavity. Their resistance is checked at room temperature using the temperature mapping system. Any broken thermometers are replaced.

8. Finally the test stand is transferred to the cryostat for testing.

4.6.2 Cavity cooling

Immediately prior to transferring liquid helium to the cryostat, the outer jacket is filled with liquid nitrogen. Overnight pre-cooling of the cryostat and cavity to 77 K is not carried out, because of the danger of hydride precipitation at the rf surface during the slow cooldown (see Section 3.3.3).

The transfer of cryogens takes about 2 hours. 250 l of liquid helium are needed for a test lasting 12 hours.

4.6.3 Thermometer calibration

Following the transfer of liquid helium, the cryostat is evacuated to lower the bath temperature. During this time, the Macintosh continually measures the temperature of the germanium thermometer. At user specified temperature intervals (usually about 0.1 K) the computer scans the carbon thermometer array to obtain the resistance of each thermometer as a function of temperature. Following every scan, the data is saved to the hard drive, to minimize the impact of a system crash. At any time, the user can examine the calibration data of a thermometer along with the best fit of the form (4.17). An example of the computer display during the thermometer calibration phase is shown in Figure 4.17.

When the bath temperature has been lowered to 1.6 K, the calibration is complete, and the computer calculates the fit parameters in (4.17) for the entire thermometer array. The data is used later for temperature map acquisitions.

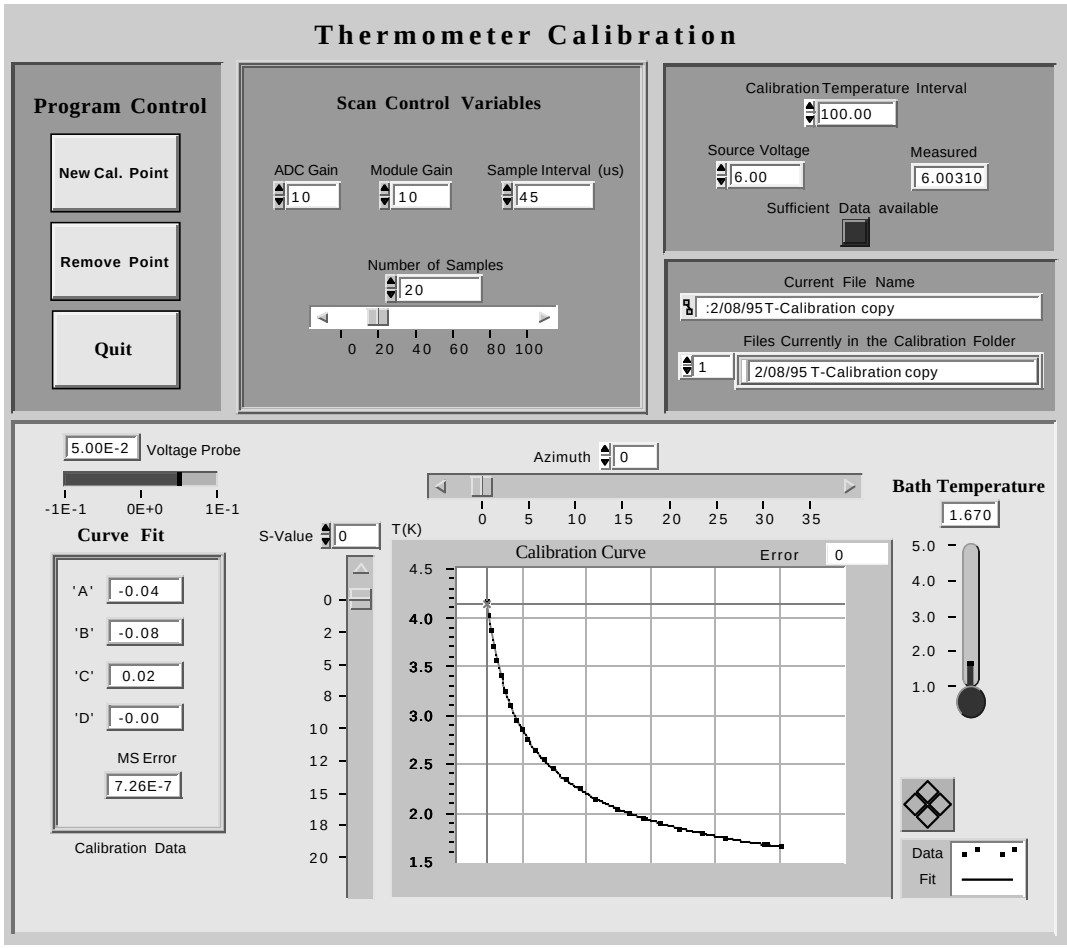

Figure 4.17: User interface for the calibration of the carbon thermometers during the initial cooldown of the cavity from 4.2 K to 1.6 K.

4.6.4 Calibration of the Q_0 measurement system

The setup now is ready for the calibration of the Q_0 versus $E_{\rm pk}$ measurement system. Part of the procedure is automated and other parts are performed manually. The appropriate computer user interface is shown in Figure 4.18. The calibration is performed without the solid state amplifier at a low electric field (the oscillator alone is sufficient to achieve $E_{\rm pk} \approx 2$ MV/m.

Initially the cavity is operated out of lock by switching off the feedback system. Hence all power is reflected at the cavity input coupler. A measurement of the forward and reflected power at the directional couplers on the top plate of the test stand ($P_{\rm f,d}$ and $P_{\rm r,d}$ respectively) thus permits us to determine the attenuation of the power cable leading into the cryostat. The power levels are measured manually at low power and entered into the computer. Prior to the test, the attenuation (in dB) between points "a" and "b" (A_{ab}) and points "b" and "c" (A_{bc}) in Figure 4.5 are measured with a network analyzer. This data is also entered in the computer. At a later time the computer then calculates the attenuation of the cryostat cable between the top plate and the cavity, which is given by

$$A_{bd}\ ({\rm dB}) = 10 \log \left(\frac{10^{-A_{bc}/10} P_{\rm r,d}}{10^{A_{ab}/10} P_{\rm f,d}} \right)^{1/2} . \tag{4.20}$$

Following this procedure, 6 m cables leading out of the shielded area to the control rack are attached to the forward power and reverse power directional couplers. The other ends are connected to the Hewlett-Packard 436 A power meter via a Hewlett-Packard 59306 A microwave switch. The transmitted power cable is also connected to the same switch. Both devices are controlled by the computer which can select between the power sources for measurements.

Next, the cavity is operated in lock and close to unity coupling. The user minimizes the reflected power by adjusting the phase of the feedback signal with the phase shifter. The computer then automatically measures the transmitted power ($P_{\rm t}$) to later calculate K_E and K_U. The computer also measures the forward power ($P_{\rm f}$) at the rack. This measurement is particularly important for the calibration of the cable attenuation A_{ae} between the power meter and the directional coupler in the shielded area. Knowledge of this attenuation is essential so that a measurement of $P_{\rm f}$ can be used to calculated the dissipated power $P_{\rm d}$.

The computer then switches off the rf power and triggers the digital oscilloscope to captures the decay of the emitted (= reflected) power. The trace is downloaded to the computer via the GPIB interface. It permits the extraction of $\hat{P}_{\rm e}^{\rm inst}$ and the steady state $\hat{P}_{\rm r}$, the latter being obtained from the cw data before the input power is switched off. The decay time τ is also computed.

Finally, the rf power is switched on once more and the cavity is taken out of lock again. All power is reflected. Another oscilloscope trace is obtained and downloaded to yield $\hat{P}_{\rm f}$. We measure $\hat{P}_{\rm f}$ in this manner because our solid state amplifiers have long switch-on times and the first peak in Figure 4.4 does not accurately reflect $\hat{P}_{\rm f}$.

The computer now possesses all the information needed to determine the attenuations in various cables, to calculate Q_0 and $E_{\rm pk}$, and to determine K_E and K_U. The following

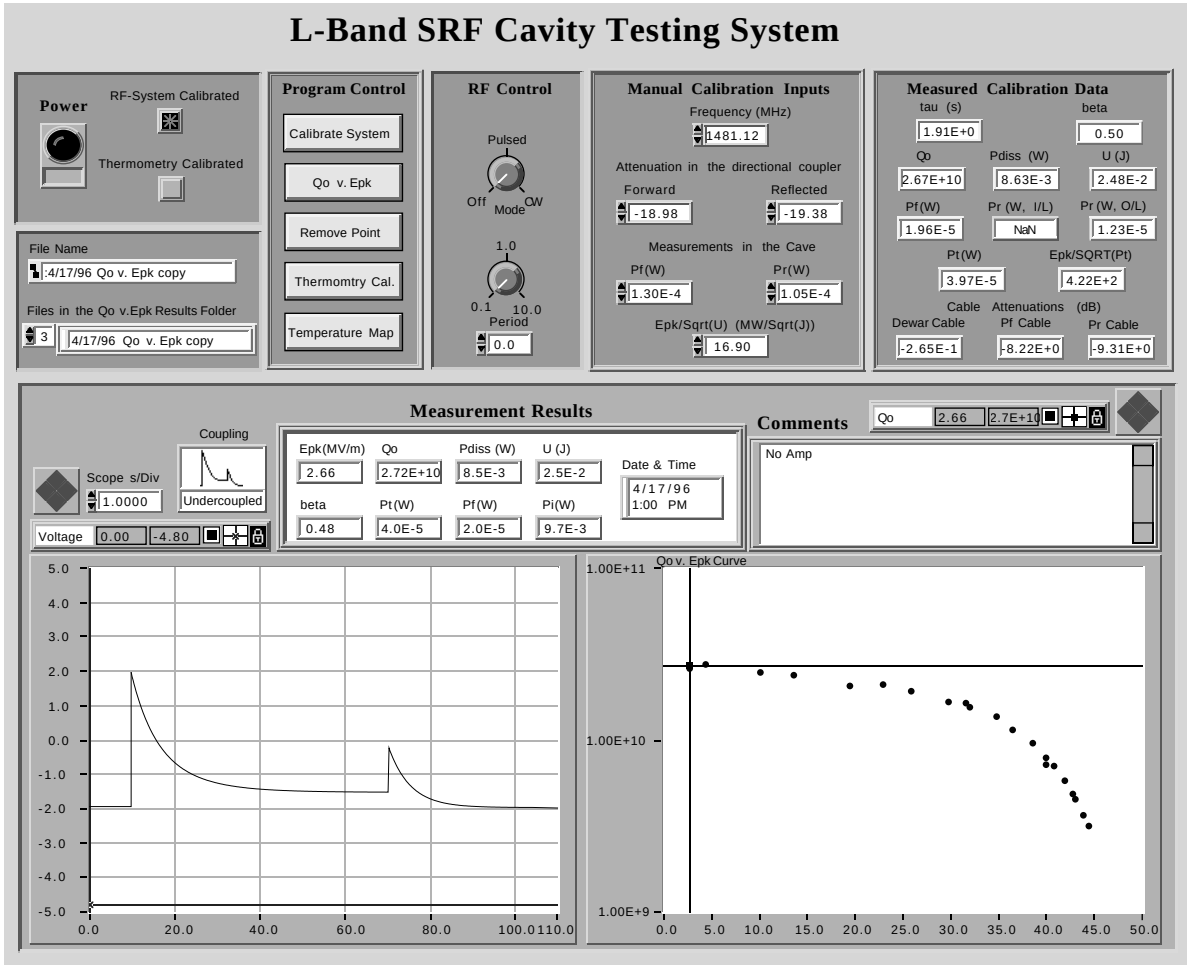

Figure 4.18: User interface for the calibration of the Q_0 versus $E_{\rm pk}$ measurement system. The same program is used for subsequent Q_0 measurements.

are the expressions used in calculations:

$$A_{bd}\ (\mathrm{dB}) = 10\log\left(\frac{10^{-A_{bc}/10}P_{\mathrm{r,d}}}{10^{A_{ab}/10}P_{\mathrm{f,d}}}\right)^{1/2} \tag{4.21}$$

$$\beta_1 = \frac{1}{2\sqrt{\frac{\hat{P}_{\mathrm{f}}}{\hat{P}_{\mathrm{e}}^{\mathrm{inst}}}}-1} \tag{4.22}$$

$$\beta_2 = \frac{1\pm\sqrt{\frac{\hat{P}_{\mathrm{r}}}{\hat{P}_{\mathrm{f}}}}}{1\mp\sqrt{\frac{\hat{P}_{\mathrm{r}}}{\hat{P}_{\mathrm{f}}}}} \tag{4.23}$$

$$\beta = 0.5\times(\beta_1+\beta_2) \tag{4.24}$$

$$P_{\mathrm{d}} = P_{\mathrm{f}}\frac{4\beta}{(1+\beta)^2}10^{(A_{ab}+A_{bd}-A_{ae})/10} \tag{4.25}$$

$$Q_0 = (1+\beta)\omega_0\tau \tag{4.26}$$

$$U = \frac{P_{\mathrm{d}}Q_0}{\omega_0} \tag{4.27}$$

$$E_{\mathrm{pk}} = \kappa_U\sqrt{U} \tag{4.28}$$

$$K_E = \frac{E_{\mathrm{pk}}}{\sqrt{P_{\mathrm{t}}}} \tag{4.29}$$

$$K_U = \frac{U}{P_{\mathrm{t}}}. \tag{4.30}$$

The information is written to a file for backup purposes in case of a system crash.

4.6.5 Data acquisition

At this point the calibration for the entire system is complete. The user now can toggle back and forth between the Q_0 versus E_{pk} measurement screen (Figure 4.18) and the temperature mapping program (Figure 4.19). These programs are used to systematically measure the cavity quality as a function of the electric field level and to monitor the temperature of the cavity surface.

4.6.5.1 Q_0 measurements

The Q_0 versus E_{pk} measurements are nearly identical to the calibration just described. At a given field level, measurements of P_{f}, P_{t}, $\hat{P}_{\mathrm{f}}$, $\hat{P}_{\mathrm{e}}^{\mathrm{inst}}$, and $\hat{P}_{\mathrm{r}}$ are completed in the same way as during the system calibration. However, the decay time of $\hat{P}_{\mathrm{r}}$ is not needed. Similarly, $P_{\mathrm{f,d}}$ and $P_{\mathrm{r,d}}$ do not have to be remeasured.

The computer then performs the calculations for the Q_0 extraction. The β_1, β_2, β, and P_{d} values are obtained from the same expressions used during the system calibration ((4.22)–(4.25)). However, E_{pk}, U, and Q_0 are calculated using the following expressions:

$$E_{\mathrm{pk}} = K_E\sqrt{P_{\mathrm{t}}} \tag{4.31}$$

$$U = K_U P_{\mathrm{t}} \tag{4.32}$$

$$Q_0 = \frac{\omega_0 U}{P_{\mathrm{d}}}. \tag{4.33}$$

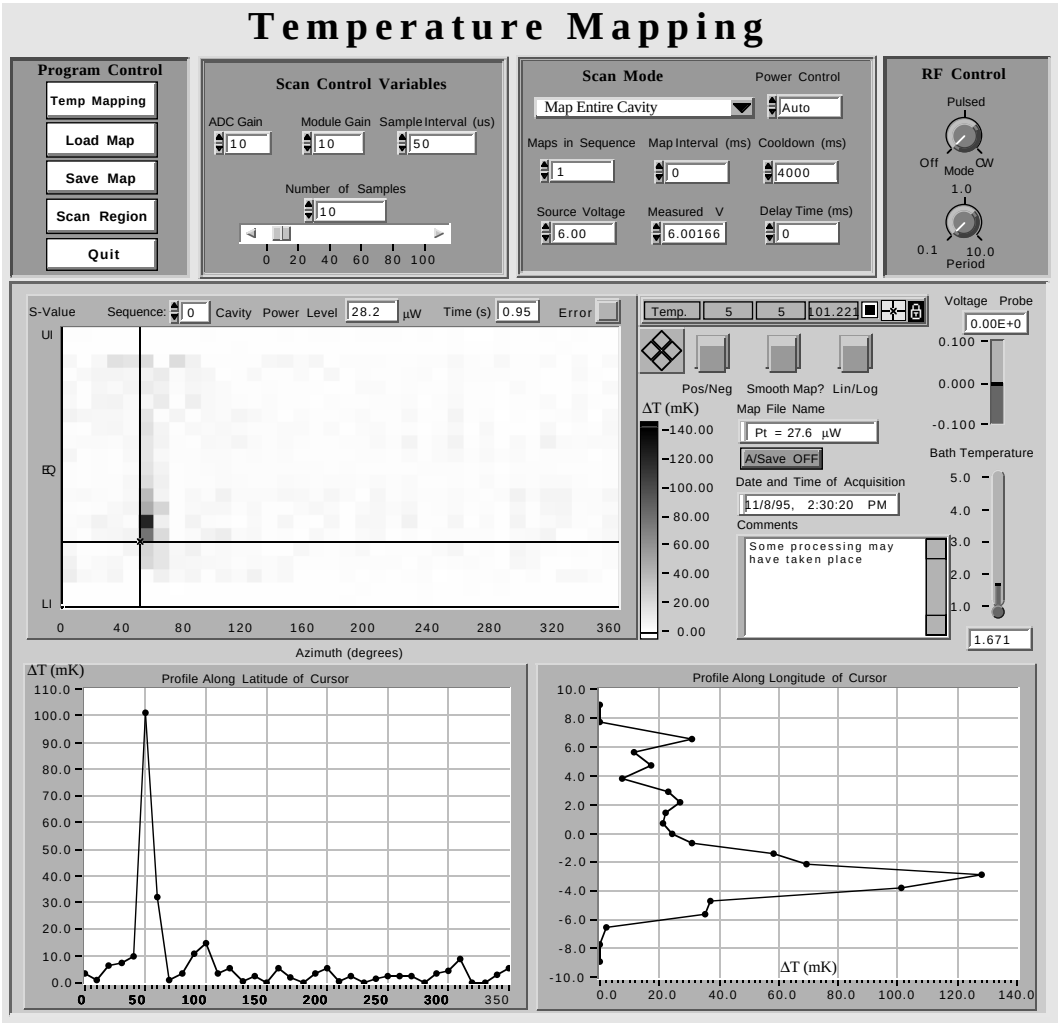

Figure 4.19: User interface of the temperature mapping program.

4.6.5.2 Temperature mapping

At any time the user can switch to the temperature mapping program to operate the thermometry system (Figure 4.19). Generally, temperature maps are obtained at $E_{\rm pk}$ intervals of 0.5 MV/m or less, especially when field emission is active and small increments in $E_{\rm pk}$ result in large changes in the emission current.

In its basic mode, the thermometry system measures the resistance of each thermometer as described in Section 4.5.3, while the cavity is operated in lock. Following the scan, the computer measures $P_{\rm t}$ to determine $E_{\rm pk}$. The computer then switches off the rf power and waits for the fields to decay before scanning the thermometers a second time. Subsequently, the calculations are performed to convert the measured resistances to temperatures (ΔT's).

The measured ΔT's are displayed in a flattened view of the cavity and can be saved on the hard drive together with the run-time parameters, the date and time, the bath temperature, and various other parameters. A single thermometer in the map can be

selected by moving a cursor to the desired thermometer. The temperature profiles along the latitude and longitude of the selected thermometer are displayed in separate graphs. The latter is particularly important when studying field emitters (see Section 4.8).

The entire process from the beginning of a temperature scan to the display of the temperature map requires only 10 – 15 s. Hence, it is simple to monitor the cavity temperature at small intervals of $E_{\rm pk}$ and to observe abrupt changes in heating. This fact illustrates one of the advantages of this system.

Many parameters used by the thermometry system are under control of the user. Among these are the scan rate, the number of scans used to calculate the average voltage drop across each thermometer, the amplifier gains, and the region of the cavity that is scanned.

A feature that proved to be very useful when studying cavity quenches, is the system's ability to acquire up to 100 temperature maps in rapid succession. At its fastest setting in this "movie" mode, a map can be acquired approximately once every 140 ms. This interval is short enough for us to be able to witness the evolution of thermal breakdown or similar phenomena. (An example of such a movie is given later in Chapter 7, Figure 7.22.)

4.6.6 RF and helium processing

Generally, the temperature distribution at low fields is fairly uniform. However, once intermediate fields of about 15 to 25 MV/m are achieved, field emission may become active. The heating due to field emitters increases exponentially with the electric field and quickly begins to dominate the temperature maps. An example is shown later in Figure 4.22. At the same time x-rays are observed by the detector in the test area.

On occasion, raising the fields even further results in the abrupt extinction of an emitter. Such events are called *rf processing* and will be discussed in Chapters 5 and 6. Usually the 250 W of rf power available from the solid state amplifier is insufficient to rf process emitters. In many cases one therefore attempts a procedure known as *helium processing*.

Helium processing involves administering small amounts of filtered helium to the cavity. This has to be done carefully to avoid stirring up dust in the vacuum lines, that may contaminate the cavity. Typical helium pressures as measured by the cold cathode gauge *at room temperature* are 0.14 mtorr. Taking into account the efficiency of the cold cathode gauge (which is calibrated for nitrogen), the actual pressure is on the order of 1 mtorr. Above this pressure, discharge occurs when the rf power is switched on, and the fields cannot be raised. At pressures much below 1 mtorr, on the other hand, helium processing has proven to be unsuccessful in extinguishing emitters. Usually we raise the pressure until gas discharge is encountered before reducing the pressure to slightly below discharge. At this point helium processing is performed, usually by applying the maximum available rf power. In some cases, when processing is successful, field emission from the dominant emitter ceases and the electric field can be raised further (the helium is evacuated again before the fields are increased). However, on occasion we also observe the activation of new field emitters by helium processing and a corresponding reduction of the Q_0. Such events are described in Chapter 5.

4.6.7 Thermal cycling

In many cases the effect of a thermal cycle on the measured losses was studied. When cycling to room temperature, the cavity and cryostat are left undisturbed for over a week, before retransferring helium.

On occasion, the cavity was cycled to intermediate temperatures. In this case a cryogenic linear temperature sensor (CLTS) was used to gauge the temperature.

4.7 Microscopy

If interesting defects are detected during tests, the possibility exists for a microscopic examination of the interior of the cavity.

The test stand is warmed to room temperature and all thermometers are removed. The outside of the cavity is thoroughly degreased. The cavity then is detached from the test stand and the bottom flange is blanked off with a teflon plate. The interior of the cavity is pressurized with dry, filtered nitrogen gas via a valve in the blank off plate. The nitrogen gas not only serves to keep the cavity interior dust free but it also preserves "starbursts" associated with field emitters (see Section 3.2.1).

While the cavity is pressurized, the beam tubes are cut off with a pipe cutter in a class 1000 clean room. Cuts are made about 2 cm from the irises (see Figure 4.20(a)). The resultant openings are capped off, and an overpressure of nitrogen is maintained in the cavity. A final cut is made along the equator using the large pipe cutter shown in Figure 4.20(b).

The two half cells so obtained fit in a specially enlarged scanning electron microscope (SEM) chamber provided they are tilted by about 30° (Figure 4.21).

The SEM permits the examination of the rf surface by secondary electron emission. The spatial resolution is on the order of 200 nm. Energy dispersive x-ray (EDX) analyses of contaminants are also possible for foreign particulates bigger than 500 nm.

We are able to examine most of the interior surface by rotating the half cell about the beam axis and moving it along the y-axis of the SEM's stage. The location of defects, as determined by thermometry, are known in terms of ϕ and S, where ϕ is the angle to the defect around the beam axis and S is the distance of the defect from the equator along the cavity contour. We wrote a program that projects the defect coordinates onto the SEM's x–y plane.

4.8 Field emission trajectory simulations

Defects that cause high ohmic losses are straight forward to locate in the SEM because their heating in the temperature maps coincides with the defect location. In contrast, field emitters are more difficult to pinpoint. What follows is a short explanation of the procedure used to determine the location of emitters using the thermometry data.

Micron sized field emission sites are not detectable by their Joule heating. Rather one observes the heat produced by the field emission electrons when they are accelerated by the cavity fields and impact the walls elsewhere. If the cavity is operated in the TM_{010} mode, the electrons follow trajectories that lie entirely in the ρ–z plane of the emission site. Electrons emitted at different phases of the rf cycle follow different trajectories.

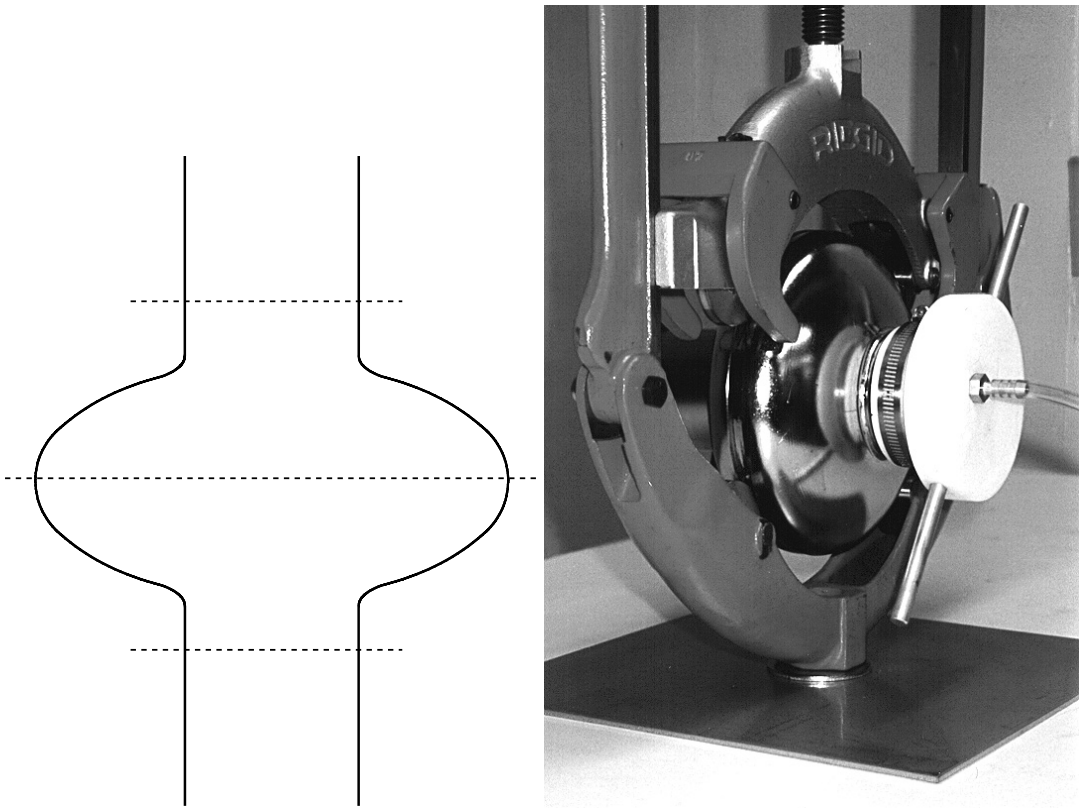

(a) (b)

Figure 4.20: (a) Schematic showing the cuts made to ready the cavity for microscopic examination. (b) Following the removal of the beam tubes, the cavity equator is cut with a large pipe cutter. At all times the inside of the cavity is pressurized with filtered nitrogen gas to minimize dust contamination and to preserve starbursts.

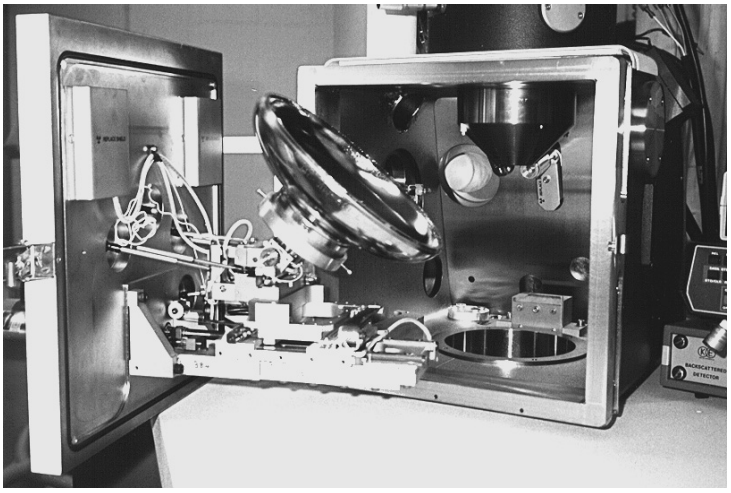

Figure 4.21: Photograph of the SEM used for cavity examination. The commercial chamber was enlarged by a stainless steel collar to accommodate a complete half cell.

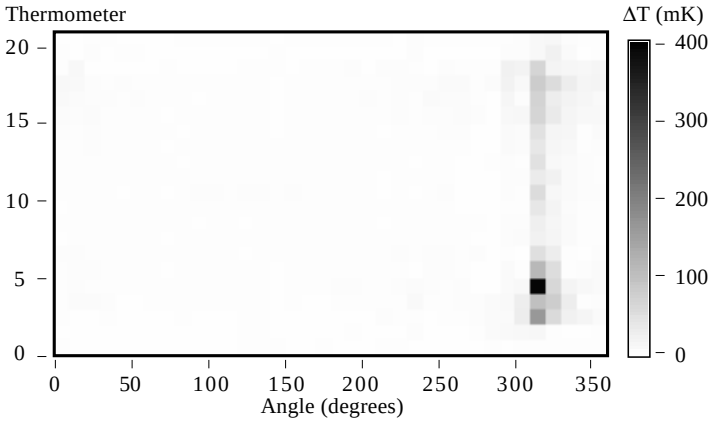

Figure 4.22: Temperature map of cavity LE1-20 at $E_{\rm pk} = 17.4$ MV/m. Field emission heating is apparent at 310°.

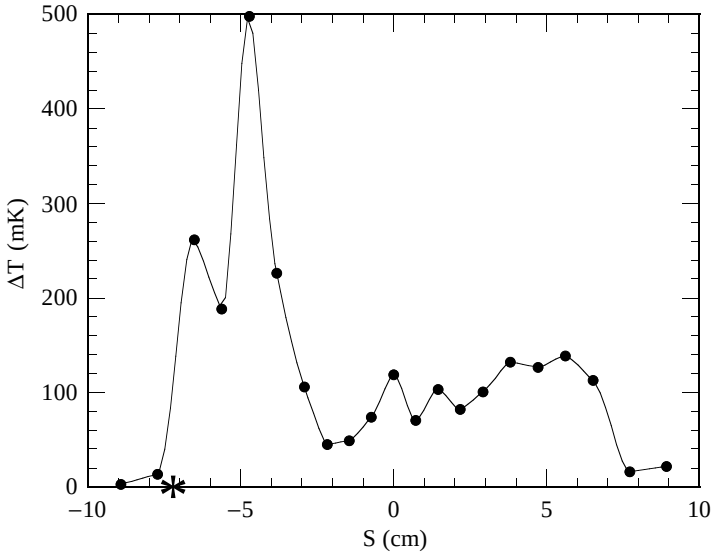

Figure 4.23: Temperature profile along 310° in Figure 4.22 at 17.4 MV/m. The asterisk marks the calculated emitter location.

Hence a "fan" of charge is produced and field emission heating is characterized by a line of heat at $\phi = \phi_0$ and/or at $\phi = \phi_0 + 180°$ where ϕ_0 is the azimuth of the emission site. This situation is depicted in Figure 4.22, the line heating at 310° being very apparent. Figure 4.23 depicts the heating at 310° as a function of distance (S) from the cavity equator. The asterisk, which marks the location of the emission site, clearly does not coincide with the peak in the heating. A plot of $\log(\Delta T)$ versus $E_{\rm pk}$ of the hottest thermometer illustrates the fairly abrupt transition from ohmic heating to field emission heating at 11.8 MV/m, and the subsequent exponential rise of ΔT with $E_{\rm pk}$ (see Figure 4.24).

To be able to determine the emitter location we have to "backtrack" from Figure 4.23. The following is an outline of the three step approach used to find the emitter.

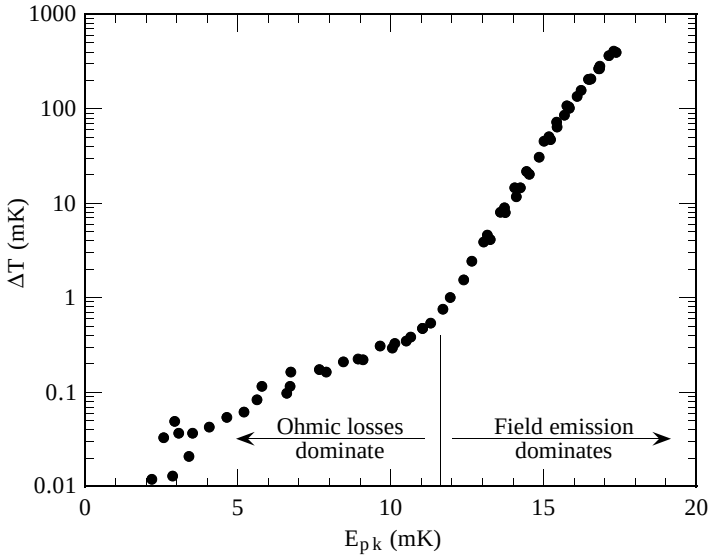

Figure 4.24: Temperature recorded by thermometer four at 310° versus $E_{\rm pk}$. Note the logarithmic scale. The exponential rise above about 11.8 MV/m confirms that the heating is field emission related.

Initially the field distribution of the cavity is obtained using the code SUPERFISH. [26] This need only be done once at one field level. The field distribution is then used for trajectory calculations in a program called MULTIP. [15, 118]

The relativistic equations of motion for a charge q with mass m are

$$\frac{d\mathbf{x}(t)}{dt} = \frac{1}{\gamma}\mathbf{u}(t) \tag{4.34}$$

$$\frac{d\mathbf{u}(t)}{dt} = \frac{q}{m}\left[\mathbf{E}(\mathbf{x},t) + \frac{\mu_0}{\gamma}\mathbf{u}(t)\times\mathbf{H}(\mathbf{x},t)\right], \tag{4.35}$$

where $\mathbf{x}(t)$ is the position of the charge at time t, $\mathbf{E}(\mathbf{x},t)$ and $\mathbf{H}(\mathbf{x},t)$ are the electric and magnetic fields, respectively, and

$$\gamma = \frac{1}{\sqrt{1-(|\mathbf{v}|/c)^2}}. \tag{4.36}$$

In (4.36) $\mathbf{v}$ is the velocity of the charge which is related to the proper velocity $\mathbf{u}$ by $\mathbf{v} = \mathbf{u}/\gamma$.

The user supplies the peak electric field in the cavity, which is used by the code to scale the field map obtained with SUPERFISH. MULTIP divides the rf period into a user-determined number of time intervals of length $\Delta\varphi/\omega_0$, where $\Delta\varphi$ is the phase advance and ω_0 is the cavity angular frequency. At the beginning of each interval, an electron is emitted from location $S = S_0$ with an energy K_0. Its trajectory is determined by integrating the equations of motion above for a preset number of rf cycles, or until the trajectory crosses one of the cavity boundaries. When the latter occurs, the impact conditions are stored for later use. If desired, secondary electrons can also be included in the calculation. Figure 4.25 depicts the trajectories of electrons originating at the site

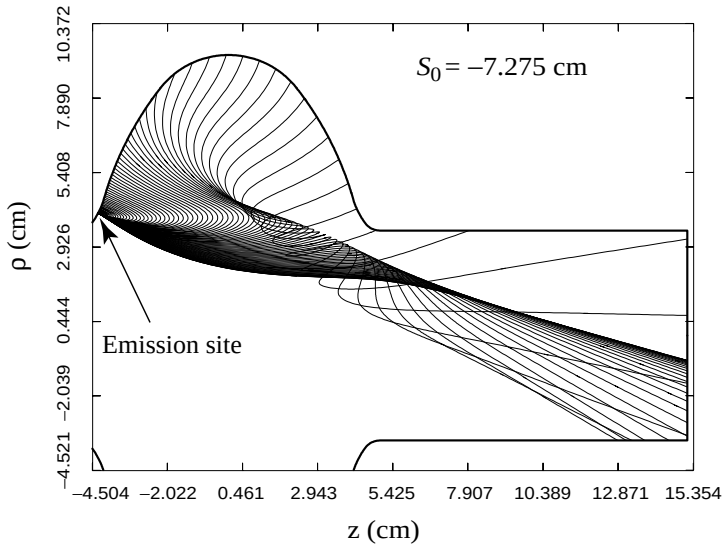

Figure 4.25: Electron trajectories in an LE1 cavity, originating at the point marked with an asterisk in Figure 4.23 at intervals of $1/200^{\text{th}}$ of the rf cycle. The trajectories lie in the ρ–z plane of the emitter. $E_{\text{pk}} = 17.38$ MV/m and the emission energy is 0 eV.

marked in Figure 4.23. A two-dimensional plot is sufficient, since the trajectories lie in the ρ–z plane of the emission site. The fan produced by charges emitted at different phases hints at the line heating measured by thermometry.

So far, none of the characteristics of the field emitter itself have been included. This is done in a third step using a program called POWER [15], which combines several functions. First, it calculates the total charge emitted in the various time intervals $\Delta\varphi/\omega_0$ for which trajectories were calculated by MULTIP. For niobium, the emitted current (in amperes) is given by the modified Fowler-Nordheim equation (3.3), which evaluates to

$$\begin{aligned} I_{\text{FN}} = 3.85 \quad &\times \quad 10^{-7}\ \text{A/V}^2\, A_{\text{FN}}\, \frac{(\beta_{\text{FN}} E_{\text{em}})^2}{t^2(y)} \\ &\times \quad \exp\left(-5.464 \times 10^{10}\ \text{V/m}\, \frac{v(y)}{\beta_{\text{FN}} E_{\text{em}}}\right), \end{aligned} \tag{4.37}$$

where E_{em} is the electric field at the emission site, and $y = 9.48{\times}10^{-6}\ (\text{m/V})^{1/2}\sqrt{\beta_{\text{FN}} E_{\text{em}}}$. (More details are given in Section 3.2.1.) Knowing the charge emitted in each interval, the program can compute the current density of the impacting electrons along the cavity wall.

The trajectory calculations also yield the energy of the impacting electrons. POWER can therefore determine the time-averaged power density deposited in the wall as a function of position. At each point, the power density is proportional to the product of the current density and the impact energy.

In turn, the power dissipation is used to calculate the energy flux at the helium side of the cavity wall. To do this, the user supplies the full width at half maximum (FWHM) of the temperature distribution on the outside of the wall due to a point heat source on the inside. This number is obtained with the thermal code HEAT that takes into account the wall thickness, its thermal conductivity, and the Kapitza conductance of the

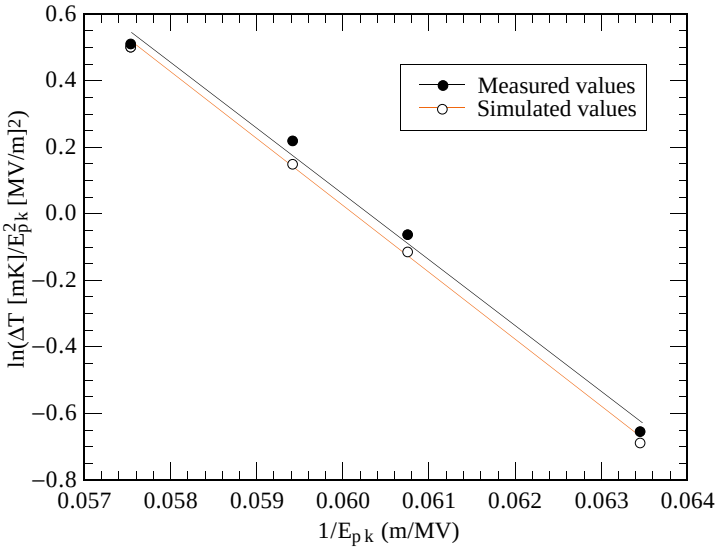

Figure 4.26: Fowler-Nordheim plot comparison of measured data and simulated data. In the simulation, the emitter is located at the asterisk in Figure 4.23 ($S_0 = -7.275$ cm, $\beta_{\mathrm{FN}} = 400$, $A_{\mathrm{FN}} = 1.58 \times 10^{-12}$ cm^2).

wall–helium interface. [119] POWER then spreads the energy dissipated by the impacting electrons using a Gaussian distribution. By overlapping the distributions from each impact point, the approximate power flux at the exterior cavity surface is obtained.

Assuming we know the temperature measured by a thermometer for a given power flux (K_T) across the cavity–Helium boundary, the flux profile can easily be converted to a temperature profile. Typically, K_T is on the order of 1 – 2 K/(W/cm^2). However, K_T varies from one thermometer to another and from cavity to cavity, due to differing surface characteristics, variations in thermometer contact pressure and intrinsic differences between thermometers.

For a given field level, the temperature profile is primarily dependent on S_0, A_{FN} and β_{FN}. These parameters must be varied until a reasonable match between the simulated and measured temperature profiles is obtained.

It is helpful to consider the temperature profiles at several different field levels, especially when determining β_{FN} and A_{FN}. In many cases $v(y)$ and $t(y)$ are approximately constant over the range of interest. Thus a plot of $\ln(\Delta T/E_{\mathrm{pk}}^2)$ versus $1/E_{\mathrm{pk}}$ for a thermometer yields a near-linear dependence, the gradient of which can be used to estimate β_{FN}.[4] Analogous plots can be made with the simulation results. A comparison of the two, as in Figure 4.26, allows one to home in on a reasonable value for β_{FN}.

Once β_{FN} is known, the magnitude of the heating is used to determine the effective emission area A_{FN}. One therefore obtains a series of simulated profiles, as in Figure 4.27 that match the measured data.

For cross reference, it is useful to compare the total power dissipation in the cavity obtained from Q_0 versus E_{pk} measurements with the computed value from these simula-

[4]More precisely, one should plot $\ln(\Delta T/E_{\mathrm{pk}}^{3.5})$ versus $1/E_{\mathrm{pk}}$, because ΔT is a measure of the *time average* of $I_{\mathrm{FN}}E_{\mathrm{pk}}$. However, the exponential term in (3.3) dominates, so that little is lost by plotting $\ln(\Delta T/E_{\mathrm{pk}}^2)$ versus $1/E_{\mathrm{pk}}$. See Reference [73] for more details.

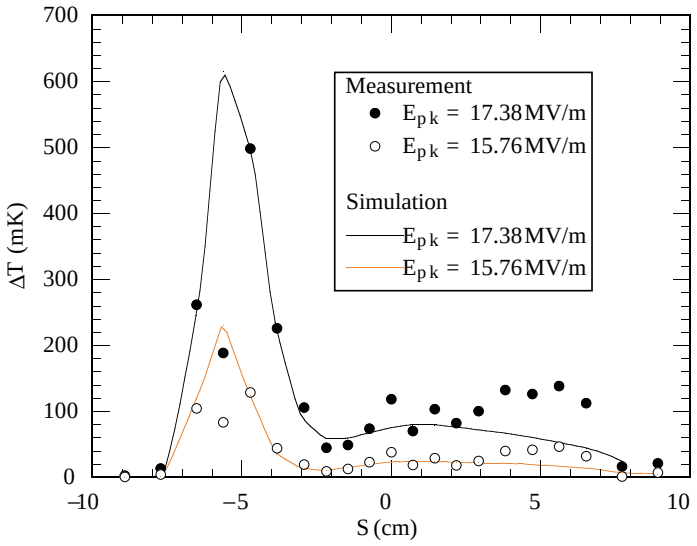

Figure 4.27: Comparison of the simulated and measured temperature profiles. ($S_0 = -7.275$ cm, $\beta_{\mathrm{FN}} = 400$, $A_{\mathrm{FN}} = 1.58 \times 10^{-12}$ cm^2). The low values measured by the fourth thermometer from the left are probably due to an abnormally low thermometer sensitivity.

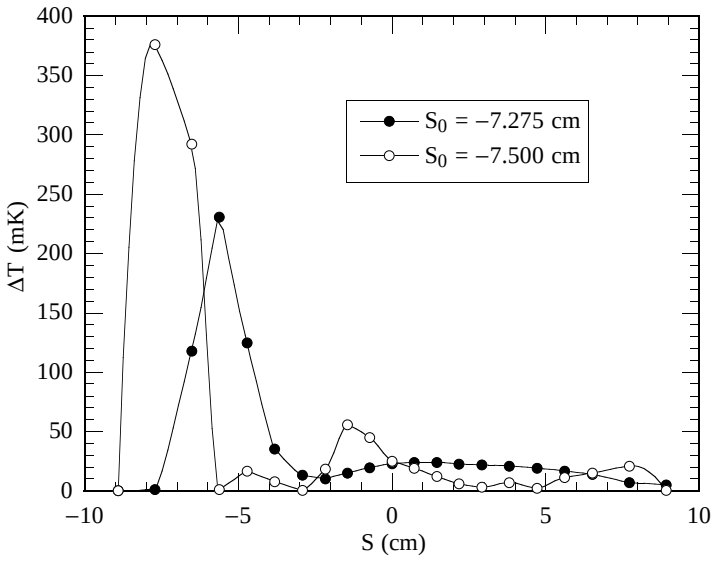

Figure 4.28: Comparison of simulated temperature profiles at $E_{\mathrm{pk}} = 15.76$ MV/m for slightly displaced emitters. ($\beta_{\mathrm{FN}} = 400$, $A_{\mathrm{FN}} = 1.58 \times 10^{-12}$ cm^2).

tions. Provided a single emitter is the dominant source of power dissipation in the cavity, the two should agree fairly well. The total emitted current can therefore be determined within a factor of three or so. The current density, on the other hand, depends strongly on β_{FN} and cannot be calculated precisely. Typically, the uncertainty in β_{FN} can be as high as ± 40 for $\beta_{\mathrm{FN}} = 250$, which, at normal field levels, results in uncertainties of a factor of ten or more in j_{FN}.

The response of different thermometers to the same power flux can vary, in the worst case, by up to a factor of two.[5] The low reading of the fourth thermometer from the left in Figure 4.23 is probably due to such a variation. One might be concerned that this variation, combined with a thermometer spacing on the order of 0.75 cm, will make it exceedingly difficult to determine the location of an emitter. Fortunately, one finds that for emitters in high electric field regions (where the dominant ones usually are located), the temperature profiles vary significantly for small changes in S_0. For example, a shift of the emitter in Figure 4.27 by 2.25 mm to the left results in a drastically different profile. This is shown in Figure 4.28.

Generally, one therefore is able to determine the emitter location to within a few millimeters in latitude and a few degrees in longitude. For example, the predicted and actual location of the emission site discussed in this section were 2.9 mm (in S) and 2° (in ϕ) apart.

4.9 Other analysis tools

We wrote a program in LabVIEW to aid with the analysis of the hundreds of temperature maps generated by each test. It gathers all the temperature data in a single file and permits the user to examine this file in different ways. A selection of the analysis options is listed in Appendix A.

[5] Such extreme variation, though, is rare.

Chapter 5

Field emission

5.1 Introduction

This chapter is devoted to our results that shed light on the chief high field loss mechanism — field emission. It is the main limiting factor in state of the art superconducting cavities, frequently preventing the attainment of fields in excess of $E_{\rm pk} = 40$ MV/m. Thus, to be able to achieve, for example, the prerequisite $E_{\rm pk} = 50$ MV/m in the thousands of cavities required for TESLA, it is imperative that we understand field emission and learn to eliminate it. Field emission is also important in normal conducting cavities and other areas such as high voltage vacuum.

Altogether, more than 30 emitters were studied in detail. We start by giving an example of field emission that is well described by the modified Fowler-Nordheim equation (Equation 3.3). However, many field emitters display anomalous behavior that is not described by the Fowler-Nordheim equation. Such behavior includes activation, noisy emission characteristics, and extinction. We will discuss all three cases in an attempt to catalog the various types of emitter behavior. In doing so, information as to the mechanisms responsible for enhanced ($\beta_{\rm FN} \gg 1$) field emission can be obtained.

In particular, both the activation and extinction of emitters are of great practical importance, because the former degrades the cavity performance whereas the latter improves the cavity. Thus, it is crucial that we gain a better understanding of the mechanisms involved, so that we may learn how to prevent activation, and how to facilitate extinction.

We will show that in some cases particle motion can result in the activation of field emitters.[1] In these cases it appears that the MIM or tip-on-tip model describes emission well. However, we will also demonstrate that more subtle mechanisms involving the adsorption (desorption) of gases play an important role in the activation (deactivation) of emitters.

In the end, we will present several field emitters that melted the rf surface and in some cases exploded ("rf processed"). Such a violent event spells the end of a field emitter's "life" and proves to be very beneficial for enhancing a cavity's performance. Therefore, it is important that the process leading from steady state field emission to emitter explosion be thoroughly investigated. Similar rf processed emitters have been studied in the past [17] and it was believed that excessive Joule heating by the emis-

[1] A more detailed discussion of particle motion in cavities is given later in Chapter 8.

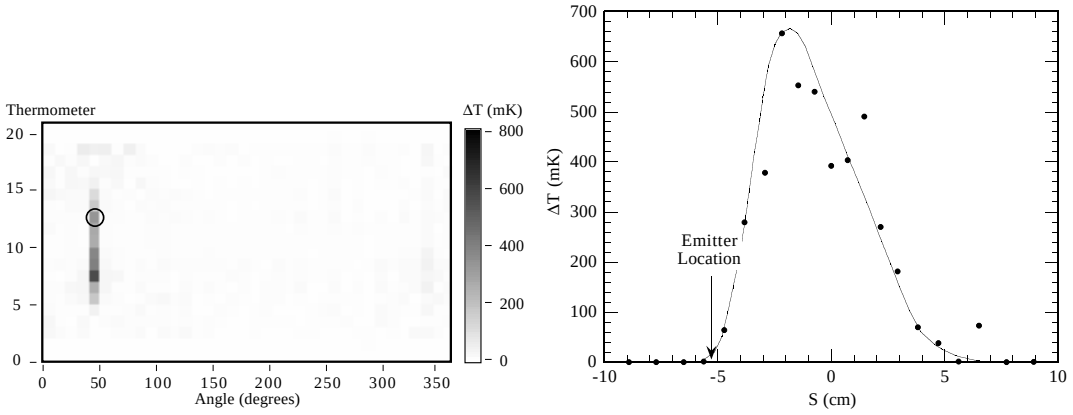

(a) (b)

Figure 5.1: (a) Temperature map of cavity LE1-17 at 22 MV/m showing line heating due to an emitter at 40°. The heating of the circled site as a function of $E_{\rm pk}$ is shown in Figure 5.2. (b) Temperature profile along 40°.

sion current was responsible for the explosion. However, we will use newly gathered microscopic evidence to identify several stages in an emitter's "life" leading up to the explosion. A new model of processing is developed that attributes a key role to gases evolving from the emitter *prior* to the explosion. These gases are ionized by the emission current and form a plasma. The plasma, in turn, is responsible for a drastic increase of the power dissipated at the emission site and finally the explosion of the emitter. In the following chapter we then describe numerical simulations designed to test this model.

5.2 Well behaved field emission

The study of field emitters is greatly complicated by the fact that many exhibit very diverse characteristics. It is hopeless to establish a complete "catalog" of emitter classes that pretends to describe all forms of field emission behavior encountered in cavities. Similarly, a single model is probably insufficient to explain all observed emission characteristics. In many cases the problems are exacerbated by the fact that the statistics we have been able to gather is limited, making it difficult to determine whether some observed emission behavior is unique to only one emitter or shared by others as well.

To be able to appreciate the different behaviors encountered, we briefly present a classic, well behaved emitter whose characteristics are described by the Fowler-Nordheim equation.

Figure 5.1(a) depicts a temperature map obtained with cavity LE1-17, showing the classic line heating due to a field emitter at 40°. The corresponding temperature profile along 40° is shown in Figure 5.1(b). No significant heating is observed at the emission site. Field emission from this site gradually started up at around $E_{\rm pk} = 15$ MV/m and was well behaved from the outset. No sudden changes in emission characteristics were observed and the ΔT versus $E_{\rm pk}$ curve in Figure 5.2(a) could be traced out reversibly. A Fowler-Nordheim plot of the temperature data also serves to illustrate the field emission nature of the heating (Figure 5.2(b)).

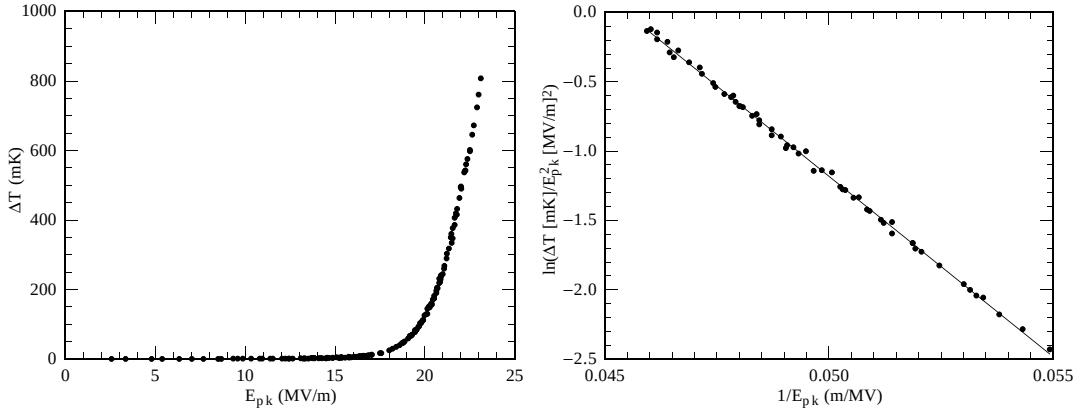

(a) (b)

Figure 5.2: (a) Temperature signal of the circled site in Figure 5.1 as a function of $E_{\rm pk}$. No abrupt changes were observed. (b) Fowler-Nordheim plot of the same temperature data (above $E_{\rm pk} = 18$ MV/m).

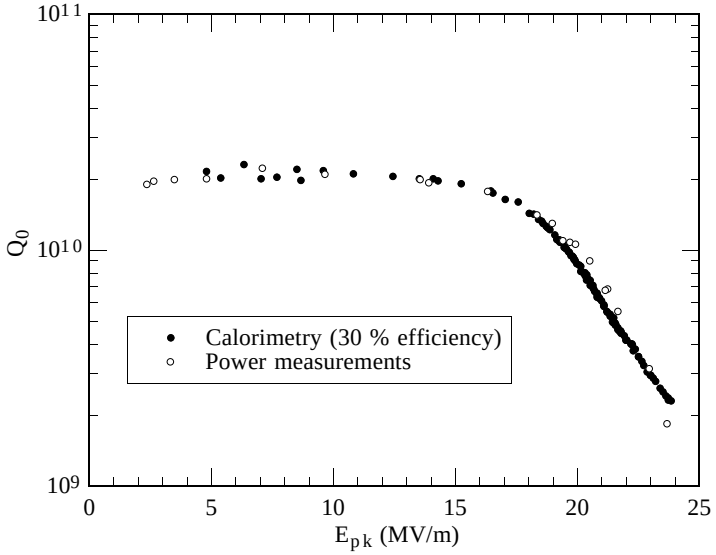

Figure 5.3: Cavity quality of LE1-17 as a function of $E_{\rm pk}$. Shown are Q_0 results from both power measurements and calorimetry. The thermometer efficiency was 30 %.

Corresponding to the exponential increase in power losses, the Q_0 of the cavity rapidly declines above 15 MV/m (see Figure 5.3). This fact is also corroborated by Q_0 data extracted from the calorimetry measurements. X-rays were registered above 14 MV/m, confirming field emission activity. The emitter persisted up to the highest field achieved in the cavity without any changes. Only helium processing, which we will discuss later, was effective in eliminating this emitter.[2]

In Figure 5.4 we present an emission site that was located using thermometry. These

[2]No microscopy data on the original emitter is available because helium processing destroyed it.

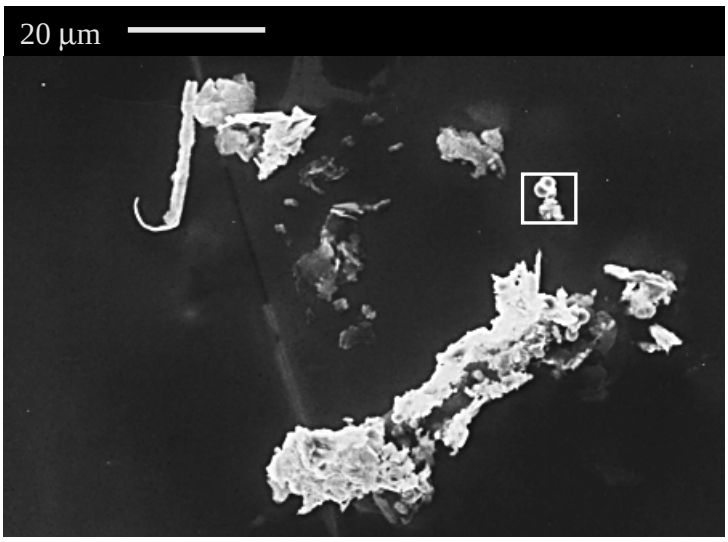

Figure 5.4: Emission site found in cavity LE1-Heraeus. The debris consists of iron, chromium and nickel (presumably stainless steel). The framed region is shown enlarged later in Figure 5.25.

particles were found within 2 mm of the predicted location in cavity LE1-Heraeus.[3] This site might be considered to be typical of most emitters. It is conducting and has many jagged features that can result in substantial field enhancement. In fact, for many years it was believed that all emission sites are of this type. Hence the term "field enhancement factor" is used for β_{FN}.

Although we present these two emitters as being "generic" or "classic", in reality almost all emitters we studied were not as well behaved. In many cases, emission characteristics vary abruptly when, for example, E_{pk} is increased or helium gas is in the cavity. These changes are almost always irreversible. Such behavior can be due to several different mechanisms which we will discuss. Similarly, dc field emission studies carried out at Wuppertal [46] also found that about 40 % of all emitters did not show stable emission. We will also show, that in several cases studied the microscopic appearance of emitters is not like the site shown in Figure 5.4, ruling out geometric field enhancement as the single cause of field emission.

Rather than present all emitters studied, we attempt to categorize emitters according to their behavior and will show examples from each category. However, one should bear in mind that no two emitters behave exactly the same, so that in some cases it is difficult to assign an emitter to a particular category.

5.3 Activation of field emission

5.3.1 Particle arrival

In many cavities an abrupt "activation" of field emitters is observed when the electric field is raised for the first time. This situation is exemplified by the maps in Figure 5.5.

[3] Our confidence that the particles were involved in emission was established by the presence of melted regions discussed in Section 5.5.2.

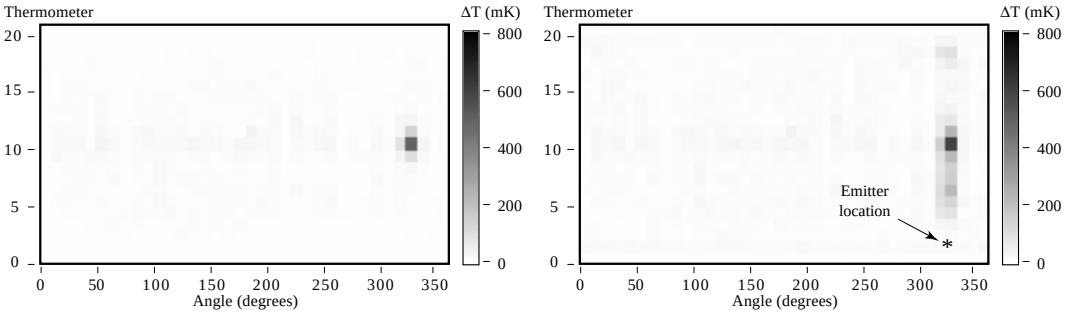

(a) (b)

Figure 5.5: Temperature map of cavity LE1-23 at 33.5 MV/m (a) prior to any significant field emission activity, (b) at the same field after emission heating activated along 320°. The hotspot at the equator is not field emission related.

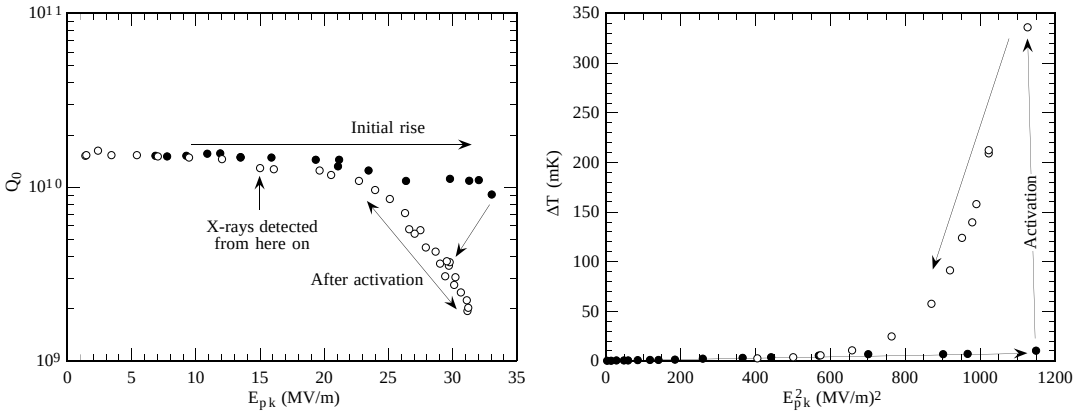

(a) (b)

Figure 5.6: (a) Q_0 versus $E_{\rm pk}$ results obtained with cavity LE1-23 before and after the activation of field emission shown in Figure 5.5. (b) Plot of ΔT versus $E^2_{\rm pk}$ recorded by resistor 6 at 320°, showing the activation process and persistant field emission following activation.

When the fields in this cavity were raised for the first time, little x-rays were detected and no field emission was apparent in the temperature maps (see Figure 5.5(a)). However, when the field was raised to 33.5 MV/m, heavy x-rays suddenly appeared and strong field emission heating was observed along 320° (see Figure 5.5(b)). The calorimetry data is confirmed by power measurements of the Q_0, shown in Figure 5.6(a). The large reduction of the high field Q_0 after the activation of field emission is very apparent.

The plot of the temperature signal recorded by resistor 6 at 320° in Figure 5.6(b), demonstrates the abrupt activation of field emission and the fact that the process was irreversible. Even when the electric field was lowered, the field emission free state was *not* recovered.

Electron trajectory calculations predict that the emission site was located at $S_0 = -7.2$ cm, this place being marked by the asterisk in Figure 5.5(b). An analysis of the low field temperature signal recorded by the nearest thermometer revealed that the

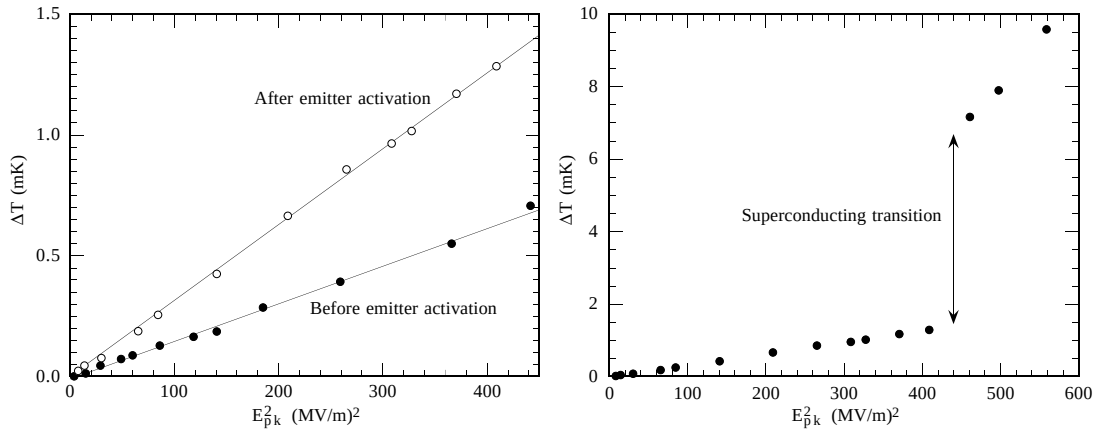

Figure 5.7: (a) Low field temperature signals recorded by thermometer 2 at 320° with cavity LE1-23. This resistor was closest to the predicted field emission site shown in Figure 5.5. A linear dependence of ΔT on $E^2_{\rm pk}$ demonstrates that the losses are ohmic in nature. (b) Reversible change in ohmic losses recorded by the same thermometer later in the test. The transition persisted even after cycling the cavity to room temperature.

ohmic losses (linear in $E^2_{\rm pk}$) more than doubled at this site (see Figure 5.7(a)). The temperature increased from 0.6 mK to 1.25 mK at 20 MV/m. No changes in ohmic losses were observed away from the emission site. Note that it is only thanks to the high sensitivity of our thermometry system that we were able to detect this small but crucial change in losses.

Subsequently, when we raised the fields a second time to 32 MV/m, the heating at the emission site jumped abruptly once more, while the field emission related heating along the azimuth remained unaffected. Only the ohmic losses at the emission site itself changed. Interestingly, the losses reduced to the original levels when the field was lowered to 21 MV/m. This transition, as shown in Figure 5.7(b), was *reversible* and always occurred at 21 MV/m, even after we thermally cycled the cavity to room temperature. The emission characteristics were also unaffected by the temperature cycle.

Based on the results presented in Figure 5.7, and the fact that the additional losses were unaffected by temperature cycling, we concluded that we had witnessed the arrival of a particle. This particle then initiated field emission. Such events are interesting in their own right and are discussed in more detail in Chapter 8. There we present several other examples of particle arrival observed during cavity operation. Not all particles were field emitting.

The transition recorded in Figure 5.7(b) suggests that the particle is weakly superconducting. Changes in its thermal contact, composition or morphology brought about by field emission related or magnetic heating then lowered the field at which the particle goes normal conducting, resulting in the reversible transition we observed.

In Section 8.4, dedicated to our observation of particle motion, we develop an expression that permits us to estimate the particle radius ($r_{\rm d}$) based on the thermometry

data. We find that

$$r_{\rm d} \approx \sqrt{\frac{c_{\rm d}\Delta T}{\pi \epsilon_T \eta_T R_{\rm d}}}\frac{1}{H} \tag{5.1}$$

(see Equation 8.8). Here H is the local magnetic field, η_T is the thermometer efficiency, $c_{\rm d}$ is a correction factor to compensate for the distance between the thermometer and the particle, $R_{\rm d}$ is the particle's surface resistance and ϵ_T is a cavity dependent parameter.[4]

The temperature rose by 5.9 mK at 21 MV/m due to the transition from the superconducting to the normal conducting state. In addition, we had previously recorded an increase of 0.7 mK at 21 MV/m because of the arrival of the particle, when it was still superconducting. In total, therefore, the normal conducting particle was responsible for an increased heating of 6.6 mK. This value enables us to estimate the particle size.

Comparison of the Q_0 from power measurements with that obtained from calorimetry show that the mean thermometer efficiency was $\eta_T = 40$ %. At $E_{\rm pk} = 21$ MV/m, the magnetic field at the emitter was $H = 286$ Oe ($= 2.3 \times 10^4$ A/m). Later microscopy results will show that the particle was well anchored to the rf surface, and we anticipate, that even in the normal conducting state, its temperature was not much above $T_{\rm b}$. Given that $R_{\rm d} = 10$ mΩ, (5.1) yields a particle radius of[5]

$$r_{\rm d} = 32\ \mu{\rm m}.$$

Note that we used $\epsilon_T = 4.1$ K/W and a factor $c_{\rm d} = 4.3$ to compensate for the distance between the thermometer and the actual particle site.

Upon examining the cavity in the electron microscope, we found the particle in Figure 5.8 within 0.5 mm of the predicted location in S and 2.7° in ϕ. The main contaminants found were titanium, carbon, oxygen and chlorine. The particle had clearly melted and some cratering is visible. The size of the particle is close to our theoretical predictions. Furthermore, titanium is known to be a superconductor, although its critical temperature is lower than our cavity operating temperature. However, it is possible that the critical temperature is elevated by the other contaminants found in the particle (including, perhaps niobium).

5.3.2 Gases

In over 20 cases of activation studied only four show evidence that activation was due to the arrival of a particle. In many of the remaining cases the activation could be correlated with other events in the cavity, which strongly suggest that gases play an important role in the enhancement of field emission.

5.3.2.1 Activation during thermal breakdown

Consider, for example, the temperature maps depicted in Figure 5.9. These maps describe the evolution of a field emitter responsible for heating the cavity irises at both 120° and 300°. Initially no field emission was detected at these sites, although emission was active elsewhere in the cavity (map (a)). The dark band along the cavity equator is

[4] ϵ_T is the temperature rise at the exterior of the cavity wall per unit power dissipated in a point defect on the inside. It is obtained from thermal codes and is tabulated in Table 8.1.

[5] Many metals have $R_{\rm s} \approx 10$ mΩ at low temperatures.

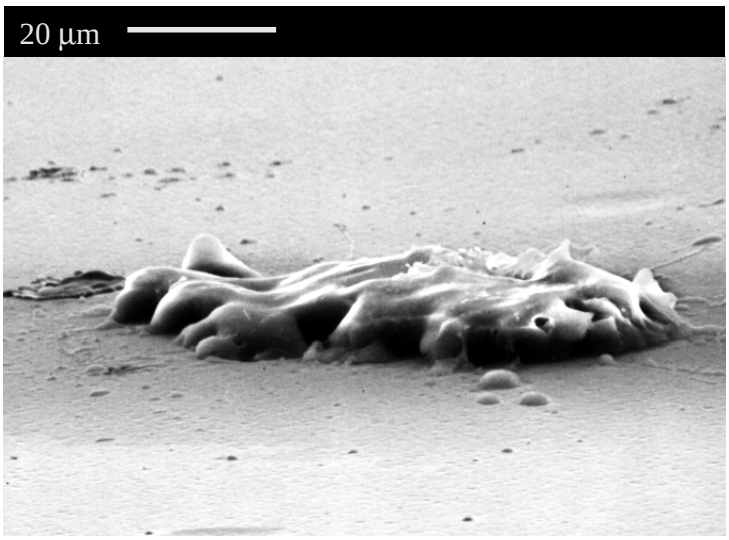

Figure 5.8: Particle found at the site responsible for the emission heating in Figure 5.5(b). The main elements identified by EDX analysis (apart from niobium) were titanium, carbon, oxygen, and chlorine. The picture was taken at a grazing angle to show the relief of the particle.

not emission related and is discussed in Section 8.2. At 38 MV/m the cavity was limited by defect related thermal breakdown centered on 180° (map (b)). Following repeated breakdown events, emission heating at 120° and 300° activated irreversibly (map (c)). Trajectory calculations show that the heated areas on opposing sides of the cavity are produced by the same emitter. This assumption is confirmed by the observation that the sites show correlated changes in emission characteristics.

Later in the test, helium liquid was retransferred to the cryostat. During the transfer the bath level dropped below the cavity equator. In the process gases were released from the vacuum parts that warmed to above 4.2 K. A corresponding pressure rise was observed at the cold cathode gauge. When the cavity was fully immersed in liquid helium again, E_{pk} was raised once more. Surprisingly, the field emission heating had increased further. Subsequent attempts at helium processing the emitter reduced the heating somewhat, but not to levels prior to the liquid helium retransfer.

A thermal cycle of the cavity to room temperature deactivated the newly created sites again, leaving only the original emitters (map (d)). However, we were able to reactivate the heating at 120° and 300° during another session of thermal breakdown and attempted helium processing (map (e)). The emission heating was substantially greater than that following the initial activation before the thermal cycle.

To further demonstrate the nature of the field emission heating, the temperature signals recorded by the thermometer at the circled site in Figure 5.9(a) are depicted in Figure 5.10. Although the trend of the heating at this site is clearly exponential in nature, it is very noisy.

A microscopic search for the field emitter failed to turn up any unique sites that could unequivocally be identified as being responsible for the field emission (we usually look for signs of plasma activity (starbursts), melting, or craters). Hence, the helium processing that led to a reduction of field emission on the first day could not have been

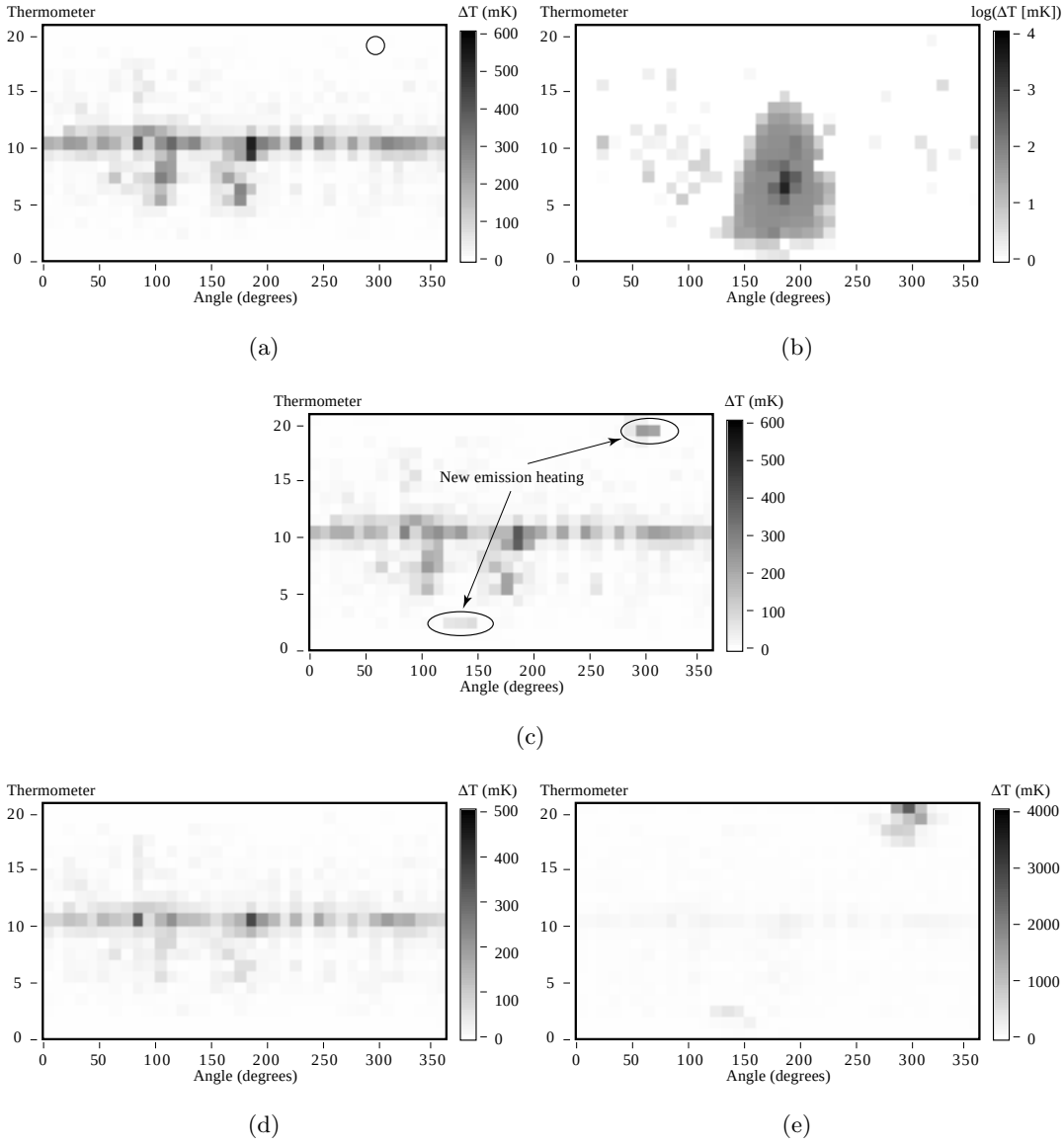

Figure 5.9: Evolution of field emission heating at 120° and 300° during a test of cavity LE1-34. (a) Temperature map at 36 MV/m, prior to emission activation. (b) Defect related thermal breakdown at 38 MV/m. (c) Field emission heating is activated at 120° and 300° (E_{pk} = 37.5 MV/m). (d) Deactivation of field emission by thermal cycling (E_{pk} = 33 MV/m). (e) Reactivation of field emission by thermal breakdown and helium admission (E_{pk} = 33 MV/m).

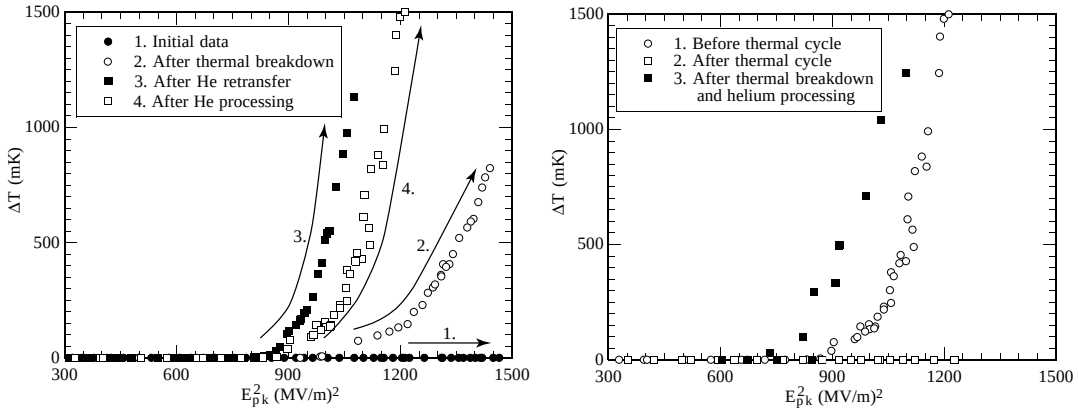

Figure 5.10: Temperature recorded by the thermometer at the circled site in Figure 5.9(a) as a function of $E^2_{\rm pk}$. (a) Initial activation and subsequent behavior during the first test. (b) Behavior following a thermal cycle of the cavity to room temperature.

of a destructive nature like the rf processing events described in the introduction to field emission (Section 3.2.1).

Our results suggest that gases play an important role in the activation of emitters such as the one just described. During thermal breakdown, the temperature of 10's of $\rm cm^2$ of the cavity is raised to above 20 K, aiding the desorption of gases, in particular hydrogen. These are rapidly adsorbed in the cold parts of the cavity and can condense on particles, making them field emit. Gases evolving from a heated particle, whose temperature can be much higher than 20 K may contribute as well.[6] It would appear that even small amounts of gas are sufficient to activate field emission. As discussed in Section 3.2.1, one possible emission enhancement mechanism is by means of resonant tunneling via localized energy levels created by the adsorbates.

Subsequent thermal cycling serves to redistribute the gases in the cavity or change the chemical properties of the adsorbates, thereby deactivating the emitter again. Reactivation of the emission at the same site by new gases is then possible, as was demonstrated by the reactivation after a combination of renewed thermal breakdown and attempted helium processing (both were in progress at the same time).

Helium processing on the first day of testing reduced field emission heating by a little. This result is consistent with the theory that helium processing can alter the composition of the emitter surface and/or remove surface adsorbates to reduce the emission. We will show later, that a gas discharge in a helium atmosphere can indeed desorb gases. In Chapter 7 we will also demonstrate that discharges during thermal breakdown and multipacting may also desorb gases.

Our assumption that adsorbates influence the emission process is supported by the fact that the emission current was noisy. Energy deposited by the current in the emitter is bound to affect the surface composition and hence the emitter characteristics. (We will show in Section 5.5.2 that Joule losses by the emission current can occasionally

[6] In Section 7.2.2 we will show that particles can become very hot due to the power dissipated by the magnetic field.

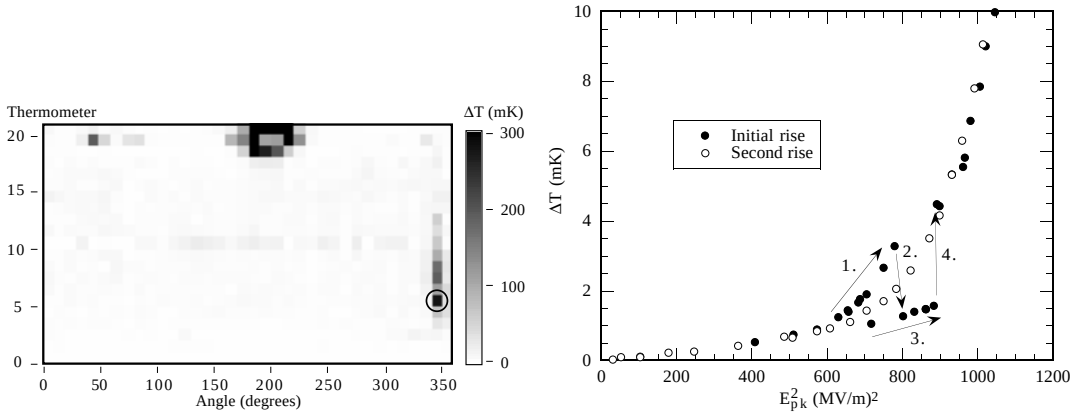

(a) (b)

Figure 5.11: (a) Temperature map of cavity LE1-21 at $E_{\rm pk} = 38$ MV/m showing field emission heating along 340°. The emitter had previosuly deactivated at 28 MV/m and then re-activated at 30 MV/m. (b) Sequence of temperature data recorded by the circled thermometer in (a).

be sufficiently intense to cause local heating.) As demonstrated by room temperature cycling, temperatures far below the emitter's melting point are sufficient to bring about a reduction in field emission. Therefore it is plausible to suggest that local temperature changes from Joule heating due to the field emission current will cause fluctuations in the current.

In support of our results we reference past studies [19] which demonstrated that the same emitters can repeatedly be activated by oxygen admitted to the cavity and deactivated again by thermal cycling. The stability of dc field emitters has also been shown to be greatly influenced by adsorbed gases. [20]

5.3.2.2 Activation during multipacting

Apart from three activation cases recorded as a result of thermal breakdown, we were also able to correlate three cases of emitter activation with the onset of two-point multipacting. Again, these observations point to the important role played by gases in enhancing field emission.

We defer the discussion of our evidence that two point multipacting occurs in the LE1 cavity shape to Chapter 7 (Section 7.3). For now it suffices to say that a multipacting threshold was discovered at about $E_{\rm pk} = 29 - 30$ MV/m and that sporadic multipacting continues up to at least 38 MV/m in Mark I cavities. The multipacting we observed was characterized by a sudden quench of the cavity and a subsequent increase of the residual losses along the cavity equator. We also have evidence that gases are desorbed at the equator during these events. We believe such gases can then activate emitters.

An example of multipacting activated emission is depicted in Figure 5.11. Unlike the previous two emitters we discussed, this site began field emitting gradually, as is expected from the Fowler-Nordheim law. However, the emitter was noisy, even at fields as low as 20 MV/m. On a couple occasions the heating reduced abruptly (not shown in Figure 5.11(b)). At 28 MV/m virtually all field emission related heating ceased (transi-

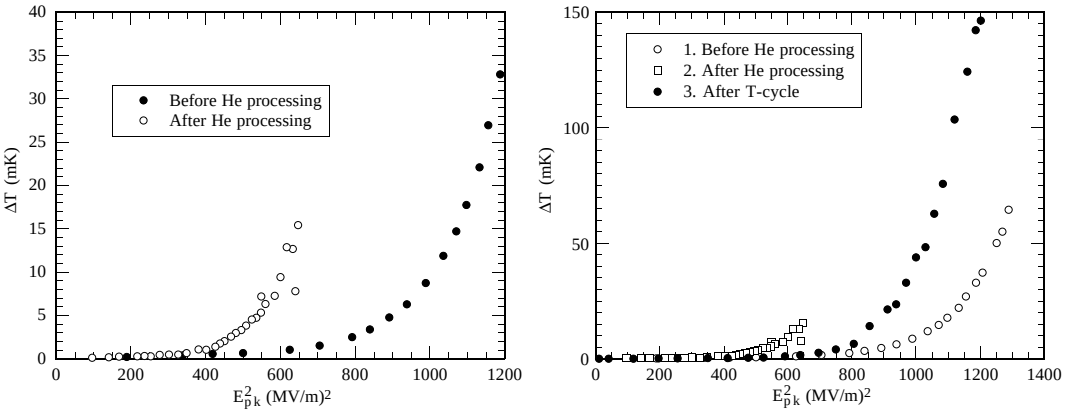

(a) (b)

Figure 5.12: Temperature signals recorded by the circled thermometer in Figure 5.11 (a) before and after attempted helium processing and (b) after a thermal cycle to room temperature.

tion 2 in Figure 5.11(b)). A slight reduction in x-ray activity was also recorded. Shortly thereafter, a multipacting related breakdown event was observed at 29.4 MV/m, leading to augmented equator losses. Raising the fields further to 29.9 MV/m brought about increased x-ray activity and the reactivation of the emission heating along 340° (transition 4 in Figure 5.11). At slightly higher fields still, more multipacting was recorded.

The previous field emission activity rules out particle arrival as the cause for the emitter activation. Instead we again suspect gases, that are desorbed by multipacting electrons[7], to be responsible for the activation process.

The emitter's propensity to be affected by gases is further demonstrated by the enhancement of field emission activity following helium admission in the cavity and attempted helium processing (see Figure 5.12(a)), and the subsequent reduction of emission activity to intermediate levels following a room temperature thermal cycle of the cavity. Once again the emission heating is a little noisy.

A microscopic examination of this emitter revealed the presence of several particles, in part molten, all surrounded by a starburst. Some of the particles are shown in Figure 5.13. We suspect that melting and the starburst were due to an rf processing event recorded at a later time in the test sequence (not shown here). We will discuss such events in more detail in Section 5.5.3. Carbon and oxygen were detected with EDX at the sites that had not melted completely. These particles did not charge up in the SEM, illustrating that they were conducting.

Because of the conducting nature of the particles, we suspect that in this case perhaps a combination of the MIM model and adsorbed gases supplied during multipacting and helium processing is required to explain the enhancement of the field emission current (see Section 3.2.1).

[7]In Chapter 7 we will present evidence that gas desorption during multipacting is likely.

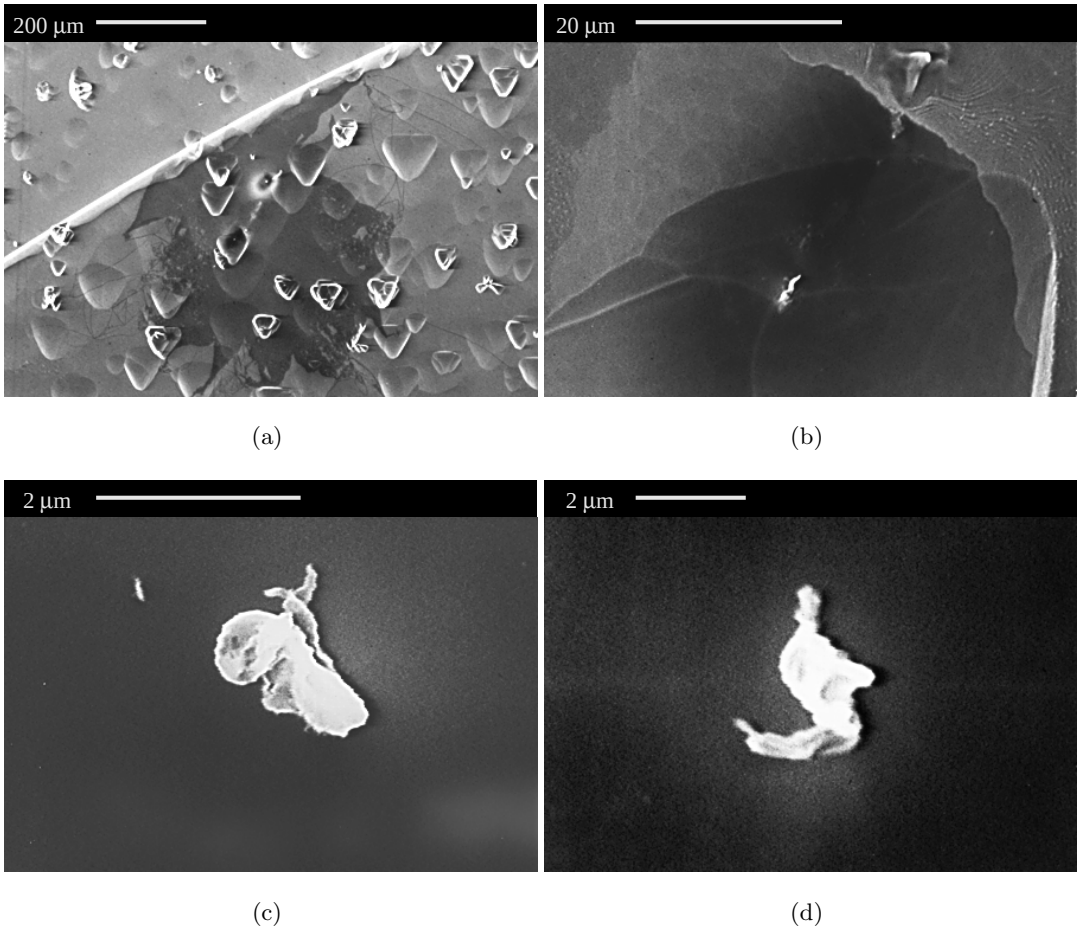

Figure 5.13: Starburst and some of the debris found at the emission site responsible for the heating along 340° in Figure 5.11. Carbon and oxygen were detected at those sites that did not melt completely. The numerous pits in (a) are due to the etching process. Previous work has shown that they have little influence on the emission process. [17]

5.3.2.3 Activation during helium processing

In some of the previous examples of gas activated emitters, we saw that helium processing[8] can increase the emission activity of sites that were already field emitting. Helium processing can also "awaken" dormant emitters. We observed at least five such events.

Figure 5.14(a) depicts a temperature map of cavity LE1-21, obtained following helium processing at 38 MV/m in an attempt to eliminate the emitter at 190° near the top iris. About 1 mtorr helium (measured at room temperature) was present in the system during helium processing. The gas had been admitted very slowly through the 0.3 μm filter to avoid particle contamination of the cavity. Following helium processing strong, but noisy, field emission heating was detected in the circled region at 0°. The response

[8]Helium processing here refers to the admission of helium to the cavity *and* the application of rf power. It does not necessarily mean that emitters were successfully extinguished. Nevertheless, we continue to use the term "processing" because of its wide spread usage by the superconducting rf community in this context. Implied is that helium processing was attempted.

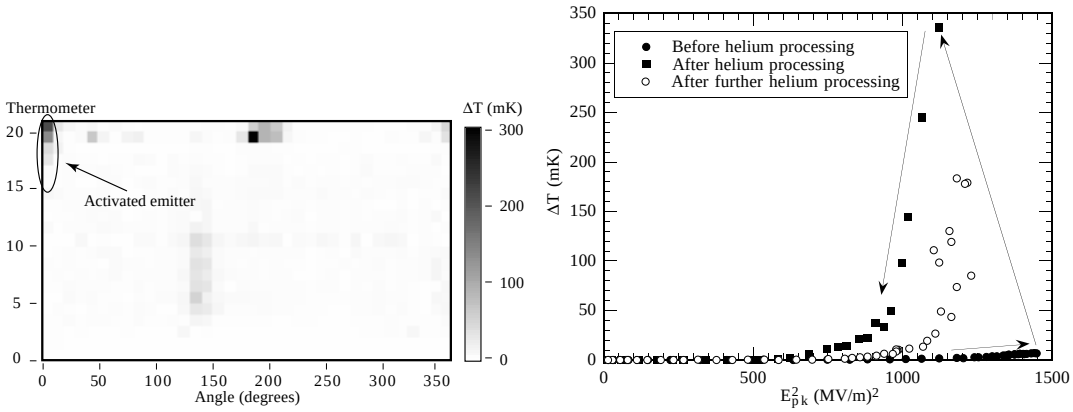

(a) (b)

Figure 5.14: (a) Temperature map of cavity LE1-21 at 32.6 MV/m after helium processing at 38 MV/m. The circled emission heating was activated during helium processing. (b) Temperature signal recorded by thermometer 20 at 0° during the test.

of thermometer 20 at 0° during the test is depicted in Figure 5.14(b). A very small amount of emission heating had been recorded here previously during multipacting, but it stopped shortly thereafter. We thus can rule out particle contamination by the helium as the cause for field emission activation.

Further helium processing later in the test (at 35 MV/m) reduced the heating a little, but the emitter became much noisier. Subsequently, we cycled the cavity to room temperature and all emission heating at 0° was deactivated. A final session of helium processing mildly reactivated the emitter (not shown), but the heating recorded was not nearly as strong as that depicted in Figure 5.14.

A microscopic search of the emitter region failed to locate any site that had distinguishing features, such as local melting or cratering, in order for us to be sure of the identity of the site. Similar to the emitter in Figure 5.10 any benefits gained from the second session of helium processing must have been due to subtle changes, possibly related to the desorption of gases (more on this in Sections 5.5.1 and 5.5.5).

5.3.2.4 Activation during rf processing

The emission site shown at 340° in Figure 5.11 rf processed later in the test and produced the molten feature shown in Figure 5.13(b). Although we have not yet discussed rf processing in detail, there is evidence that certain processing events, which melt the rf surface, are associated with the evolution of significant amounts of gas (see Section 5.5.3 and Chapter 6). Similar observations have been made with dc discharge experiments. [21,69,120,121] We therefore were not very surprised to find that a new emitter activated (at 300°) when the emitter at 340° rf processed. Although the new emitter was weak up to the maximum field achieved in the cavity ($E_{\rm pk} = 38$ MV/m), its activity is quite apparent when the difference of the cavity's temperature after and before the processing of the 340° emitter is considered (Figure 5.15). Later the newly activated emitter reduced when cycled to room temperature. Helium processing served to enhance emission a little, but the current became more noisy.

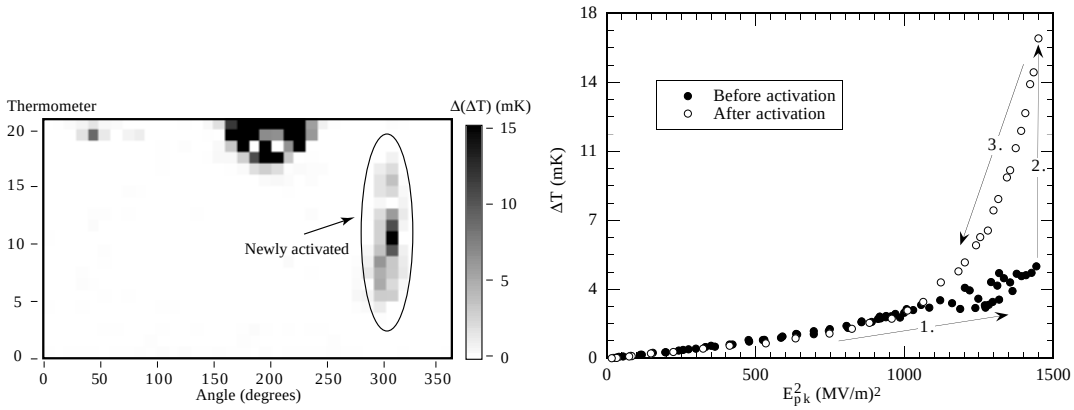

(a) (b)

Figure 5.15: (a) Temperature difference of cavity LE1-21 at 38 MV/m after and before the emitter in Figure 5.11(a) at 340° rf processed. Note that only increases are shown (difference > 0). The line heating along 300° reveals that a new emitter is active. The additional heating at the top iris is unrelated. (b) Temperature recorded by thermometer 9 at 300° as a function of E^2_{pk} showing the sudden activation event. No enhanced low field heating was detected near the predicted emitter location.

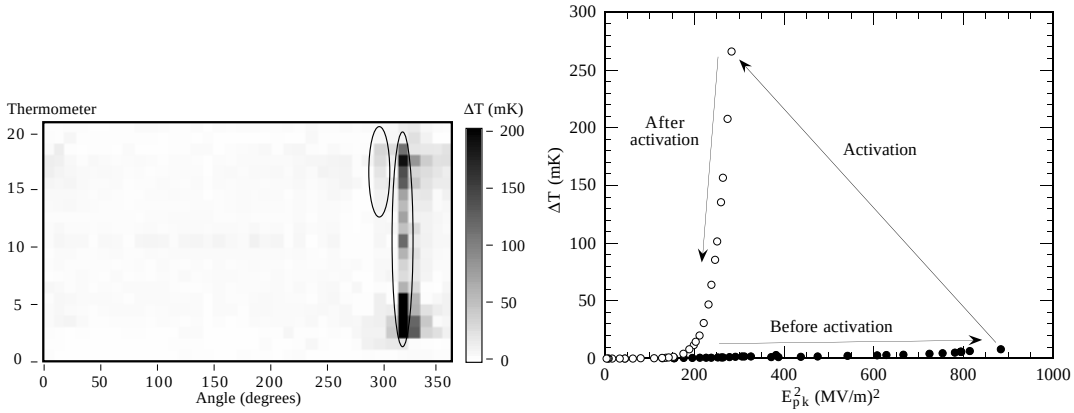

(a) (b)

Figure 5.16: (a) Temperature map of cavity LE1-20 at 17 MV/m showing two field emitters (circled) that activated simultaneously at 29 MV/m. (b) Temperature recorded by resistor 4 at 310° before and after the activiation event.

5.3.2.5 Simultaneous activation

Finally, we wish to draw attention to the pair of emitters shown in Figure 5.16 that activated simultaneously in cavity LE1-20 at 29 MV/m. The temperature signal as a function of E^2_{pk} of the stronger emission site is also shown in Figure 5.16(b). Both emitters were successfully helium processed later and identified in the electron microscope, thereby confirming our assertion that the thermometry data reflects the activity of two distinct emitters. The emission site at 290° was located near the top iris, the site at

310° was in the bottom half of the cavity. The distance between the two was more than 10 cm. Unless the emitters activated simultaneously by pure coincidence, we have further evidence that events elsewhere in the cavity can affect field emitters separated by large (cm) distances.

There is also evidence that some regions along the equator increased their low field losses at the time of activation, suggesting limited multipacting activity (as discussed later in Section 7.3). Although insufficient data is available to make a clear case here, multipacting events were definitely observed earlier in the test. Considering, that activation occurred at the threshold field for multipacting, it is possible that gases released during brief multipacting activated both emitters.

5.4 Emission mechanisms

We have identified two mechanisms responsible for frequently observed activation of field emission — particle arrival and gas adsorption. These observations can be used to extract information on the conditions required for enhanced ($\beta_{\mathrm{FN}} \gg 1$) field emission.

5.4.1 MIM and tip-on-tip model

Activation by particle motion is consistent with the hypothesis that enhanced field emission can be explained by either geometric field enhancement (tip-on-tip) or the MIM model. During the activation process, a particle is dislodged from the rf surface by electric forces, vibration or some other mechanism and strikes the cavity elsewhere. Field emission may ensue.

The titanium particle shown earlier in Figure 5.8 is an example of such emission. Thermal cycling had no effect on its emission characteristics, and it was still active at the conclusion of the rf tests. High magnification pictures of the emitter (Figure 5.17) show some jagged tips still exist, although most of the particle had melted.

Field emission based on the tip-on-tip model certainly seems possible for this particle, although microfeatures not resolved in the SEM may be needed to explain its high $\beta_{\mathrm{FN}} = 200$ value that we obtained from simulations. Alternatively, the MIM model based on the niobium–niobium oxide–titanium sandwich may also account for the ongoing field emission. The information available at present is not sufficient to distinguish between the two mechanisms.

Another, similar, emitter was shown earlier in Figure 5.4. This emitter also survived temperature cycling and was active at the end of the test after which the cavity was dissected for examination. Again, the conducting nature of the particle and its many jagged features suggest field emission was by geometric field enhancement and/or the MIM model.

An attempt to dislodge the stainless particles with a jet of 15 psi nitrogen gas was unsuccessful, proving that emitting particles can adhere strongly to the cavity surface. Such strong adhesion was observed in other instances at Saclay [64] and by us as well. Little difference was seen, when we used a jet of CO_2 crystals, except that the molten spheres disappeared. We suspect that their adhesion to the rf surfaces had reduced due to necking when they melted.

Both the titanium and stainless steel particles conform with the emerging view that metallic particulates are responsible for enhanced field emission. In fact, sensitive Auger

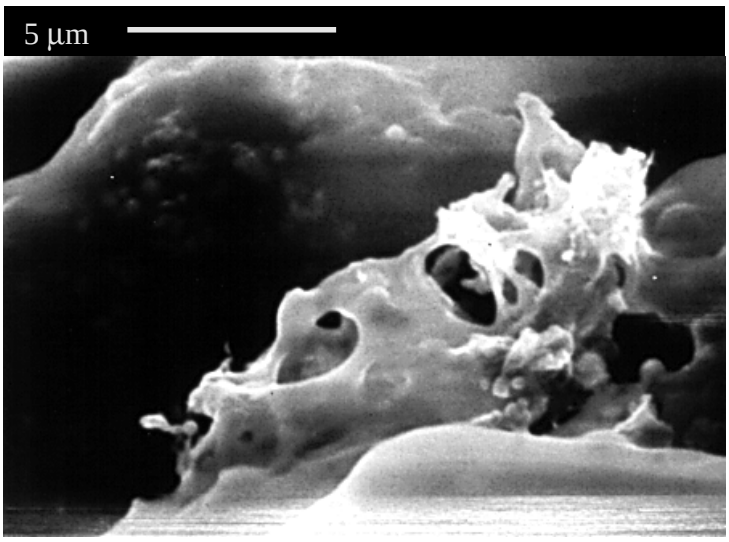

Figure 5.17: High magnification picture of the titanium emitter in Figure 5.8 showing some emission tips remain despite the fact that the particle had melted to a large extent.

and EDX analyses of exploded field emitters in mushroom cavities were always able to identify some foreign elements at the emission sites studied. [65] In the present series of tests we also found conducting elements in 63 % of the emission sites that could be clearly identified. Of the remaining 37 % of emitters, the emitters had melted extensively (as described in Section 5.5.3) and we suspect that the poor sensitivity of our EDX system prevented us from finding contaminants.

However, not all particulate emitters have obvious pointed projections. Similar to the previous two emitters, the conducting particle in Figure 5.18 was also shown to be active when testing was stopped. Its β_{FN} was 190, but no projections could be found. It is unlikely that sites like these can emit by simple geometric field enhancement. To explain the high β_{FN} values one has to revert to the MIM model.

5.4.2 Adsorbates

As already mentioned in the introduction to field emission (Section 3.2.1), there are cases where the MIM and tip-on-tip models are unable to explain all field emission. In several instances discussed in Section 8.4 we observed particle motion that did not lead to field emission. Other laboratories also found that of the typical 100 particles/cm^2 only a fraction ($\approx$ 10 %) of all particles emit. [52, 53] In one laboratory, intentionally introduced MoS_2 particles were found to emit. But many MoS_2 particles were also found *not* to be emitters. As far as the SEM micrographs (1 μm resolution) could reveal, there was no difference in appearance between emitting and non-emitting particles. [52]

Earlier, we described many cases where the activation of emitters is precipitated by other events in the cavity, especially thermal breakdown, multipacting, helium processing and rf processing (of another emitter). The common denominator of all these events appears to be the evolution of gases that subsequently can adsorb on and affect other parts of the cavity. In several cases we found that such gases were able to reactivate dormant emitters that had previously been emitting and then deactivated.

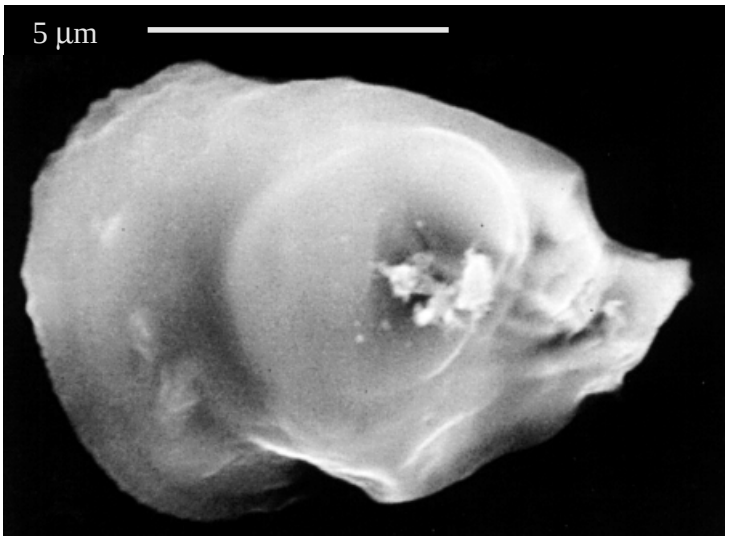

Figure 5.18: Field emitter found in cavity LE1-20. Emission activity from the site was recorded at the end of the rf test. Carbon, oxygen, iron, chromium, and nickel were among the foreign elements detected.

We attribute these cases to adatoms that facilitate field emission by the resonant tunneling mechanism discussed in Section 3.2.1. Alone, this mechanism is incapable of creating very high β_{FN} values, but if it acts in tandem with another mechanism, such as the one described by the MIM model, significant field emission may be possible.

An example of such cooperation was provided by the emitter we presented in Figure 5.13. Several particles, some molten, were found at this site. Although the emitter had almost completely extinguished by the end of the test, some emission activity was still apparent in the temperature maps. Our data demonstrated that the emitter's strength was profoundly affected by gases (see Figure 5.12). Activation of this emitter was correlated with multipacting in the cavity. Further enhancement of the emitter was brought about by helium processing, but a room temperature cycle decreased its strength again. Hence, the presence both of conducting particles and surface adsorbates proved to be important for enhanced field emission.

Finally, we present one surprising case where we observed field emission right up to the end of the cavity test, but instead of a particle at the predicted emitter site, we located a residue and small craters in a discolored region (shown in Figure 5.19). The site was found within 3 mm of the predicted location. An EDX analysis failed to detect any foreign elements. The null result with EDX puts an upper limit of about 300 nm on the thickness of any contaminants in the discolored region.

We cannot rule out completely that a particle had previously existed at the site and dislodged when we cut the cavity apart. However, this is unlikely to have happened based on our past experience that emitting particles adhere strongly to the rf surface (see, for example, the stainless steel emitter discussed earlier). Work done by others confirms that emission particles "weld" to the rf surface. [64, 67] This site provides an example of field emission from a non-particulate site that was very active. There is also no case here for any geometric enhancement. We must therefore consider the possibility that emission solely based on the MIV and/or the resonant tunneling models can occur

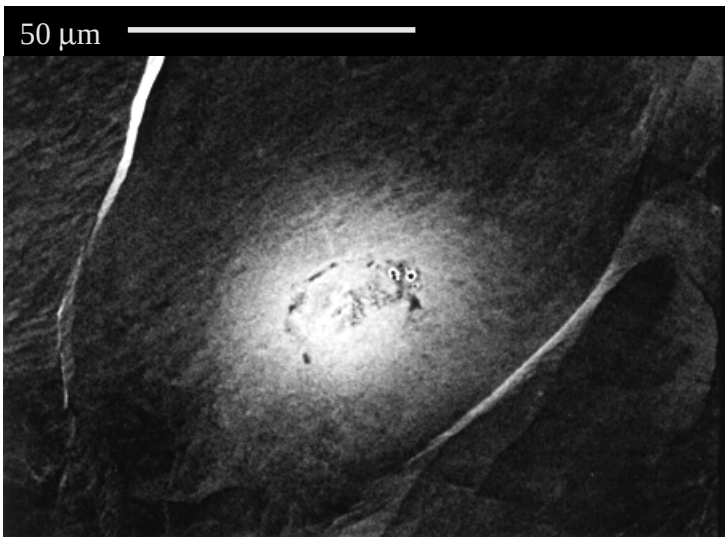

Figure 5.19: Emission site found in cavity LE1-27 that was active at the end of the test.

in rf cavities in limited cases. It should be emphasized, though, that this type of emission is rare. In an overwhelming number of cases, particles are found at active emission sites.

5.5 Emitter deactivation

5.5.1 Gas desorption

In the previous sections we already mentioned on several occasions that gas activated emission sites have been observed to deactivate following a thermal cycle to room temperature or by helium processing (see, for example, the emitter in Figure 5.9). On occasion even a spontaneous reduction was observed.

An example is shown in Figure 5.20. Emission along 50° in cavity LE1-34 activated at 32.4 MV/m. No other event in the cavity could be correlated with the activation. Later in the test the same emitter partially rf processed at 35.2 MV/m. However, following a thermal cycle, the emitter became stronger than ever before, confirming that the processing event was not due to the destruction of the emission site. Instead, we suspect that adatoms were removed, resulting in the reduction of emission. Finally, helium processing all but eliminated emission again. Temperature data taken while helium processing was being performed shows that emission along 50° was very noisy at first, sometimes even exceeding the cw heating observed prior to helium processing (Figure 5.21(a)). For comparison, we show the temperature signal of another field emitter in the cavity (Figure 5.21(b)), which did not fluctuate strongly. It proves that the noise of the 50° emitter is not due to field fluctuations in the cavity. After about 20 seconds, emission is almost completely extinguished along 50°. The lack of an abrupt transition demonstrates that the emission characteristics were altered without an explosive destruction of the emitter — contrary to some other sites we will be presenting shortly. Instead we suspect that helium ions sputtered adsorbates and thereby reduced the emitter's strength. Not surprisingly, we were unable to find a site in the SEM with distinct melted features that would clearly identify the emitter.

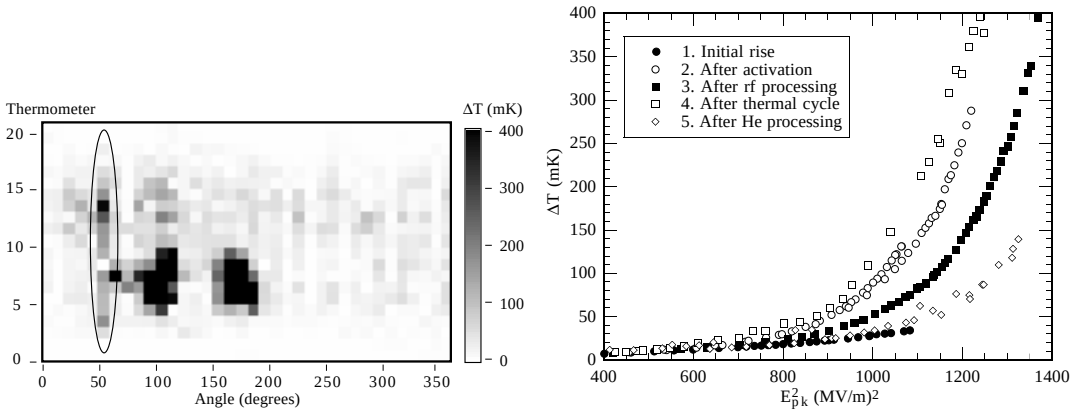

(a) (b)

Figure 5.20: (a) Temperature map of cavity LE1-34 at 37 MV/m, showing field emission heating along 50° that activated at 32.4 MV/m. (b) Temperature signal recorded by thermometer 13 at 50° following various events.

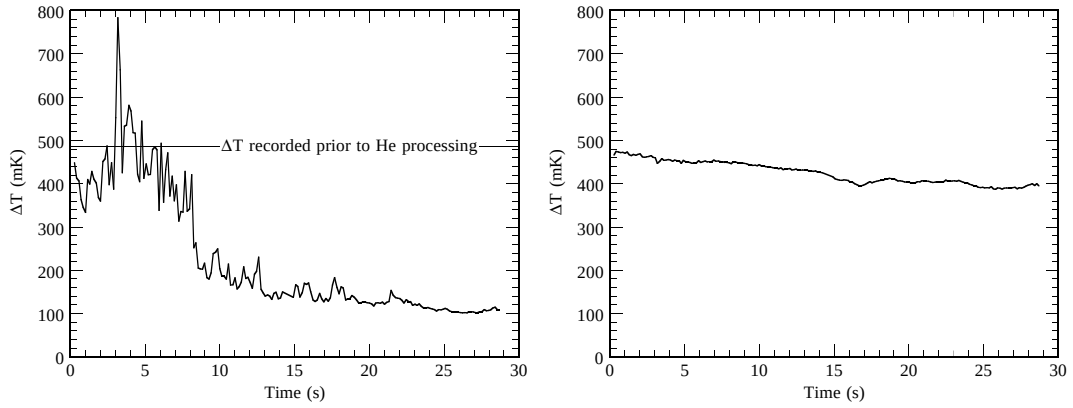

(a) (b)

Figure 5.21: Temperature signal of (a) thermometer 13 at 50° during helium processing, (b) thermometer 6 at 100° (covering a different field emitter) during helium processing.

Thus, both rf and helium processing can progress by the desorption of adatoms or an alteration of the emitter surface composition, even when little energy (relative to that required for melting) is supplied to the emission site. This energy can be either due to the Joule heating by the emission current itself, thermal cycling, or electron and ion bombardment during helium processing. However, the energy is insufficient to significantly alter the emitter's appearance, so that we are unable to identify these sites in the electron microscope by molten features.

In one experiment we demonstrated the ability of a discharge to remove adsorbates by using the following procedure: First we adsorbed gases on the rf surface by letting several torr of filtered helium gas rush into the cold system. The test stand was then evacuated again to less than 10^{-4} torr. Low field temperature data confirmed that the

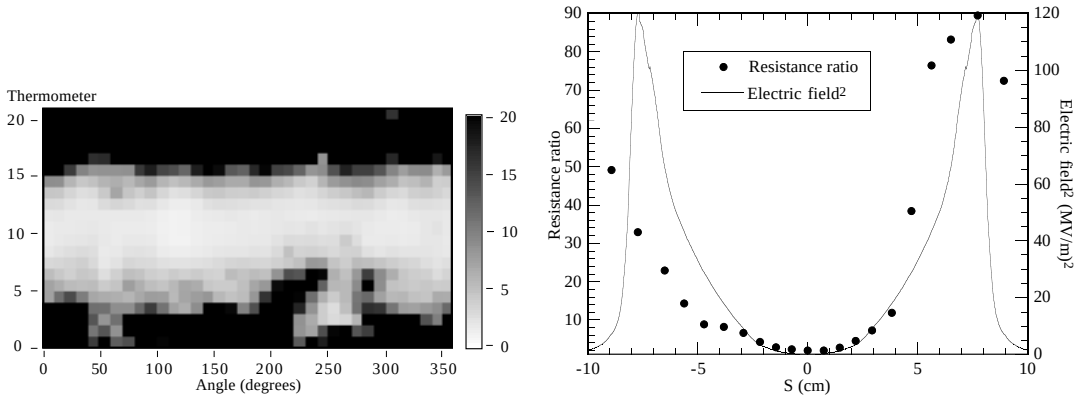

(a) (b)

Figure 5.22: Ratio of the surface resistance at 11 MV/m after and before several torr of helium were administered to cavity LE1-31. (a) Ratio map of the entire cavity. (b) Same data as in (a) but summed over all thermometer boards at each latitude. The square of the surface electric field is included to illustrate that the losses are mainly dielectric in nature.

surface resistance had increased substantially following the procedure (Figure 5.22(a)). Correspondingly, the Q_0 also dropped by a factor of 10. Most increases were observed in high electric field regions, so they must be dielectric in nature. Figure 5.22(b) shows that the increased losses roughly follow the square of the electric field. The quadratic nature of these losses was also demonstrated by a field independent Q_0. We suspect that the losses are caused primarily by impurity gases in the helium rather than the helium itself, because no R_s changes were observed when helium was administered very slowly, giving the impurity gases a chance to condense before they ever reach the cold cavity.[9] At higher fields it became apparent that a new field emitter had been activated by the gases (Figure 5.23(a)). Then, at 25.3 MV/m, the fields in the cavity suddenly collapsed and we observed a large reduction of the surface resistance along the azimuth of the field emitter (Figure 5.23(b)).

In most places, the surface resistance reduced to levels between those measured before the helium was administered and those measured just before the discharge. In some cases, though, the surface resistance reduced to values lower than those achieved at any time previously in the cavity test (see Figure 5.24).

It is likely that we witnessed a discharge fueled by helium remaining in the cavity and/or gases desorbing from the rf surface by field emission electron bombardment. We see, that a discharge is very effective at removing lossy surface adsorbates, even those that were not artificially introduced. Presumably similar events take place during regular helium processing on a smaller scale. The removal of gases then explains why emitters as in Figure 5.21(a) reduce their emission activity.

Both rf processing and helium processing by desorption has also been proposed by, for example, Halbritter. [57] He claims that a field emitter reduces its strength during rf processing when hydrogen from hydrocarbons desorbs, leading to their dehydrogenation.

[9] A thermal cycle with another cavity treated in the same manner reduced this type of losses back to original levels, thereby proving that the increases are *not* due to particles.

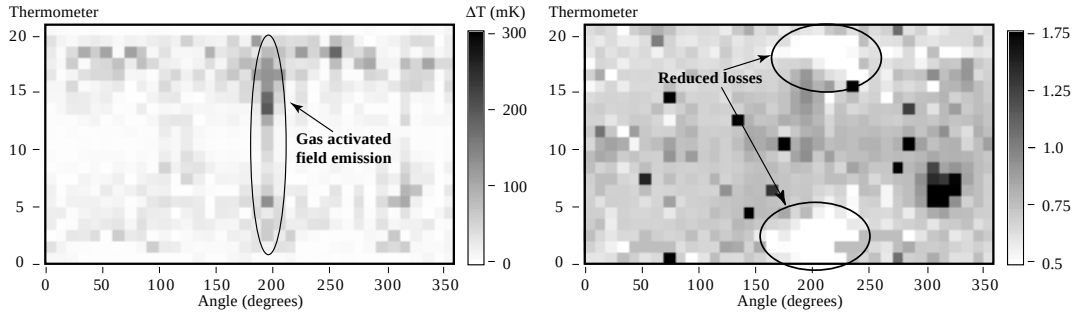

(a) (b)

Figure 5.23: Temperature map of cavity LE1-31 at 25 MV/m showing a field emitter that activated after several torr of helium gas was administered to the cavity. (b) Ratio of the surface resistance after and before a discharge event at 25.3 MV/m. (Ratio taken at $E_{\mathrm{pk}} = 8$ MV/m.)

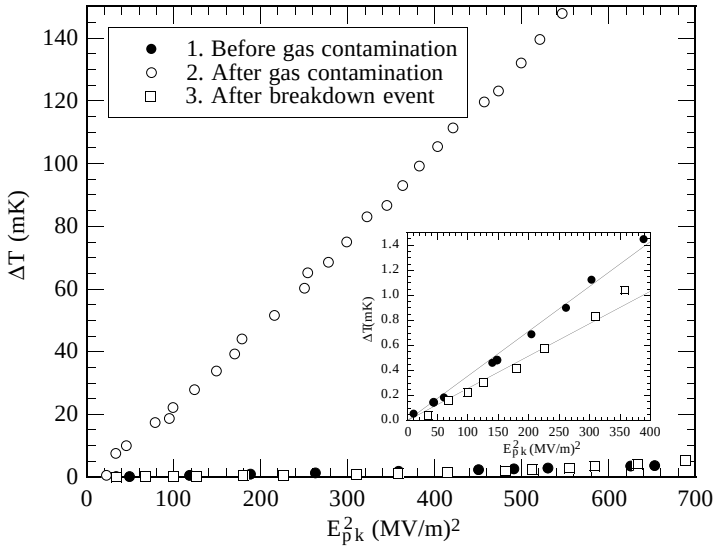

Figure 5.24: Temperature recorded by resistor 18 at 220° before and after cavity LE1-31 was "contaminated" with helium. Following a breakdown event, the temperature signals reduced to below pre-helium levels (see inset).

The remaining chains have many inelastic resonances for electron scattering. They trap slow electrons and prevent them from gaining the energy required by the MIV/MIM model for field emission.

Helium processing, Halbritter proposes, progresses along similar lines due to desorption of water molecules by helium ion impact. As explained in Section 3.2.1, it is thought that water is important in enhancing field emission by resonant electron tunneling. The gradual removal of water then reduces the emission current slowly, as observed in Figure 5.21(a).

Helium processing by desorption of adatoms was also postulated by Schwettman *et al.* [45] Similar to our results shown in Figure 5.21(a), they too observed very noisy field emission behavior during helium processing, associated with a gradual decline of the

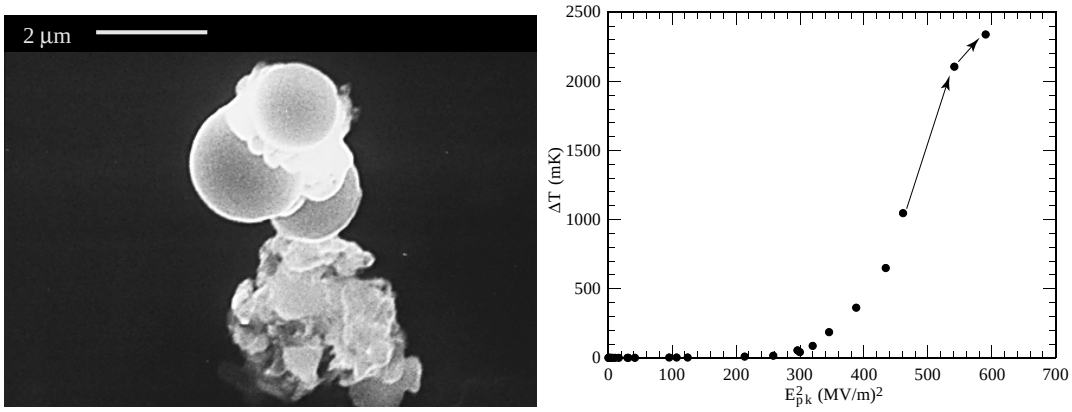

(a) (b)

Figure 5.25: Magnified view of the framed region in Figure 5.4 showing several molten spheres. (b) Heating due to impacting field emission electrons recorded near the emitter. Although the emitter never processed completely some reduction in ΔT is visible at the highest field levels.

mean emission current.

Irrespective of the precise mechanism, it turns out that most of the processing events we observed fall into this category of "processing by adatom desorption." Of more than 19 extinguished emitters, over two thirds could not be identified by any special features in the electron microscope.[10] Unfortunately, as we have shown, emitters that deactivate by gas desorption or due to superficial changes (especially due to a thermal cycle) often reactivate following renewed gas adsorption. The benefit gained from such "processing" may thus be limited. For lasting improvements, one must completely destroy the emitter. Such events will now be discussed.

5.5.2 Emitter melting

Our observations and other experiments in the past have shown that the current density drawn from a field emitter can exceed that required to melt the local environment. [16, 63] Melting occurred, for example, at the stainless steel emitter depicted earlier in Figure 5.4. The framed region is enlarged in Figure 5.25(a), showing several molten spheres of stainless steel. The associated heating (by the impacting electrons) recorded in Figure 5.25(b) demonstrates the strong emission activity in progress. At the very highest field level, some reduction in heating can be observed. This may be associated with the melting of the emission tip in (a). Since there are many jagged tips present on the emitter, we expect emission to occur at several sites simultaneously. The melting of an individual tip, hence, only has a small effect on the average emission characteristics of the particle.

Melting also took place at the emission sites in Figures 5.8 and 5.19. In the latter case the niobium surface even exceeded its melting temperature (2740 K) in a few small places (the craters).

[10] In the next section we will discuss another class of processed emitters that had very unique features which clearly distinguished the emission site from other particles in the cavity.

Calculations for rf field emission [63] and dc field field emission measurements [22,69, 122,123] indicate that the current density required to melt emitters is about 10^{11} A/m^2. Field emission simulations as described in Section 4.8 indeed yield a peak j_{FN} of over 10^{11} A/m^2 for our molten emitters. The agreement is encouraging. However, we need to point out that the indiscriminate use of β_{FN} to calculate j_{FN} in Equation 3.3 is unlikely to yield the true current density, because little correlation has been observed in the past between the emission area and A_{FN}. Furthermore, since we expect emission from possibly many tips on a particle as in Figure 5.4, at best only an average value for j_{FN} can be obtained. Thus, calculated j_{FN} values should only be considered a rough approximation of the true current density.

5.5.3 RF processing

It has been shown that if E_{pk} is increased beyond the threshold for emitter melting, the heating at the emission site becomes very severe, and the emitter explodes and extinguishes ("processes"). [16, 63] Such events were also observed in dc field emission (see, for example, Reference [124]).

5.5.3.1 Large scale melting

Certainly such events were observed in our experiments as well. Figure 5.26(a) depicts a field emitter in cavity LE1-27, that rf processed between 24 and 27 MV/m. Although the temperature data on this emitter is somewhat scarce, the discontinuous nature of the temperature signature is clearly visible in Figure 5.26(b). During the test, the rf processing event was marked by a sudden collapse of the cavity fields as all stored energy was dissipated in a fraction of a second.[11] Such a collapse was observed during all processing events of this type and should be contrasted with the slow helium processing in Figure 5.21(a). Only heating due to ohmic losses remained after the rf processing event. Some "pre-processing" is visible in Figure 5.26(b) that suggests partial melting of the emission site similar to that observed in Figure 5.25 may have occurred.[12] We did not perform a thermal cycle on this emitter. However, emission sites with similar molten features (see next paragraph) were cycled, and on no occasion did they reactivate. We therefore believe that this emitter no longer is capable of field emission.

Figure 5.27 depicts the debris field we found within 3 mm of the predicted emitter location. Nothing else indicative of field emission (e.g., starbursts, molten particles ...) was found in the microscope within many centimeters of this site. A faint 500 μm starburst, indicative of an explosion, surrounds the actual emission site. The magnified views of the emitter reveal a nearly 80 μm long but narrow region of molten material (mostly niobium), debris (mostly carbon and oxygen) and some discoloration of the rf surface (no contaminants found by EDX analysis).

Such molten features have been found in 5.8 GHz [63, 65], 3 GHz [16] and now in 1.5 GHz cavities. In all cases they are believed to be the remnants of permanently processed emitters. In the case of 3 GHz cavities this was borne out by thermometry

[11] In the next chapter we will show experimental results and calculations which demonstrate that the stored energy is dissipated in less than 1 μs.

[12] The dip in heating was observed in many other places around the cavity as well. A reduction in x-ray bombardment from the emission current may have been responsible for the dip. However, we should point out that a systematic measurement error could be at fault as well.

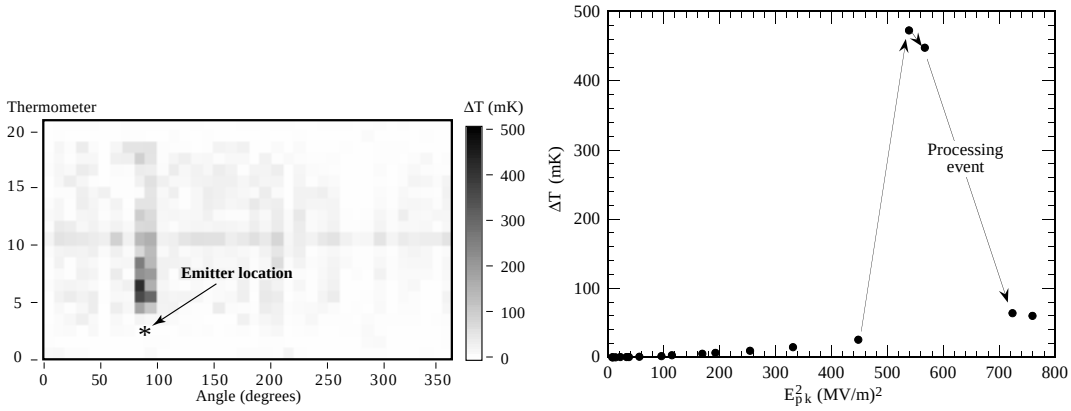

(a) (b)

Figure 5.26: (a) Temperature map of cavity LE1-27 at 24 MV/m, showing field emission along 85°. Shortly after this map was obtained the emitter rf processed. (b) Temperature signal recorded by thermometer 6 at 80° before and after the processing event.

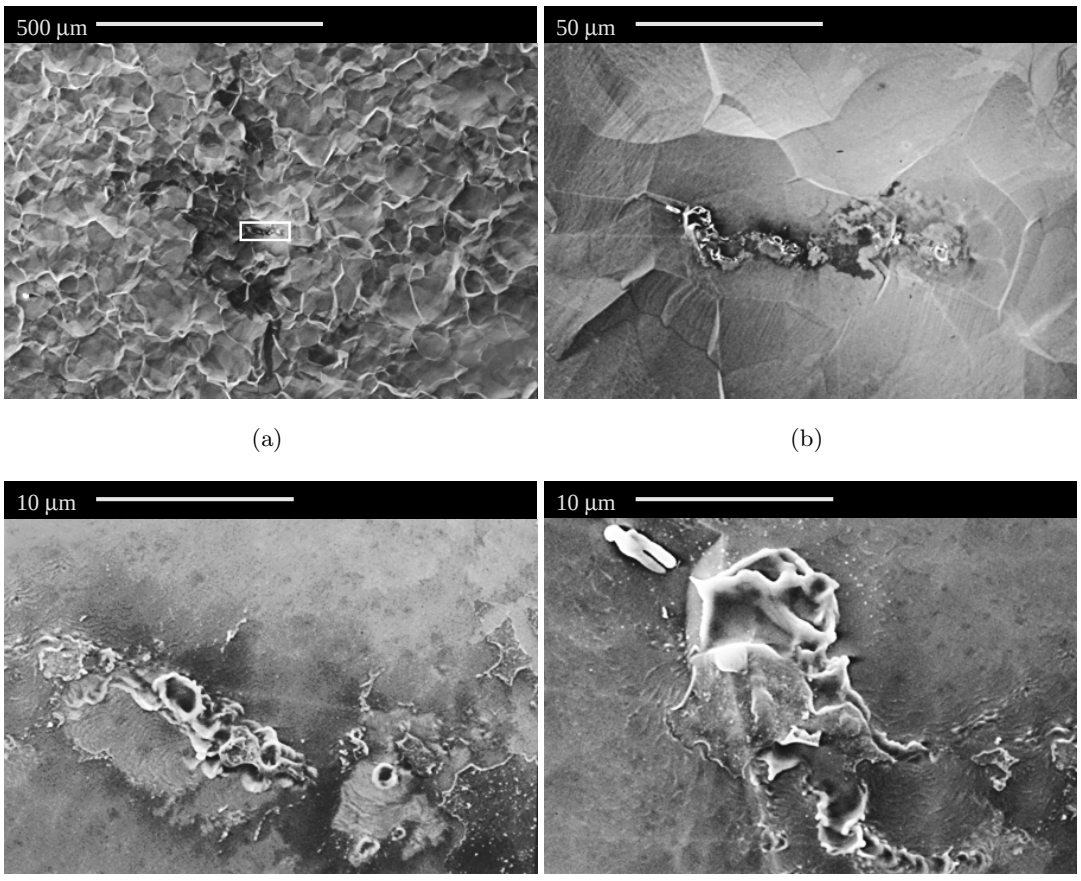

(a) (b)

(c) (d)

Figure 5.27: (a) Picture of the field emitter responsible of the heating in Figure 5.26. (b) Magnified view of the framed region in (a). Magnified views of (b) are shown in (c) & (d).

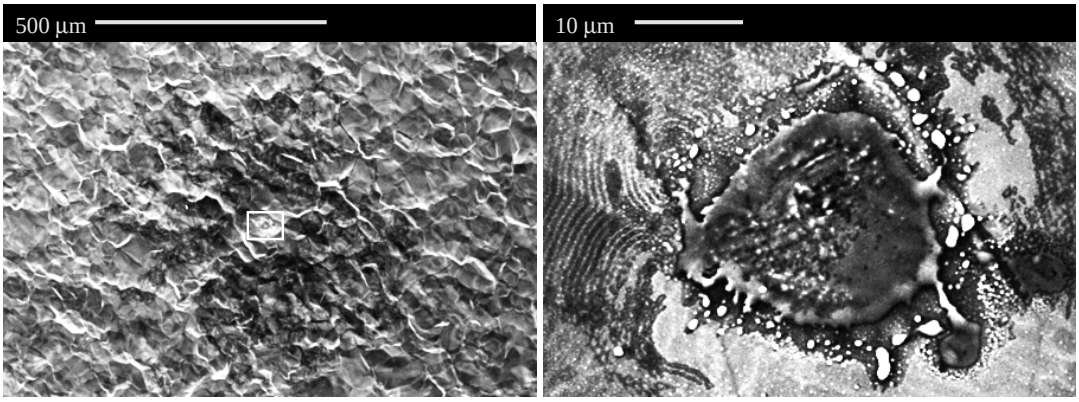

(a) (b)

Figure 5.28: (a) Low magnification picture of an rf processed emitter in cavity LE1-CEBAF and (b) a magnified view of the framed portion in (a). Indium was the dominant impurity found by EDX analysis. (Due to the fact that the cavity had not been annealed previously, the niobium grains of the cavity wall are small, resulting in the rough appearance of the rf surface.)

data. The assumption was that, upon raising the electric field, the Joule heating by the field emission current becomes severe enough for the entire particle to melt and boil (rather than just the emission tip). An explosion ensues, creating a plasma that is responsible for the starburst formation. Hence the same mechanism (Joule heating by the emission current[13]) is responsible for both the localized melting, such as in Figure 5.25(a), and the complete rf processing[14] of an emitter.

Another site that rf processed is shown in Figure 5.28. This site extinguished at about 25 MV/m (see Figure 5.29(a)) resulting in a substantial improvement of the cavity quality (Figure 5.29(b)). Similar to the previous emitter, we observed some pre-processing before the complete extinction, possibly due to localized melting of emission tips.

A 500 μm starburst, although faint, is visible against the high contrast background of the grains. At the center we found a 27 μm region of molten indium (and possibly niobium) surrounded by small micron sized indium droplets. Such spheres were found out to a distance of about 100 μm from the emission center. Presumably, they were ejected during the explosion of the emitter.

Low field temperature data of the thermometer closest to the emitter location is presented in Figure 5.30. A reduction in ohmic heating, as observed in this figure, was only recorded at the emission site and the neighboring thermometer. It appears that prior to rf processing, an indium particle was present on the rf surface which then was vaporized. Seals between the cavity and the stainless steel test stand are a probable source of the indium. When they are removed between tests with copper scrapers it is not uncommon for particles to drop into the coupler region. In all likelihood other,

[13]Technically, there are other active heating mechanisms due to the emission current, such as Nottingham heating (or cooling). The exact mechanisms are, though, not pertinent to this discussion, so that we include them in the term "Joule heating."

[14]Note that this does not include emitters that processed due to gas desorption or some similar mechanism as discussed in Section 5.5.1. For convenience we will limit the term "rf processing" in the remainder of this chapter and the next chapter to the permanent extinction of emission by melting.

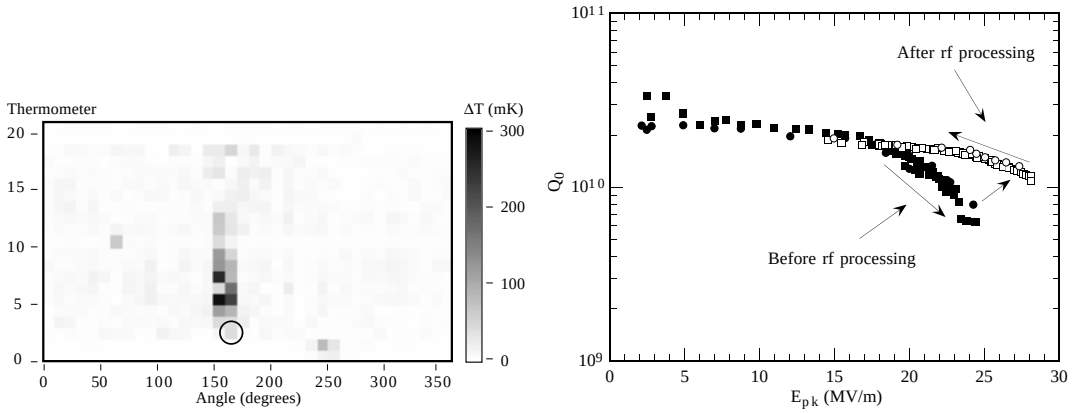

(a) (b)

Figure 5.29: (a) Field emission heating at 24.4 MV/m due to the emitter in Figure 5.28, and (b) Q_0 versus $E_{\rm pk}$ results prior to and after rf processing. The circles are results obtained from power measurements, the squares are Q_0 values deduced from calorimetry.

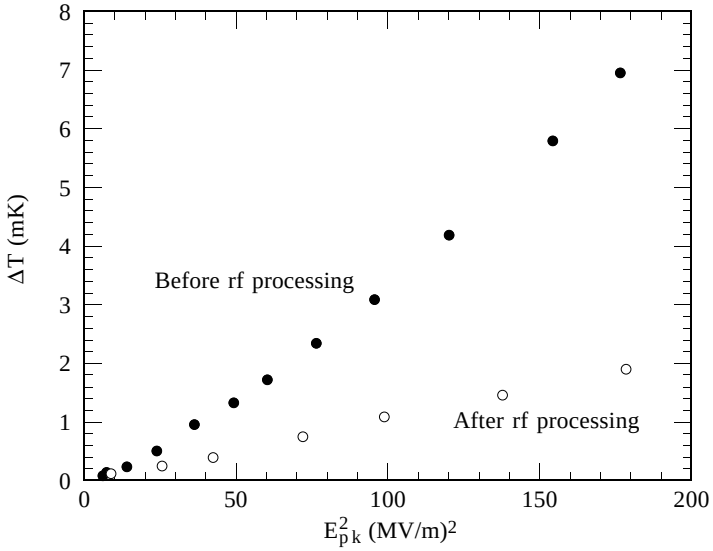

Figure 5.30: Low field temperature signal recorded by the circled thermometer in Figure 5.29(a).

normal conducting, contaminants capable of augmenting the power dissipation were also present in the particle.

The particle's large ohmic losses can only be explained if we assume that it was normal conducting, even at low field. This situation is possible, if the thermal contact to the rf surface is weak, so that magnetic heating raises the temperature of this particle. (In Chapter 8 (Section 8.4) we discuss the fact that *loosely* adhering particles are typically heated to 100 K with one milliwatt of dissipated power.) Upon processing, most of the indium was vaporized. The indium that remained became thermally well anchored so that it remained superconducting.

We can estimate the particle size using Equation 5.1 (derived in Section 8.4). At

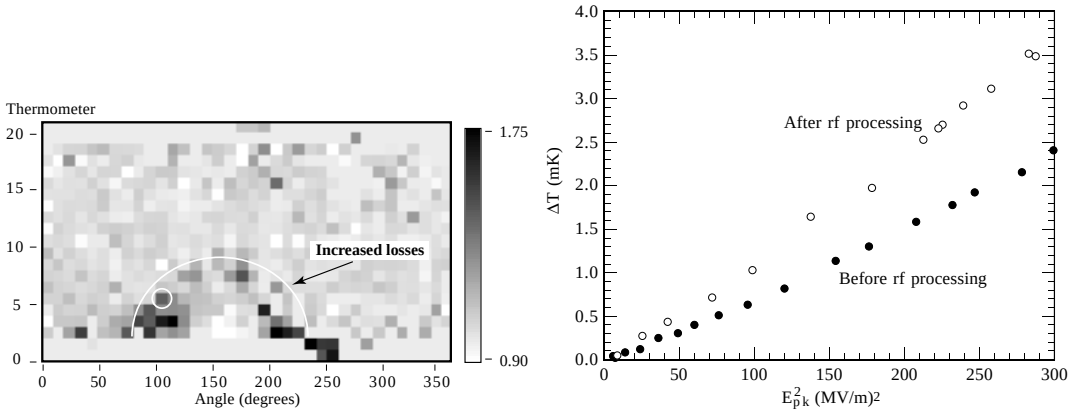

(a) (b)

Figure 5.31: (a) Ratio of the surface resistance in cavity LE1-CEBAF after and before the processing event in Figure 5.29. (b) Temperature signal recorded by the circled thermometer.

10 MV/m the reduction of ohmic heating due to rf processing was about 2.2 mK. The surface resistance of *high purity* normal conducting indium at room temperature is about 20 mΩ. [125] Since we do not know the temperature of the particle prior to rf processing, we use this value in Equation 5.1 to calculate the size. We find that $r_{\mathrm{d}} \approx 30\ \mu$m ($H = 150$ Oe, $\epsilon_T = 1.42$ K/W, $c_{\mathrm{d}} = 1.6$ and $\eta_T = 30$ %). If the base of the particle deposited most of the debris in Figure 5.28, then the agreement with our microscopy results is quite good.

To check for consistency we can determine, at what field such a particle would initiate thermal breakdown. From Equation 3.15 one finds that $H_{\mathrm{tb}} = 633$ Oe, or $E_{\mathrm{pk}} = 42.5$ MV/m. It is gratifying to see that thermal breakdown is not predicted up to the processing field and was not observed.

5.5.3.2 Explosion

We now turn to a comparison of the low field heating in the cavity before and after the rf processing event. This is shown in Figure 5.31(a). The response of a single thermometer is also shown in Figure 5.31(b). Increased losses within approximately 4.6 cm of the emitter are visible. Note the low temperature signals that need to be resolved for this effect to be noticed, which explains why such losses were not observed with other thermometry systems.

It appears as if matter (probably indium) was ejected from the emission site and increased the surface resistance of the surrounding area. The small molten droplets in Figure 5.28 support this assertion. Clearly rf processing is a very violent event. The particle heating must have been so severe, that an explosion was caused. The usual shape of starbursts around emitters also points to the explosive character of the event.

The low field cavity Q_0 was about 2×10^{10}, so that the average surface resistance was $R_{\mathrm{s}} = 270\ \Omega/(2 \times 10^{10}) = 13.5$ nΩ. The mean increase recorded in the affected region in Figure 5.31(a) was only 24 % or 3 nΩ.

We now present a simple calculation to estimate whether indeed sufficient material

was present in the original particle to account for the increased losses.

Most of the ejected material must have been in the form of gas or droplets smaller than the detection limit set by the SEM (≈ 0.2 μm). For estimation purposes, we assume that droplets, radius $\rho_{\rm d}$, were ejected. If the original emitter was of radius $r_{\rm d}$ then $N = (r_{\rm d}/\rho_{\rm d})^3$ droplets were created. These droplets spread over an area $A = \pi(4.6\text{ cm})^2$ and expose an effective area of $N2\pi\rho_{\rm d}^2$ of superconducting indium to the rf fields. The theoretical increase in the surface resistance of the region is

$$\Delta R_{\rm s} = \left(\frac{r_{\rm d}}{\rho_{\rm d}}\right)^3 \frac{2\pi\rho_{\rm d}^2}{A} R_{\rm In}. \tag{5.2}$$

Solving for $\rho_{\rm d}$ one finds

$$\rho_{\rm d} = \frac{2\pi r_{\rm d}^3 R_{\rm In}}{A\Delta R_{\rm s}}. \tag{5.3}$$

Equation 5.3 represents the maximum possible radius the droplets can be, if the original indium particle at the emission site is to produce an increase $\Delta R_{\rm s}$ in ohmic losses. Superconducting high purity indium has a surface resistance of $R_{\rm In} \approx 3 \times 10^{-6}$ Ω at 1.7 K. [126, 127] For the measured value $\Delta R_{\rm s} = 3$ nΩ one finds that

$$\rho_{\rm d} = 0.03\ \mu\text{m} = 300\ \text{Å} \tag{5.4}$$

is the maximum droplet size. Other, normal conducting, impurities (especially copper and stainless steel) were probably present in the original particle as well, so a larger $\rho_{\rm d}$ is possible.

300 Å particles are impossible to detect in our SEM. More important, though, is the fact that the particle size is not smaller than the London penetration depth of indium (300 Å at $T = 0$). [126] Hence the magnetic field is attenuated in the indium particles and does not "see" the niobium underneath. In other words, we are justified to treat the droplets as bulk material. However, indium's coherence length is $\xi_0 = 3000$ Å [126], so that a modification of $R_{\rm In}$ may be required. Hence we wish to emphasize that the above calculation can, at best, only be considered a rough estimate.

We are not claiming that the explosion of the original emitter actually creates a shower of particles with radius exactly $\rho_{\rm d}$. Much smaller particles are possible, or perhaps a fairly uniform coverage of the rf surface with indium results. Given an atomic volume of 2.6×10^{-29} m^3 and an atomic radius of 2 Å for indium [128], we could expect about 10 % of a monolayer coverage in the region that increased $R_{\rm s}$. However we do not know what the effective surface resistance of this In/Nb system is.

5.5.3.3 A simple rf processing sequence by Joule heating

Based on the emitters presented in Sections 5.5.2 and 5.5.3, it would appear that there are three distinct stages in the "life" of a field emitter.

1. *Pre-melting* At reasonably low fields, emission is active and degrades the cavity quality. The current density is insufficient to melt (and alter the appearance) of the emitter. Events such as gas adsorption or desorption can affect the emitter's strength.

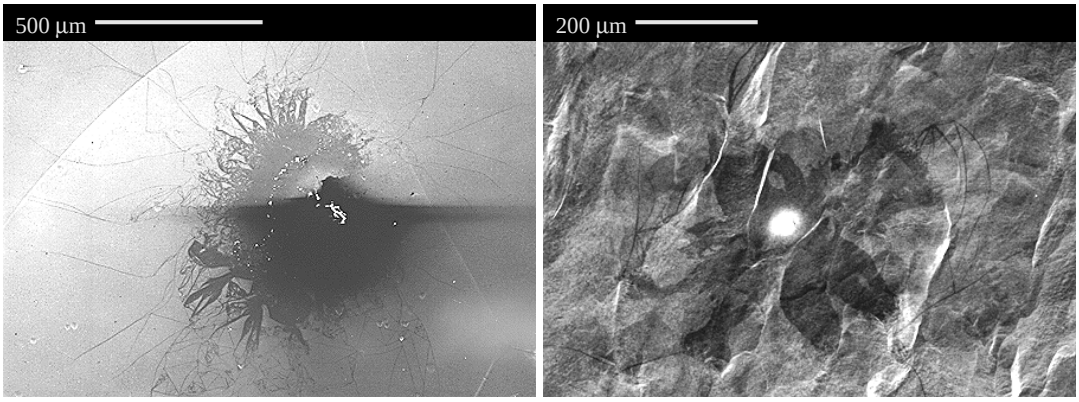

(a) (b)

Figure 5.32: (a) Emission site found in cavity LE1-23. The central region is magnified in Figure 5.8. (b) Emission site found in cavity LE1-27. The central region is shown magnified in Figure 5.19. Both emitters were active at conclusion of the rf test.

2. Melting As the electric field is raised the current density increases exponentially. When it exceeds about 10^{11} A/m^2 the emission tip begins to melt (see for, example, Figure 5.25(a).) The dimensions of the molten region are ≤ 1 μm.

3. Explosion At even higher electric fields, the Joule losses of the emission current become so severe, that the entire particle ($\approx$ 10 μm) explodes and extinguishes. During the explosion a plasma is created that is responsible for starburst formation.

However, questions remain. How does an emitter get from stage 2 to stage 3? How does emission stop? A reasonable assumption is that emission will cease as soon as the emitter melts. Other tips on a particle may continue to emit until they melt as well. However, unless all emission tips have the same $\beta_{\rm FN}$ parameter, we would not expect them to melt simultaneously. In this case rf processing would not be the abrupt event that is observed. Furthermore, a processed emitter should consist of a series of molten tips, rather than a large mass of molten material with crater like features as in Figures 5.27 and 5.28.

In past studies with 5.8 GHz mushroom cavities [63, 65] the presence of a starburst was considered an indication that an emitter had processed completely. In the present studies we were therefore surprised to find emitters that were active at the end of our tests, yet they were surrounded by a starburst! Two examples are shown in Figure 5.32. These pictures are low magnification views of the emitters previously shown in Figures 5.8 and 5.19. *In both cases, thermometry data showed that field emission was still active at these sites at the conclusion of the rf tests.*

These pictures are good examples of the types of starbursts so frequently found around emission sites. The presence of a starburst *before* the processing of the emitter establishes that a plasma can be present *during* the field emission stage and is not simply the result of the explosion that extinguishes the emitter.

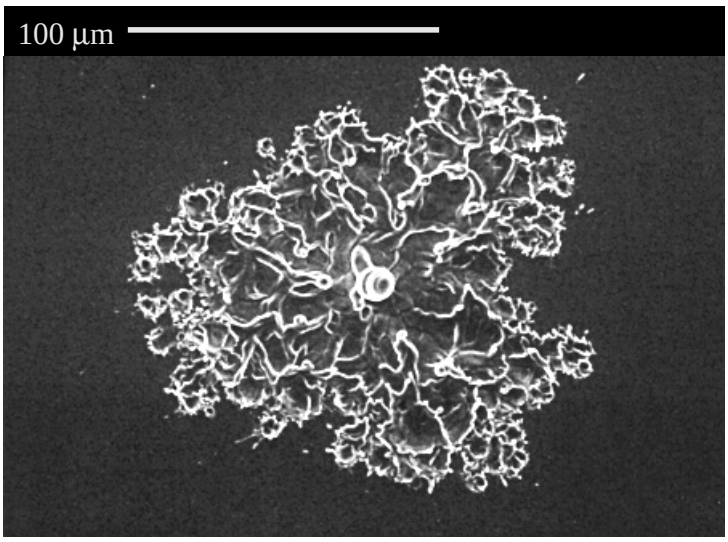

Figure 5.33: An emission site found cavity LE1-Heraeus. No foreign material was detected by EDX analysis. Thermometry data on this site is not available, but we suspect that it had ceased to emit, considering that it had thoroughly melted.

We will try to show, that a plasma is critical to bridging the gap between stage 2 and 3 in the sequence of events described above. That is, a plasma is required to melt a region significantly larger than a micrometer and thus is essential during the rf processing stage.

5.5.3.4 Joule heating by the emission current

To understand how rf processing progresses we need to determine how effective the emission current is at melting the rf surface. In particular, we have to find out, whether the emission current is capable of melting large regions as in Figure 5.27 and even larger areas as in Figure 5.33. To this end we present a simple calculation that is sufficient for an order of magnitude estimate.

In Chapter 3 (Section 3.2.2) we developed an expression to calculate the temperature profile near a defect (radius r_{d}) dissipating power $\dot{Q}$. We obtained

$$T(r) = T_{\mathrm{b}} + \frac{\dot{Q}}{2\pi\kappa_T r} \qquad (r_{\mathrm{d}} \leq r \ll d), \tag{5.5}$$

where T_{b} is the bath temperature, κ_T is the thermal conductivity of niobium and d is the thickness of the cavity wall.

We can use this expression equally well to calculate the temperature profile near a field emitter, provided we use the emission current dissipated Joule losses for the power $\dot{Q}$. Without knowing the exact loss mechanisms involved we can determine an upper limit on $\dot{Q}$ by taking into account the fact that our thermometry system has never been able to detect a temperature signal due to the field emission Joule losses. Background temperature signals when field emission is active are typically 20 mK. Hence any Joule losses resulting in ΔT's less than about 40 mK will go undetected.[15]

[15]We believe that in some cases we should have been able to detect Joule losses quite a bit less than

As will be discussed in Section 8.4, the temperature rise at the niobium–helium interface due to power dissipated in a point defect is $\epsilon_T \approx 1.4$ K/W (see Table 8.1). When taking into account a thermometer efficiency of 30 % we see that Joule losses will go undetected if $\dot{Q} \leq 100$ mW.

Niobium melts at $T_{\rm m} = 2740$ K. We are interested in the distance $r_{\rm m}$ from the emitter center where the temperature drops below $T_{\rm m}$. This distance is readily obtained by solving (5.5) for r. One finds

$$r_{\rm m} = \frac{\dot{Q}}{2\pi\kappa_T T_{\rm m}}. \tag{5.6}$$

In obtaining (5.6) we ignored $T_{\rm b}$ since $T_{\rm m} \gg T_{\rm b}$. For niobium $\kappa_T \geq 50$ W/Km for $T \geq 2$ K [129], so that the use of $\kappa_T = 50$ W/Km yields an upper limit for $r_{\rm m}$. In that case

$$r_{\rm m} \leq 0.1 \ \mu\text{m}. \tag{5.7}$$

We see that the size of the molten zone barely exceeds (if at all) the size of typical field emission areas. Joule heating may be called upon to explain the small craters in Figure 5.19, but certainly the field emission current alone is incapable of melting niobium as much as 100 μm across, as observed in Figure 5.33.

One may argue that larger regions will melt, if field emission occurs from a particle that is not thermally well anchored to the rf surface. The original particle in Figure 5.8 might have been of this type. In such cases one defines the contact resistance $\mathcal{R}$ by:

$$T_{\rm d} - T_{\rm b} = \mathcal{R}\dot{Q}, \tag{5.8}$$

where $T_{\rm d}$ is the particle temperature (more on this in Section 8.4). Measurements of $\mathcal{R}$ for iron and niobium particles on a niobium substrate have shown that for all particles studied 10^5 K/W $< \mathcal{R} < 1.6 \times 10^5$ K/W. [67, 130] To estimate whether the particle in Figure 5.8 could melt, we need to know the Joule losses suffered by the emission current more precisely. In general, the power $P_{\rm FN}$ dissipated by a time averaged current $\bar{j}_{\rm FN}$ is

$$P_{\rm FN} = \bar{j}_{\rm FN}^2 \rho \ell A_{\rm d}, \tag{5.9}$$

where $A_{\rm d}$ is the emission area, ρ is the particle resistivity and ℓ is the distance traversed by the emission current in the bulk. For a typical metal at high temperatures, $\rho \approx 10^{-6}$ Ωm. For lack of concrete numbers we shall take ℓ to be about the size of the emission region ($\ell = 0.1$ μm) and $A_{\rm d} = 0.01$ μm^2. If $\bar{j}_{\rm FN} = 10^{11}$ A/m^2 then[16]

$$P_{\rm FN} = 10 \ \mu\text{W}. \tag{5.10}$$

At this power level we expect the temperature rise of the entire particle to be

$$\Delta T = 1 \text{ K}. \tag{5.11}$$

40 mK, so that 40 mK is a very conservative estimate.

[16] We have to use the average emission current rather than the instantaneous current given by (3.3). If the Fowler-Nordheim equation (3.3) is averaged over one rf cycle, one finds that $\bar{j}_{\rm FN} \approx j_{\rm FN}/10$ to $j_{\rm FN}/5$. Hence $\bar{j}_{\rm FN} = 10^{11}$ A/m^2 is about the maximum field emission current that can be expected for typical emitters. See, for example, Reference [73] for more details.

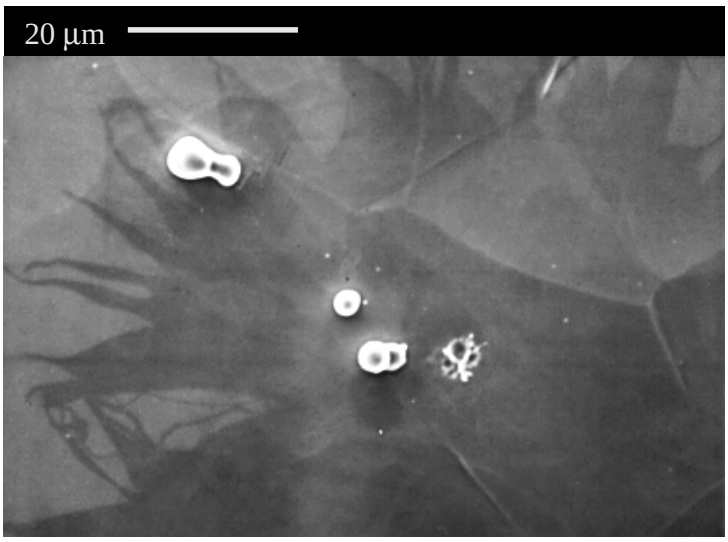

Figure 5.34: A field emitter found in a 5.8 GHz mushroom cavity. The previously molten iron particulate to the top left is too large to have been ejected by the craters, and it is likely that it was melted by the same plasma that produced the starburst.

This simple calculation therefore demonstrates that the field emission current cannot melt large particles, even if they are in bad thermal contact with the rf surface. Calculations show that another loss mechanism involved in field emission, Nottingham heating, is also incapable of supplying the energy needed to melt the emitter. [131]

Should melting nevertheless occur, the experiments described in Reference [130] demonstrated that the contact resistance drops dramatically when the particle begins to melts at its base, thereby preventing the melting of the entire particle. We made a similar observation with a copper particle described later in Section 7.2 (Figure 7.13). In that case, the base of the particle was melted by rf heating[17], yet the rest of the particle remained solid.

Our estimates show that the field emission current alone is incapable of melting anything more than the very local environment, such as a microtip. Certainly structures like as those in Figure 5.33 *cannot* be created by Joule losses if $j_{\mathrm{FN}} \leq 10^{12}$ A/m^2.

5.5.4 Refined model of the evolution of field emission

If the field emission current is unable to melt large particles and large areas of the niobium surface, what is the source of the power dissipation?

When considering this question, the starbursts found around active emission sites that progressed beyond the initial melting stage give us a vital clue. The plasma must, in fact, play an important role in the final stages *before* rf processing. Evidence from microscopy studies that followed mushroom cavity tests also substantiate this claim. For example, Figure 5.34 depicts a 100 μm starburst centered on small craters found in this cavity. Molten stainless steel was found at the periphery of the starburst. These particles are clearly too large to have originated from the craters, yet evidently had melted. It is

[17]Note that, unlike field emission heating, rf heating can supply milliwatts of power.

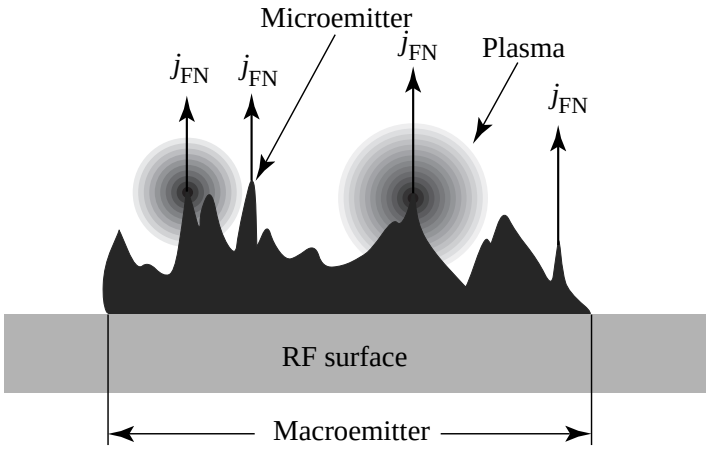

Figure 5.35: Schematic drawing illustrating a region of enhanced field emission (macroemitter) which is predominantly emitting from small areas within (microemitters). Due to the intense heating at the microemitters, neutrals are being desorbed and are ionized by the emission current.

unlikely, that the particles would melt at the same time the central crater was created, unless some mechanism linked the two events. The plasma that was responsible for the starburst formation provides such a common link. As we will show, it is capable of melting particles by enhancing field emission and by ion bombardment.

To explain the source of this plasma and its effect on the emitter in the absence of a processing event (as in Figure 5.32) we propose to modify the three step model of the evolution of field emitters by introducing the important effects created by the plasma. A qualitative description of the model is developed here. In the next chapter we then attempt to quantify certain aspects of this model with a simulation program called MASK.

For convenience we will refer to a region of enhanced field emission as a "macroemitter." An example would be one of the stainless steel particles in Figure 5.4. It is reasonable to assume that several sites on such a particle, which we will call "microemitters", are capable of field emission. However, the enhancement factor (β_{FN}) varies locally and since emission is exponential in field, a few (or perhaps only one) microemitters dominate. This situation is illustrated in Figure 5.35.

Once the current density exceeds a threshold of about 10^{11} A/m^2, individual microemitters melt and cease to emit.[18] The stainless emitter in Figure 5.4 was at that stage when the rf test was ended. However the overall emission characteristics of the macroemitter are only slightly changed because a number of microemitters may be active simultaneously. This "pre-processing" explains why, on occasion, the emission current reduces a little when the fields in the cavity are raised for the first time. (See, for example, Figures 5.25 and 5.26.)

Due to the heating, neutral matter outgases or desorbs from the surface and a gas cloud builds up in the vicinity of the emitter. Common adsorbates in cavities are water,

[18] One may argue that an emitter that becomes hot enough to melt will continue to emit thermionically, even if the field enhancement is small. However, even at the melting temperature of niobium (2740 K), the thermionic current density is many orders of magnitude lower than the field emission current densities observed. [132, 133]

hydrocarbons, hydrogen and carbon dioxide. [95] Material from the bulk of the melting microemitter will also contribute to this gas. The density near the emitter depends critically on the temperature of the microemitter, the surface condition of the emitter and the surrounding area, and its response to deposited energy on submicrosecond time scales. Very high gas densities are possible. If a single monolayer (2×10^{19} m^{-2}) of adsorbates is desorbed in 0.1 μs, the density will be on the order of 2×10^{23} m^{-3} (at temperatures of ≈ 1000 K). The gas density declines rapidly with increasing distance from the emitter, and the length scale of the high density region is set by the size of the microemitter (i.e., where most of the neutral gas release occurs).

At typical field levels in cavities (30 MV/m), emitted electrons gain 30 eV within a micrometer of the rf surface. At this point they are able to ionize most gases. Almost all ionization occurs at distances less than a few micrometers from the rf surface, because the product gas density $\times$ ionization cross-section[19] is maximized in this region. The region of ionization is moved even closer to the rf surface if the electric field is enhanced by the emitter geometry. Little difference of the cross-section exists between most elements, apart from the noble gases and very light elements. To first order the ionization process should therefore be independent of the emitter composition.

The newly created ions, in turn, are accelerated by the fields towards the macroemitter and upon impact produce further heat and release more neutrals. This process provides positive feedback for the evolution of gas. If individual microemitters explode, the neutral gas density is further enhanced and a starburst may be produced while the macroemitter is still active.

Since the ions are much heavier than electrons, they move at most a few micrometers in one rf cycle. Consequently, most are "trapped" near the emitter, leading to a rapid buildup of positive charge. Because of the proximity of the positive ion cloud to the rf surface, electric fields far in excess of the externally applied field can develop, and a drastic enhancement of the field emission current results.

The positively charged cloud also serves to neutralize the increased emission current, that otherwise can be limited in magnitude by space charge effects. In the absence of any screening, the original Fowler-Nordheim equation (Equation 3.2) is known to breakdown for $E > 6$ GV/m (when j_{FN} approaches 3×10^{11} A/m^2), the reason being that the self field of the current inhibits additional field emission (space charge effects). [54, 134, 135] This effect is even more pronounced for enhanced field emission described by Equation 3.3 because the current density is high but $E \ll 6$ GV/m, so that relative to the applied field the current's self field is stronger. Hence, space charge can limit the current density to considerably less than 10^{12} A/m^2 (we return to this matter in Chapter 6). In such a situation the screening by newly created ions can have a dramatic impact, allowing stronger field emission than would otherwise be possible.

Furthermore, the electric field of the ions prevents the emission beam from expanding radially as it passes through the ion cloud. In this manner, the production of new ions is concentrated in the volume nearest to the emitter where the positive space charge is most effective at enhancing the emission process.

If sufficient positive charge builds up in the ion cloud, electrons are captured to produce a quasi-neutral plasma. To maintain neutrality, a potential between the plasma and the rf surface develops that inhibits the flow of the very mobile electrons back to

[19] For most gases, the cross-section peaks between 15 and 100 eV.

the surface (sheath formation). [136] Sheaths are a general characteristic of a plasma in contact with a conductor. The electric field in the sheath is of order of [137]

$$E_{\mathrm{s}} = \sqrt{\frac{n_{\mathrm{e}} k_{\mathrm{b}} T_{\mathrm{e}}}{4\epsilon_0}} \ln\left(\frac{M_{\mathrm{i}}}{2\pi m_{\mathrm{e}}}\right). \tag{5.12}$$

Here n_{e}, T_{e}, and m_{e} are the electron density, temperature, and mass respectively, and M_{i} is the ion mass. Depending on the plasma conditions that prevail, this field can be very substantial and enhances field emission much beyond its steady state value. In fact, we will show in the next chapter that the fields can be so high that significant emission even takes place from surfaces for which $\beta_{\mathrm{FN}} \leq 10$ ("natural" or "genuine" Fowler-Nordheim field emission). Previously non-emitting areas of the macroemitter that come into contact with the plasma can then emit. Thus the melting of microemitters does not necessarily arrest the emission process, because enhancement mechanisms such as those described by the MIM or tip-on-tip model are no longer needed for emitter activity once a dense plasma forms. *It is this particular effect of the plasma that appears to be critical in bridging the gap between the initial melting of microemitters and the ultimate melting of the entire macroemitter.*

Given our new model, we see that the plasma serves three primary purposes:

1. *Field enhancement* The plasma enhances the electric field near the rf surface. The field emission current, which scales exponentially with the electric field, is therefore augmented very substantially. Since the ohmic power dissipation increases quadratically with I_{FN}, the emitter temperature rises enormously, and much more neutral gas evolves and becomes available for ionization.

2. *Ion bombardment* The heavy ions in the plasma are accelerated towards the rf surface and upon impact release even more gas and charged particles. They also raise the emitter temperature.

3. *Charge neutralization* The plasma neutralizes the emission current to eliminate space charge effects that otherwise would limit the emission current density to less than 10^{11} – 10^{12} A/m^2.

Critical to this model is the fact that it contains a powerful positive feedback loop for the production of new ions. In other words, once the creation of ions becomes significant, the process is self amplifying and an exponential growth of the plasma density is expected. Thus, not only are we dealing with a highly non-uniform plasma, but the entire process is also very non-stationary.

Ultimately, the effect of the plasma is to dramatically increase the power dissipation in the field emitter, be it by field emission Joule losses or ion bombardment. Eventually, the power deposition is so great, that the entire macroemitter melts and explodes (rf processes). It is then no longer capable of enhanced field emission at the usual cavity operating fields.

The energy required to maintain this rapid plasma production, current growth and increase in dissipated power is taken from the energy stored in the cavity fields, which quickly decays. Hence we always observe that the fields collapse during successful rf processing. In the next chapter, simulations will show that processing events can take place in much less than 1 μs!

To summarize, we elaborate on the simple sequence of events listed earlier that were thought to lead to rf processing. But now we add some important modifications due to the role played by the plasma.

1. *Pre-melting* At low fields, emission is active from individual microemitters and degrades the cavity quality. The current density is insufficient to melt (and alter the appearance) of the emitter.

2. *Melting* As the electric field is raised the current density increases exponentially. When it exceeds about 10^{11} A/m^2 microemitters begin to melt. Neutral gas evolves from the emitters and expands freely.

3. *Ion production* Shortly after the gases are released, electron impact ionization begins near the emitter. The heavy ions don't move far in an rf period and accumulate in the vicinity of the emitter. Eventually electrons are captured and a plasma is formed.

4. *Current growth* Provided the density is high enough, the ion cloud results in field enhancement, emission current neutralization and bombardment of the rf surface. Even low β_{FN} regions of the macroemitter that come into contact with the plasma begin to emit. All of these effects serve to augment the total emission current, the power dissipation, and the gas/ion production. A limit is only set by the energy stored in the cavity at the onset of rf processing.

5. *Explosion* Due to the positive feedback loop that is created, the macroemitter temperature rises very rapidly and ultimately the complete emitter melts/explodes.

The entire feedback loop is also summarized in Figure 5.36.

5.5.4.1 Current threshold

Based on the five stages of field emission discussed in our revised model, we can identify two important thresholds that need to be exceeded for rf processing to take place.

First, individual microemitters have to melt. To satisfy this condition, the emission current density needs to be greater than about $j_{\mathrm{min}} = 10^{11}$ A/m^2 based on calculations discussed in Reference [63]. However, once the emission current density does exceed j_{min}, a sufficiently dense plasma is needed to actually bring about rf processing. This second requirement implies that the ionization rate of the local gas by the emission current has to exceed a minimum value. Equivalently, one can identify a threshold emission current I_{min} that needs to be exceeded before rf processing can occur.

It is important, at this time, to distinguish between the simple three step processing model reliant entirely on Joule heating and our new model which includes important plasma effects. In both cases, a current density threshold exists, based on the requirement that the emission site melt. However, a current threshold does *not* exist in the old, three step model since it relies completely on Joule heating by the emission current to bring about an explosion.

To determine the current threshold, it is convenient to plot the maximum current drawn from a number of the field emitters we studied versus the current density.[20] Such a plot is shown in Figure 5.37. In the graph we distinguished between emission sites

[20] We are assuming here there is at least some correlation between j_{FN} and the true current density.

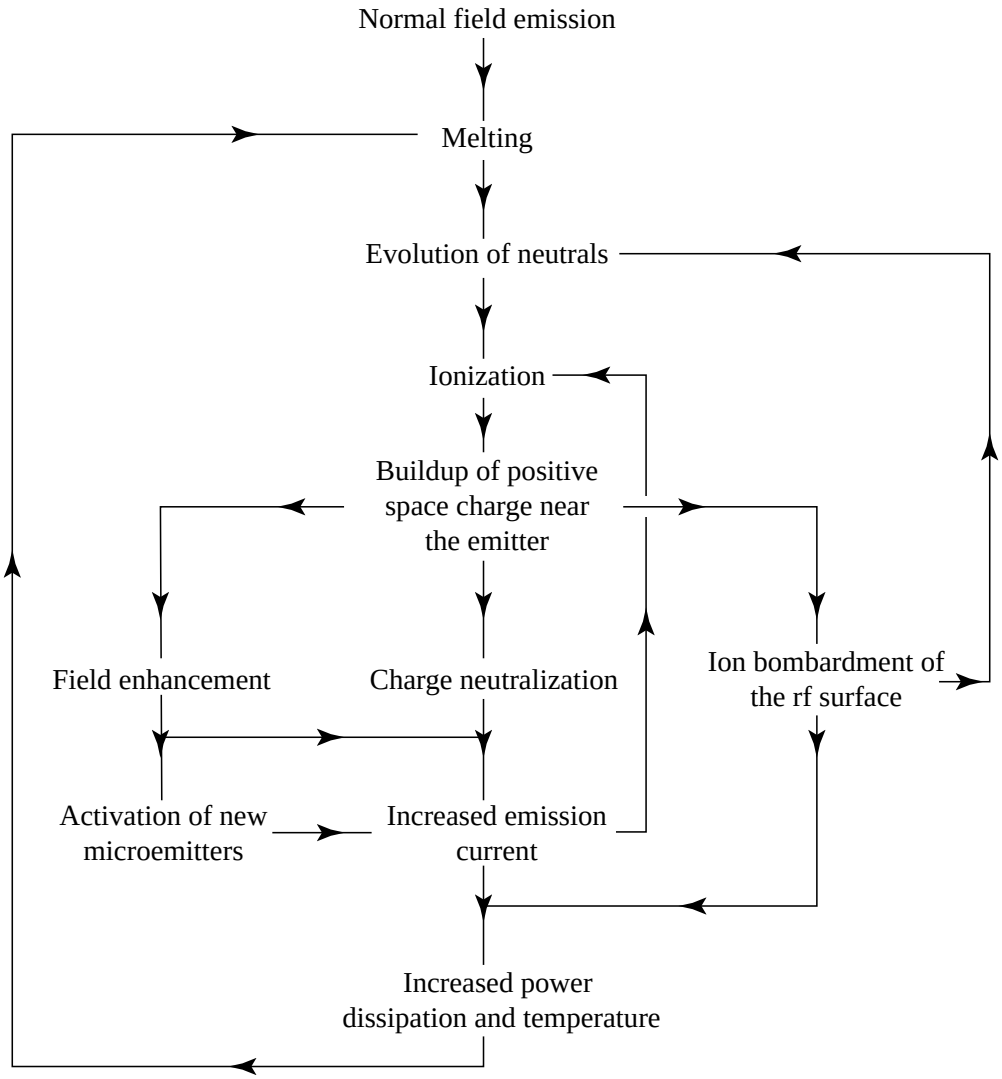

Figure 5.36: Flow chart of the feedback loop leading up to rf processing.

that had a starburst and those that did not. The latter category includes emitters that showed up in the temperature maps, but not in the SEM. We were unable to clearly identify these emitters in the SEM at their predicted location because they showed no melting or plasma features.

Since plasma production and rf processing go hand in hand, current density and total current thresholds apply equally to starburst formation. The latter threshold may be a little lower than $I_{\min}$. Emitters that lie in the upper right hand quadrant of Figure 5.37 satisfy these conditions.

The current density threshold appears to be indeed about 10^{11} A/m^2 in agreement with References [22, 63, 69, 122]. The current threshold we observe is on the order of 0.05 mA, although the threshold for rf processing should be slightly higher. At present, though, our statistics are insufficient for us to be able to extract a reliable value.

A total current threshold $I_{\min}$ was also observed in 3 GHz high pulsed power ex-

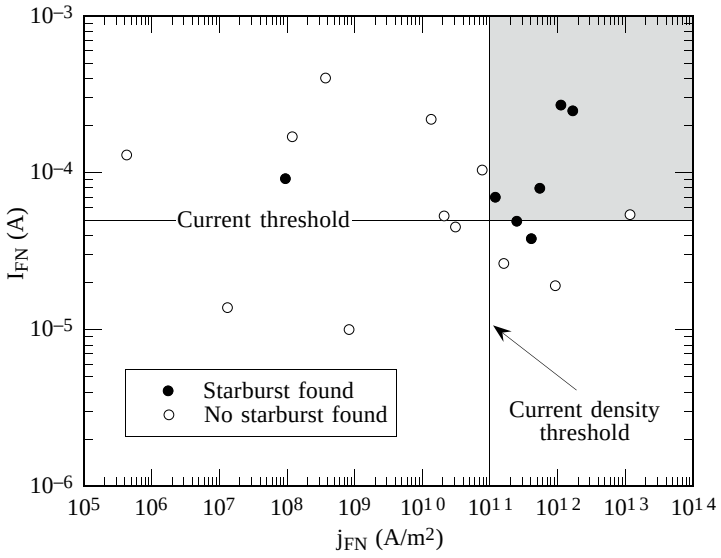

Figure 5.37: Plot of the peak current recorded during an emitter's "life" versus the peak current density observed. All emitters that created a starburst are marked by solid circles.

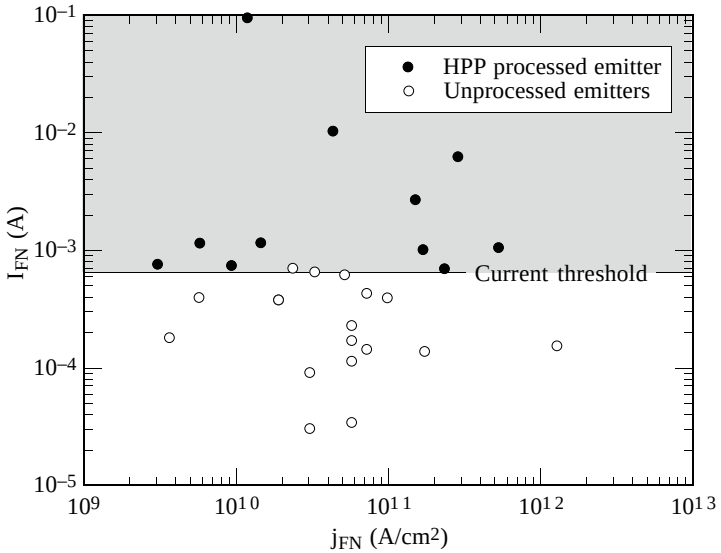

Figure 5.38: Plot of I_{FN} versus j_{FN} obtained by extrapolating cw values to fields achieved during high power processing of 3 GHz cavities during experiments described in Reference [17].

periments [17], although its underlying cause remained a mystery at the time. In these experiments, the β_{FN} and A_{FN} parameters of emitters were measured at low power during cw operation of the cavity. Using these values an estimate was then obtained for the current and current density achieved during the application of high pulsed power (that drove the cavity fields much higher than was possible with cw power). A distinction is made between emitters that successfully rf processed and those that did not (see Figure 5.38).

The results suggest that the processability of an emitter depends on the peak current

achieved. In this case a threshold of 0.6 mA seems appropriate. This value is higher than the one we obtained from our data. It is possible that the discrepancy is due to the fact that a slightly higher current is required to process an emitter than to create a starburst. Differences may also be due to the higher cavity frequency (3 GHz versus 1.5 GHz). However, we consider it likely that the indiscriminate application of the Fowler-Nordheim equation at high fields using β_{FN} and A_{FN} values obtained at low fields to be incorrect, because (a) space charge effects will reduce the emission current, and (b) changes in β_{FN} and A_{FN} can occur at intermediate field levels. Thus the currents achieved during high pulsed power processing possibly were lower than the estimated values.

It is interesting to note that a current density threshold is not apparent in Figure 5.38. This is likely to be an artifact of the simpler analysis of the thermometry data, which was performed differently to ours. In all cases β_{FN} was not included in the $v(y)$ and $t(y)$ functions in Equation 3.3. Hence the j_{FN} values (but not the I_{FN} values) obtained in Reference [17] are all underestimated by *at least* a factor of 10. If β_{FN} had not been omitted, most, if not all, emitters shown in Figure 5.38 would lie above the threshold of $j_{\min} = 10^{11}$ A/m^2 that we observed.

5.5.5 Supporting evidence

5.5.5.1 Helium processing

In Sections 5.3.2 and 5.5.1 we showed that the presence of helium in the cavity when rf power is applied can affect the emission characteristics of emitters, especially those that are known to have been activated by gases. In some cases, the emitter becomes stronger (for example Figure 5.14). In many cases, though, a reduction or the complete elimination of field emission was observed (for example Figure 5.20). In the latter example we showed that the reduction in field emission was not abrupt, but took place over a period of 20 seconds.

In these and similar cases, microscopic searches to locate the emission sites proved futile, showing that helium processing was not due to an explosive event. Instead, we suspect that the bombardment of the emitter by helium ions had resulted in subtle (and in some cases reversible) changes to the rf surface, be it by gas desorption, adsorption or ion implantation. These changes were sufficient to reduce or enhance field emission, although the effect may not always be permanent.

There is, however, another distinct category of helium processed emitters we have not yet mentioned, that lends support to our new emitter processing model. In several cases, a permanent and very abrupt (subsecond) extinction of field emission by helium processing was recorded. Subsequently large molten regions were found in the SEM.

Two such emitters are shown in Figures 5.39 and 5.40. In both cases a very large area of molten material is present at the center of a starburst. No foreign materials were detected by the usual EDX analysis in either case. Their appearance is very similar to that of rf processed emitters. For the first time we have, therefore, been able to definitively prove that helium processing can also extinguish emitters by an explosive process akin to rf processing.

The temperature data recorded for the first emitter is shown in Figure 5.41. Prior to helium processing the electric field was raised to 17.4 MV/m. About 1 mtorr of helium

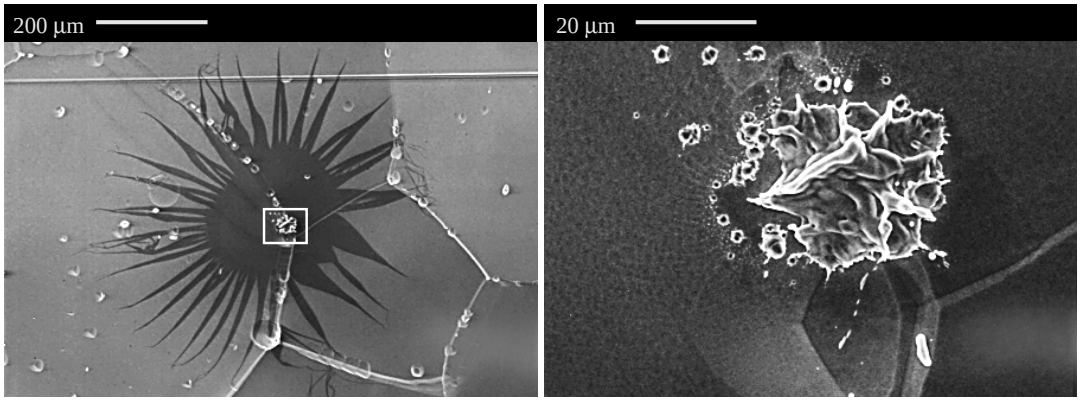

(a) (b)

Figure 5.39: Emitter that helium processed in cavity LE1-20 at 17 MV/m. No foreign materials were detected by EDX analysis. The temperature data is shown in Figure 5.41.

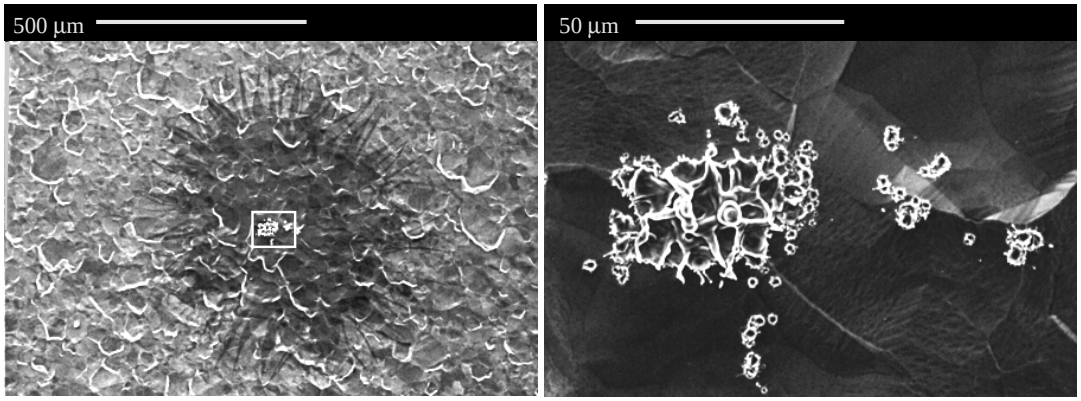

(a) (b)

Figure 5.40: Field emitter that helium processed in cavity LE1-17 at 25 MV/m. No foreign materials were detected by EDX analysis.

gas (measured at room temperature) was then administered slowly to the cold cavity and rf power was applied. *At no time during helium processing did the applied power exceed levels prior to helium processing.* Nevertheless, when rf power was applied to the cavity, an abrupt (subsecond) processing event was recorded, similar to that seen during rf processing, and the cavity fields collapsed.[21] Helium processing completely eliminated the emission. No new field emission activity was detected following the processing event. Even a thermal cycle to room temperature failed to reactivate the emitter.

From the SEM photographs, we see that in both cases[22], helium processing had a destructive and permanent effect on the emitters. The extensive melting must have occurred during the helium processing rather than before, since we did not observe any

[21] This situation is to be contrasted with the gradual processing observed with the emitter in Figure 5.21 during non-destructive helium processing.

[22] The second site was helium processed in the same manner.

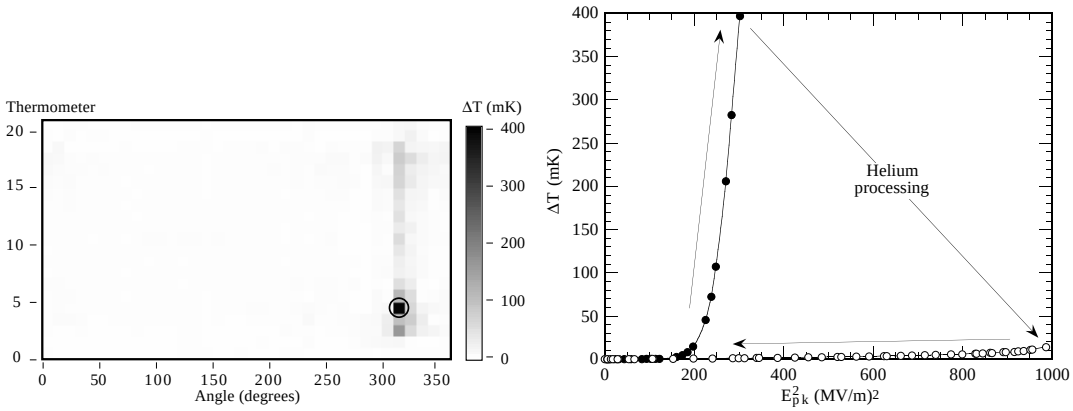

(a) (b)

Figure 5.41: (a) Temperature map obtained at 17 MV/m with cavity LE1-20 prior to helium processing of the emitter at 310°. (b) Temperature signal recorded at the circled site.

rf processing.

The SEM micrographs suggest that the mechanism responsible for helium processing is identical to rf processing. In some cases rf processing may be limited by too little ion production, because either the neutral gas density or the emitted current (or both) is too low. However, the admission of helium gas to the cavity increases the rate of ion production by augmenting the gas density (directly or by additional ion bombardment). The emitter then is able to process. Hence, this type of helium processing serves to precipitate the processing event by artificially increasing the ion production. The success of helium admission in triggering the explosive event demonstrates the important role played by ions during rf processing.

5.5.5.2 Satellite craters

Frequently, many small craters in a circle near a central emitter are found in rf cavities (see Figures 5.39 and 5.42) and in dc discharge experiments [138]. These are also explained by plasma enhanced field emission. Small defects or particulates are likely to exist in the vicinity of a macroemitter and provide emission centers that activate when the plasma from the central emission site envelopes them. Liquid drops, ejected from the central emitter by the plasma pressure, as in Figure 5.28(b), will also serve as new emission sites in the high fields created by the plasma.[23] Microtips can also be created due to stretching of liquids in the presence of a strong electric field and have been observed in dc field emission. [68] The central "bulb" in Figure 5.40 suggests that such stretching occurs during rf processing as well. Geometric field enhancement in excess of $\beta_{\mathrm{FN}} = 10$ can result from this stretching mechanism. [68] Any of these features are then potential sources of powerful field emission (provided a plasma is present to enhance the electric field), leading to the formation of "satellite" craters.

Auger and EDX analyses of field emitters in the past have shown that foreign ele-

[23] We have no evidence that these sites are capable of field emission at normal cavity fields ($E_{\mathrm{pk}} \approx$ 30 MV/m), when no plasma is present.

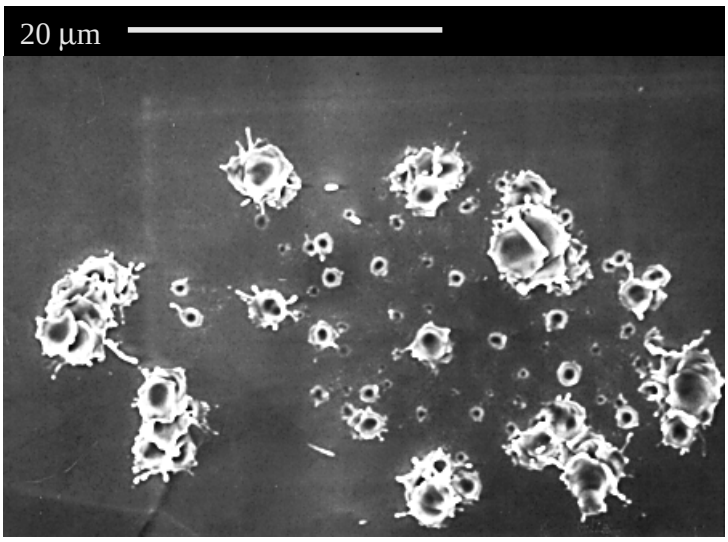

Figure 5.42: An example of craters in a 5.8 GHz mushroom cavity.

ments can always be found at the central emission site whereas in many cases satellite craters lacked contaminants. [65] This fact is consistent with the idea that satellite emitters become active due to plasma field enhancement, and therefore even simple geometric structures made of niobium or small foreign particles can emit. Any contaminants remaining after these sites explode are then very difficult to detect.

5.5.5.3 Starburst sizes

Further evidence of plasma activity *during* the rf processing stage is also provided by the observation that the starburst size scales inversely with the rf frequency (for the available data at 1.5 GHz, 3 GHz, and 5.8 GHz). The sizes of a number of starbursts are shown in Figure 5.43. Although there is a significant spread, the average starburst size shows the inverse frequency scaling.

Since the rf frequency governs the size of starbursts, they must be produced during the rf processing event, rather than afterwards, when the fields in the cavity have already collapsed. Our model of the positive feedback mechanism involving ion production suggests that plasma formation occurs in a very short time. Computer simulations presented in the next chapter, show that the duration of the explosive event can be as short as one rf cycle. The $1/f$ scaling of the starburst size could therefore be a direct consequence. An expansion velocity on the order of 10^6 m/s is then required to explain the observed starburst sizes. Such expansion rates are indeed predicted for electrons emitted from plasmas during dc discharges. [69]

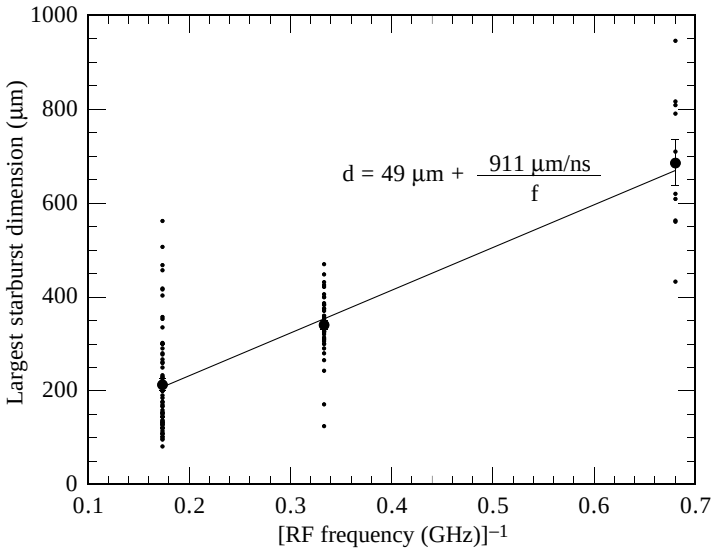

Figure 5.43: Maximum starburst dimension versus rf frequency, measured at 1.5 GHz, 3 GHz, and 5.8 GHz. The large solid circles represent mean values, and the small dots denote values for individual starbursts.

Chapter 6

RF processing by discharge

6.1 Introduction

In the previous chapter we proposed a revised model of rf processing. In this model, the ionization by the field emission current of gases evolving from an emitter and the resultant plasma production play a crucial role in melting large emission sites. The qualitative details of this model are discussed in Section 5.5.4.

In this chapter we will develop a more quantitative analysis of the model. However, an analytical treatment is exceedingly difficult, if not impossible, because of the many interdependent quantities involved, as was shown in Figure 5.36. For example, the magnitude of the field emission current depends on the electric field at the emitter. In turn the field is affected by the self-field of the electron current and by the ion cloud that builds up near the emitter due to electron impact ionization. However, the ionization rate again depends on the electron current and the neutral gas density in the vicinity of the emitter.

These problems are exacerbated by the fact that the region of interest is very small (10's of microns), yet includes all four states of matter, with very high temperature, density, and electric field gradients. In addition to all this, rf processing events are highly non stationary, due to the short time scales involved.

A more fruitful approach therefore is to simulate the field emission process numerically using small time steps and a discrete mesh to approximate the region of interest. Nevertheless, even in this case, the task is formidable and many simplifying assumptions need to be made. As we already demonstrated in the previous chapter with the microscopy data, rf processing is characterized by an instability. This is also confirmed by the simulations to be presented. These simulations were therefore only designed to yield order of magnitude estimates for the parameters describing the rf processing mechanism.

For the most basic computations, a code is required that calculates the fields in the simulation region self consistently, i.e., it takes into account both the boundary potentials and the charges in the simulation region.[1] Essential, also, is the ability to include a neutral gas that can be ionized by the emission current, thereby providing a source of positive ions. Fortunately, the recombination of electrons with ions can be safely ignored because recombination rates at the plasma densities we will encounter are much smaller than ionization rates (this will be shown shortly).

[1] Such programs are known as "particle-in-cell" codes.

When setting up the simulation problem, several different length scales need to be taken into consideration:

1. *Emitter size* Most microemitters appear to be about 0.5 μm or less in diameter. For accurate simulations, the mesh has to resolve this distance.

2. *Distance to the ionization region* When the emission electrons are accelerated by the applied field they gain about 30 eV within a distance as small as 1 μm. At this point they are capable of ionizing most gases. To be able to accurately simulate ionization, the mesh has to be finer than this distance. Once field enhancement due to ions commences, ionization occurs much closer to the rf surface, and the mesh needs to be considerably finer still.

3. *Size of ionization region* We need to ensure that most ionization occurs within the simulation region. In other words, the gas density should be low at the edge of the region furthest from the emitter, or the electron energy there has to be too high for ionization (or both). For an electric field of 30 MV/m, this requirement is easily satisfied for distances greater or equal to 30 μm.

4. *Extent of the plasma cloud* The ion cloud being created near the field emitter expands with time. The size of the simulation region has to be larger than the size of this cloud to minimize the impact of the (artificial) system boundaries on the field distribution. Due to computational limitations, our simulations can only cover a few rf periods. In this time, the cloud expands no more than a few micrometers.

All four length scales require simulation regions less than a few 10 μm in size. No benefit is gained by simulating the entire cavity (which would have been a hopeless task). Fortunately, on the micrometer scale we can safely ignore the curvature of the cavity wall. Thus the cavity fields, in the absence of field emission, are uniform[2] as in a parallel plate capacitor.

As it turns out, the requirement placed on the mesh density is quite stringent. Both items 1. and 2. require mesh spacings of a fraction of a micrometer. On the order of 10^4 mesh elements are needed to cover the entire simulation region. More critical still, is the fact that no particles are permitted to traverse more than one mesh element in a time step for the field solver to function. The electrons are by far the fastest, reaching speeds of 10^7 m/s. Thus time steps no larger than about $dt = 10$ fs can be taken! This fact seriously limits our ability to simulate rf processing for more than a few rf cycles, especially in the presence of field enhancement by the ions. Hence, in all cases our simulations are ended well shy of the ultimate processing event. The best we can hope to do, is to gain information on the ignition phase of rf processing.

6.2 Description of MASK

The code we chose to simulate field emission is called MASK which ran on an IBM RS/6000 workstation. The original version was developed by Science Applications International Corporation (SAIC). This FORTRAN code contained several different types of electric

[2]Provided we ignore the geometry of the field emitter.

field solvers and particle-in-cell routines which could be employed "as is." Field emission modules were already in existence as well.

Algorithms to permit the tracking of neutral particles and the ionization of these by electrons were added in a collaborative effort with SAIC. Furthermore, an adaptive time step scheme was incorporated into the code, that automatically uses the maximum permissible time step throughout the simulation.

6.2.1 The simulation setup

For the simulations we used a cylindrically symmetric parallel plate arrangement (gap length d, radius R) as shown in Figure 6.1. The emitter is located on axis on the left plate. Because of rotational symmetry about the emitter, a 2 dimensional simulation in the z–ρ plane suffices. The z–ρ plane is divided into $m \times n$ mesh elements. Various quantities relevant to the simulation, such as the electric field and charge density are evaluated at discrete time intervals at grid points which coincide either with the corners of the mesh elements, or with the half way points of the mesh elements' sides, or with the center of the elements (which of these depends on the quantity being considered). All quantities are assumed to vary linearly between grid points.

Both ions and electrons are simulated by discrete "macroparticles" (neutral particles are handled in the same fashion). A macroparticle of charge $w_s Q_s$ and mass $w_s M_s$ represents w_s true particles of specie s which each have charge Q_s and mass M_s. The "weights" w_s of the macroparticles are chosen so that the total number of macroparticles in the simulation is computationally manageable. Generally, MASK can cope with several 10,000 macroparticles at a time. It is desirable to have more than one macroparticle in each mesh element, within the region of interest.

6.2.2 Modeling field emission

The field-emissive area, radius $r_{\rm em}$, is located on axis on the left boundary. Particulate features were not included and therefore no enhancement of the electric field due to geometry occurs. The emitted current density is given by:

$$\begin{aligned} j_{\rm M} &= A_{\rm M} E_{\rm em}^2 \exp\left(-\frac{B_{\rm M}}{|E_{\rm em}|}\right) \qquad \text{when } E_{\rm em} < 0 \\ &= 0 \qquad\qquad\qquad\qquad\qquad\quad \text{when } E_{\rm em} \geq 0, \end{aligned} \tag{6.1}$$

where $E_{\rm em}$ is the instantaneous electric field at the emission site, and $A_{\rm M}$ and $B_{\rm M}$ are constants supplied by the user to the field emission routine. By referring to Equation 3.3, one finds that $A_{\rm M}$ and $B_{\rm M}$ are related to the Fowler-Nordheim parameters $A_{\rm FN}$ and $\beta_{\rm FN}$ by

$$A_{\rm FN} = 2.6 \times 10^6 \text{ V}^2/\text{A} \times \frac{\pi r_{\rm em}^2 A_{\rm M}}{\beta_{\rm FN}^2} \tag{6.2}$$

$$\beta_{\rm FN} = \frac{5.464 \times 10^{10} \text{ V/m}}{B_{\rm M}}, \tag{6.3}$$

where we have assumed $v(y) \approx 1$ and $t(y) \approx 1$.

Early into test runs of MASK, we encountered an unphysical situation due to the discrete time steps used. At high electric fields (above 100 MV/m) the current crossing

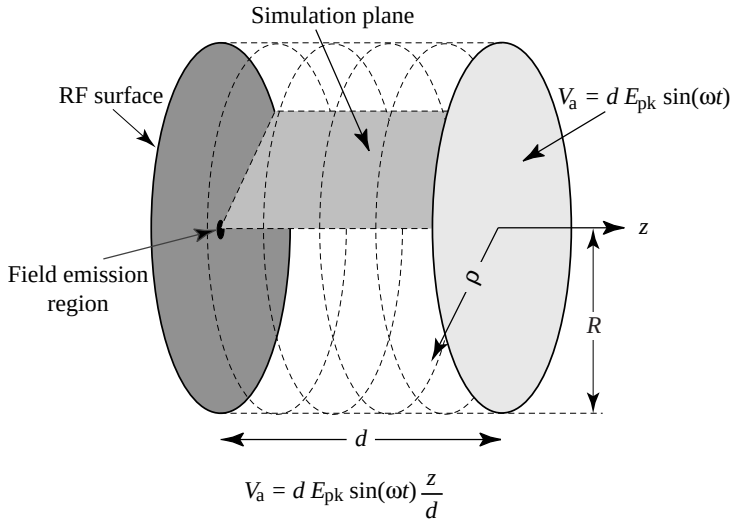

Figure 6.1: Parallel plate capacitor arrangement used to simulate field emission in cavities.

the plane of the rf surface would oscillate wildly between a large positive and a large negative value. The oscillation period was always 3 time steps, irrespective of the actual value of dt. A likely explanation of this unphysical phenomenon is as follows: Due to the exponential nature of field emission, a huge charge is emitted at high electric field in one time step . The following computational step, the field solver recalculates the fields while taking into account the negative charge just emitted. Space charge effects due to the previously emitted charge now far outweigh the applied field, so that the electric field changes sign near the rf surface. As a result, no new charge is emitted, and instead the electrons emitted the previous time step slam back into the rf surface. Stepping ahead again, no electrons are left in the simulation region so that the emitter "sees" the full applied field. Hence the entire process repeats. The oscillations we observed are therefore a direct result of the discrete time steps taken by MASK. To avoid this problem, we needed to artificially constrain the field emission current. We found it convenient to cap the field emission current at such a value that E_{em} never reverses sign due to the emitted charge.

An infinite sheet of electrons, areal density Σ_q, opposite an infinite planar, metallic surface produces an electric field E_q, where

$$E_q = \frac{\Sigma_q}{\epsilon_0}. \tag{6.4}$$

We therefore adopted the pragmatic approach, that at each time step the emitted charge may not exceed a value of

$$q_{\max} = \gamma_q \pi r_{\mathrm{em}}^2 \Sigma_q = \gamma_q \epsilon_0 \pi r_{\mathrm{em}}^2 E_{\mathrm{em}}, \tag{6.5}$$

where γ_q is a user determined parameter on the order of unity. We found that for $\gamma_q \approx 1/5$ well behaved field emission is achieved at all field values encountered in simulations.[3]

[3]Greater values for γ_q can be used as well, but although no unphysical oscillations are encountered, the field emission current does become very noisy at high fields.

Note that for typical β_{FN} and A_{FN} values, the artificial limit imposed by (6.5) with $\gamma_q = 1/5$ does not come into effect until E_{em} exceeds typical cavity fields of 30 MV/m by more than 55 MV/m.

6.2.3 Electromagnetic fields

The externally applied field is spatially uniform. Hence, an oscillating potential V_{a} was applied to the right boundary at $z = d$. The left boundary, on which the emitter is located, was grounded (0 V). On the remaining side (along $\rho = R$) a linearly increasing potential between 0 V at $z = 0$ and V_{a} at $z = d$ was imposed. In all cases the applied potentials were allowed to evolve as

$$V(t) = V_{\mathrm{a}} \sin \omega_0 t, \tag{6.6}$$

where ω_0 was either $2\pi \times 1.5$ GHz or $2\pi \times 5$ GHz.

Any charges present in the simulation region affect the fields. Such source terms are taken into account by the field solver when calculating the electric field. Particles that cross the boundaries along $z = d$, $\rho = R$ and $z = 0$ are discarded. Hence the choice of d and R influences the outcome of the simulation in two ways; the electromagnetic field distribution is altered because of the artificially imposed potentials along $z = d$ and $\rho = R$, and charges which cross boundaries no longer contribute to charge and current source terms when solving for the electromagnetic fields. However, if the distance between the region of significant charge concentration and the boundaries at $z = d$ and $\rho = R$ is chosen to be reasonably large, then the effect of the boundaries is limited.

For the simulations we tried $d = 32 \rightarrow 128$ μm and $R = 8 \rightarrow 16$ μm. In all simulations presented later a 32×8 $\mu\mathrm{m}^2$ $(z \times \rho)$ region with 128×64 mesh elements was used. Increasing the size had a negligible effect on the outcome of a simulation, which usually was stopped once the charges spread half way to the boundaries.

For an applied field of 30 MV/m, which is typical of cavity fields during low power rf processing, the applied potential V_{a} is 980 V (for $d = 32$ μm). The field emitted electrons move at most at about $v_{\mathrm{e}} = 0.06c$, where c is the speed of light. The ratio R_{F} of the magnetic force F_H to the electric force F_E experienced by the electrons is at most

$$R_F = F_H/F_E = (v_{\mathrm{e}}/c)^2. \tag{6.7}$$

This ratio is much less than unity, and hence the magnetic field generated by the charges in the simulation region can be safely ignored. One should be aware of the fact, though, that once ionization of any neutral gas present takes place, charge neutralization of the electrons in the beam due to the ions occurs. In this case $R_F = v_{\mathrm{e}}^2/(f_q c^2)$, where f_q is related to the electron charge density ρ_{e} and the ion charge density ρ_{i} by

$$f_q = \left| \frac{\rho_i - \rho_e}{\rho_e} \right|. \tag{6.8}$$

The quantity f_q takes into account the reduction in the electric force due to screening of the beam by positive charges. Using the above parameters, we see that the electric and magnetic forces become comparable for $f_q \approx v_{\mathrm{e}}^2/c^2$. Later we will show that the magnetic forces can be significant enough to cause pinching of the emission current.

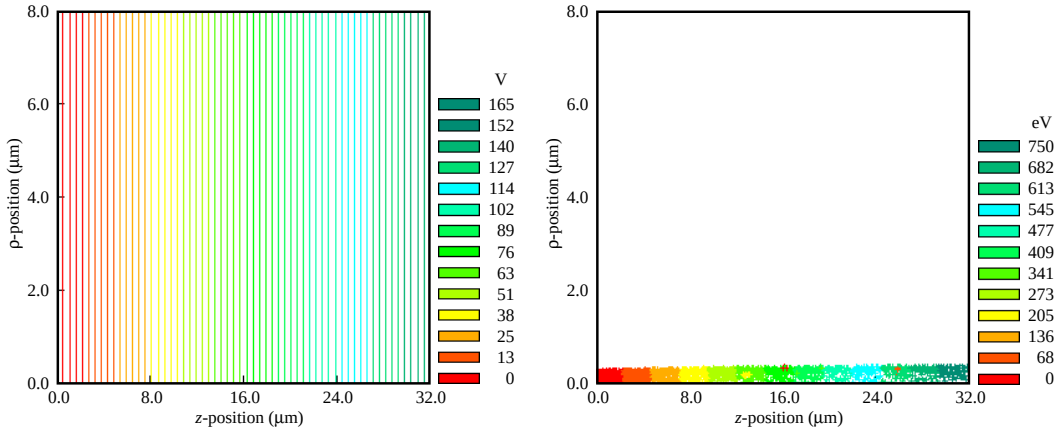

(a) (b)

Figure 6.2: Typical simulation setup: (a) Potential distribution in the simulation region due to the uniform, externally applied, electric field, (b) Injection of the field emission current into the simulation region. In the case depicted, the current's self field is significantly less than the externally applied field. Note that the aspect ratio is not 1:1 in these figures.

We also need to consider the externally applied rf magnetic field, i.e., the H_ϕ field of the TM_{010} mode. All the emitters we studied lie in the high electric field regions of the cavity (near the iris), where $E_{\rm em} \approx E_{\rm pk}$. In these areas $\mu_0 H_{\rm em}/E_{\rm em} \approx 1$ mT/(MV/m), so that at $E_{\rm pk} = 30$ MV/m the ratio of the electric to magnetic force due to the applied fields is $F_H/F_E = v_{\rm e}\mu_0 H_{\rm em}/E_{\rm pk} = 0.01 - 0.02$. Hence it is safe to ignore the externally applied rf magnetic field as well.

In our simulations we therefore only solved for the electric field. Since the electrons are non-relativistic, an electrostatic field solver was selected, allowing for significant computational time savings.

Figure 6.2(a) shows the potential distribution within the simulation region in the absence of significant numbers of charges. Similarly, Figure 6.2(b) depicts the injected field emission current which, in the case shown, is sufficiently low so that its self-field is not apparent.

6.2.4 Neutral particles

Neutral gas macroparticles (each of weight $w_{\rm n}$) can enter the simulation region from any point. To simulate the gas evolving from a melting emitter, we injected particles from the immediate vicinity of the emitter. The motion of these particles ("neutrals") is tracked by MASK as a function of time, and the code calculates the gas density at the mesh centers. In the simulations described here, neutrals were injected from a region, radius 1 μm, centered on the emission site. This size seems reasonable based on the picture of the molten microemitters in Figures 5.19 and 5.25(a). The injection of neutrals was modeled on the effusion of gas from a Knudsen cell. [139] We therefore used the following

velocity distributions [140]

$$g(v_\perp)\,dv_\perp = v_\perp \left(\frac{m_\mathrm{n}}{2\pi k_\mathrm{b} T}\right)^{1/2} \exp\left(-\frac{m_\mathrm{n} v_\perp^2}{k_\mathrm{b} T}\right) dv_\perp \qquad (v_\perp \geq 0) \tag{6.9}$$

$$g(v_\parallel)\,dv_\parallel = \left(\frac{m_\mathrm{n}}{2\pi k_\mathrm{b} T}\right)^{1/2} \exp\left(-\frac{m_\mathrm{n} v_\parallel^2}{k_\mathrm{b} T}\right) dv_\parallel. \tag{6.10}$$

Here $g(v_\perp)\,dv_\perp$ and $g(v_\parallel)\,dv_\parallel$ are the distribution functions for the particle velocity perpendicular and parallel to the rf surface respectively, k_b is the Boltzmann constant, m_n is the mass of the neutrals, and T is the temperature of the neutrals. The resultant flux distribution has a $\cos\theta$ profile, where θ is the angle to the normal of the rf surface. Plasma density distributions having a $\cos\theta$ density distribution have been observed in dc discharge experiments when discharge was initiated at a single spot. [121] In other cases, the outgassing of neutrals has been found to conform to a $\cos^n\theta,\ n > 2$ distribution. [139, 141] If the latter situation applies to our field emitters, then the simulations underestimate the gas density opposite an emitter at a given neutral flux.

Implicit in using the effusion distributions above is the assumption that the gas source at the rf surface is at an equilibrium temperature T, and we are dealing with a Maxwellian gas. Such a situation arises, for example, when outgassing occurs due to elevated temperatures.

For an ideal gas the pressure p of the gas source is related to the gas density n_n immediately at the rf surface by

$$p = n_\mathrm{n} k_\mathrm{b} T. \tag{6.11}$$

The flux F of effusing particles is

$$F = \frac{n_\mathrm{n} \bar{v}}{4}, \tag{6.12}$$

$\bar{v}$ being the mean particle velocity, which is related to the gas temperature by

$$\bar{v} = \sqrt{\frac{8 k_\mathrm{b} T}{\pi m_\mathrm{n}}}. \tag{6.13}$$

The flux of neutral particles leaving the rf surface can therefore be related to the pressure at the rf surface by

$$F = \frac{p}{\sqrt{2\pi m_\mathrm{n} k_\mathrm{b} T}}. \tag{6.14}$$

As an example, consider the effusion of 2000 K magnesium neutrals from a region, radius 1 μm, centered on the emission area. For a flux of 10^{27} m^{-2}s^{-1} the steady state neutral gas density near the emitter, as calculated by MASK, is shown in Figure 6.3. The maximum density recorded is 1.65×10^{24} m^{-3}, whereas the density at the rf surface according to (6.12) should be 3×10^{24} m^{-3}. The discrepancy of a factor of 1.8 is probably due to the fact that the mesh element closest to the rf surface extends out to 0.25 μm and because only a limited number of macroparticles can be used in the simulation, so that there are fairly large statistical variations in density from mesh element to element.

Note that a density of 3×10^{23} m^{-3} is very high; about 1/10 of an atmosphere at room temperature. It is difficult to determine whether such high densities really exist near field emitters on short time scales. No concrete measurements appear to have been carried out. In some of the dc vacuum breakdown literature, though, it is speculated

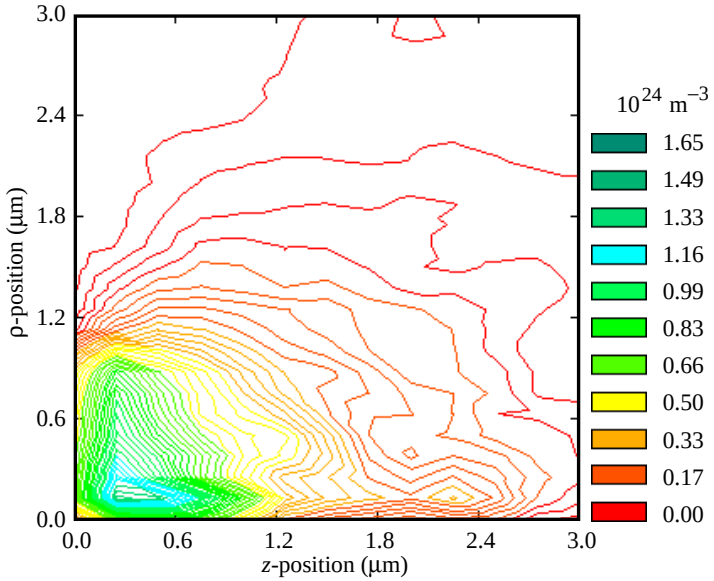

Figure 6.3: Density of magnesium gas effusing from the 1 μm region centered on axis at the left surface. The flux was 10^{27} $\mathrm{m^{-2}s^{-1}}$ and temperature of the effusing gas was 2000 K. Only the immediate vicinity of the field emitter is shown.

that densities as high as 10^{26} $\mathrm{m^{-3}}$ exist on nanosecond time scales. [22,70] We will return to this point later, during our discussion of field emission simulations.

6.2.5 Ionization and recombination

6.2.5.1 Ionization

The neutral gas in the simulation region is subject to electron impact ionization by the field emission electron beam. The ionization cross-section σ_{l+} of a gas "X" determines the rate of ion production of species X^{l+} (l = integer) by electrons via the process

$$e^- + \mathrm{X} \rightarrow (l+1)e^- + \mathrm{X}^{l+}.$$

We define the *total* ionization cross-section σ_t of an element X by

$$\sigma_\mathrm{t} = \sum_{l=1}^{\infty} l\sigma_{l+}. \tag{6.15}$$

Given the neutral gas density n_n and the electron density n_e, as well as the average electron velocity v_e in each mesh element, MASK is able to estimate the ionization rate. The rate per volume for process $e^- + \mathrm{X} \rightarrow (l+1)e^- + \mathrm{X}^{l+}$ is given by

$$\nu_{\mathrm{i},l} = n_\mathrm{n}\sigma_{l+}n_\mathrm{e}v_\mathrm{e}, \tag{6.16}$$

so that the total rate of positive charge production is

$$\sum_{l=1}^{\infty} l\nu_{\mathrm{i},l} = \sum_{l=1}^{\infty} l n_\mathrm{n}\sigma_{l+}n_\mathrm{e}v_\mathrm{e}. \tag{6.17}$$

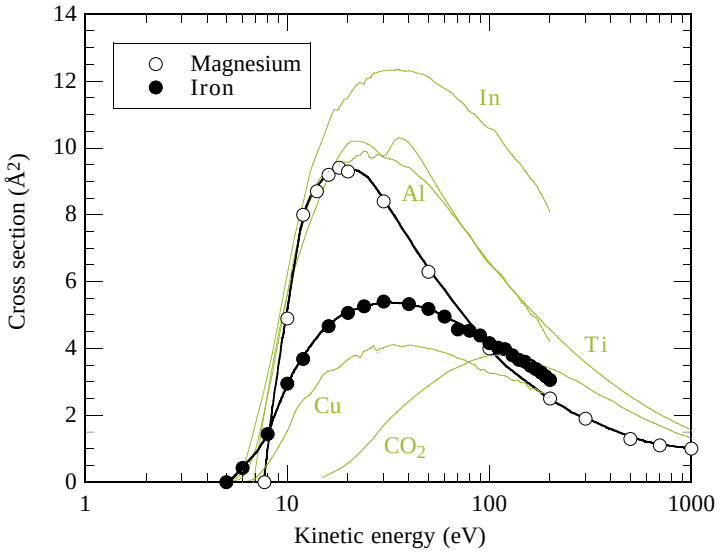

Figure 6.4: Total electron impact ionization cross-section data for magnesium [142], iron, copper, indium, aluminum [143], titanium [144] and carbon dioxide [145]. The cross-sections for iron and magnesium were used in MASK simulations. The others are included for comparison, to illustrate that within an order of magnitude, little differences exist.

To simplify the ionization routines, we chose not to treat each process in (6.17) separately. Instead, we ignored the fact that the charge to mass ratio of the ions produced by $e^- + \mathrm{X} \rightarrow (l+1)e^- + \mathrm{X}^{l+}$ scales as l. In that case the process $e^- + \mathrm{X} \rightarrow (l+1)e^- + \mathrm{X}^{l+}$ can be viewed as $e^- + \mathrm{X} \rightarrow l \times (e^- + \mathrm{X}^+) + e^-$ and we can use a single ionization rate ν_i in our simulations, where

$$\nu_\mathrm{i} = n_\mathrm{n} \sigma_\mathrm{t} n_\mathrm{e} v_\mathrm{e}. \tag{6.18}$$

In essence, we equated the rate of ion production with the rate of charge production. For all materials considered $\sigma_{1+} \gg \sigma_{l+}$ for $l > 1$ (i.e., $\sigma_\mathrm{t} \approx \sigma_{1+}$). Furthermore, the distances traveled by ions in our simulations are usually very small and hence the exact charge to mass ratio of the ions has little effect on the outcome of a simulation. Thus the penalty paid for using (6.18) is small.

The cross-section data as a function of electron impact energy for several elements was programmed in MASK (see Figure 6.4). Based on (6.18) the code continuously adds positive ions with a mass equal to that of the neutrals to the simulation region. These constitute additional source terms when computing the electric field.

Note that the ionization cross-section for many of the common materials found at field emitters in cavities (e.g., iron, indium, copper, and titanium) are very similar. Magnesium has been found in cavities on occasion as well, but not as frequently. For historical reasons many of our simulations were carried out with magnesium as the neutral gas. However, because the variation of the cross-sections is relatively small, the actual gas species being used has little bearing on the outcome of the simulation. Magnesium should thus be viewed as a generic gas in these simulations that can be replaced by any of the common metals found in cavities. Unless mentioned otherwise, we always used the magnesium cross-section in the simulations.

6.2.5.2 Recombination

Theoretically, recombination of electrons and ions to form neutrals should also be considered. The recombination rate per unit volume ν_r is given by

$$\nu_r = \alpha_r n_e n_i, \tag{6.19}$$

where α_r is the energy dependent *recombination coefficient* and n_i is the ion density. The ratio of the recombination rate to the ionization rate thus is

$$\frac{\nu_r}{\nu_i} = \frac{\alpha_r}{v_e \sigma_t} \frac{n_i}{n_n}. \tag{6.20}$$

Later we will see that for neutral densities of $n_n = 10^{24}$ m^{-3} (pressure ≈ 0.1 atm at 1000 K) the peak ion densities encountered in our simulations are about 10^{23} m^{-3}. Most of the ionization occurs at electron energies on the order of 30 eV, i.e. at $v_e \approx 3 \times 10^6$ m/s. Hence

$$\frac{\nu_r}{\nu_i} = 3 \times 10^{-8} \text{ s/m} \frac{\alpha_r}{\sigma_t}. \tag{6.21}$$

Recombination coefficients vary significantly with temperature and gas pressure and also depend on the gas specie. Furthermore, plasma conditions encountered in our simulations are non-stationary and highly non-uniform. It is therefore impossible to provide a single rate coefficient that applies in all cases. However, a literature search reveals that α_r peaks at atmospheric pressures at around 10^{-12} m^3/s (at 300 K) and declines very rapidly with increasing temperatures and decreasing pressures. [146–150] Values as low as 10^{-19} m^{-3}/s are recorded, although $\alpha_r = 10^{-13} \rightarrow 10^{-14}$ values are probably more applicable in our simulations. As a *very* conservative estimate we therefore considered $\alpha_r = 10^{-12}$ m^{-3}/s. Thus

$$\frac{\nu_r}{\nu_i} < 0.6. \tag{6.22}$$

This value represents an upper limit on the fraction and is very likely too large by at least one order of magnitude. Recombination effects therefore were of little concern in the simulations, and consequently they were ignored altogether.

We will also show below that the ion densities are at least one to two orders of magnitude lower than the neutral gas density. We therefore ignored the depletion of neutrals over time due to ionization. Furthermore, we only considered the neutral gas once a steady state density had been achieved. Hence, it was sufficient to calculate the neutral gas density in each mesh element once at the beginning of the simulation and then ignore any further motion of neutrals. This approach provided for a considerable savings in computation time. One should note, though, that this approach also assumes that the mechanism for neutral gas production is time independent. Later we will show, that this is not necessarily true and modifications are required.

6.3 Validation using Towsend discharge

Past tests have shown that simulations using MASK field solvers and charged particle routines agree with experimental results. [151,152] Since the ionization and neutral particle routines were only recently added, these still needed testing. Towsend discharge [148], which has been the subject of extensive experimental studies, was an obvious candidate for simulations because of its apparent similarity to our field emission simulations.

6.3.1 Theory of Towsend discharge

In their simplest form (and applicable here) Towsend discharge experiments consist of a voltage applied across two parallel plates separated by a distance d. The volume between the plates is filled with a gas at pressures on the order of 1 torr. An electron current I_0 is injected from the cathode into the gas-filled volume by bombarding the cathode with ultraviolet light. As the charges are accelerated by the uniform electric field, they ionize the background gas, thereby producing new electrons. The number (α_{T}) of new electron–ion pairs that are created in a distance dx is inversely proportional to the mean free path λ of the ionizing electron, i.e.,

$$\alpha_{\mathrm{T}} = \frac{\mathcal{F}(E\lambda)}{\lambda}, \tag{6.23}$$

where the function $\mathcal{F}$ depends on the energy gained by the electrons over the distance λ. The parameter α_{T} is known as the *first Towsend coefficient*. In a distance dx, n_0 electrons will, on average, create

$$dn = n_0 \alpha_{\mathrm{T}}\, dx \tag{6.24}$$

new electrons. The total electron current reaching the anode is

$$I(d) = I_0 \exp(\alpha_{\mathrm{T}} d). \tag{6.25}$$

We see that the injected current produces an electron avalanche. It is not self sustaining since it depends on the injection of charge at the cathode. One should also note, that (6.25) is only valid if (a) space charge effects due to the positive ions, which linger in the volume for a long time, are irrelevant, (b) ionizing events due to ions do not contribute significantly and (c) electron–ion recombination events are rare. Hence low injection currents are required.

The mean free path λ is inversely proportional to the gas pressure p. Thus one finds

$$\frac{\alpha_{\mathrm{T}}}{p} = \mathcal{F}\left(\frac{E}{p}\right) = \ln\left(\frac{I_0}{I(d)}\right)\frac{1}{pd}, \tag{6.26}$$

and consequently one normally plots α_{T}/p versus E/p.

6.3.2 Towsend discharge simulations

To simulate Towsend discharge with MASK we used an arrangement very similar to that described above for field emission simulations. Unlike the field emission simulations, the volume between the boundaries was "filled" with a uniform density gas (either helium or diatomic nitrogen) with densities ranging from 8×10^{21} m^{-3} to 3.3×10^{24} m^{-3}. The densities are comparable to those used later in the field emission simulations. Furthermore, the applied voltages were time independent, and the electric field solver ignored all charge source terms when calculating the electric field. In other words all space charge effects were eliminated. As a result, we could run simulations at significantly higher injection currents than used in Towsend discharge experiments, thereby reducing the short term fluctuations in the computed current reaching the anode (which result from the stochastic nature of ionization).

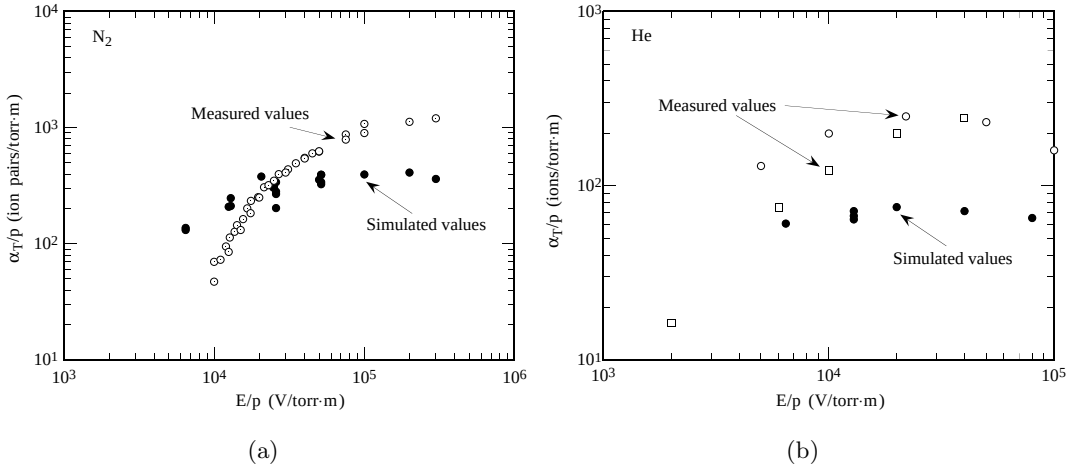

(a) (b)

Figure 6.5: Comparison of measured and simulated α_{T}/p values versus E/p for Towsend discharge in (a) diatomic nitrogen gas (b) helium gas.

The measured current at the anode was averaged over about 3000 time steps, which was approximately 25 times the time it took a single electron to travel the distance d. During the field emission simulations described later, E/p values around 4×10^5 V/(torr $\cdot$ m) were typical. Experimental data exists up to 3×10^5 V/(torr $\cdot$ m). We therefore concentrated our Towsend discharge simulations about these values.

Figure 6.5(a) compares the simulation results of α_T/p from (6.26) with measured data for nitrogen. [153,154] Similar data is plotted for helium in Figure 6.5(b). [147,155]

6.3.2.1 Nitrogen gas

In the case of nitrogen, the ion production is overestimated below $E/p \approx 10^4$ V/(torr $\cdot$ m) whereas above $E/p \approx 2 \times 10^4$ V/(torr $\cdot$ m) the ionization rate is underestimated by a factor of two to three. We believe that a dominant source of the discrepancy lies in our neglect of elastic and inelastic collisions (apart from ionization) between electrons and neutral particles. Inelastic collisions include, for example, the excitation of vibrational modes of the nitrogen molecules. Even the model of electron energy loss due to ionization used in MASK is very simple — after an ionizing event the electron energy is simply reduced by an amount roughly equivalent to the ionization potential of the gas. Hence the electron energy distribution in the simulation by no means reflects the true distribution in measured Towsend discharge. In reality one finds that, due to collisions, the thermal velocity of electrons is much higher than the mean drift velocity in the direction of the electric field. [156,157] In our simulations on the other hand, randomizing collisions are absent, so that only a drift term exists. What is the effect of this oversimplified energy distribution?

In all cases, the true mean electron energy is lowered by collisions that are absent in our simulation. Thus, at low E/p values only the high energy tail of the true distribution exceeds the ionization potential of the gas. Only a fraction of electrons are therefore available to ionize the gas. In nitrogen, for example, the average electron energy is 6.7 eV

at $E/p = 10^4$ V/(torr · m) [158][4] whereas the ionization potential of nitrogen is 14.5 eV. [159] Hence, many electrons are not able to ionize nitrogen when $E/p < 10^4$ V/(torr · m). In contrast, in our simulations every electron will eventually gain sufficient energy from the applied field to ionize the gas. It thus is reasonable to expect that below a value of about $E/p = 10^4$ V/(torr · m) the simulated current reaching the cathode exceeds the experimentally measured values.

The effect is reversed above E/p values of a few 10^4 V/(torr · m). Here collisions ensure that a significant fraction of the electron distribution remain within the range where the ionization cross-section of nitrogen is significant. Again this effect is not included in the simulations. The ionization cross-section of nitrogen begins to decline above 100 eV. If an electron in the simulations gains an energy greater than 100 eV, the probability of it causing ionization diminishes. Since ionization is the only loss mechanism included in the simulations, a large fraction of the electrons can have energies above 100 eV when the applied field is large, and it is not surprising that the α_T/p values for large E/p are lower than those obtained from direct measurements.

Other effects not included in the simulation may also contribute to the discrepancy at high E/p values, such as the release of electrons at the cathode by the impact of energetic ions. However, these are probably secondary effects.

6.3.2.2 Helium gas

Turning to the helium data, we see that both simulated and measured α_T/p values are five to six times lower at the highest E/p values than those for nitrogen. This observation is consistent with the fact that the peak ionization cross-section of helium is 5.5 times lower than that of nitrogen. The simulated and measured curves appear to cross at about $E/p = 3000$ V/(torr · m) — at a lower point than the nitrogen data. The indications are, that helium is less effective at absorbing energy from the electrons, based on the arguments presented above. Considering the absence of vibrational modes that can be excited in helium, this is not too surprising. At $E/p = 530$ V/(torr · m) the measured mean electron energy is already as high as 6.6 eV. [160]

Regarding our simulations of field emission (to be discussed next), E/p values below 10^5 V/(torr · m) are of little interest because they are not encountered in the ionization region. Thus the discrepancy below 10^4 V/(torr · m) between Towsend discharge experiments and our simulations are of no concern. However, the fact that the Towsend discharge simulations underestimated the α_T/p values above a few 10^4 V/(torr · m) may affect the field emission simulations because ionization rates are too conservative. This situation is mitigated by the fact that the path length of the field emission current through high density gas is at most a few micrometers (see Figure 6.3). Typical *peak* gas densities we will encounter are 2×10^{24} m^{-3} *or less*. At these densities, the electron mean-free-path is several micrometers, although it does vary with gas specie and electron energy. Thus the beam will undergo at most a few collisions as it passes through the gas, and elastic and inelastic collision should have little effect on the average beam energy. Hence the simulations of Towsend discharge are probably a far more stringent test of our

[4]Towsend's results being quoted here are known to be somewhat flawed due to mercury vapor contamination of the nitrogen he used for experiments. However the results are sufficiently accurate for estimating the effect of elastic and inelastic collisions.

MASK ionization routine than the field emission simulations to follow. However, for future, more sophisticated simulations that may include higher gas densities, the inclusion of elastic and inelastic charged particle–neutral particle collisions may become necessary.

6.4 Field emission simulations

Having shown that the ionization routines in MASK yield reasonable results, we proceeded to simulate field emission in the geometry outlined in Section 6.2.1. The following description of a simulation run (requiring about four hours of computing time on the RS/6000 workstation used) is to be considered a generic example of all our simulations that led to rf processing. The qualitative (and to a large extent quantitative) results are common to the other simulations we will be discussing later.

6.4.1 Simulation parameters

We chose an applied field of 30 MV/m at a frequency of 5 GHz. The size of the region studied was 32×8 μm^2 and the mesh density was 128 elements $\times$ 64 elements. The maximum electron energy to be expected is about 1000 eV. Thus a time step of $dt = 10$ fs was chosen to ensure that no electrons move more than one mesh element in dt.

The parameters chosen for the field emitter were

$$A_{\mathrm{M}} = 4.13 \times 10^9 \text{ A/MV}^2 \tag{6.27}$$

$$B_{\mathrm{M}} = 218.5 \text{ MV/m}. \tag{6.28}$$

The radius of the field emitter was 2 mesh elements ($r_{\mathrm{em}} = 0.25$ μm). This is probably somewhat larger than most microemitters in cavities, but a reduction in size is difficult because of the corresponding increased computational burden due to the finer mesh requirement.

Given A_{M}, B_{M}, and r_{em}, one finds from (6.2) and (6.3) that

$$A_{\mathrm{FN}} = 3.37 \times 10^{-14} \text{ m}^2 \tag{6.29}$$

$$\beta_{\mathrm{FN}} = 250. \tag{6.30}$$

The corresponding peak values for I_{FN} and j_{FN} given by Equation 3.3 (with $v(y)$ and $t(y) = 1$) are 0.5 mA and 1.5×10^{10} A/m^2 respectively.[5] Similar parameters have been observed for field emitters in rf cavities. Note that the geometric features of the emitter are not simulated by MASK. The parameters β_{FN} and A_{FN} are therefore not correlated with the physical size of the emission region (for example, the radius given by A_{FN} is 0.1 μm $< r_{\mathrm{em}}$). The parameters are thus only used to describe the emissive properties of the emitter. Hence the theoretical peak current density, given by $j_{\mathrm{M}} = I_{\mathrm{FN}}/(\pi r_{\mathrm{em}}^2)$, is only 2.5×10^9 A/m^2. This discrepancy with j_{FN} is not necessarily at odds with reality, since little correlation between β_{FN} (or A_{FN}) and the emitter geometry has been observed with cavity emitters (see Section 3.2.1).

[5] If $v(y)$ and $t(y)$ had been included, $j_{\mathrm{FN}} = 2.4 \times 10^{12}$ A/m^2. Due to space charge limitations the effect on the simulated emission current would, though, have been negligible. This fact is discussed in detail later.

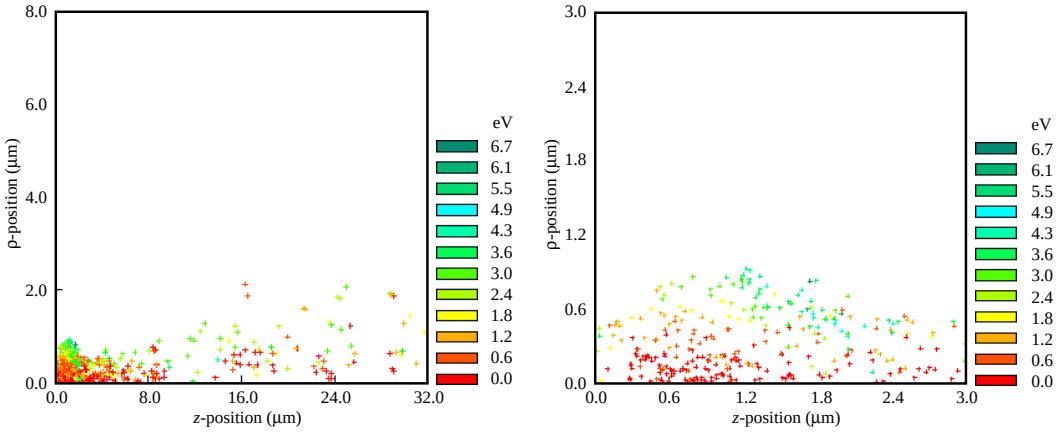

(a) (b)

Figure 6.6: Position plots of the ions after 1 1/4 rf periods. Each cross represents 10 ions. The color indicates the ion energy in eV. (a) The entire simulation region — note that the aspect ratio is not 1:1. (b) Magnified view of the 3×3 μm^2 region closest to the emitter.

The gas flux was 10^{27} m^{-2}s^{-1} at 2000 K. From (6.12) the gas density at the emitter should be 3.1×10^{24} m^{-3} although a peak density of only 1.6×10^{24} m^{-3} was recorded in the simulation. The density is higher than that used in later simulations, but the results illustrate nicely the effect of the ion production on the emission process. Later, when we reduce the gas pressure, we will see that the qualitative results do not change much, except that longer simulation times are required.

6.4.2 Simulation results

Initially, at low field levels, the field emission current enters the cavity as a pencil beam (see Figure 6.2(b)). The rate of ionization events per unit volume is given by (6.18). Most of the ions are produced in the region where the product of σ_t and n_n is maximized, i.e., within a few micrometers of the rf surface. Because of their large mass, the ions do not move quickly and they accumulate near the emitter. After 1 1/4 rf cycles (25,000 times steps) a significant number of ions have already been created, as shown in Figure 6.6. A contour plot of the total charge density near the emitter is shown in Figure 6.7. Peak densities are already at 3 kC/m^3. At this point in time the ion density was significantly greater than the electron density, so that ion number density is on the order of 2×10^{22} m^{-3}.

6.4.2.1 Ion field enhancement

In Figure 6.6 the applied rf field is at its peak, i.e., at 30 MV/m. The positive charge present near the emitter enhances the rf field further, so that the total field exceeds 30 MV/m. In Figure 6.8(a) we see that the equipotentials near the ion cloud are being distorted. The corresponding peak electric field in the z-direction is as high as 39 MV/m (Figure 6.8(b)). This value takes into account the presence of the field emission current, which offsets some of the field enhancement due to the ions. Presumably, the fields would

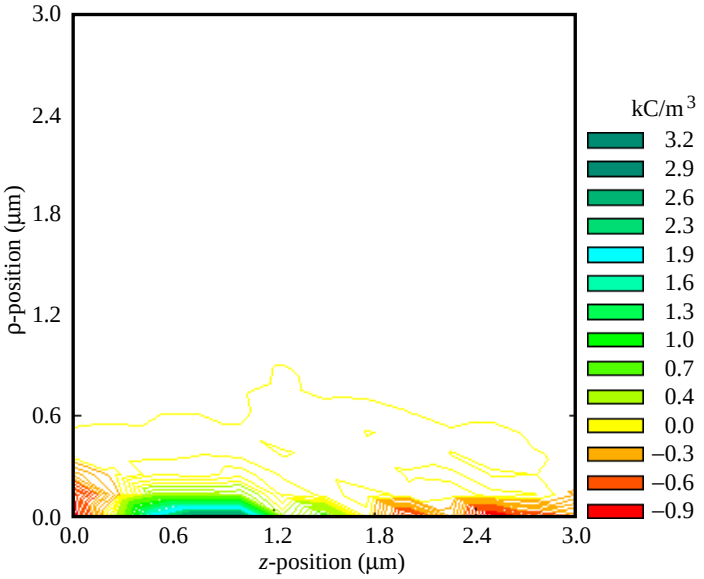

Figure 6.7: Contour plot of the total charge density in the 3×3 μm^2 region closest to the emitter after 1 1/4 rf periods.

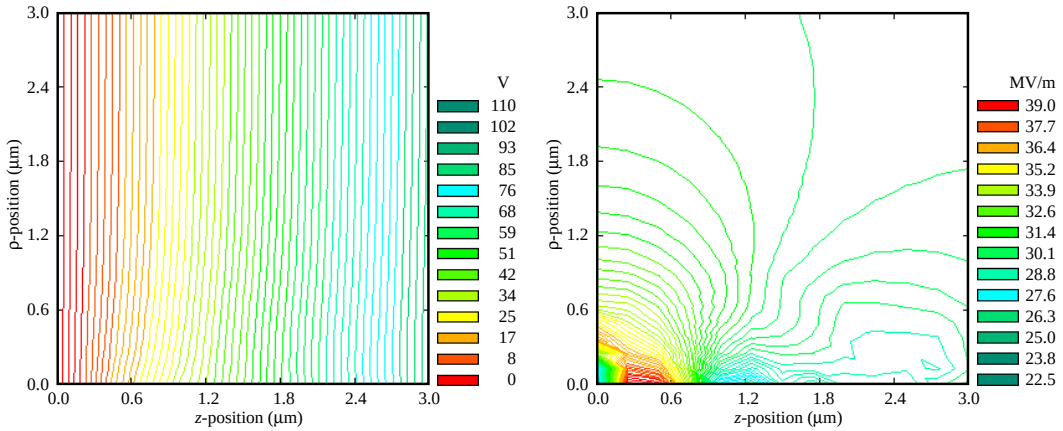

(a) (b)

Figure 6.8: Contour plots of (a) the scalar potential and (b) $-E_z$ within the 3×3 μm^2 region closest to the emitter. Both "snapshots" were taken 1 1/4 rf periods into the simulation.

be higher if the field emitter were turned off. Due to the enhancement of the electric field, the field emission current is also increased with respect to the steady state value in the absence of the ions (we will return to this point later). As the current leaves the emission site, radial electric fields due to the ions focus the electron beam within a few micrometers of the rf surface (see Figure 6.9). This serves to further concentrate the ion production in this region. Once the beam emerges at the other end of the ion cloud, its own space charge causes it to spread significantly. The greater the current, the greater this effect.

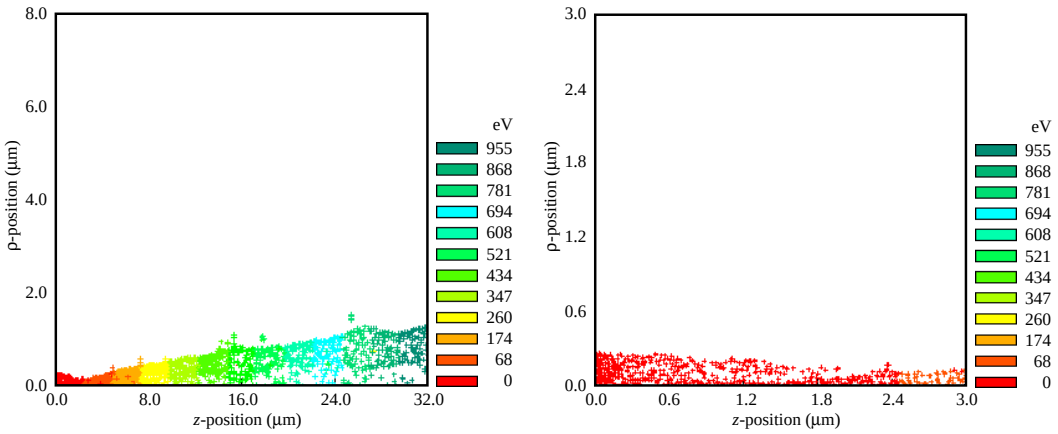

(a) (b)

Figure 6.9: Position plots of the electrons 1 1/4 rf periods into the simulation. (a) The entire simulation region — note that the aspect ratio is not 1:1. (b) Magnified view of the 3×3 μm^2 region closest to the emitter. In both cases the electron energies are given by the color of the crosses. Observe how the electric field of the ions serves to focus the electron beam within 2 μm of the rf surface.

As the simulation progresses through the half of the rf cycle when the applied rf field inhibits field emission, the ions slowly begin to spread radially due to their mutual repulsion and in the positive z-direction due to the applied rf field. The ions move at most a distance on the order of 1 μm, gaining about 30 eV. Ions heavier than magnesium (e.g., iron and indium) will move even less. Hence, by the time the third rf cycle begins, many of the ions are still in the vicinity of the emitter. This fact is clearly illustrated in Figure 6.10 which depicts the ion positions after 2 rf cycles have been completed (40,000 time steps). Despite the fact that the applied electric field at this time is zero, the electric field due to the ions at the emission site is as high as 25 MV/m (see Figure 6.11). Due to this strong electric field, electrons are being drawn from the field emitter and are trapped in the region of the ions (Figure 6.12). This process results in charge neutralization and the build up of a plasma.

By the time the simulation has advanced another 1/4 rf cycle, the plasma has more or less expelled the electric field from its interior (Figure 6.13(a)). The plasma now is quasi-neutral[6] and the density is on the order of 10^{23} m^{-3}. A potential drop between the plasma and the rf surface develops to impede the flow of the more mobile electrons back to the rf surface, so that charge neutrality is preserved. The field due to this potential is close to 120 MV/m, far in excess of the applied field of 30 MV/m at that time (Figure 6.13(b)). Shortly after this point in time, the simulation was halted, because at such high electric fields the resolution of the mesh was insufficient to yield accurate results. However, later we will demonstrate that the plasma can produce significantly stronger fields, if the simulation were to be continued.

[6]We hesitate to claim full neutrality, because some charge imbalance was still observed.

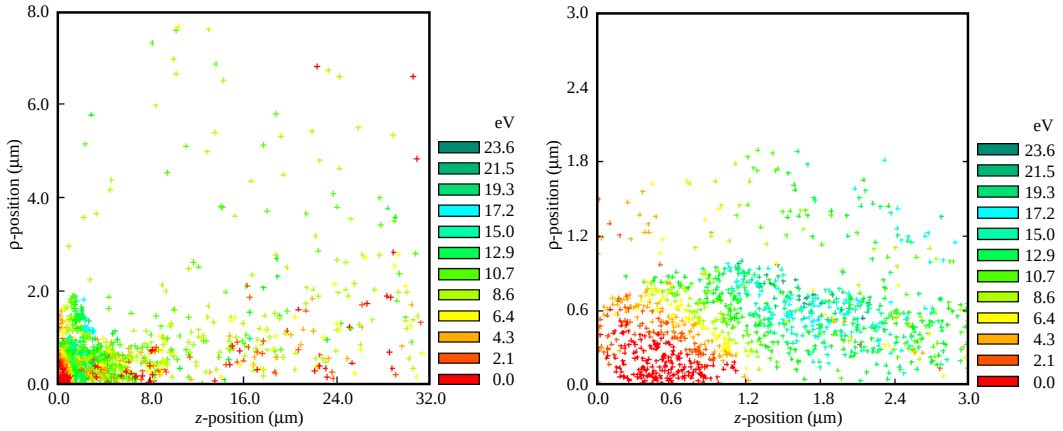

(a) (b)

Figure 6.10: Position plots of the ions after two rf periods. Each cross represents 10 ions. The color indicates the ion energy in eV. (a) The entire simulation region — note that the aspect ratio is not 1:1. (b) Magnified view of the 3×3 μm^2 region closest to the emitter.

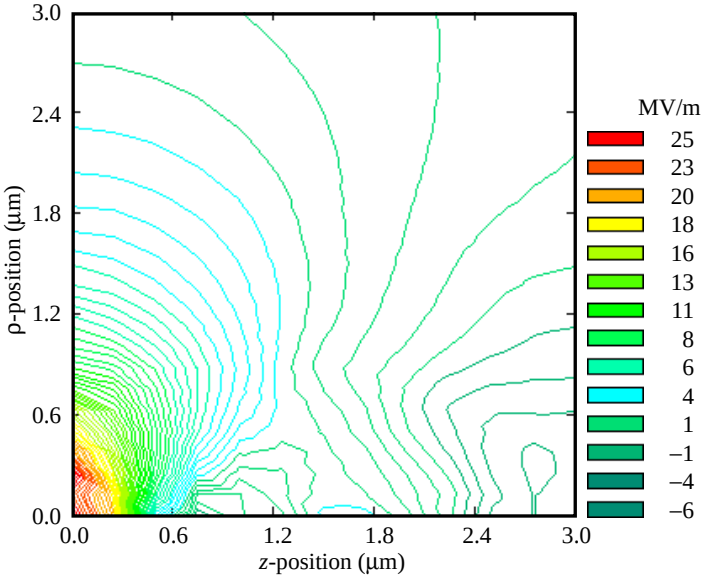

Figure 6.11: Contour plot of $-E_z$ near the field emitter at the beginning of the third rf period. The applied rf field is zero at this point in time.

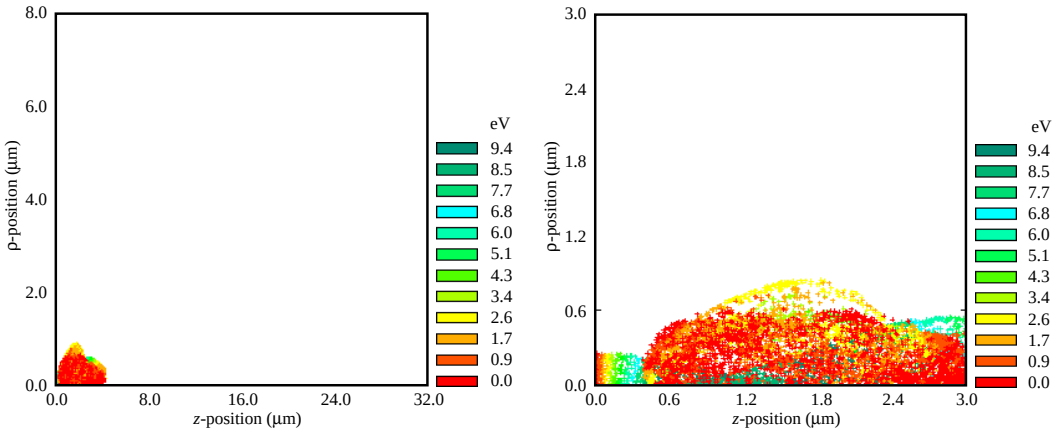

(a) (b)

Figure 6.12: Position plots of the electrons at the beginning of the third rf period. (a) The entire simulation region — note that the aspect ratio is not 1:1. (b) Magnified view of the 3×3 μm^2 region closest to the emitter. Clearly visible is the injection of emission current from the rf surface despite the fact that the applied electric field is zero.

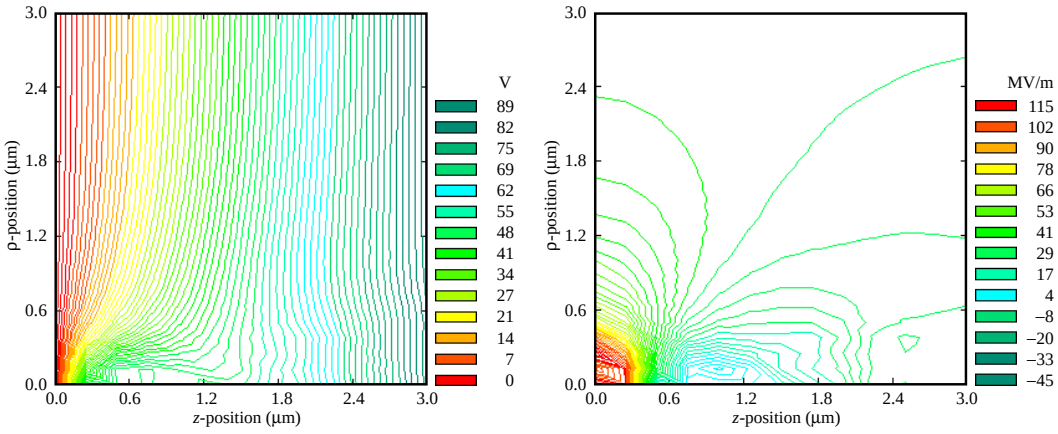

(a) (b)

Figure 6.13: (a) Equipotentials near the field emission site 2 1/4 rf periods into the simulation. (b) Contour plot of $-E_z$ at the same time. The field enhancement due to the plasma near the rf surface is very apparent.

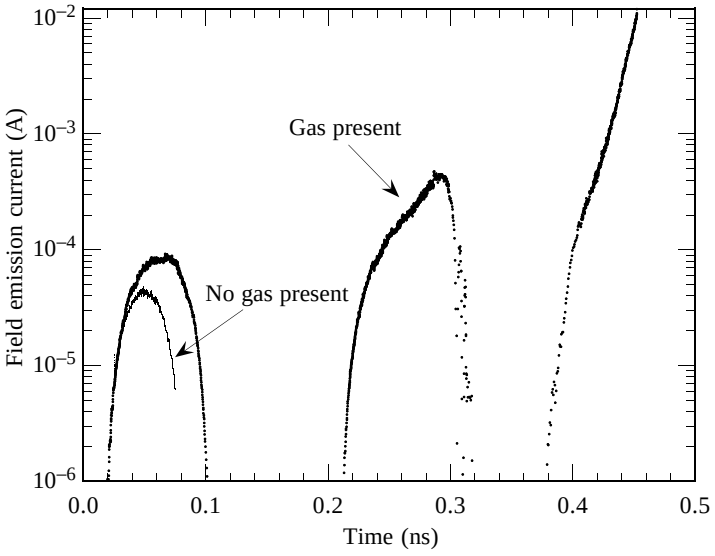

Figure 6.14: Emitted electron current versus time for a simulation including a neutral gas and the same simulation with no neutrals present.

6.4.2.2 Evolution of the emission current

Figure 6.14 depicts the field emission current as a function of time for the first 2 1/4 rf cycles. Included in the same figure is the simulated field emission current under identical circumstances if the neutral gas is omitted from the simulation. In the latter case the current never attains the 0.5 mA level predicted by (6.1) because of space charge limitations (we will discuss this point later). In contrast to this situation we find that the field emission current rises rapidly when the gas is included and ionization takes place. The ions serve two purposes. On the one hand they increase the electric field at the emission site, thereby augmenting the field emission current. On the other hand they also neutralize the emission current, so that the effect of its self-field is reduced.

Within just over two rf cycles the peak electron current has risen from 44 μA to over 10 mA — a 227 fold increase. In fact, the increase might even have been greater if it were not for the field emission limit that had to be artificially imposed to prevent the unphysical instabilities due to the discrete simulation times steps (see Section 6.2.2). Not only does the peak current rise, but the fraction of each rf cycle during which field emission is active also increases, because the ions tend to provide a dc bias to the applied rf field. Hence the average current rises even faster than the peak current.

6.4.2.3 Power dissipation

Due to the resistivity of the field emitter, the emission current causes Joule losses.[7] Since the emission current increases rapidly as the ion cloud develops, we see that the time averaged Joule losses also increase dramatically with respect to the steady state value in the absence of the neutral gas. Conservatively, one would expect the dissipated power

[7] In fact, throughout this chapter we have assumed implicitly that the initial current density is sufficient to heat the emitter and cause the release of the neutral gas used in the simulation.

to rise at least quadratically with the peak field emission current drawn, although this neglects the fact that the emitter resistivity in many cases increases with temperature. Hence the dissipated power will increase at least by a factor of $227^2 = 5.2 \times 10^4$ due to the presence of the gas.[8] In turn, such a dramatic increase in dissipation will drastically raise the emitter temperature and result in the effusion of substantially larger quantities of neutrals which become available for ionization — a fact that was not included in this particular simulation (later we discuss simulations that do attempt to include this effect). The ionization process hence is part of a positive feedback mechanism as was anticipated in the previous chapter. The greater the ionization rate, the more neutral gas becomes available, which in turn increases the ionization rate. We therefore expect the growth of the field emission current to be even more rapid than demonstrated by our simulations (we will return to this point shortly).

6.4.2.4 RF processing

Unless there is some mechanism to limit the positive feedback loop just described, it is clear that this type of field emission must end in an explosive event (rf processing). For practical purposes, we deem an emitter as being rf processed (extinguished) if the emission current in the simulation exceeds the (somewhat arbitrary) threshold of 0.01 A, i.e., when the rapid current growth (as during the third rf cycle in Figure 6.14) has been well established. We expect, that eventually the heating of the rf surface due to either the augmented field emission current or ion bombardment (or both) becomes so severe, that the macroemitter is heated to temperatures significantly above the melting point and an explosion occurs. This is consistent with theories of dc discharge, where temperatures in excess of 10^4 K have been encountered in times as short as 1 ns. [21, 161] Later we will show that field emission can continue even after the emitter melts, provided a significant number of ions are already present nearby.

Ultimately, the energy stored in the cavity sets a limit on the maximum possible current that can be emitted. Any charge absorbs energy from the cavity fields as it is accelerated through the cavity volume before impacting the cavity walls. At the impact sites, the rf surface temperature is raised and more power is absorbed, perhaps even leading to a quench. In any case, field emission must cease once the cavity energy has been drained due to the various loss mechanisms. Indeed, we found that whenever an emitter rf processed the rf fields collapsed completely, indicating that the finite stored energy is the limiting factor during rf processing. The same was observed during high power processing experiments. [162]

Our simulation predicts that an explosion will take place within a few rf cycles. At lower gas densities, the time until an explosion takes place is longer (see below), but nevertheless is on the order of several rf cycles. We assumed, that at the beginning of the simulation the neutral gas density near the emitter, in particular within the first few micrometers, has already established a quasi steady state.[9] The time taken to achieve the steady state depends on the temperature of the neutral gas. At gas temperatures on the order of 1000 K neutrals move about 1000 m/s. Hence the gas requires 5 ns to

[8] An even greater factor should be used, considering that the time average emission current rises faster than the peak current.

[9] The term steady state is actually a misnomer since the simulations have shown that the power dissipation at the emission site is anything but steady.

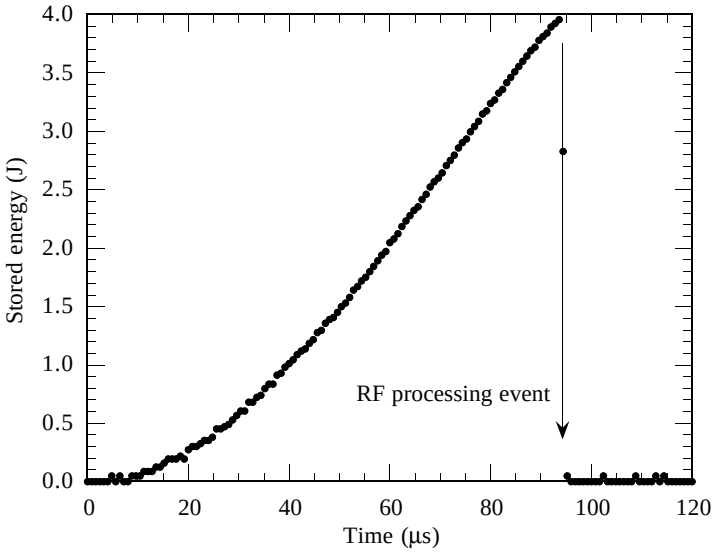

Figure 6.15: Stored energy as a function of time during the application of a 120 μs 60 kW rf pulse to a 1.3 GHz lead plated copper cavity. A processing event was observed after about 95 μs at $E_{\rm pk} = 29$ MV/m. $Q_{\rm e} = 6 \times 10^5$. [162]

travel 5 μm. In addition to this time, one needs to take into account the time it takes to substantially heat the field emission site itself. Calculations [63] have shown that a field emitter can melt niobium within as little as 1 to 100 ns, provided the current density is high enough. Other materials found at emission sites, with a lower melting temperature than niobium (e.g., iron and indium), should melt even faster.

The total time to rf process an emitter ($t_{\rm proc}$) is given by

$$t_{\rm proc} = t_{\rm heat} + t_{\rm gas} + t_{\rm expl}, \tag{6.31}$$

where $t_{\rm heat}$ is the time taken to heat the emitter in order to release the neutral gas, $t_{\rm gas}$ is the time required by the gas to move a few micrometers, and $t_{\rm expl}$ is the time until an explosion takes place. Given the time scales discussed above, we can expect an emitter to rf process in a time on the order of a few nanoseconds to 1000 ns.

These times are consistent with processing times observed in rf cavities. Figure 6.15, for example, depicts the stored energy in a 1.3 GHz cavity as a function of time during the application of a 60 kW, 120 μs rf pulse. The time between data points is 800 ns. RF power was applied at time $t = 0$. Because the input coupling to the cavity was very strong ($Q_{\rm e} \approx 6 \times 10^5$), the stored energy rose very quickly to 4 J. At that point $E_{\rm pk} = 29$ MV/m and an emitter processed. The processing event was accompanied by a brief burst of x-rays and at the same time the stored energy was drained in less than 800 ns. Such rapid dissipation of the stored energy is inconsistent with thermal breakdown (requiring milliseconds) and we conclude that most of the power must have been dissipated in the field emission current itself. Hence, on average, the current dissipated *at least* 4 J/800 ns $= 5 \times 10^6$ W of power.

Typically field emitters prior to rf processing at 30 MV/m dissipate anywhere between ten and several hundred watts of power at currents around 0.5 mA.[10] Taking

[10]This is the power dissipated when the emitted charges are accelerated by the cavity fields.

100 W as a reasonable value, we find that a lower limit on the emission current *during* the processing event is given by $(5\times10^6$ W/100 W$)\times0.5$ mA $= 25$ A! Peak currents may even be considerably higher, especially if the rf processing event takes significantly less than 800 ns. Of course, this simple estimate ignores items such as space charge effects, since we simply scaled the power dissipated by the cavity field in the emission current linearly with the magnitude of the current. However, the estimate does illustrate that enormous currents are *feasible* during rf processing. Since the maximum current recorded in our simulation was only 10 mA we see that our calculations were ended long before the ultimate processing event. Reference [23] describes four stages of dc breakdown: pre-breakdown, ignition, current growth, and arcing. Steady state rf field emission is to be compared with dc pre-breakdown. Our simulations then enter the ignition phase and the beginning of the current growth phase, but are stopped long before the maximum current is ever achieved (arcing).

Sub-microsecond processing times have also been observed in pulsed dc vacuum discharge experiments. [21, 121, 122, 163] Pre-breakdown currents in dc discharge experiments are in the 0.1 mA to 10 mA range. [122, 164] Again these values are consistent to an order of magnitude with rf field emitters. During the dc breakdown phase these investigators and others measured currents from 1 to 100 A, which are commensurate with our rough estimate of the peak rf processing current.

6.4.2.5 Plasma density

By the end of the simulation, ion densities have risen to $\approx 3\times10^{23}$ m^{-3}. Such densities are high for most types of steady state plasmas. [165] For transient plasmas these densities are, however, not unrealistic and densities as high as 10^{26} m^{-3} have been observed in cathode flares, which are created at the cathode during explosive dc field emission. [21, 69, 121] It is likely that the plasma densities of $\approx 3\times10^{23}$ m^{-3} observed during our simulations constitute a lower bound on the densities that occur during rf processing. We anticipate, that if the simulation could be continued further in time, the plasma density would continue to rise due to the enhanced emission current and the increased neutral gas density produced by the large power dissipation at the emission site.

6.4.3 Summary of the processing sequence

Before we move on to the discussion of more detailed simulations, we reiterate the salient facts of rf processing deduced from the results presented so far. These features are common to all our simulations.

In the absence of any ionizable gas, we found that the emission current does not exceed a fairly low value (44 μA), despite the fact that the theoretical current given by Equation 6.1 is 500 μA. The self field of the emission current is responsible for this discrepancy. Steady state emission currents from real cavity emitters have been observed at the 500 μA level. Such high currents are probably attained with the assistance of geometric field enhancement by the macroemitter. (The consequences of the omission of emitter geometry in our simulations is discussed later). Nevertheless, as we demonstrated in Chapter 5, the heating due to such currents alone is incapable of exploding an entire macroemitter. Because of space charge limitations, we suspect that even higher steady state currents cannot be achieved.

The situation changed drastically when the ionization of gas evolving from the emitter was included in the simulation. At an initial gas density of about 3×10^{24} m^{-3} (at the rf surface) ions were rapidly produced by the emission current in a single rf cycle.[11] Most ions are created within a few micrometers of the emission site. Due to their large mass, the ions remain in the emitter vicinity for several rf cycles, and a high density ion cloud builds up. So far we identified two important functions of this ion cloud. 1. It creates electric fields at the emission site far in excess of the applied field, and 2. it neutralizes the emission current so that the space charge limits mentioned above no longer apply. (A third function, the bombardment of the rf surface by ions, will be discussed later.) These effects combine to increase the emission current by several orders of magnitude. In turn, the rate of ion production is raised as well. The ionization process is therefore self amplifying and leads to a runaway situation. The power dissipated by the emission current (and the bombarding ions, as we will see later) increases so dramatically that ultimately the macroemitter is destroyed (rf processing). Due to the elevated temperatures additional large quantities of neutral gas are also released, that further contribute to the runaway situation. Only the finite energy stored in the cavity appears to limit the entire process.[12] Based on the simulation, the positive feedback mechanism is so powerful that rf processing times should be considerably less than 1 μs. This time scale is consistent with experimental observations.

6.5 Critical gas density

6.5.1 Introduction

The results obtained from the simulation described in the previous section should be considered typical. The qualitative features are common to *all* our simulations that led to rf processing. Nevertheless, parameters such as the neutral gas density, r_{em}, β_{FN}, A_{FN}, E_{pk} and the rf frequency can have an impact on the quantitative aspects of a simulation. So far we have only explored a limited region of this parameter space.

Of particular interest to us was the determination of the gas density required at the outset of the simulation to initiate rf processing. For example, the simulation described above used a fixed gas density of about 3×10^{24} m^{-3}, which is fairly high. Our objective was to determine whether such high densities are necessary and, if not, we wanted to find a reasonable estimate of the lowest possible *initial* density required for rf processing. We call this threshold value the "critical density." Once known, the critical density can then be used to determine whether such values are feasible near cavity emission sites.

In this section we will show that successive reductions of the gas density in the simulations by factors of 1/2 quickly eliminate the explosive behavior. Based on these simulations, critical densities on the order of 10^{24} m^{-3} are predicted. Varying parameters like the rf frequency only has a small impact on this value.

However, in our discussion earlier, we already pointed out that the gas density at real emitters increases whenever the dissipated power is augmented. When we include this effect in simulations (as discussed in Section 6.5.4), we find that predicted critical densities are lowered dramatically — to between 3×10^{20} m^{-3} and 3×10^{22} m^{-3}. A

[11] Later we will show that the same can be true when considerably lower initial densities are used.

[12] As we will see later, even the melting of individual microemitters cannot stop the runaway situation. In fact, the released gases only add further fuel to the feedback loop.

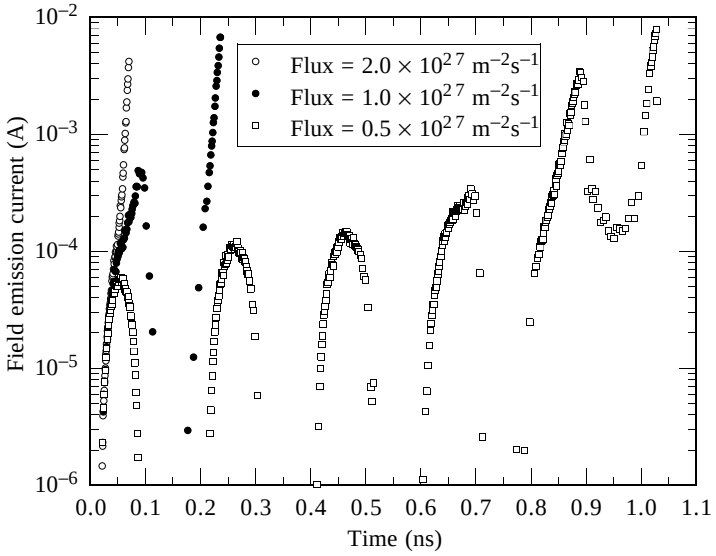

Figure 6.16: Field emission current versus time for different gas effusion rates ($T = 922$ K).

comparison of these densities with the vapor pressure of common emitters shows that such values are feasible near real field emitters.

A number of other factors affecting the critical gas density are also discussed in this section. In all cases we are led to believe that the true critical density is even lower than that predicted by our simulations. For example, space charge effects due to our inability to simulate the macroemitter geometry limited our steady state emission currents to about 1/10 of measured currents. To compensate, initial gas densities in the simulations need to be about 10 times higher to initiate processing. Geometric field enhancement also moves the region of dominant ionization (determined by the electron energy) closer to the rf surface, thereby increasing the impact of the ions on the emission process. A simple simulation with an increased applied field and a finer mesh shows that again the computed critical density is overestimated due to the omission of the emitter geometry. Mesh size considerations also forced us to use current densities lower than expected with real emitters. Hence, reduced ion densities result, raising the critical gas density once more. Finally, we also ignored the release of neutral gases due to the ion bombardment of the rf surface, so yet again the critical density is overestimated. All these effects will be discussed later in more detail.

Since many of the qualitative results of the following simulations are similar to those described earlier, we will not discuss each one in detail. Rather, we will concentrate on the main results. Note also, that in the following descriptions it is implied that all parameters (E_{pk}, A_{M}, B_{M}, mesh parameters, dt ...) are the same as described above, *when not stated otherwise*.

6.5.2 Reduction of the gas flux

Figure 6.16 depicts the field emission current as a function of time for simulations in which the gas was permitted to effuse at different rates. The temperature of the source in this case was always 922 K, the melting point of magnesium. The gas flux was varied

from 0.25×10^{27} m^{-2}s^{-1} (results not shown) to 2×10^{27} m^{-2}s^{-1}. The corresponding theoretical gas density at the rf surface ranged from $\approx 1.1 \times 10^{24}$ m^{-3} to 8.9×10^{24} m^{-3}. These densities are about 1/25 to 1/3 the atmospheric density at room temperature (2.5×10^{25} m^{-3}). All other parameters were identical to those in the simulation described in Section 6.4.

We found that even small changes to the neutral gas density had a profound effect on the outcome of the simulations. At a neutral gas flux of 2×10^{27} m^{-2}s^{-1}, the breakdown avalanche occurs within the first rf cycle. Halving the gas flux delays the explosion until the beginning of the second rf cycle. After reducing the flux by 1/2 again, the time until the onset of the explosion took four times longer still and did not occur until the fifth rf cycle. Finally we reduced the flux by 1/2 again, to 0.25×10^{27} m^{-2}s^{-1}. In this case a steady state was achieved and no explosion was recorded (not shown in Figure 6.16). In going from a neutral gas flux of 2×10^{27} m^{-2}s^{-1} to 0.25×10^{27} m^{-2}s^{-1} (a reduction by 1/8), the explosion occurring in less than 0.5 ns was completely eliminated. Hence, it would seem, that a critical gas density of between 1 and 2×10^{24} m^{-3} at the emission site is required for rf processing.

It is difficult to estimate whether gas densities on the order of 10^{24} m^{-3} are feasible. Part of the difficulty lies in the fact that neither the monolayer composition of the rf surface nor the temperature of the emission site are known in detail.

6.5.2.1 Comparison with vapor pressure data

A reasonable assumption is, that for steady state field emission a microemitter needs to be solid. Hence, the melting point provides an upper bound on the microemitter temperature. Given the vapor pressure at that temperature we can calculate the gas density (n_{v}) at the emission site (the "vapor density") using the ideal gas law. The vapor density then constitutes an upper limit on the initial gas density to be used in simulations.

Consider, for example, a magnesium field emitting particle on the rf surface. Its vapor density versus temperature is shown in Figure 6.17 along with that of iron. The vapor density rises very rapidly with temperature. An approximation of the data sufficient for our purposes is given by

$$n_{\mathrm{v}} = c_1 \times 10^{-c_2/T}, \tag{6.32}$$

where c_1 and c_2 are fit parameters and T is the emitter temperature. For magnesium $c_1 = 6.68 \times 10^{29}$ m^{-3} and $c_2 = 6823.6$ K.

The melting point of magnesium is 922 K. At this temperature, the vapor pressure is about 2.8 torr [167] and the corresponding vapor density is 2.9×10^{22} m^{-3}. On the other hand, the estimated critical density based on the simulations is $1 \rightarrow 2 \times 10^{24}$ m^{-3}. This value is $34 \rightarrow 68$ times greater than the vapor density at 922 K. To achieve the critical density, the emitter temperature would need to be raised to about 1170 K $\rightarrow$ 1235 K, a fairly small amount because of steep increase in vapor pressure with temperature.

Magnesium is a rather favorable candidate because it has a high vapor pressure at its melting point. The vapor density of other elements more commonly found at emission sites have vapor densities two or three orders of magnitude lower at their respective melting points. Iron, for example, melts at 1808 K, at which temperature the vapor density is only 3×10^{20} m^{-3}. [167]

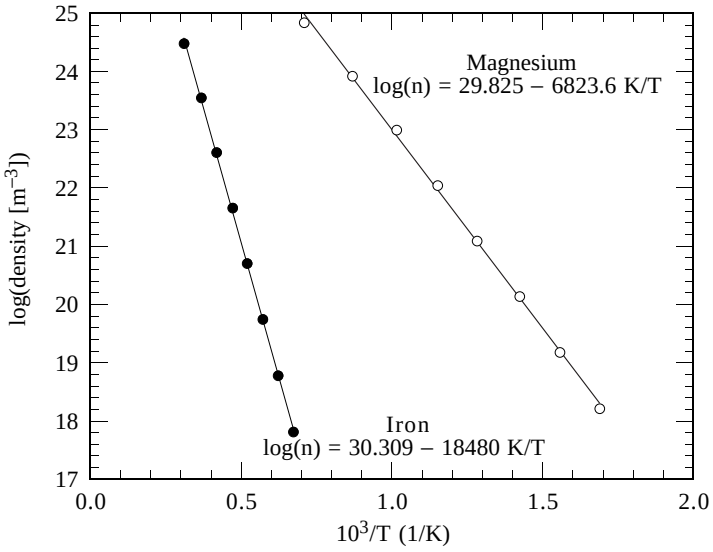

Figure 6.17: Logarithm of the "vapor density" versus inverse temperature for magnesium and iron. [166]

Thus one would have to conclude that the vapor density is unlikely to be sufficient to initiate rf processing. However, there are numerous items that we neglected to take into account which probably invalidates this conclusion. We will return to this matter shortly.

6.5.3 Frequency dependence of the critical density

The critical gas density determined so far does vary somewhat with the simulation parameters, and this still needs to be studied in more detail. In many cases the effect probably is small. For example, lowering the rf frequency slightly reduces the gas density required for rf processing. Compared in Figure 6.18 are the emission currents versus time obtained from simulations at 5 GHz and 1.5 GHz. One finds that rf processing with a neutral flux of 5×10^{26} m^{-2}s^{-1} takes place earlier at 1.5 GHz than at 5 GHz. The reason lies in the fact that the length of time over which field emission is active in one rf cycle is greater at 1.5 GHz than at 5 GHz (although, of course, the time averaged current over an rf cycle is the same). Hence there is more time for a significant number of ions to be produced during the positive half of an rf cycle, before the applied potential changes sign. This suggests that field emitters in low frequency structures may be more easily processed than those in high frequency structures. On the other hand, should the critical ion density not be achieved during the positive half of one rf cycle at 1.5 GHz, then many ions are lost in the subsequent negative half cycle, because of the long time available for ions to be accelerated away from the rf surface and to spread laterally due to their mutual repulsion. Therefore less retention of ions near the emitter occurs from rf cycle to rf cycle which tends to cancel out the benefits mentioned earlier. Hence, the variation of the critical neutral gas density required for processing is probably small when comparing 1.5 GHz and 5 GHz cavities.

Both at 1.5 GHz and 5 GHz no processing was observed when the gas flux was

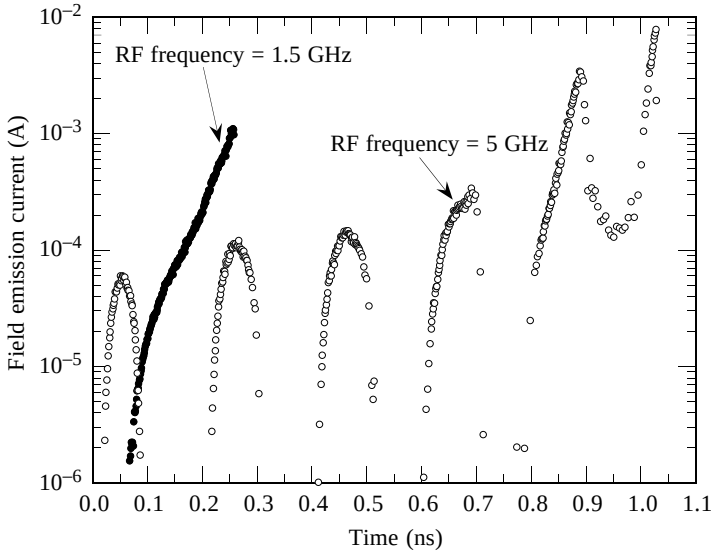

Figure 6.18: Field emission current versus time at 5 GHz and 1.5 GHz. In both cases the gas flux was 5×10^{26} $\mathrm{m^{-2}s^{-1}}$.

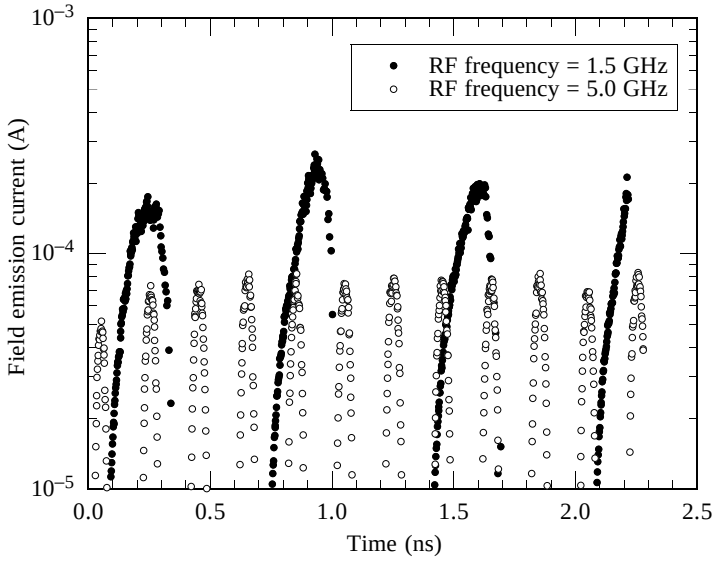

Figure 6.19: Field emission current versus time at 5 GHz and 1.5 GHz. In both cases the gas flux was 2.5×10^{26} $\mathrm{m^{-2}s^{-1}}$. No processing event was recorded.

2.5×10^{26} $\mathrm{m^{-2}s^{-1}}$. However the average emission currents achieved were greater at 1.5 GHz than at 5 GHz (see Figure 6.19), suggesting that in the former case the gas density was very close to being critical.

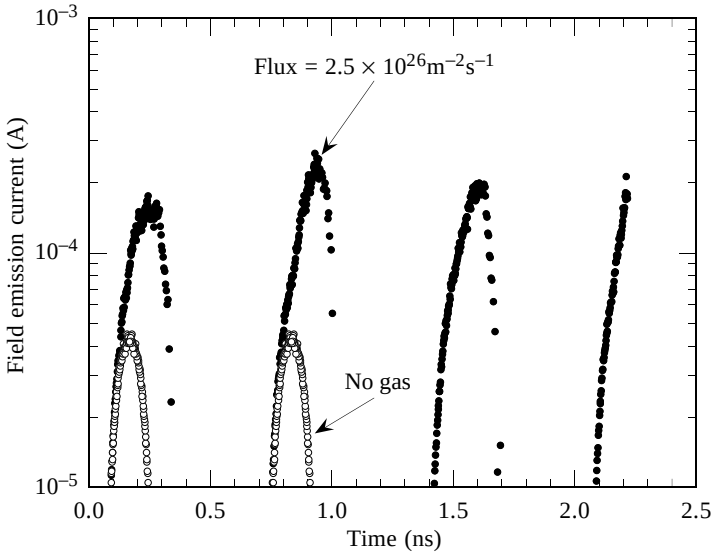

Figure 6.20: Field emission currents drawn when (a) no neutral gas is present, (b) the gas flux is 2.5×10^{26} $m^{-2}s^{-1}$. No processing event was observed.

6.5.4 Time dependent gas flux

6.5.4.1 Argument for varying the gas flux

Despite the slight frequency dependence, it would seem that the critical gas density is on the order of $1 \rightarrow 2 \times 10^{24}$ m^{-3}. However, this number is likely to be much too high because so far the neutral gas density was always fixed at its initial value. In reality the situation is different, since the gas density will rise with time as the power dissipated in the emitter increases.

We compared, for example, the field emission current drawn in the absence of any neutral gas with that drawn in the presence of a relatively low density gas (both at 1.5 GHz). The results are shown in Figure 6.20. Even when the neutral gas is present, explosive behavior is not observed in this simulation, and a steady state seems to have been attained. The *time averaged* current is 42 μA. This value is to be contrasted with an average current of 3.5 μA when no neutrals are present. Similarly, the peak currents differ as well; 266 μA when the gas is present and 44 μA if no gas is present. Gas ionization augmented the peak current by a factor of 6. The average current even increased by a factor of 12, because not only is the peak current higher, but also field emission remains active over a larger fraction of each rf cycle.

We therefore concluded, that the power dissipation at the emission site will increase with time as the ionization of the gas proceeds *even if no rf processing occurs* (in the simulation). A very simple estimate is that power dissipation scales quadratically with the average field emission current. Hence, a factor of $12^2 = 144$ constitutes a lower bound on the increased power dissipation. In using this value, we underestimate the true dissipation because we ignored the increase in emitter resistivity with temperature (for conductors) and with current density. [168] We expect the temperature of the emitter surface to increase linearly with the dissipated power, provided the specific heat and thermal conductivity remain reasonably constant with temperature. In turn, the amount

of neutral gas effusing from the surface will also increase. The vapor pressure of most materials rises very rapidly with temperature. For example, iron at its melting temperature (1808 K) has a vapor pressure of 54.6 mtorr. If the temperature increases by a factor of 1.06 to 1920 K, the vapor pressure nearly doubles to 100 mtorr. Certainly, even a pressure increase by a factor of two be significant enough to bring about an explosion in Figure 6.20.

6.5.4.2 Simulation with adaptive gas flux

A precise treatment of the variable neutral gas density, where the rate of neutral particle injection is governed by the emitter temperature, was beyond the scope of the studies described here.

A simpler approach is to "pretend" that the emitter temperature increases instantaneously with the square of the time average emission current $\bar{I}_{\mathrm{FN}}(t)$ (since we assume that the Joule losses scale as $\bar{I}_{\mathrm{FN}}^2$). Whenever this temperature increases, the gas density in the simulation is assumed to increase as well. The increase can be estimated by using the vapor pressure and the temperature of the emitter material.

The following illustrates this approach: At the beginning of each simulation, we assume that the emitter is very close to the melting point. For magnesium we therefore start at 922 K. The neutral gas flux is set to an arbitrary value, the objective being to lower the density in successive simulations until no processing is observed. Based on the arguments above, the steady state temperature of the emitter at time t is approximated by

$$T \approx T_0 \left(\frac{\bar{I}_{\mathrm{FN}}(t)}{\bar{I}_{\mathrm{FN}}(t=0)} \right)^2, \tag{6.33}$$

where T_0 is the temperature at $t = 0$.

Given the temperature at time t, we can calculate the increased vapor density. From (6.32) one obtains the factor $f_{\mathrm{d}}(t)$, where

$$\log[f_{\mathrm{d}}(t)] = \log\left[\frac{n_{\mathrm{n}}(T_l)}{n_{\mathrm{v}}(T_0)}\right] = -c_2 \left(\frac{\bar{I}_{\mathrm{FN}}(0)^2 / I_{\mathrm{FN}}(t)^2 - 1}{T_0} \right), \tag{6.34}$$

which is a measure of the factor by which the original gas density has to be multiplied. In other words, at time t, the gas density at any place in the simulation region is given by $n_{\mathrm{n}}(t) = f_{\mathrm{d}}(t) n_{\mathrm{n}}(0)$, $n_{\mathrm{n}}(0)$ being the gas density at the beginning of the simulation.

Unfortunately this approach still requires significant computational resources because simulations have to be extended over at least one rf cycles each time $\bar{I}_{\mathrm{FN}}$ is calculated. We therefore decided to replace $\bar{I}_{\mathrm{FN}}(t)$ by $I_{\mathrm{pk},l}$, the latter being the peak current recorded *up until* simulation step l. We expect that this replacement underestimates the ratio $\bar{I}_{\mathrm{FN}}(t)/\bar{I}_{\mathrm{FN}}(0)$ in (6.33) (and hence the gas density), because, as discussed earlier, $\bar{I}_{\mathrm{FN}}$ increases faster than I_{pk} once field enhancement due to the ions becomes significant.

In the simplified approach $f_{\mathrm{d}}(t) \to f_{\mathrm{d},l}$, where:

$$\log(f_{\mathrm{d},l}) = \log\left[\frac{n_{\mathrm{n}}(T_l)}{n_{\mathrm{v}}(T_0)}\right] = -c_2 \left(\frac{I_{\mathrm{pk},0}^2 / I_{\mathrm{pk},l}^2 - 1}{T_0} \right), \tag{6.35}$$

$I_{\mathrm{pk},0}$ being the peak field emission current in the absence of any neutral gas. In the case of magnesium we used $c_2 = 6823.6$ K (see Figure 6.17), $I_{\mathrm{pk},0} = 44$ μA (43.7 μA was the

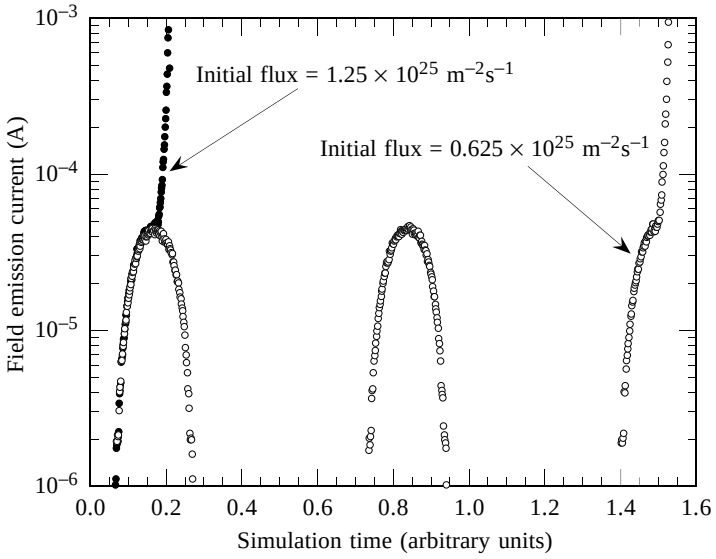

Figure 6.21: Field emission current versus "simulation time" at a low initial neutral gas flux ($n_n(0)$). Throughout the simulation the gas density was increased to reflect the increase of the peak field emission current.

peak current recorded when no gas was present) and $T_0 = 922$ K. In determining $I_{\mathrm{pk},l}$ during a simulation, we calculated a running average of 100 time steps to avoid jitter affecting the results.

When calculating the ionization rate at a given location at time step l, the gas density then used was $n_{\mathrm{n},l} = f_{\mathrm{d},l} n_{\mathrm{n}}(0)$. The factor $f_{\mathrm{d},l}$ was adjusted whenever the peak current increased. However we did cap $f_{\mathrm{d},l}$, so that the neutral gas flux never exceeded 2×10^{27} m^{-2}s^{-1}. Such a flux would be achieved at about 1400 K when starting at $T = 922$ K with vapor pressure of 2.8 torr.

The price paid in using this approach is that we no longer were able to evaluate the temporal evolution of the emission current. This is due to the fact that we adjusted the emitter temperature and the gas density instantly whenever I_{pk} increased. In reality, the temperature and gas density increase gradually. However, at this point we were more interested in determining at what initial gas density an emitter processes and not necessarily how quickly, so that this penalty did not concern us.

Figure 6.21 illustrates some of the results we obtained using the adaptive approach just described. When the initial gas flux was 1.25×10^{25} m^{-2}s^{-1} processing took place fairly early into the simulation. A reduction of the flux by 1/2 delayed processing. For a gas flux of 0.625×10^{25} m^{-2}s^{-1} the density at the emission site is 2.8×10^{22} m^{-3} at 922 K. This density is slightly *below* the magnesium vapor density at 922 K (2.9×10^{22} m^{-3}).

In fact our cautious approach in calculating the dissipated power and the gas density (by using $I_{\mathrm{pk},l}$ rather than $\bar{I}_{\mathrm{FN}}$) implies that the critical gas density is considerably lower than 2.8×10^{22} m^{-3}. From our simulations it appears that eventually an avalanche situation is encountered whenever the initial gas density is sufficient to create only a few ions near the emitter within a time on the order of one rf cycle. These ions only enhance the current by a small fraction, but this is enough to augment the power dissipation and increase the gas density further, thereby bringing about the avalanche.

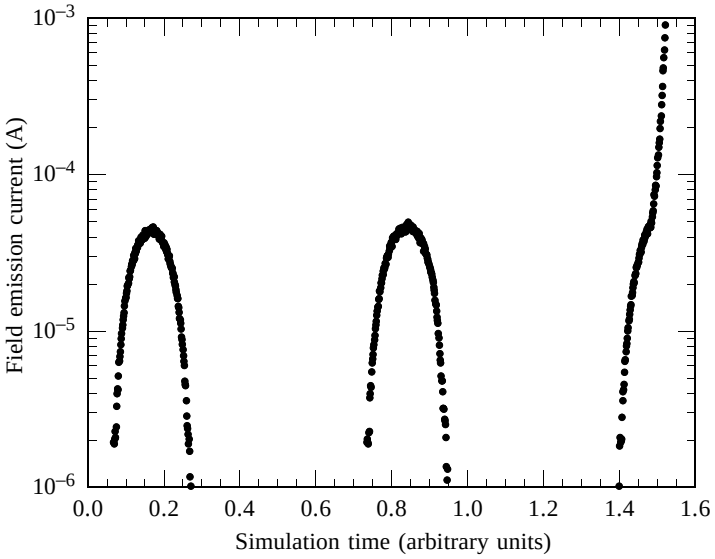

Figure 6.22: Field emission current versus "simulation time" when iron is permitted to initially effuse at a rate of 6.25×10^{24} $\mathrm{m^{-2}s^{-1}}$ at 1808 K. Throughout the simulation the gas density was increased to reflect the increase of the peak field emission current.

When the gas flux was 6.25×10^{24} $\mathrm{m^{-2}s^{-1}}$ (gas density $\approx 3 \times 10^{22}$ $\mathrm{m^{-3}}$), about 230 ions (i.e., of order 100) were created in half an rf cycle. Although we cannot give a definite number for the critical density, it is likely that the true value will not be lower than about $1/100 \times 6.25 \times 10^{24}$ $\mathrm{m^{-2}s^{-1}} = 6.25 \times 10^{22}$ $\mathrm{m^{-2}s^{-1}}$ (gas density $\approx 3 \times 10^{20}$ $\mathrm{m^{-3}}$) based on our criterion above. At this density only a few ions are created in an rf cycle. An outgassing rate of 6.25×10^{22} $\mathrm{m^{-2}s^{-1}}$ is achieved at temperatures of about 750 K, well below the melting point of magnesium. We therefore conclude that magnesium emitters indeed process due to ion field enhancement.

Figure 6.22 depicts the evolution of the field emission current when magnesium is replaced by 1808 K iron neutrals outgassing at 6.25×10^{24} $\mathrm{m^{-2}s^{-1}}$. The corresponding gas density at the rf surface is 3×10^{22} $\mathrm{m^{-3}}$. The factor of 1/100 we discussed above brings this density close to iron's vapor density of 3×10^{20} $\mathrm{m^{-3}}$ at 1808 K. Thus again processing should be possible.

6.5.5 Other factors affecting the critical gas flux

Nevertheless, even if we do take into account the factor 1/100 discussed above, the critical iron gas density required to initiate processing lies on the borderline of what we consider reasonable, based on iron's vapor pressure.

However, other factors impact our simulations which, if they had been included, would be sufficient to bring about the processing of iron (and other) emitters at fairly low gas densities. We alluded to several of these earlier and consider the following among the most important.

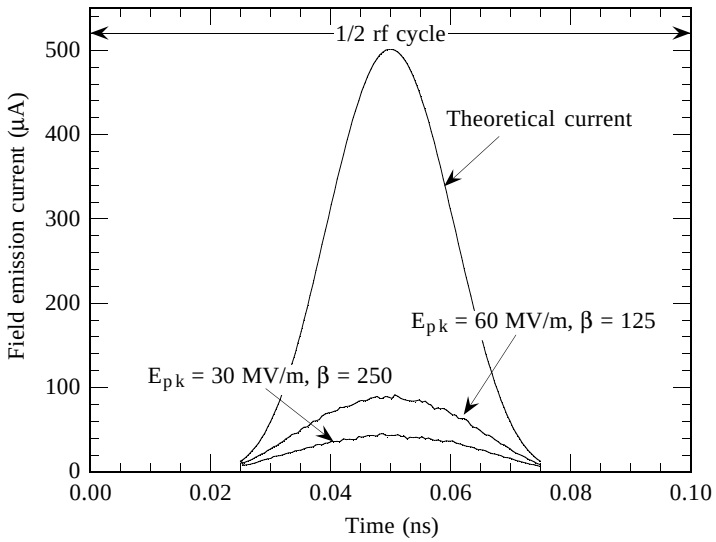

Figure 6.23: Field emission current versus time as obtained from simulations without a neutral gas present and from (6.1).

6.5.5.1 Space charge effects

At 30 MV/m the peak field emission current given by Equation 6.1 is $I_{\rm pk}^{\rm th} = 0.5$ mA for our simulation parameters ($A_{\rm M} = 4.13 \times 10^9$ A/MV^2, $B_{\rm M} = 218.5$ MV/m, and $r_{\rm em} = 0.25$ μm). Similarly, the maximum experimentally observed peak field emission currents in rf cavities are on the order of 0.1–1 mA (see Figures 5.37 and 5.38). In our MASK simulations, however, such high currents are not achieved *in the absence of an ionizable gas*.

Figure 6.23 depicts the simulated current as a function of time, when no neutral gas is included in the simulation. The highest current achieved is only 44 μA at 30 MV/m, about 1/10 of the current we would expect from (6.1). The reason for this is simple: the electric field of the emitted electrons partially cancels the externally applied field. Since field emission scales exponentially with the local electric field ($E_{\rm em}$), even a small reduction of $E_{\rm em}$ will substantially affect the emission current. To test this hypothesis we doubled the applied electric field to 60 MV/m while halving $\beta_{\rm FN}$ so that $I_{\rm pk}^{\rm th}$, as given by (6.1), remains unaffected. Figure 6.23 illustrates that the simulated field emission current roughly doubles as well, although it still falls short of the theoretical value. Not surprisingly, increasing $\beta_{\rm FN}$ or $A_{\rm FN}$ (while keeping $r_{\rm em}$ constant) had no significant effect on the total current. In contrast, if $r_{\rm em}$ was increased and $A_{\rm FN}$ decreased to keep $I_{\rm pk}^{\rm th}$ constant, then the simulated emission current increased.

Similar to the total current, a discrepancy between the simulated and real current densities is also observed. The current densities, as calculated by the Fowler-Nordheim equation, are reported to be as high as 10^{11} A/m^2. On the other hand, the steady state peak current densities that we obtained from our simulations are only 2.2×10^8 A/m^2 at 30 MV/m and 4.6×10^8 A/m^2 at 60 MV/m — significantly less than those from experiments.

Two possible explanations for the discrepancy between experimental results and our simulations are as follows.

1. It may be wrong to blindly apply the Fowler-Nordheim equation to cavity field emitters, in order to extract the current density. The total current is known reasonably well, because the power absorbed by the current from the cavity fields can be obtained from "traditional" Q_0 versus $E_{\rm pk}$ measurements (see Section 4.8). However, little correlation has been found between the parameter $A_{\rm FN}$ (the effective area) and the true physical area of an emitter. [46] Hence, it is incorrect to assume that the real current density j is related to the current $I_{\rm FN}$ by $j = j_{\rm FN} = I_{\rm FN}/A_{\rm FN}$. Given, for example, $I_{\rm FN} = 100\ \mu$A and $A_{\rm FN} = 10^{-15}$ m^2 one might believe that $j = 10^{11}$ A/m^2 whereas in reality the physical emitting area may be larger, thereby reducing j. Furthermore, the current density need not be uniform over the entire region of the microemitter. In this case the current density may locally be very high, so as to cause melting, but the average current density is substantially lower than 10^{11} A/m^2 so that space charge effects are not as severe.

2. The simulations completely neglect the geometry of the field emitter. Our experiments (see Chapter 5) and others have shown that most emission sites are associated with conducting particles, many of which are on the order of 10 μm in size. Even a smooth, conducting sphere will enhance the electric field by a factor of 4. [47] Consider, for example, emission from a microemitter less than 0.25 μm in radius, sitting on a 10 μm macroemitter. If the latter has a geometric enhancement factor of 10, the electric field within several microns of the microemitter will then be 10 times the applied field. Hence, the relative effect of the field emission space charge is diminished considerably and correspondingly the current can be increased. Our results shown in Figure 6.23 suggest that in this case the simulation currents would be comparable to the currents observed in rf cavities.

   Apart from the macroemitter geometry, the microemitter itself also contributes to field enhancement. However because of its smaller scale it will not only enhance the externally applied field, but also the field due to the negative space charge of the emission current. Hence, the microemitter is less effective than the macroemitter at increasing the space charge limited current density.

In light of the results presented in Figure 6.23 we conclude that our simulations underestimate the rate of ion production when compared with experimental results. Since our simulation current was too low by almost a decade we were forced to use higher gas densities. It is therefore reasonable to assume that the true critical gas density is *lower*, by the same factor of 10, than predicted by our simulations.

6.5.5.2 Geometric field enhancement

In addition to the relaxation of the space charge limit placed on the current, electrons will also gain energy more rapidly in the geometrically enhanced field. This, too, has an important effect on the critical gas density, which was ignored in the simulations. For example, if the geometric field enhancement factor is 10, then emission electrons will gain 30 eV in a distance of about 0.1 μm (if the externally applied field is 30 MV/m). This distance needs to be contrasted with a value of 1 μm in the absence of any geometric enhancement, as in the simulation. As a consequence of the emitter geometry, the region of dominant ionization is moved considerably closer to the rf surface, and field

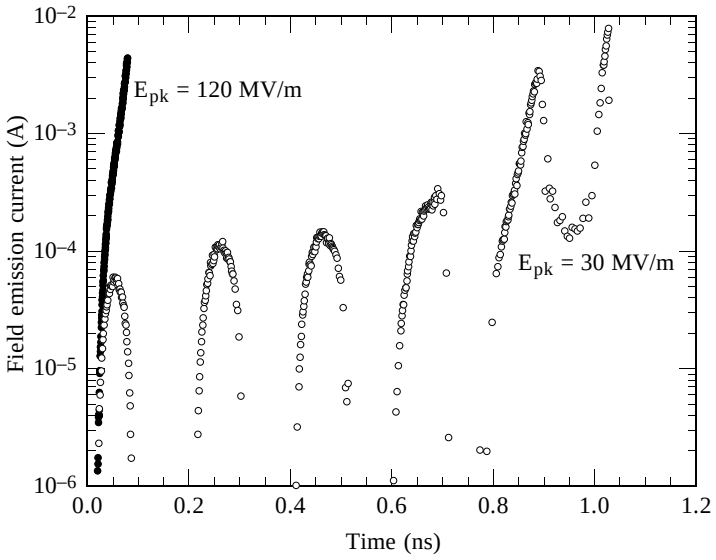

Figure 6.24: Simulated emission current when the applied peak electric field is increased from 30 MV/m to 120 MV/m. In both cases the gas flux was fixed at 5×10^{26} $\mathrm{m^{-2}s^{-1}}$.

enhancement due to the ions is increased. Fewer ions are therefore needed to achieve the same effect. Furthermore, the geometric field enhancement shifts the zone of dominant ionization into higher gas densities, so that more ions are produced per unit charge emitted.

To perform a simple check on how an enhanced applied field affects the outcome of a simulation we repeated the simulation with a gas flux of 5×10^{26} $\mathrm{m^{-2}s^{-1}}$ presented in Figure 6.16.[13] This time the applied field was quadrupled to 120 MV/m and the size of the simulation region was reduced to 8×8 $\mu\mathrm{m}^2$ so that a finer mesh could be used. The assumption was, that the field enhancement due to say a 15 μm spherical macroemitter is fairly uniform over the entire simulation region and hence equivalent to our quadrupling the applied field. The MASK results are shown in Figure 6.24, and it is very apparent that processing occurs much earlier into the simulation. Equivalently, we expect processing to occur at a lower critical gas density.

In general though it is problematic to include the emitter geometry in simulations. Much of the difficulty is due to the enhanced electric field. The mesh size needs to be small enough, so that the potential difference across one mesh element does not exceed the ionization potential of the gas used in the simulation. Otherwise ionization near the rf surface will not be modeled properly. For peak electric fields of perhaps 200 MV/m, the mesh spacing should not exceed 0.05 μm. On the other hand, the size of the simulation region has to be on the order of 10 μm or more for us to be able to track ions over several rf cycles and to include the macroemitter. The number of mesh elements therefore needs to be prohibitively large. In addition to this, the time step has to be sufficiently small, so that electrons with several hundred eV kinetic energy don't move more than one mesh element in one time step. For a mesh size of 0.05 μm one therefore finds that $dt < 4$ fs. To simulate a single rf cycle alone requires 167,000 time steps at 1.5 GHz! In these first

[13] The simulation did not use an adaptive gas density.

simulation efforts, with the computing power available to us, such simulations were not feasible. A possible solution to this dilemma is to use a variable mesh density, with a very fine mesh near the rf surface where electron energies are low, and a coarse mesh further from the emitter, where a fine resolution is not required.

6.5.5.3 Surface composition and ion bombardment

In all our simulations the gas release was governed by the vapor pressure of the heated emitter. In reality the monolayer composition of the rf surface may play an important role, and the use of the metal vapor pressure constitutes, at best, a lower limit on the gas pressure. The true gas density will depend critically on the condition of the first few monolayers of the emitter and the surrounding rf surface, and how these layers react to deposited energy on sub-nanosecond time scales. Studies have shown that the rf surface, prepared in the standard manner, is covered by several monolayers of hydrocarbons, water, and fluorine (> 50 Å [65]), and the oxide layer is 60 Å thick. [169] In particular, hydrocarbons are physisorbed and can be desorbed reasonably easily. Adsorbed hydrogen at cryogenic temperatures is also common. If just one monolayer (areal density 2×10^{19} atoms/m^2) is released over a period of 500 rf cycles (5 GHz) at typical thermal velocities of 1000 m/s, then over this short time scale the gas density at the emission site will rise to a density on the order of 10^{23} m^{-3}. This density already exceeds the values we obtained from MASK simulations for the critical density.

Even though the ions do not move very far in one rf cycle, they can gain several hundred eV, especially if the electric field is enhanced by the emitter geometry. During the positive half of the rf cycle, the ions are accelerated towards the rf surface. Upon impact, they are capable of sputtering the rf surface and releasing neutral atoms, secondary ions and electrons. For clean target surfaces, neutral particle yields vary significantly with ion type, energy, and the target specie, but do not exceed a few atoms per ion up to ion energies around 100 eV. [170–172] Little information is available on the secondary neutral particle yield for cryogenic targets covered by adsorbates we commonly encounter in rf cavities. One study [173] conducted at cryogenic temperatures revealed that for one monolayer hydrogen coverage of copper, the yield of H_2 molecules can be as high as 10^4 molecules/ion when sputtered by 5 keV H^+ ions. At 20 keV little difference was seen. Ions heavier than hydrogen may be even more effective as sputtering agents. However, even 2 keV electrons were able to sputter close to 10^3 molecules/electron if the target was covered by one monolayer.

Hydrogen is certainly one of the common adsorbates on cryogenic surfaces. [95] Even room temperature discharge experiments with copper electrodes previously subjected to heat treatment and/or electropolishing and solvent rinsing revealed that up to 10^{13} molecules were released during a microdischarge. [120] Hydrogen and hydrocarbons were the main constituents.

In our MASK simulations we found that for an initial gas flux of 10^{25} m^{-2}s^{-1}, about 320 ions impacted a region radius 0.4 μm centered on the emitter during the 1/2 rf period (at 1.5 GHz) while field emission was active. The simulation was carried out at $E_{\mathrm{pk}} = 120$ MV/m to take into account macroemitter field enhancement. The peak impact energy recorded was 800 eV, the mean energy being 200 eV. The corresponding power flux into the area is 31 MW/m^2. If each ion releases only 10 adsorbate molecules, then the increased molecular flux during the positive half of the rf cycle is 10 neutrals/ion $\times$

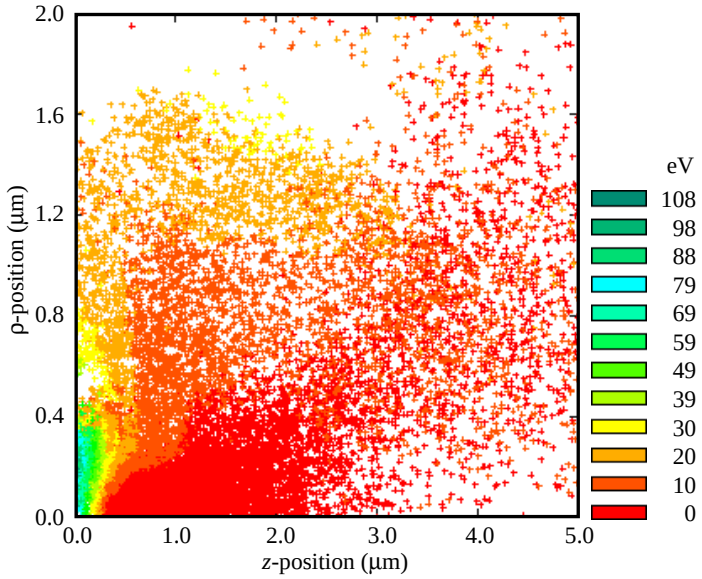

Figure 6.25: Ion bombardment of the rf surface once a plasma has been established near the emitter. The ions are accelerated by the potential created between the plasma and the rf surface. Applied field = 30 MV/m. Note that the aspect ratio is not 1:1.

320 ions $\times$ 3 $\times$ 10^9 $s^{-1}/\pi(0.4 \times 10^{-6}$ m$)^2$ = 2 $\times$ 10^{25} $m^{-2}s^{-1}$. This value exceeds the original flux used in the simulation by a factor of 2! The desorbed material will move at velocities up to 1000 m/s. Hence, after only one or two rf cycles the desorbed gas will have traveled to the point where the electrons have the optimal energy for ionization.

Once a dense plasma is formed, the rate of ion bombardment increases even further due to the large potential drop between the plasma and the rf surface. Figure 6.25 depicts a situation where the acceleration of ions in the boundary layer between the plasma and the rf surface is clearly visible. Not only will these ions sputter neutral atoms and molecules, but they also contribute to the power dissipation at the emission site. In the situation depicted in Figure 6.25 the average power dissipation from $\rho = 0$ to $\rho = 0.5$ μm was 2×10^{10} W/m^2. This value only considers the kinetic energy of the ions. In addition to this, one should really take into account the recombination energy released when ions and electrons recombine at the rf surface.

The power dissipated by the field emission current per unit area in the rf surface is given by

$$\frac{dP_{\rm FN}}{da} = \bar{j}_{\rm FN}^2 \rho \ell, \tag{6.36}$$

where ℓ is the distance traversed by the emission current in the rf surface of resistivity ρ and $\bar{j}_{\rm FN}$ is the time averaged emission current. For lack of any concrete numbers, we shall assume that this distance is comparable to the size of a microemitter, i.e., $\ell \approx 0.5$ μm. If $\bar{j}_{\rm FN} = 10^{11}$ A/m^2 and $\rho = 10^{-6}$ Ωm, one finds that[14]

$$\frac{dP_{\rm FN}}{da} = 5 \times 10^9 \text{ W/m}^2. \tag{6.37}$$

[14] 10^{11} A/m^2 is the maximum time averaged steady state current density to be expected from rf cavity field emitters.

Hence the power dissipated by the bombarding ions even this early into the rf processing sequence exceeds the Joule heating by the field emission current by a factor of four. Still, at this point the dissipated power is not yet sufficient to melt the entire macroemitter.

We therefore conclude that ion desorbed adsorbates may play an important role in initiating rf processing and that ion bombardment (in the later stages of rf processing) contributes significantly to raising the emitter temperature. Not surprisingly, the initiation of dc breakdown is observed to be very sensitive to the surface state of the electrodes. [23]

It is therefore important to gain more insight into the composition of the rf surface following standard cavity treatment techniques. In particular, adsorbate effusion rates from the rf surface over very short time spans need to be known as a function of localized energy dissipation and ion bombardment rates. Similarly the composition of the released gas has to be determined before accurate rf processing models can be developed.

6.6 Critical current

In all the simulations described, the peak field emission current prior to rf processing was on the order of 50 μA. Since the ionization rate is directly proportional to both the gas density and the total emission current, it stands to reason that the critical gas density increases if the field emission current is decreased. Our simulations demonstrated that for currents on the order of 50 μA the critical density is close to the density that can be reasonably expected to exist in the vicinity of a nearly-molten emitter. A reduction of the current by a factor of 1/10 would increase the critical density by 10, which may never be attained during steady state field emission. We therefore concluded that a total emission current threshold (about 50 μA) has to be exceed before an emitter can process, *irrespective* of the current density, provided the current density exceeds the threshold to produce the initial critical gas density.[15] This observation is in agreement with our experimental results in Chapter 5 which showed that both a critical current density and a critical current must be exceeded for starburst formation (see Figure 5.37). The total current threshold on the order of 50 μA is also consistent with the experimental results presented in Figure 5.37. However, we need to caution that this may be fortuitous, since the critical current depends on the density of gas present. The density, in turn, is ill determined since we do not know in detail the monolayer composition of the rf surface.

6.7 "Natural" field emission

Irrespective of the initial critical gas density required for rf processing, we have shown that the plasma which forms near the emitter produces a substantial electric field at the rf surface. Figure 6.26 depicts the results from one such simulation discussed earlier (see Figure 6.16, in particular the curve marked "flux = 0.5×10^{27} $m^{-2}s^{-1}$"). Plotted is the surface electric field as a function of radial position along the rf surface at the end of the simulation. The field emission current was "turned" off once it had attained a peak

[15] The threshold current density cannot be determined from our simulations, because the heating by the emission current was not included in our program. Rather, we simply assumed that the current density was sufficient to produce whatever gas density was being used in the simulations.

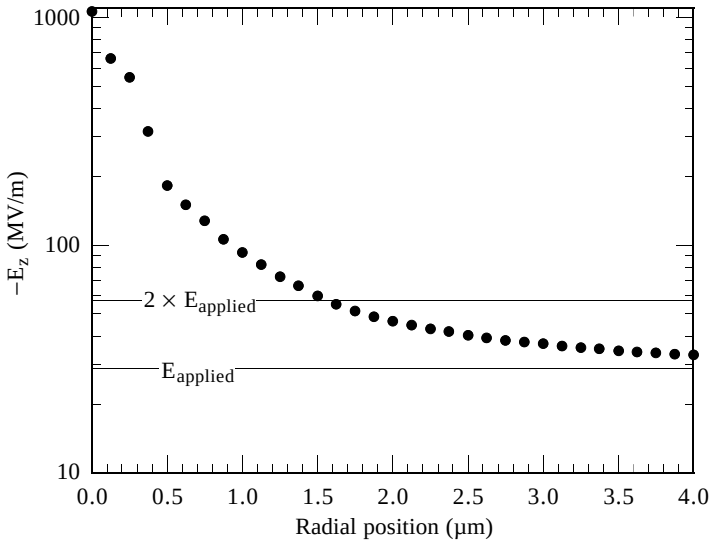

Figure 6.26: $-E_z$ versus radial position along the rf surface at the end of a simulation leading to rf processing. The field emission current was "turned off" shortly before this point in time. Note the semilogarithmic scale.

value of 0.01 A, i.e., once the rapid current increase due to the ion field enhancement had begun. A small fraction of an rf cycle later, the simulation was ended.

Figure 6.26 demonstrates the enormous fields that are possible due to the accumulation of ions near the emitter. Even though the externally applied field at this time was a mere 28.7 MV/m, the field at the emission site exceeds 1000 MV/m. Even six emitter radii out from the symmetry axis the electric field is 60 MV/m, more than twice the applied field. Greater fields probably occur, if the simulation did not have to be ended at this point in time due to the inadequate mesh size.

An important conclusion to be drawn from this result is that nearby microemitters will become active, even if their β_{FN} values are low. The original emitter with $\beta_{\mathrm{FN}} = 250$ was active at 30 MV/m. It stands to reason that now any microemitters up to a distance of 1.5 μm from the original emitter which have a $\beta_{\mathrm{FN}} \geq 125$ will emit at the same current density as the original emitter. Within a radius of 1 μm even β_{FN} values as low as 25 are sufficient for significant emission. Overall, a relatively large area is now capable of emission and a very large current can be drawn without excessive current densities being necessary (thereby bypassing space charge limitations). These large currents then are responsible for further neutral gas release and ion production and the spreading of the plasma cloud, to envelope other parts of the macroemitter. Ultimately, the entire macroemitter should therefore process.

It is also important to note that on axis the electric field exceeds 1 GV/m. At these field levels "natural" field emission becomes possible. The term "natural" in this case implies that only geometric field enhancement with β_{FN} values less than 10 is required for strong field emission. This type of emission is to be contrasted with "enhanced" field emission with $\beta_{\mathrm{FN}} = 100 \rightarrow 500$ commonly found in cavities, which requires non-geometric enhancement mechanisms to achieve such high β_{FN} values (see Section 3.2.1 and Chapter 5). At fields on the order of a few GV/m even a perfectly smooth (possibly

molten) sphere will field emit. Small bumps in the niobium rf surface will also emit. If the ionization process is permitted to continue beyond the end of our simulations, local fields on the order of 5 GV/m may be possible, at which point even a flat niobium surface field emits (and, more importantly, begins to melt due to the emission current). The field emission process at this time is no longer reliant on the presence of foreign particulates on the rf surface. We expect, therefore, that field emission progresses beyond the melting stage of the original microemitter and does not cease until all stored energy in the cavity is dissipated in the rising current. In fact, calculations [68, 161, 174] of the cathode temperature in dc discharges have also shown that the temperature locally far exceeds the melting point of the cathode. Thus, once rf processing has been initiated, it does not stop until all stored energy has been "consumed", regardless of the fact that the original microemitter may no longer be capable of emitting in the absence of a plasma. This statement is supported by the experimental data presented earlier, where we found that rf processing events are always associated with a total collapse of the cavity fields (see Figure 6.15).

6.7.1 Sheath formation

Similar observations have been made in pulsed dc discharge experiments where plasma creation has been shown to be critical in maintaining a discharge and creating new field emitters in the vicinity of the initial emission site. [22, 68] Even if no electric field is applied, discharges can be initiated by artificially creating a dense plasma by shining a laser on the cathode. [70, 137] The laser power density required to initiate (unipolar) arcing is about 5×10^{10} W/m^2, which interestingly is close to the 2×10^{10} W/m^2 recorded in our simulation due to ion bombardment (see Section 6.5.5).

It can be shown that whenever a neutral plasma comes in contact with a conducting wall, a "sheath" develops at the interface region. In this region the electron density is depleted because the electrons are very mobile and are lost to the wall. As a result a potential V_s between the plasma and the wall develops, to impede the flow of electrons to the wall. [136] In this manner charge neutrality is maintained in the plasma. The voltage drop across the sheath is approximately given by [137]

$$V_\mathrm{s} = \frac{k_\mathrm{b}T_\mathrm{e}}{2e}\ln\left(\frac{M_\mathrm{i}}{2\pi m_\mathrm{e}}\right). \tag{6.38}$$

Here T_e is the electron temperature, M_i is the ion mass and m_e is the electron mass. The thickness of the sheath is on the order of the plasma's Debye length λ_D, where λ_D is given by

$$\lambda_\mathrm{D} = \sqrt{\frac{\epsilon_0 k_\mathrm{b}T_\mathrm{e}}{n_\mathrm{e}e^2}} \tag{6.39}$$

(see, for example, Reference [136]). Hence the electric field in the sheath is of order

$$E_\mathrm{s} \approx \frac{V_\mathrm{s}}{\lambda_\mathrm{D}} = \sqrt{\frac{n_\mathrm{e}k_\mathrm{b}T_\mathrm{e}}{4\epsilon_0}}\ln\left(\frac{M_\mathrm{i}}{2\pi m_\mathrm{e}}\right). \tag{6.40}$$

Solving for n_e, one finds

$$n_\mathrm{e} = \frac{4\epsilon_0 E_\mathrm{s}^2}{k_\mathrm{b}T_\mathrm{e}\ln^2(M_\mathrm{i}/2\pi m_\mathrm{e})}. \tag{6.41}$$

We encountered electron energies in the plasma on the order of a few eV (see, for example, Figure 6.12). Similar electron temperatures were also measured in dc discharge experiments. [21, 121] For $M_i = 24$ amu we therefore require a plasma density of $n_e = 6 \times 10^{23}$ m^{-3} to achieve an electric field of 1 GV/m. This density is comparable to the plasma densities we recorded during our simulations.

Peak plasma densities recorded during dc discharge experiments can be as high as 10^{26} m^{-3} [21], when the discharge current is on the order of 10's of Amperes. Even higher densities are reported in Reference [69]. Assuming that similar densities are achieved in rf cavities, and that $T_e = 5$ eV, then we expect the field near the emitter to be about 13 GV/m. This value is greater than the field required to draw an emission current density of 10^{12} A/m^2, even without any geometric field enhancement.

This model of an expanding high density plasma creating the conditions required for natural field emission therefore predicts that broad areas of the rf surface in contact with the plasma will emit and melt. This serves to explain why frequently areas several 10's of micrometers in diameter of molten niobium ("broccoli") are found at emission sites (see, for example, Figure 5.33).

6.7.2 Satellite craters

So-called satellite craters, which often surround an emission site in rf cavities (see Figures 5.39 and 5.42) and in dc discharges [138], are also explained by this mechanism. Small defects or particulates are likely to exist in the vicinity of a macroemitter and act as emission centers once the plasma from the central emission site envelopes them. Ejected liquid drops from the central emission site will also serve as emission sites if they come into contact with the plasma. They too may explode in the same event. The pressure exerted on the molten rf surface by the highly non-uniform plasma can exceed 1000 atm at densities of 10^{26} m^{-3} and plasma temperatures of 5 eV. These forces tend to eject material laterally. [22] Ejected drops out to tens and even hundreds of micrometers have been observed in several cases (see, for example, Figure 5.28). Microtips can also be created due to stretching of liquids in the presence of a strong electric field and have been observed in dc field emission. [68] The central tip of "broccoli" features found at cavity emission sites suggest that such stretching occurs during rf processing as well (see Figure 5.40). Geometric field enhancement in excess of $\beta_{FN} = 10$ can be the result of this stretching mechanism. [68] All these features are potentially powerful field emitters, *provided they come into contact with the plasma.*

Auger and EDX analyses of field emitters in the past have shown that foreign elements can always be found at the *central* emission site whereas *in many cases satellite craters lacked contaminants.* [65] This fact is consistent with the idea that satellite emitters become active due to plasma field enhancement, whereby even simple geometric structures made of niobium or small foreign particles can emit and explode. Any remaining contaminants are then very difficult to detect.

6.8 Starburst formation

We believe that starburst formation is directly related to the generation of a plasma during rf processing. Experimental evidence pointing to this fact was already presented in the previous chapter. The mechanisms leading to the star-shaped and filamentary

structure of most starbursts, however, are still not explored by simulations due to the starburst's large size (> 100 μm). We can only speculate at this point in time as to their nature. The structure of a starburst suggests that it is created due to an instability, possibly resulting from the self magnetic field of the augmented emission current. We presume that such an instability will most likely manifest itself when the emission current is at its peak, i.e., during half of an rf cycle. If so, this model is capable of explaining the inverse frequency scaling of starbursts, as shown in Figure 5.43. However, since at present we can only speculate, we defer the discussion of the model to Appendix B.

6.9 Summary

We have shown by simulations that the electron impact ionization of neutral gases released by a field emitter can drastically affect the temporal evolution of the field emitter. The qualitative model of rf processing discussed in Chapter 5, in particular Figure 5.36, has been confirmed by the MASK simulations.

Ions are created within a few micrometers of the rf surface and produce a substantial field enhancement at the emission site, leading to a large increase of the field emission current over the sub-milliampere currents observed in steady state operation. Correspondingly, the power dissipated by the emission current in the emitter increases substantially, thereby augmenting the gas evolution (and hence the ion production). Ion bombardment of the rf surface also augments the surface temperature and desorbs neutral gases from the rf surface. Simulations predict that the minimum ("critical") gas density initially required at the emission site to process an emitter lies in the range of 3×10^{20} m^{-3} to 3×10^{22} m^{-3}. Due to numerous simplifying assumptions made for the simulations, especially our neglect of the emitter geometry, we believe that the true critical density may be considerably lower still. These densities are consistent with the vapor pressure of metallic emitters near their melting point. However, we suspect that adsorbed gases may be a significant source of neutral gas during the initial phase of rf processing. These gases are released due to the high temperatures created by field emission Joule heating and to a large extent by ion bombardment.

Our thermometry results predict that a fairly high current density ($\approx 10^{11}$ A/m^2) is required to melt an emitter in order for the critical gas density to be attained. *However, the rf processing mechanism itself is dependent on the total emission current rather than the current density.* The critical current required to rf process an emitter depends directly on the critical gas density and is ill determined at present. Our simulations yield a value of $50 - 100$ μA as an estimate of the critical current.

During rf processing, electric fields as high as 10 GV/m may be produced by the plasma, and field emission currents rise into the ampere and 10 ampere ranges. Locally, electric fields are so large that unassisted ("natural") field emission becomes possible over a significant region of the macroemitter. This mechanism is responsible for melting areas of the rf surface on the order of 10 μm in size and initiates field emission at nearby weaker emitters. Once natural field emission is initiated, field emission does not cease until all stored energy in the cavity has been dissipated in the emission current. This process requires less than 1 μs. Since substantial portions of the macroemitter have now melted, it is no longer capable of field emitting at low (≈ 30 MV/m) fields. In essence the emitter has rf processed.

Chapter 7

New insights into thermal breakdown and multipacting

7.1 Introduction

We now leave the realm of field emission and discuss our studies of two further high field loss mechanisms — thermal breakdown and multipacting. Thermal breakdown, in particular, is still one of the main limitations of superconducting cavities, despite recent advances in improving the purity of niobium. Apart from thermal breakdown being induced by field emission, we will show that both particles and weld defects can be the source of breakdown.

Although thermal breakdown is interesting in its own right, we will also discuss the surprising discovery that it increases the cavity's residual resistance. This holds true even at low fields when thermal breakdown is no longer active, as is confirmed by a reduction of the cavity quality. We will show, that the losses are likely due to the creation and trapping of magnetic flux during the thermal breakdown event.

Furthermore, we already provided examples of field emission activation due to gases released during thermal breakdown (see Chapter 5). Thermal breakdown, thus, can also affect the high field losses in a cavity. Hence, for several reasons, it is important to understand the causes of thermal breakdown and to eliminate them.

It was believed that multipacting does not occur in the elliptical (LE1) cavity shape. Certainly this shape has been proven to be free of one-point multipacting. Our discovery by high speed thermometry of two point multipacting along the equator therefore came somewhat as a surprise. We will show temperature maps that reveal multipacting in progress and describe numerical simulations which confirm the temperature data. Although multipacting itself could be processed away and did not limit the cavity performance, we will demonstrate that, similar to thermal breakdown, it increases low field losses by flux trapping. There even are indications that in one case such trapped flux was subsequently responsible for precipitating thermal breakdown at high fields.

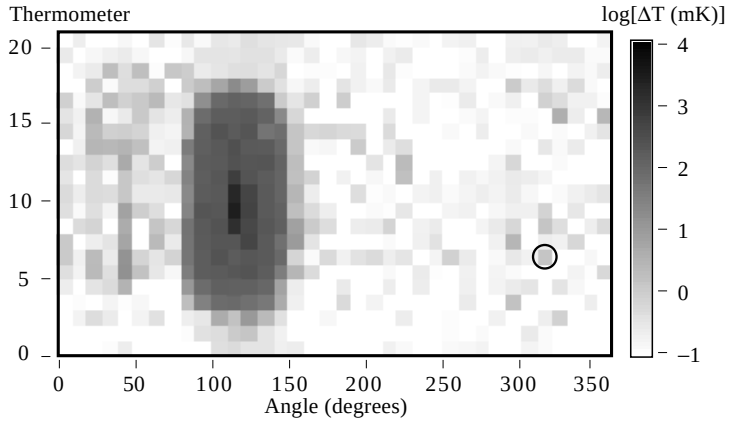

Figure 7.1: Single map from a sequence of temperature maps obtained while thermal breakdown was in progress in LE1-31. During the acquisition of this map at $E_{\rm pk}$= 32.5 MV/m a quench occured. The acquisition time of this map was 0.14 s. The logarithm of ΔT is plotted to demonstrate the extended nature of the breakdown affected area. The temporal evolution of the circled site's temperature is plotted in Figure 7.3.

7.2 Thermal breakdown

7.2.1 Observation of typical breakdown events

One of the strengths of our thermometry system lies in its ability to time resolve subsecond processes. By taking a "movie" of temperature maps (time interval 0.14 s) we can identify the location of thermal breakdown very precisely. Altogether, we observed various types of thermal breakdown in seven cavities, and the following are representative examples.

7.2.1.1 Thermal breakdown triggered by defects

Figure 7.1 depicts an example of thermal breakdown in progress. During the quench temperature signals far in excess of 1000 mK were observed locally.[1] Using cw maps obtained prior to the breakdown we were able to correlate an unusually high resistivity region with the center of the breakdown region (see Figure 7.2). The temperature of the circled region in Figure 7.1 as a function of time is depicted in Figure 7.3, which illustrates the repetitive nature of thermal breakdown, as discussed in Section 3.2.2. All breakdown events in this cavity were essentially the same as those shown in Figure 7.1. No field emission heating could be correlated with the breakdown area and all attempts to process the cavity to higher fields failed. Thermal cycling also had no effect on the nature of the thermal breakdown. In another, similar case of a thermal breakdown limited cavity (LE1-32) we even re-etched the cavity to remove more than 20 μm from the rf surface, only to find that the breakdown field had not changed significantly. This observation demonstrates the persistent nature of some defects.

[1]Note that the thermometers are only calibrated up to a ΔT of 2600 mK. Greater values were obtained from an extrapolation of the thermometer calibrations and are unlikely to be accurate.

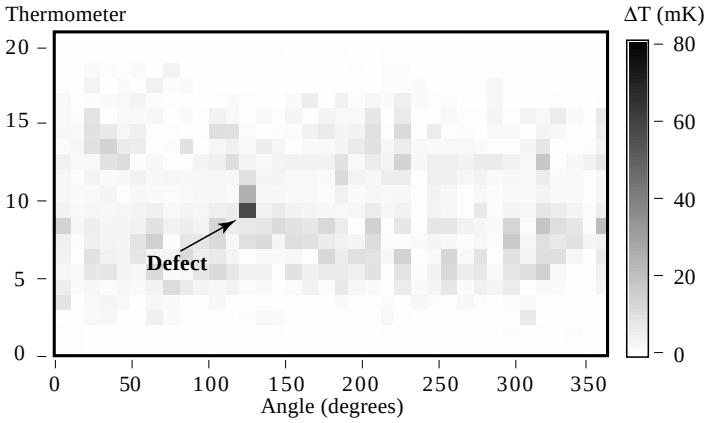

Figure 7.2: Temperature map at 29.6 MV/m of the same cavity as in Figure 7.1, taken before any thermal breakdown events we recorded.

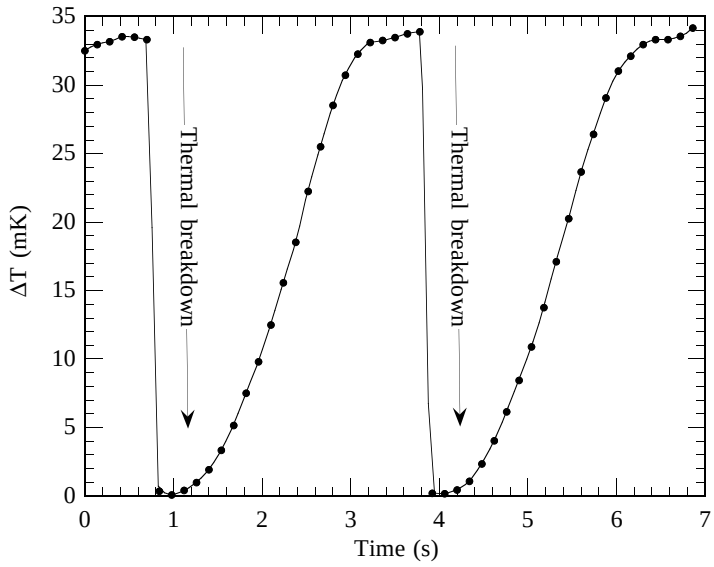

Figure 7.3: Temperature signal of the circled site in Figure 7.1 as a function of time.

7.2.1.2 Thermal breakdown triggered by field emission

We also observed field emission induced thermal breakdown, as shown in the temperature map of cavity LE1-21 at 28.4 MV/m (Figure 7.4(a)). In this case, the breakdown site was correlated with field emission related heating in the general vicinity (see Figure 7.4(b)), whereas no low field defect could be identified at that location. Note that the center of the breakdown region does not coincide with the maximum cw heating (or the actual location of the emitter). This is due to the fact that breakdown is initiated in a region where the heating by the field emission electron bombardment is significant, *and* the magnetic field is large, so that the breakdown region can "propagate."

It is possible to process through field emission related thermal breakdown by eliminating the emitter. For example, we were able to successfully process the emitter in Figure 7.4 and thermal breakdown ceased to occur at 28.4 MV/m. This proves that

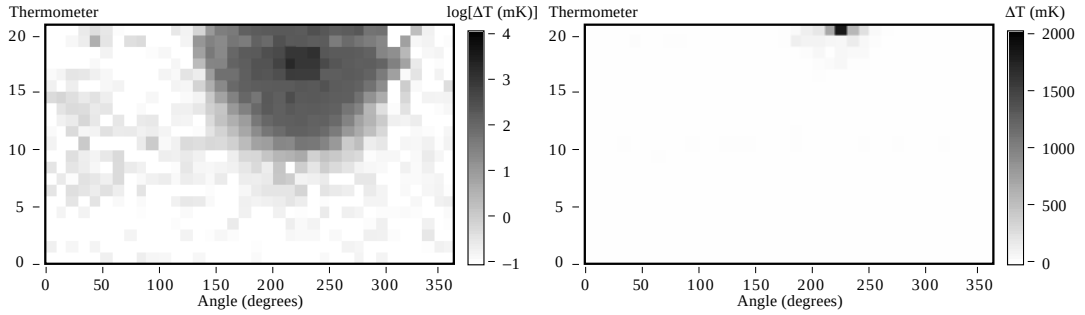

(a) (b)

Figure 7.4: (a) Temperature map taken while field emission induced thermal breakdown was in progress in cavity LE1-21. The peak electric field was 28.4 MV/m. Note that the logarithm of ΔT is plotted to demonstrate the extended nature of the breakdown affected area. (b) High field temperature map taken before thermal breakdown occured in (a). The field emission related heating at 220° is responsible for the thermal breakdown.

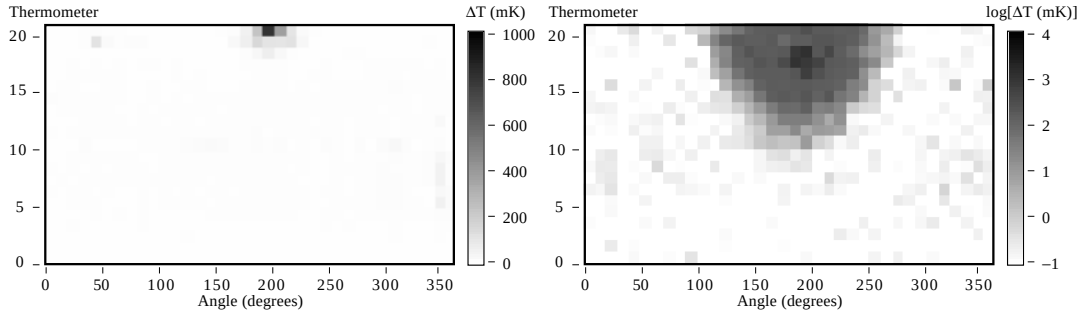

(a) (b)

Figure 7.5: (a) Field emission site that appeared at 190° in cavity LE1-21 after the site in Figure 7.4(b) processed. At 38 MV/m this site initiated thermal breakdown as shown in (b).

thermal breakdown was indeed caused by field emission bombardment and not by a stable defect. When we raised the fields further, another emitter became active at 190° as shown in Figure 7.5(a). This site also caused thermal breakdown (now at 38 MV/m) as shown in the same figure. Again the center of the breakdown region does not quite coincide (in S) with the peak heating due to the field emitter. Similar results have been obtained with field emitters in other cavities.

7.2.2 Microscopic analysis of defects

Similar to the breakdown site in Figure 7.2, defect related breakdown occurs mostly on or very near the equator (high magnetic field region). Four out of 10 cavities were limited by breakdown sites in this category (a fifth cavity was limited by defect related breakdown several centimeters from the equator). Although the magnetic field is high in this region, it actually peaks some distance from the equator and is significant over a considerable fraction of the cavity (see Figure 2.2). A priori one would therefore expect

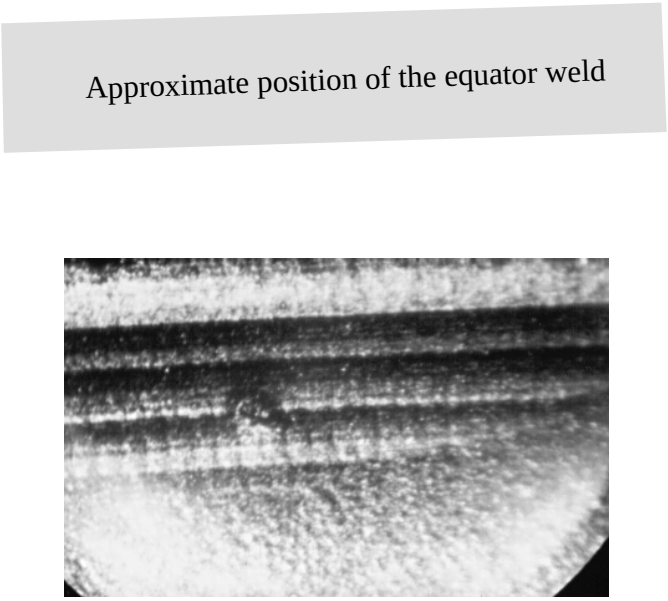

Figure 7.6: Defect found in cavity LE1-31 at the thermal breakdown site in Figure 7.1. Its size is estimated to be about 1 mm. The breakdown field was $E_{\rm pk} = 32.5$ MV/m, $H_{\rm tb} = 790$ Oe.

breakdown sites to be evenly distributed throughout the high magnetic field region. However, since the defects lie preferentially on or near the equator, we suspect that the electron beam welding process along the equator introduces an unusually high number of defects. In one case, for example, the breakdown center was correlated with the end of the weld. Possible defects include contaminants concentrated at the rf surface by the welding process or geometric defects due to, for example, weld spatter.

7.2.2.1 Non-particulate defects

Unfortunately, we were unable to examine most weld defects under the microscope, because the cavities were cut along the seam. In the case of the thermal breakdown depicted in Figure 7.1, we chose not to destroy the cavity and examined it with a mirror instead. The large (≈ 1 mm) defect shown in Figure 7.6 was found at the location predicted by temperature maps. The defect appears to be due to a spattering process which may have occurred during welding. It survived a 1 hour etch in nitric acid which is consistent with it being made of niobium. Figure 7.7 depicts the temperature signal recorded at the site versus $E_{\rm pk}^2$. A similar plot for a random site in the same cavity is included for comparison. A linear dependence of ΔT on $E_{\rm pk}^2$ is expected for ohmic power dissipation, provided $R_{\rm s}$ is constant. Clearly this is not the case for the thermal breakdown site. In fact, the temperature signal follows very closely a $\Delta T \propto E_{\rm pk}^4$ dependence.

Figure 7.8 is another example of a defect that was closely correlated by thermometry to be the source of thermal breakdown at 38 MV/m (925 Oe). No foreign materials were detected by an EDX analysis. Depth profiling indicates that the defect is a depression at least 100 μm deep, with steep walls.

At fields just below the breakdown threshold, field emission activity was visible in the vicinity of the defect, as shown in Figure 7.9(a). However, the center of thermal

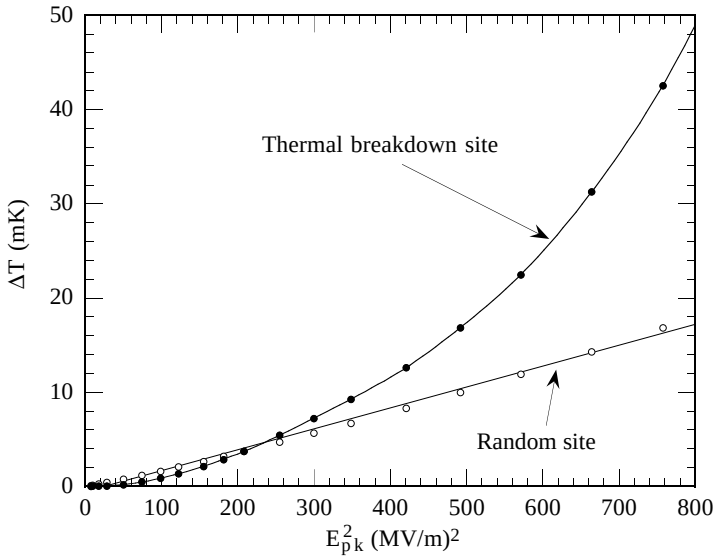

Figure 7.7: ΔT versus $E_{\rm pk}^2$ recorded at the site shown in Figure 7.6. A second, random site from the cavity is included for comparison. A linear dependence indicates regular ohmic heating with $R_{\rm s}$ = constant.

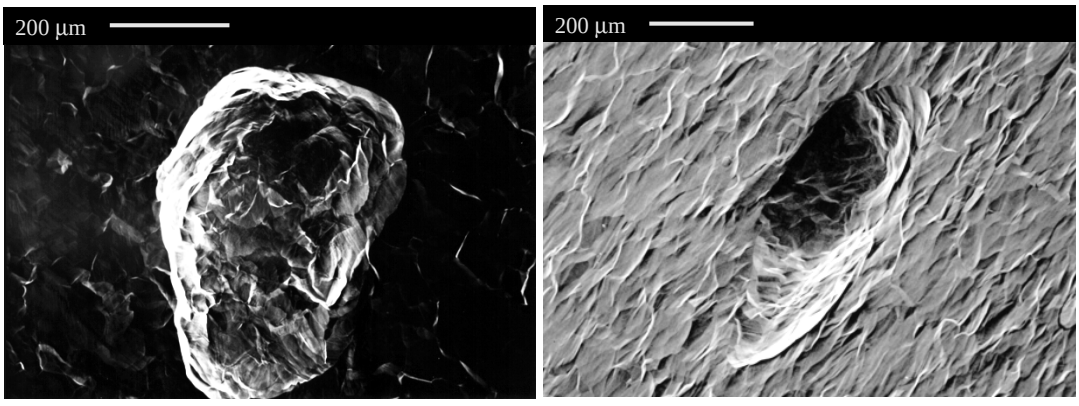

(a) (b)

Figure 7.8: Defect found in cavity LE1-34, which was limited by thermal breakdown centered on this site at $E_{\rm pk}$ = 38 MV/m, $H_{\rm tb}$ = 925 Oe. (a) Picture taken at normal incidence, (b) same feature observed at a glancing incidence.

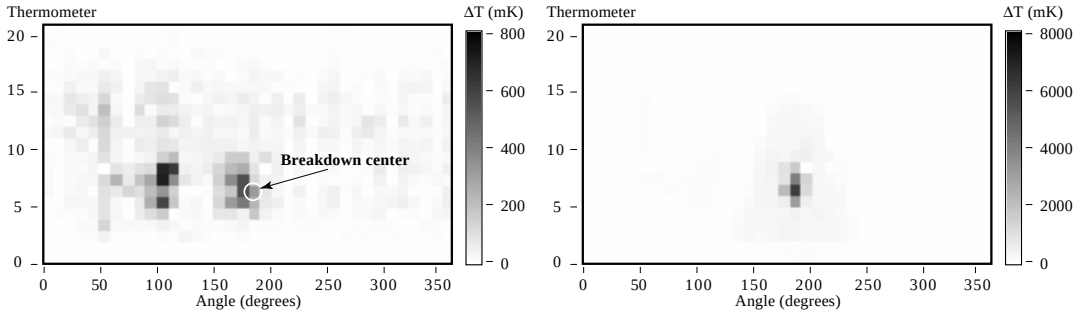

(a) (b)

Figure 7.9: Cavity LE1-34 (a) just before thermal breakdown, and (b) during thermal breakdown. Both maps were obtained at ≈ 38 MV/m.

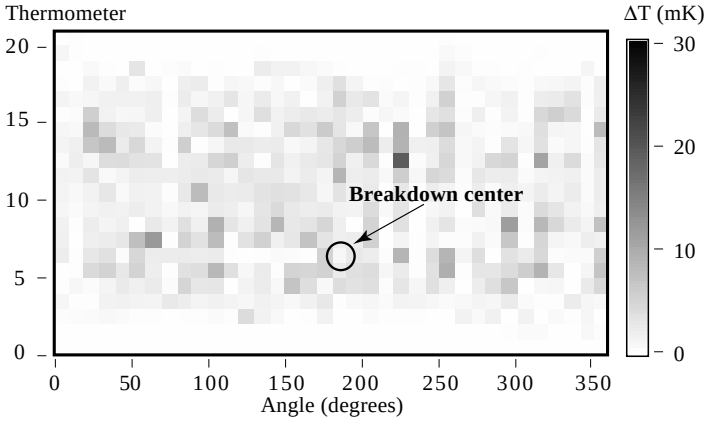

Figure 7.10: Temperature map of cavity LE1-34 at low fields before thermal breakdown in Figure 7.9. No unusually high losses were detected at the breakdown location.

breakdown occurring in Figure 7.9(b) is shifted by 10° with respect to the field emission heating and is centered on the defect in Figure 7.8. The defect did *not* cause any unusual resistive heating at low fields, as demonstrated in Figure 7.10. We therefore suspect that it is the combination of field emission heating and the magnetic field enhancement by the defect that precipitated thermal breakdown. It may even be possible that the superheating field (depressed at high temperatures) was exceeded locally due to field enhancement, so that breakdown was initiated by H rather than H^2 (see Section 3.2.2). Calculations with SUPERFISH for a 90° corner demonstrated that the field enhancement at the corner scales as $R^{1/3}$, where R is the radius of the corner. [175] A magnetic field enhancement of over a factor of 10 was calculated for $R = 25$ μm. Thus, it is possible that such enhancement at the edges of the pit in Figure 7.8 caused H to exceed $H_{\rm sh}$, thereby precipitating thermal breakdown.

Similar observations were made in the past with holes in TIG welds. [75] Figure 7.11 shows an example of such a site, this one having triggered thermal breakdown at 155 Oe. Again we observe sharp corners, capable of enhancing the magnetic field.

To ensure that the thermal breakdown was not caused by some other, highly resistive

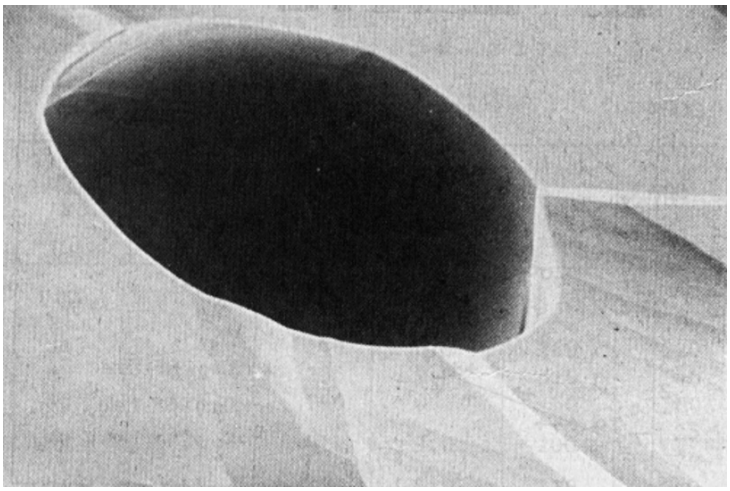

Figure 7.11: A hole in a TIG weld, which caused thermal breakdown at 155 Oe. The diameter is about 130 μm.

particle, we can calculate the particle size required to trigger thermal breakdown at 925 Oe. If $R_s = 10$ mΩ then Equation 3.15 yields a particle 56 μm in diameter. It is unlikely that such a large particle would have gone undetected in the microscope. Furthermore, we would have certainly been able to detect the low field heating of such a particle. Thus we can rule out the possibility that breakdown was initiated by a high loss particle.

7.2.2.2 Particulate defects

The two defects shown earlier are part of the niobium material. This need not be always the case. Figure 7.12(a) depicts a temperature map obtained with cavity LE1-Heraeus, showing a potential breakdown site. This site did not cause breakdown in the cavity up to a emission limited field of $E_{pk} = 24.5$ MV/m. The heating at this site is consistent with ohmic losses as is demonstrated by Figure 7.12(b).

The copper particle in Figure 7.13 was responsible for the power dissipation. Other elements found included carbon, oxygen, and some iron. Interestingly, this site is not a weld defect or an inclusion. Rather, it appears to have fallen into the cavity following or during the cavity cleaning procedure. Copper scrapers are commonly used to prepare the test stand flanges, so it is not surprising that copper particles contaminated the cavity. The rf probes and the gaskets of the vacuum system are also made of copper and are a potential source of particles.

A root-like structure at the particle's base appears to have attached itself firmly to the rf surface. The roots seem to have melted during the test. This fact demonstrates that even ohmic heating can raise the temperature of defects to above their melting point, most likely at an early stage. This fact will be discussed in more detail in Section 8.4 which deals with particles in cavities. A loosely adhering particle is not in good thermal contact with the rf surface and hence little power input (≈ 10 mW) is required to raise its temperature. [130] However, once the contact areas melt, defect cooling by the substrate is substantially improved and the particle temperature remains below the melting point.

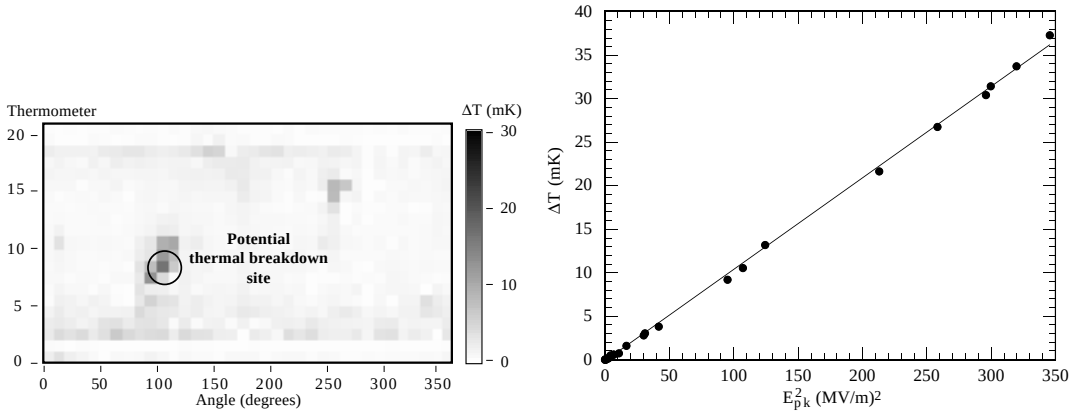

(a) (b)

Figure 7.12: (a) Temperature map of cavity LE1-Heraeus at 14.6 MV/m. A potential thermal breakdown site is circled. (b) Temperature signal of the circled site as a function of $E^2_{\rm pk}$. The linear dependence demonstrates that the heating is ohmic and that $R_{\rm s}$ is field independent.

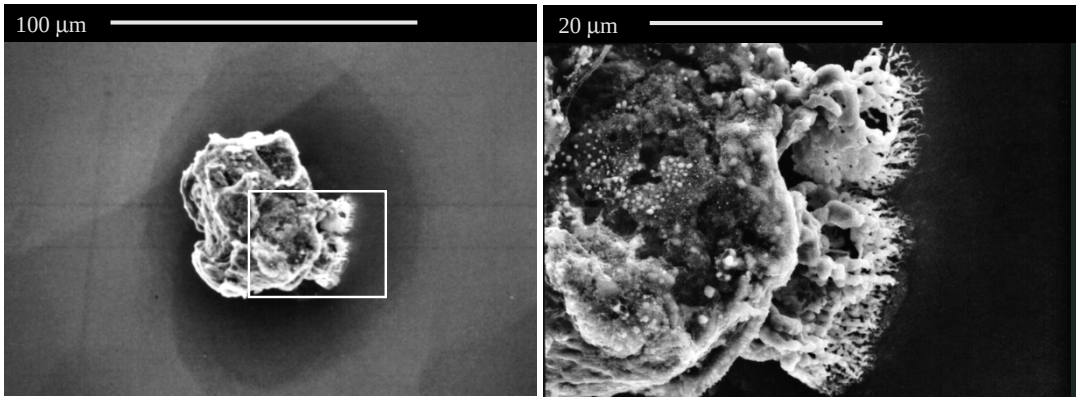

(a) (b)

Figure 7.13: A particle found at the circled location in Figure 7.12. The right image is a magnified view of the framed area. The main contaminants were copper, carbon, oxygen, and iron.

By this time the particle in Figure 7.13 had attached itself firmly to the rf surface. We were unable to dislodge the particle with a 15 psi nitrogen gas jet. Studies at Saclay have also shown that such "welding" of particles to the rf surface occurs for field emitters when the base partially melts. [64, 67]

At $E_{\rm pk} = 18.7$ MV/m a temperature rise of 37 mK was measured. The magnetic field at the defect is about 460 Oe (= 36,600 A/m). We recorded a low field Q_0 of 6×10^9 and a thermometer efficiency of 25 %. The expected background heating due to the niobium surface resistance should amount to about 3.5 mK in this case, and the particle is responsible for a ΔT of 33.5 mK.

Calculations based on Equation 8.8 derived in Chapter 8 show that the size of the particle found in the microscope is consistent with the temperature signals we recorded.

In Section 8.4 we show that the particle size is roughly given by

$$r_{\rm d} \approx \sqrt{\frac{c_{\rm d}\Delta T}{\pi\epsilon_T\eta_T R_{\rm d}}}\frac{1}{H}. \tag{7.1}$$

H is the local magnetic field, η_T is the thermometer efficiency, $c_{\rm d}$ is a correction factor that is unity in the case presented here, $R_{\rm d}$ is the particle's surface resistance and ϵ_T is a cavity dependent parameter.[2] We don't know the surface resistance of the particle, in part because its temperature is not known. Pure copper at room temperature has an $R_{\rm d} = 10$ mΩ. To take into account the other contaminants detected we consider 20 mΩ to be a reasonable value for $R_{\rm d}$. Using (7.1) with $\epsilon_T = 1.3$ mK/mW one finds $r_{\rm d} = 35$ μm. This value agrees surprisingly well with the size of the defect in Figure 7.13.

Given the size of the particle we can estimate the field at which we can expect thermal breakdown to take place. The actual radius of the particle is roughly 20 μm. Using the simulation results depicted in Figure 3.11, we find a breakdown field of almost 950 Oe for RRR 300. Note that the simulations were carried out for $R_{\rm d} = 8$ mΩ. Using the scaling of $H_{\rm tb}$ with $R_{\rm d}$ in (3.15) we therefore anticipate a breakdown field of $H_{\rm tb} = 950$ Oe $\times \sqrt{8/20} = 600$ Oe for the copper particle. The corresponding peak electric field is 24.4 MV/m.

The simple model of Equation 3.15 yields $H_{\rm tb} = 31.5$ MV/m which compares favorably with the simulation results. During the actual tests of the cavity, it was shown to be breakdown free up to 24.5 MV/m at which point field emission loading prevented us from raising the fields further. The calculations suggest that thermal breakdown was imminent.

7.2.3 Cavity quality degradation

We will describe below the new discovery, that thermal breakdown can change the low field losses. In the past this effect could not be observed due to insufficient temperature resolution of thermometry systems and/or due to their insufficient speed, so that it was difficult to obtain extensive and accurate pre- and post-breakdown data.

7.2.3.1 Modification of the surface resistance

Consider, for example, the defect related thermal breakdown in progress in Figure 7.14(a). This defect was persistent. Neither thermal cycling nor a 20 μm chemical etch had any significant effect on the breakdown field. (Later, the breakdown center was correlated with the end of the equator weld.)

Figure 7.14(b) compares the cavity low-field surface resistance after a series of thermal breakdown events with the surface resistance beforehand, by taking the ratio. The surface resistance before and after was measured at $E_{\rm pk} = 10$ MV/m, well below the breakdown field of ≈ 20 MV/m.

Most of the cavity is unaffected by thermal breakdown. However, the region directly involved in the quench has clearly increased its surface resistance by a substantial amount. The increases recorded were as high as a factor of 16. Figure 7.15 depicts the changes undergone by one of the affected sites as thermal breakdown progressed. In

[2] ϵ_T is the temperature rise at the exterior of the cavity wall per unit power dissipated in a point defect on the inside. It is obtained from thermal codes and is tabulated in Table 8.1.

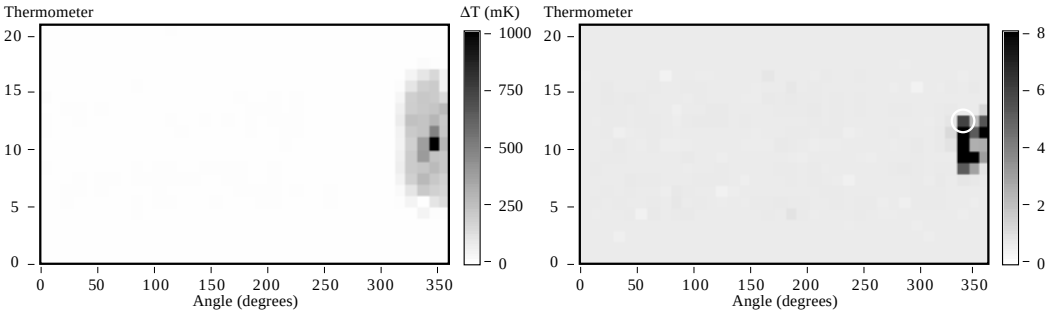

Figure 7.14: (a) Defect initiated thermal breakdown in progress in cavity LE1-32. Even a 20 μm etch was unable to remove the defect. (b) Ratio of the surface resistance after several breakdown events to that before breakdown. Dark regions indicate that the surface resistance increased.

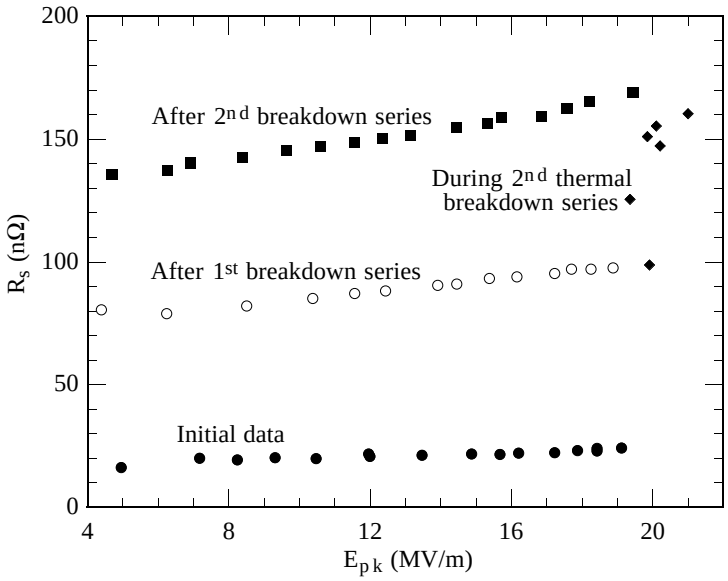

Figure 7.15: Surface resistance at the circled site in Figure 7.14(b) during and following a series of thermal breakdown events in the cavity.

particular we found that multiple breakdown events could result in successively larger $R_{\rm s}$ values, as is revealed by the data obtained during the second series of breakdown events.

Prior to any breakdown events, the recorded surface resistance was about 15 nΩ, close to the mean cavity surface resistance of 14 nΩ ($Q_0 = 2\times10^{10}$). The total effect of all the breakdown events was to raise the surface resistance by a factor of nine to 135 nΩ! If the entire cavity had been affected in this manner, the Q_0 would have dropped to 2.2×10^9. In fact, only a small fraction of the cavity surface is involved in the process, so that the Q_0 drop is significantly less. Nevertheless a Q_0 degradation was observed, as shown in Figure 7.16, which corroborates the calorimetry data.

The effect of thermal breakdown on the cavity $R_{\rm s}$ described here was observed in *all*

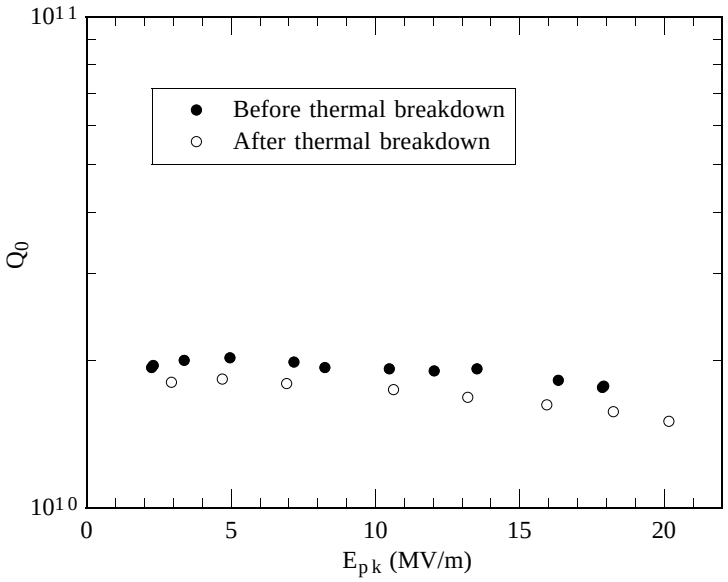

Figure 7.16: Q_0 versus $E_{\rm pk}$ data obtained from power measurements on cavity LE1-32, prior to and after thermal breakdown events like those in Figure 7.14(a).

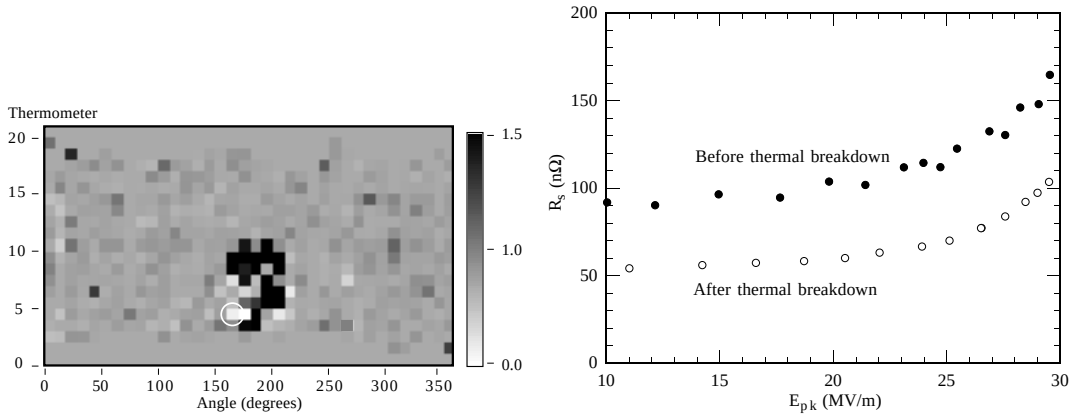

Figure 7.17: Changes of $R_{\rm s}$ following thermal breakdown in cavity LE1-34 at 37 MV/m. (a) Ratio of $R_{\rm s}$ at 12 MV/m after and before thermal breakdown, showing that both increases as well as reductions in $R_{\rm s}$ occured. (b) $R_{\rm s}$ versus $E_{\rm pk}$ of the circled site in (a) showing that the surface resistance reduced following thermal breakdown.

cavities that were limited by defect related thermal breakdown. In some cases, however, a few sites towards the periphery of the affected region would actually reduce their surface resistance, as shown in Figure 7.17.

Whenever we cycled an afflicted cavity to room temperature, the surface resistance of breakdown affected regions would revert to their original values prior to any thermal breakdown. If thermal breakdown was triggered again following the thermal cycle, the $R_{\rm s}$ would increase once more. A second thermal cycle could be used to remove the losses

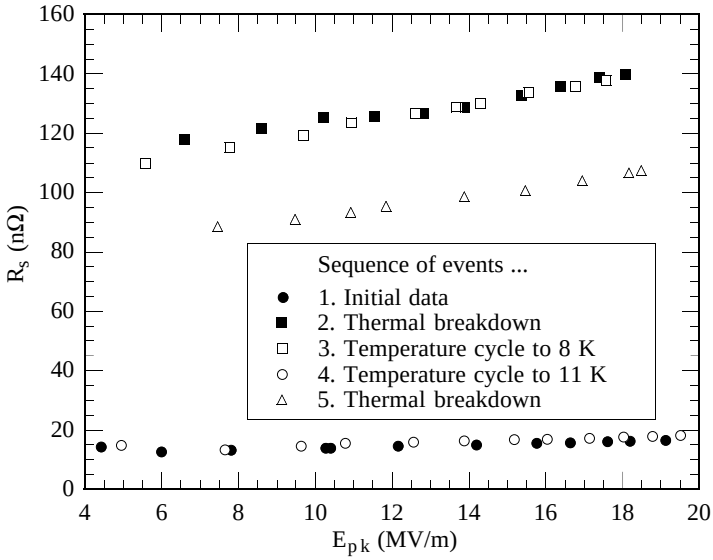

Figure 7.18: Surface resistance recorded by thermometer 11 at 330° with cavity LE1-32 (just below the circled site in Figure 7.14(b)). The data was obtained in the following sequence: 1. before any thermal breakdown, 2. following a series thermal breakdown events, 3. following a thermal cycle to 8 K, 4. following a second thermal cycle to 11 K, and 5. following a new series of thermal breakdown events.

again.

To investigate this effect further, we attached a cryogenic linear temperature sensor (CLTS) to the equator of cavity LE1-32 near the thermal breakdown center in Figure 7.14(a). The cavity fields were raised until thermal breakdown was observed. Low field data prior to and after thermal breakdown confirmed that the R_s increased as in Figure 7.14(b). Liquid helium was then transferred out of the cryostat until the CLTS temperature drifted to a desired value. A retransfer of liquid helium then rapidly cooled the cavity to 4.2 K before we pumped the bath to further lower the temperature to 1.6 K.

A temperature cycle to 8 K had no effect on the cavity surface resistance. Surprisingly, though, upon cycling to 11 K all increased losses reduced back to their original values.[3] These results are shown in Figure 7.18. Following the temperature cycle to 11 K, the cavity fields were raised once more until thermal breakdown took place, again resulting in increased low field losses. In many cases (as in Figure 7.18) the order of magnitude of the increases was the same as previously. However, the actual values were not identical to those observed after the first breakdown sequence.

Initially we had suspected that gases evolving from the hot defect were being redistributed near the breakdown site, resulting in the increased losses. This hypothesis was however ruled out by the results from the thermal cycles to 8 K and 11 K. Furthermore, this theory is inconsistent with the observation that the increased losses saturate following a few breakdown events, yet after a temperature cycle to 11 K they are reactivated to their full extent by a new series of breakdown events.

[3]Tests of another cavity showed that regions which reduced their losses were unaffected by a cycle to 12 K, a point we will return to shortly.

7.2.3.2 Flux trapping explanation

Our data suggests that the critical temperature $T_c = 9.22$ K plays an important role in eliminating augmented rf losses. In fact the losses we observed are reminiscent of a similar effect detected in Nb_3Sn coated niobium cavities. These cavities were investigated because Nb_3Sn has a critical temperature almost twice that of pure niobium (18.2 K). Tests have shown that Q_0 values in excess of 10^{10} can be achieved. [176] Curiously, though, the Q_0 would degrade drastically, falling by more than a factor of two, if the cavity was cooled through 18.2 K at rates exceeding one Kelvin every five minutes. [177]

This result was attributed to currents driven by a strong thermovoltage that is generated between the niobium and Nb_3Sn layers. These currents produce magnetic flux that is trapped if the cavity is cooled too rapidly, resulting in increased losses. [177]

Similar to our observations with niobium cavities, a quench in a Nb_3Sn cavity resulted in increased losses, that could only be removed by warming the cavity above T_c and cooling slowly again. The increased losses were also explained by the thermovoltage theory, since the cavity is cooled very rapidly through T_c following thermal breakdown.

However, in the case of our niobium cavities no two dissimilar metals exist, yet we observe the same (although reduced) effect. Hence, we must consider the temperature gradients, rather than thermocouple effects, as the driving force behind the flux generating currents.[4] This phenomenon is known as the *Seeback effect*. [178]

Following thermal breakdown and the collapse of the cavity fields, a centimeter sized region surrounding the defect is normal conducting. The cavity then is cooled very rapidly by the helium bath, and calculations show that the normal conducting region shrinks and disappears in as little as a few to 10's of milliseconds. [73, 179] These times are consistent with our observation that two successive temperature maps, taken 0.14 seconds apart, never capture the same thermal breakdown event. Large, radial temperature gradients, that drive the thermocurrents, exist near the rapidly shrinking normal conducting–superconducting boundary. Magnetic flux created by the thermocurrents can be trapped as the niobium reverts to the superconducting state. An increased surface resistance results.

It should be emphasized that there are two important aspects to this flux trapping mechanism: 1. high temperature gradients are essential to create magnetic flux, and 2. rapid temperature changes are needed when cooling through T_c to trap the flux.

The electric field generated by the Seeback effect is given by

$$\mathbf{E} = S_T \boldsymbol{\nabla} T, \tag{7.2}$$

S_T being the thermopower. [178] We already showed that defect temperatures can be very elevated with respect to the helium bath. Furthermore, during thermal breakdown, temperatures over a large region easily exceed T_c as demonstrated by our thermometry results.

Thermopowers vary in sign and magnitude from material to material and are temperature dependent. At room temperature, observed thermopowers for niobium are on the order of microvolts/Kelvin [180], whereas at cryogenic temperatures, values for silver and copper[5] are about 1/10 of a microvolt/Kelvin near 10 K. [181, 182] The length scale

[4] We should point out, that the shielded earth's magnetic field cannot account for the increased losses, since it can maximally contribute about 10 nΩ to the surface resistance (see Section 3.3.1).

[5] We were unable to find thermopower measurements for niobium at low temperatures.

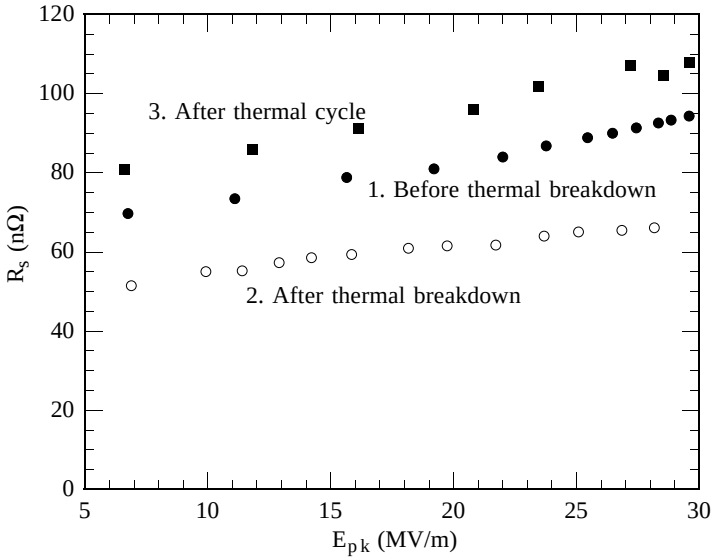

Figure 7.19: Surface resistance versus $E_{\rm pk}$ of a region in cavity LE1-31, which reduced its losses following thermal breakdown as in Figure 7.1.

over which temperatures vary during thermal breakdown is set by the size of the breakdown region, which is on the order of a few centimeters. The minimum temperature difference expected over this distance is at least 10 K. Hence the *smallest* temperature gradient to be expected is about 2 K/cm. The thermoelectric field developed in this case will be about 0.2 μV/cm. Given a resistivity of 0.062 $\mu\Omega$ cm for $\approx$ 300 RRR niobium at cryogenic temperatures [183], the current density (j_T) driven by the thermogradient is on the order of

$$j_T \approx \frac{0.2\ \mu\text{V/cm}}{0.062\ \mu\Omega\ \text{cm}} = 3\ \text{A/cm}^2. \tag{7.3}$$

The magnetic fields created by such current densities are on the order of 1.9 Oe at a distance of 1 cm. Past measurements have shown that the sensitivity of $R_{\rm s}$ to flux trapping is about 0.35 nΩ/mOe (see Section 3.3.1). [90] If all of the flux created by thermopower is trapped, $R_{\rm s}$ changes as high as 660 nΩ should be observed. Considering our lack of concrete data on the actual temperature gradients and thermopowers occurring during thermal breakdown our experimental values agree reasonably well with the estimate.

7.2.3.3 Reduction of the surface resistance

Although a thermal cycle to $\approx$ 11 mK eliminated increased losses due to thermal breakdown, even a cycle to temperatures on the order of 200 K had no effect on reduced loss regions. Only a complete cycle to room temperature was successful in reversing the effect of thermal breakdown (see Figure 7.19). It is therefore impossible that flux trapping is responsible for $R_{\rm s}$ reductions.[6] Instead, we suspect that due to the elevated temperatures occurring at or in the vicinity of the defect, gases such as hydrogen evolve, causing a local discharge. This discharge may be brought about by field emission activity nearby. The discharge, in turn, cleans the rf surface, desorbing further gases and reduces the surface

[6]Indeed, it would have been difficult to explain a *reduction* of losses by flux *trapping*.

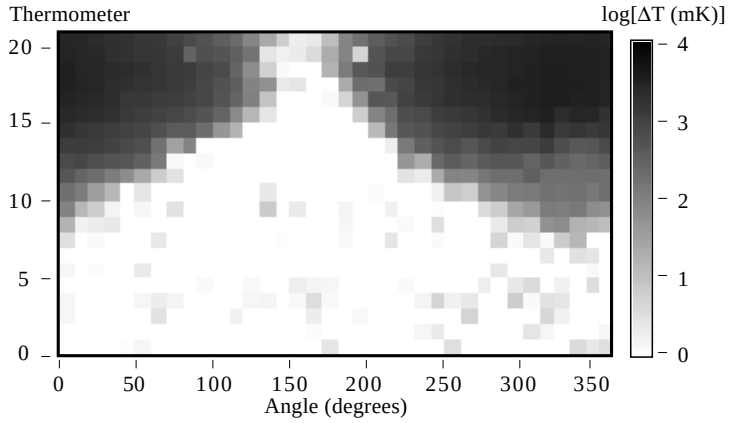

Figure 7.20: Cavity quench due to inadequate cooling by the helium bath of cavity LE1-33. The bath level at this time was roughly at the height of the equator.

resistance. The reductions in cavity LE1-34 may have been due to such field emission induced discharge because of the proximity of the emitter at 170° (see Figures 7.9 and 7.17).

We observed similar discharge related cleaning during multipacting (to be discussed in Section 7.3) and after discharge initiated by helium gas (see Section 5.5.1). Especially in the latter case, we were able to show that R_s reductions were due to gas removal from the rf surface. In all cases when the cavity was cycled to room temperature the reductions were reversed, whereas cycles to intermediate temperatures had no effect.

Unfortunately, as we demonstrated in Chapter 5, gases evolving during thermal breakdown are also occasionally responsible for the activation of field emission. Thus, not only does thermal breakdown degrade the low field Q_0, but it has the potential for significant Q_0 reductions at high fields, below the breakdown threshold. This fact provides a further incentive to avoid thermal breakdown.

7.2.3.4 Flux trapping during field emission related breakdown

Unlike the case of thermal breakdown caused by a defect, less severe R_s changes were observed following field emission related breakdown. This fact is also consistent with our theory that flux trapping is responsible for the R_s increases. Defect related thermal breakdown grows from a microscopic region and therefore we expect large thermal gradients. In contrast to this situation, field emission electrons bombard and heat large regions, and less severe temperature gradients are generated when thermal breakdown is initiated. Especially in the examples in Figures 7.4 and 7.5, thermal breakdown is not centered on the hottest field emission region and we expect thermal gradients to be less than in defect related breakdown. The lack of large gradients explains why the magnetic flux generated is not as substantial as for defect related breakdown.

Similarly, flux trapping and the associated increase in R_s does not occur when a cavity quench occurs due to low liquid helium levels. We observed such a breakdown in cavity LE1-33, where almost the entire upper half cell became normal conducting, as shown in Figure 7.20. In this case, the absence of large thermal gradients is clear. Furthermore, the time it took the cavity to recover from the quench was as long as a few

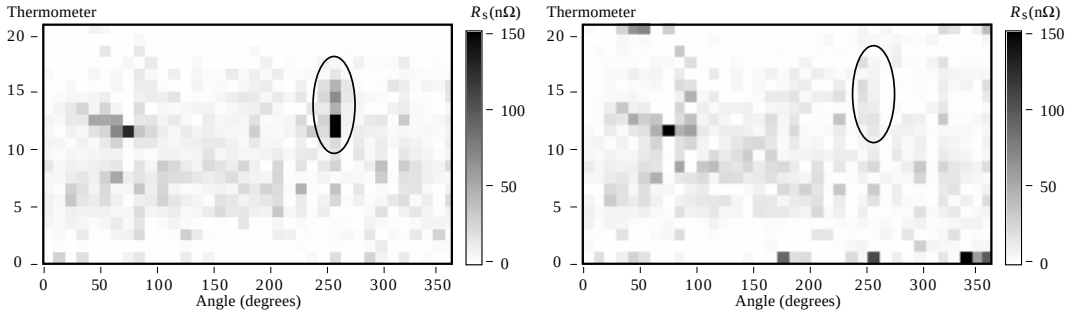

(a) (b)

Figure 7.21: Map of the surface resistance of cavity LE1-33 at $E_{\mathrm{pk}} = 12$ MV/m. (a) Before the quench in Figure 7.20 occured, and (b) after the quench. The region circled had previously increased its surface resistance due to defect related thermal breakdown.

tenths of a second because of poor cooling by the bath, rather than milliseconds during regular thermal breakdown.

By coincidence, defect initiated thermal breakdown had previously occurred in this cavity, and increased R_{s} values were recorded in the region circled in Figure 7.21(a). Some reductions were also observed. Following the quench due to the low liquid helium level, the increased losses disappeared again (see Figure 7.21(b)), whereas reduced loss regions on the whole were unaffected (not visible in Figure 7.21).

These observations are entirely consistent with the thermal cycling experiments discussed earlier. The defect initiated thermal breakdown trapped flux in the rf surface, increasing R_{s}. Then the quench due to the low helium bath level increased the temperature above T_{c}, thereby freeing the flux again. Because of the absence of large temperature gradients, no new flux was trapped as the cavity cooled, and the original low R_{s} state was maintained. Evidently subsecond thermal cycles are sufficient to reduce losses, in agreement with the theory that flux trapping is the cause of the high R_{s} regions. Reduced loss regions are not affected by the entire process, because the temperatures involved are insufficient to redistribute gases.

7.2.4 Summary

We have found that thermal breakdown continues to limit the maximum attainable field in a significant fraction of RRR = 300 cavities. We observed both defect and field emission related breakdown. A continued effort is therefore required to improve the purity (i.e., the thermal conductivity) of cavities, while also trying to avoid field emission.

Although the magnetic field is strong over a large fraction of the cavity surface, defect induced breakdown occurred primarily along the equator weld region or nearby. We therefore suspect that the e-beam welding introduces unusually many defects. Improvements in cavity performance should thus be possible by refining the welding procedure.

Particulates dropping into the cavity during cavity preparation can also be potential thermal breakdown sites. We have shown that the magnetic field is able to heat these to very high temperatures because of the poor thermal contact between the particle and

the niobium substrate.

Not only does thermal breakdown limit the maximum attainable magnetic field, but it also increases the low field surface resistance of the region involved in breakdown. We showed that these losses in all likelihood are due to trapped magnetic flux produced by thermogradient currents during the breakdown event. Very similar effects were also observed during multipacting induced breakdown (to be presented next).

We also presented preliminary evidence that suggests gases evolve from the high temperature regions during thermal breakdown. These gases can result in a discharge triggered by, for example, field emission electrons, which removes surface contaminants from the rf surface and reduces its surface resistance in some places. Unfortunately, the evolution of gases can also activate field emitters, as was shown in Chapter 5.

7.3 Multipacting in LE1 cavities

We now turn to our discovery of multipacting in the LE1 cavity shape. First we present a generic example of multipacting in progress as observed by our high speed thermometry system. Sensitive measurements at low fields before and after such multipacting events reveal that the surface resistance of the equator changes due to multipacting. The mechanism, we believe, is again flux trapping as during thermal breakdown.

Numerical trajectory simulations that confirm the observed multipacting are then discussed. We also draw on the experience of other laboratories with similar cavity shapes to corroborate our experimental results.

7.3.1 Experimental results with cavity LE1-21

7.3.1.1 Breakdown events

During tests of LE1-21 (a Mark I cavity), the fields would periodically collapse once every few seconds when a threshold field of $E_{\rm pk} = 29.4$ MV/m was exceeded. The self-pulsing continued for about 20 seconds, after which the fields in the cavity could be raised further, before a similar phenomenon was again encountered at a slightly higher field level. We will show later that these events are induced by multipacting that can be processed easily. By processing through weak multipacting barriers, we eventually were able to achieve $E_{\rm pk} = 38$ MV/m. At that point field emission and related thermal breakdown prevented us from reaching higher fields.

Figure 7.22 depicts three temperature maps taken in rapid succession (0.15 s intervals) to capture transient events. The first map depicts the temperature distribution at $E_{\rm pk} \approx 30$ MV/m, just before a breakdown event. A field emitter is visible at the top iris at 190°. The breakdown event is recorded in the following map. Significant heating is visible over a large fraction of the cavity, the high temperature region being centered on the equator. Within less than 0.15 s the fields have completely collapsed and the cavity cools (third map). The temperature of the circled thermometer as a function of time is displayed in Figure 7.23 to illustrate the repetitive nature of the breakdown.

We found that the breakdown events commence when the temperature, or equivalently $E_{\rm pk}$, exceeds a threshold value. Although this behavior has some similar features to defect induced thermal breakdown, the four distinct observations below show that a defect cannot be the cause of the quenches.

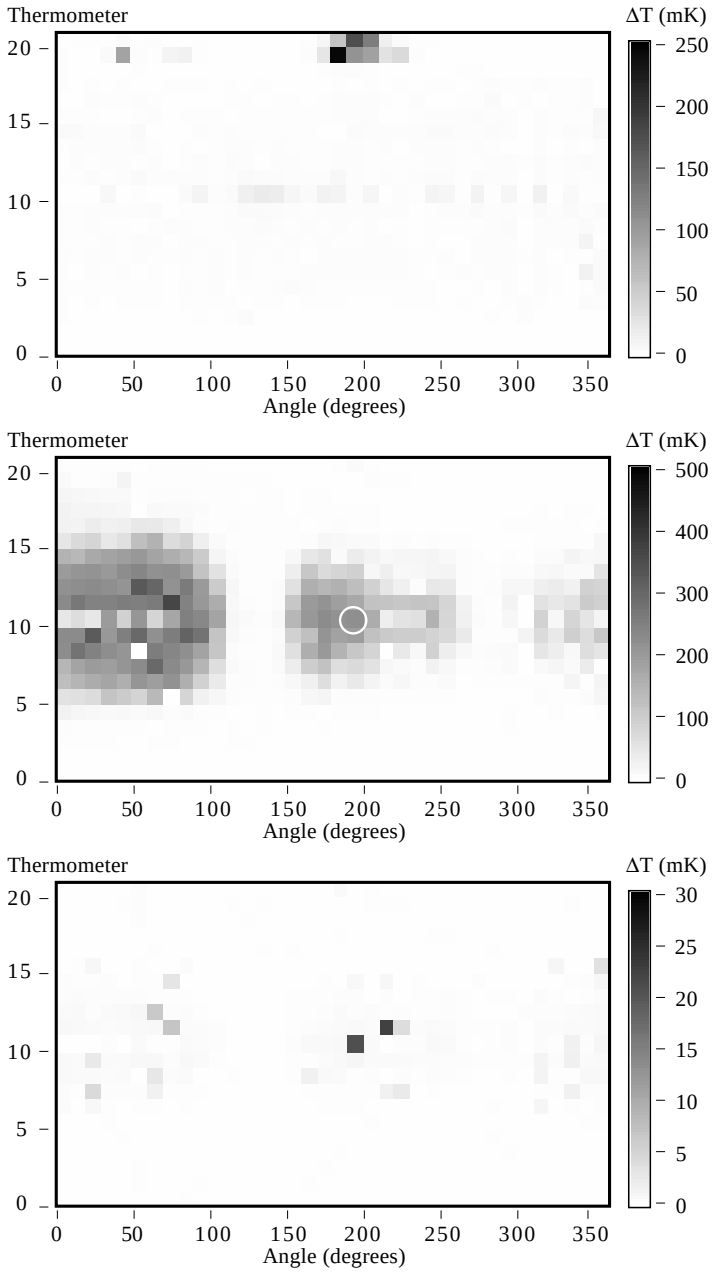

Figure 7.22: Series of temperature maps taken during a test of cavity LE1-21 while multipacting was active at $E_{\mathrm{pk}} \approx 34$ MV/m. The map interval is about 0.15 s.

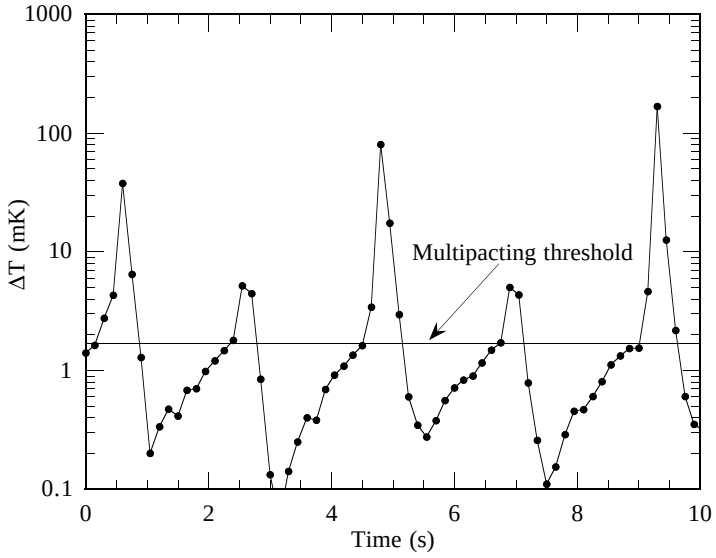

Figure 7.23: Temporal evolution of the temperature recorded by the thermometer circled in Figure 7.22. Note the logarithmic temperature scale.

1. The temperatures recorded during breakdown never exceeded a few hundred millikelvin. Defect related thermal breakdown, on the other hand, usually results in temperature rises at the defect far exceeding 1000 mK.

2. Several distinct areas in the equator region of the cavity show breakdown related heating rather than being centered on a singular defect.

3. Defect related thermal breakdown cannot be processed away, whereas we had no trouble increasing $E_{\rm pk}$ after 20 s or so of processing.

4. Subsequent breakdown events originate in different parts of the cavity, as shown in Figure 7.24.

Once the cavity had been "conditioned" at a given field level, no further breakdown events were recorded up to that field. However, upon thermally cycling to room temperature, reconditioning of the cavity was required as breakdown was again encountered, starting at about 30 MV/m. As we will discuss, this is a characteristic of multipacting.

7.3.1.2 Low field losses

Breakdown events occurred only at field levels of 30 MV/m and higher. Yet, as with thermal breakdown, the low field resistance of the cavity was affected by these events. Figure 7.25 depicts the ratio of the cavity's low field surface resistance after and before a series of breakdown events. Most of the equator region increased its $R_{\rm s}$ dramatically, although some areas actually reduced their losses. The remainder of the cavity was largely unaffected. Overall, the region covered by the equator thermometers and their nearest neighbors increased its surface resistance by more than a factor of two, as shown in the histogram in Figure 7.26(a). Thermometers further from the equator registered little change (Figure 7.26(b)). Individual sites increased their surface resistance more

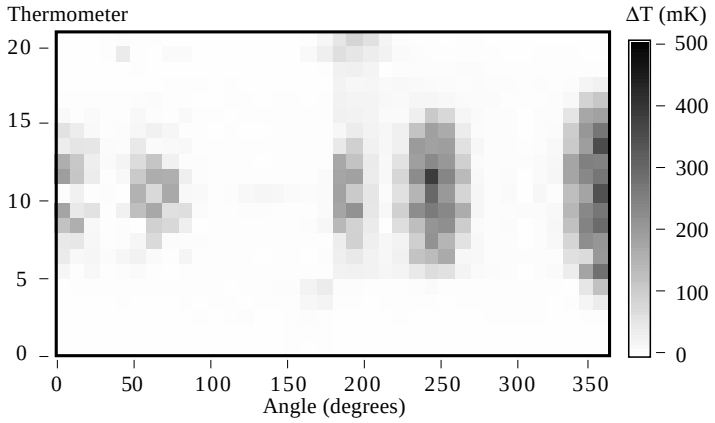

Figure 7.24: Breakdown temperature map taken during the same breakdown sequence as the maps in Figure 7.22.

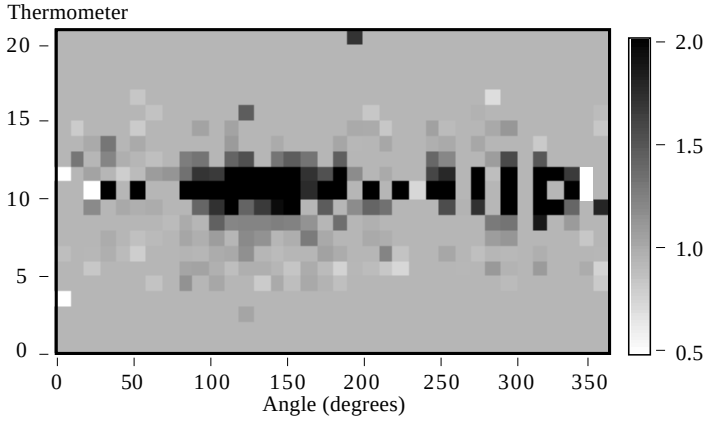

Figure 7.25: Ratio of the surface resistance after and before a series of breakdown events in cavity LE1-21. Dark regions represent increased surface resistance, while light regions denote decreases.

(see Figure 7.27(a)). Increases by as much as a factor of seven were recorded. Also, a few sites reduced their R_s close to zero (see Figure 7.27(b)).

A given site could change its surface resistance numerous times following repeated breakdown events. In some cases R_s would increase several times (Figure 7.28(a)), so that in the end a total increase by as much as a factor of 6-10 was recorded. Other sites initially increased their surface resistance, only to reduce R_s to intermediate levels during a subsequent breakdown event (Figure 7.28(b)).

Following thermal cycling to room temperature, all R_s changes due to breakdown were reversed and the original R_s "landscape" was recovered. Thermal cycles to intermediate temperatures $T_c < T < T_{room}$ were not attempted with this cavity. However, other cavities underwent breakdown events similar to those described here and we will discuss them shortly. In these cases, increases and reductions of R_s along the equator were also observed but only regions that increased R_s recovered their original values following a cycle to intermediate temperatures.

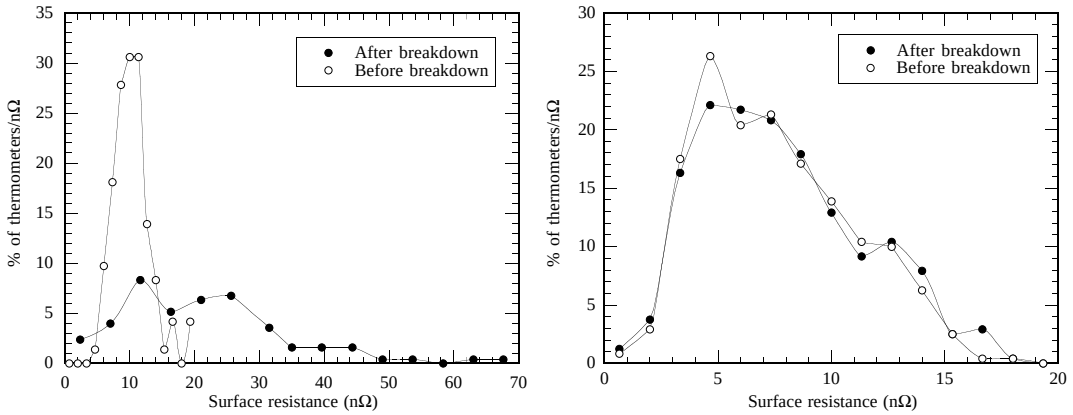

Figure 7.26: Histogram of R_s of sites covered by (a) the equator thermometers and their nearest neighbors, and (b) non-equator thermometers (3–7 and 13–17 on each board). In (a) the mean surface resistance increased from 10.3 nΩ to 21.4 nΩ following a series of breakdown events whereas in (b) the mean surface resistance did not change significantly.

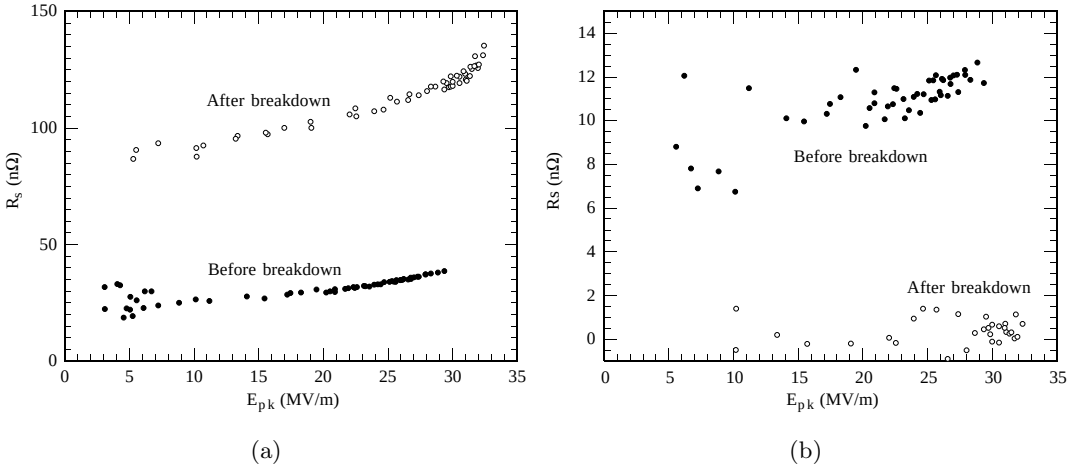

Figure 7.27: Surface resistance versus $E_{\rm pk}$ before and after breakdown. (a) Equator site at 140° which increased R_s during breakdown, and (b) equator site at 340° which reduced R_s during breakdown.

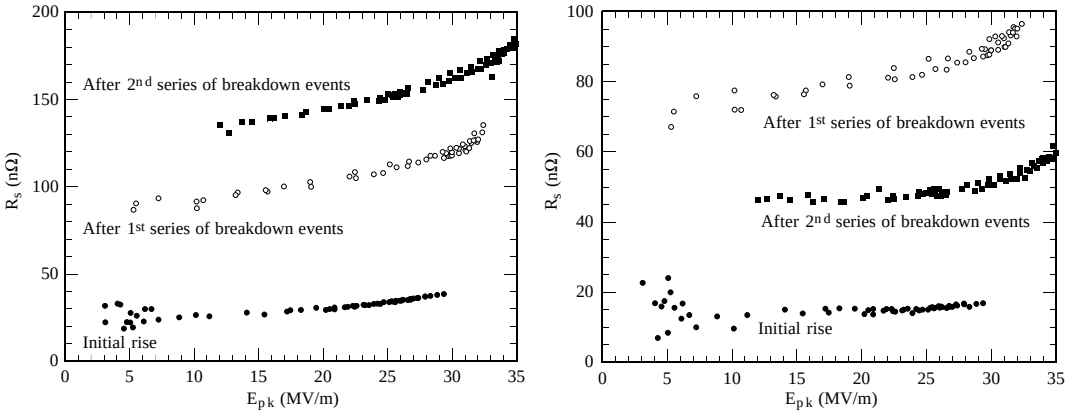

Figure 7.28: Effect of multiple breakdown events on the surface resistance of individual sites. (a) Equator site at 140° and (b) equator site at 150°.

7.3.2 Discussion

7.3.2.1 Multipacting induced breakdown

The R_s changes described here are reminiscent of the low field losses resulting from defect induced thermal breakdown. Again, we suspect that the increased losses are due to flux generation by thermocurrents during the breakdown events and its subsequent trapping as the cavity is rapidly cooled through T_c (see Section 7.2.3).

No single defect can be responsible for initiating the quenches discussed above. Since the low field losses are only affected by the breakdown mechanism in a thin band centered on the equator, the results suggest that the breakdown *source* is concentrated along the equator, creating large thermal gradients in this narrow region.

These and other observations are consistent with multipacting as the cause of the breakdown. According to simulations (discussed below) the threshold field for multipacting should be 30 MV/m, which is the level at which breakdown was first observed. Since we were readily able to process through the breakdown, the multipacting electron energies must lie close to the points where the secondary emission coefficient (SEC) crosses one (lower and upper crossover). Only sites on or close to the cavity equator change their R_s during breakdown, leading us to conclude that this region must be involved in very localized (in S) electron bombardment that ultimately results in a quench and flux trapping. Judging from the symmetrical heating about the equator, multipacting is likely to be of a two-point nature. Due to the strong magnetic field in this region, the normal conducting region grows rapidly to cover a large portion of the cavity, as confirmed by the temperature maps.

7.3.2.2 Multipacting simulations

To confirm our hypothesis, we ran multipacting simulations similar to those described in Reference [2]. We used the finite element code SUPERLANS [27, 28] to solve for the electromagnetic fields of the TM_{010} mode at one value of E_{pk}. The program MULTIP

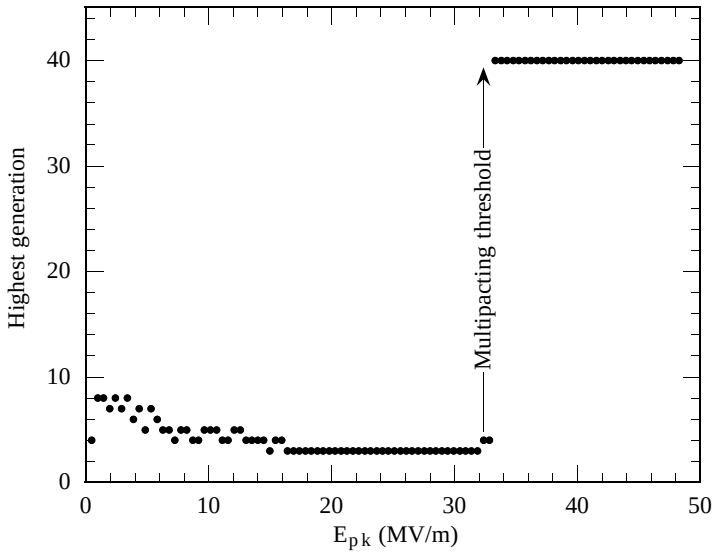

Figure 7.29: Highest electron generation recorded for all simulated $(S_0^{(j)}, \varphi_0^{(j)})$ pairs versus $E_{\rm pk}$ for Mark I cavities. A trajectory calculation was automatically stopped when the $40^{\rm th}$ generation was reached, the assumption being that a multipacting trajectory had been found. The electron emission energy was 3 eV.

[15,118] was then used to calculate trajectories for electrons emitted at numerous points $S_0^{(j)}$ of the cavity wall and at various emission phases $\varphi_0^{(j)}$. The electric field was also varied. The trajectories were computed using the relativistic equations of motion in Equations 4.34 and 4.35.

For each pair $(S_0^{(j)}, \varphi_0^{(j)})$ the electron trajectory was integrated until it impacted a cavity wall. When this happened, a new electron was emitted at that site, provided the SEC at the impact energy exceeded one *and* the electric field pointed towards the wall. If one (or both) of these conditions was not satisfied, then the number of electron generations created up until this point was recorded, and calculations were started for a new pair $(S_0^{(j)}, \varphi_0^{(j)})$ and/or another value for $E_{\rm pk}$. Trajectory calculations for a given $(S_0^{(j)}, \varphi_0^{(j)})$ pair were terminated when the $40^{\rm th}$ generation was created, the assumption being that a stable multipacting trajectory had been found.

Electron emission energies used in the calculations ranged from 0 eV to 3 eV, and $E_{\rm pk}$ was varied from 0 to 50 MV/m. The SEC was taken to be greater than one between 20 eV and 3000 eV. These values are reasonable for a wet treated niobium surface (see Figure 3.14).

Depicted in Figure 7.29 is the highest electron generation recorded for all simulated $(S_0^{(j)}, \varphi_0^{(j)})$ pairs as a function of $E_{\rm pk}$. We see that Mark I cavities are predicted to be multipacting free only up to about 32 MV/m, a value that is very close to our experimental observations of breakdown.

Our calculations showed that electron trajectories starting a fair distance from the equator drift towards the equator within a few generations. It is for this reason that elliptical cavities are so effective at suppressing one-point multipacting (see Section 3.2.3). However, for $E_{\rm pk} \geq 32$ MV/m electrons emanating within only 0.2 mm of the equator

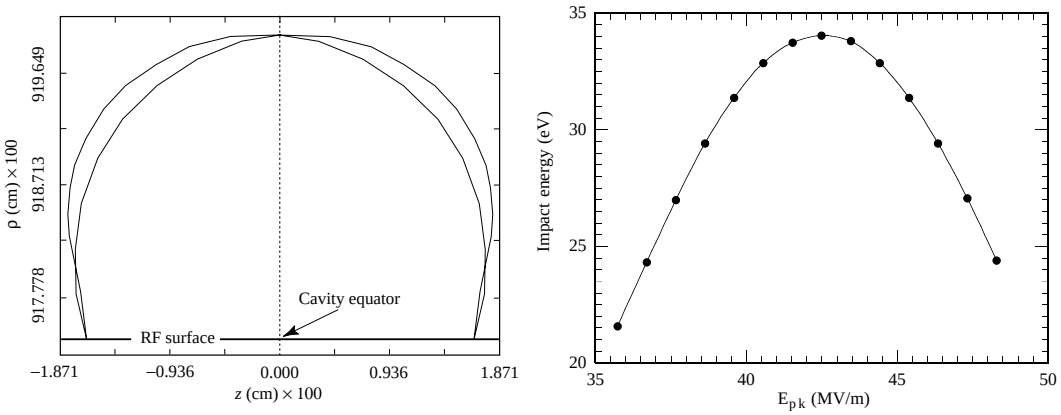

(a) (b)

Figure 7.30: (a) Stable, two-point multipacting trajectories at 37 MV/m near the equator of Mark I cavities. Secondary emission was perpendicular to the rf surface. (b) Electron impact energy as a function of $E_{\rm pk}$.

with an initial energy of 2 or 3 eV follow a trajectory to the symmetry point on the other side of the equator in 1/2 an rf period. Secondaries released at the impact site then follow a similar path back to the originator location. An example of the trajectories is shown Figure 7.30(a). This situation constitutes two-point multipacting of the first order. Two narrow ranges of start phases, separated by 1/2 an rf cycle, lead to this type of multipacting. ($2\pi \times 0.32 < \varphi_0 < 2\pi \times 0.38$ and $2\pi \times 0.82 < \varphi_0 < 2\pi \times 0.88$.)

Depicted in Figure 7.30(b) are the electron impact energies as a function of $E_{\rm pk}$ if the secondaries are emitted with an energy of 2 eV. As predicted, the energies are very close to the lower crossover of the SEC. When the emission energy was increased to 3 eV, or the emission direction was tilted by 30°, the impact energies increased slightly, so that the curve in Figure 7.30(b) shifted to lower $E_{\rm pk}$ values. In these cases the impact energy exceeded 20 eV slightly below 32 MV/m.

Our simulations indeed confirm the hypothesis that the electron impact energies are very close to the lower crossover. Desorption of surface adsorbates by electron bombardment and possibly even a local gas discharge will lower the SEC, thereby arresting multipacting. The regions that reduce $R_{\rm s}$ during the multipacting process are indicative of the desorption process. (We already demonstrated in Section 5.5.1 that discharges can "clean" the rf surface.) Desorption also explains why the multipacting center constantly shifts to different places of higher SEC around the equator. The resultant change in surface composition then arrests the multipacting. Our interpretation is supported by the fact that thermal cycling reactivates multipacting at the lowest field ($\approx$ 30 MV/m) by redistributing gases in the cavity. We know that such a redistribution of gases does take place, because the regions which *reduced* their losses during multipacting reverted back to their original $R_{\rm s}$ after a complete room temperature cycle, whereas they were unaffected by intermediate thermal cycles. The contribution of the adsorbates to the surface resistance appears to be on the order of 10 nΩ or less, based on Figure 7.27(b).[7]

[7]One should bear in mind that, due to the variation of the thermometer efficiency, it is difficult to

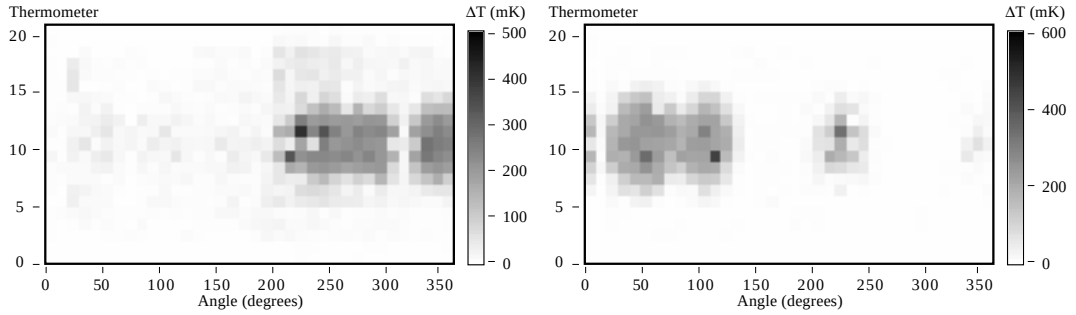

(a) (b)

Figure 7.31: Multipacting related breakdown at two different times in cavity LE1-17. The peak electric field was about 32 MV/m.

Note that the impact energy rises with increasing field up to at least the low 40 MV/m's. It therefore is not surprising that multipacting reappeared at successively higher fields when we raised the fields for the first time. At each field level, multipacting progressed until the SEC was lowered below one. Then, when the field was increased again, the impact energy rose and the SEC exceeded unity once more. Further processing was then required before higher fields could be attained. Provided the cleanliness of the rf surface is maintained, and it is not re-exposed to gases, multipacting is no longer active at lower fields. In cavity LE1-21 multipacting continued up to the maximum field attained (38 MV/m). Based on Figure 7.30(b) we expect that multipacting would have been active up to about 42.5 MV/m if the cavity had not been limited by thermal breakdown.

7.3.3 Results with other LE1 cavities

7.3.3.1 Cavity LE1-17

Of all the other cavities that we tested which reached at least $E_{\rm pk} = 30$ MV/m, only cavity LE1-17 was of the Mark I type. This cavity displayed the same breakdown features as cavity LE1-21, starting at 32 MV/m. In particular, we again found that large areas were affected by breakdown, which tended to shift from event to event (Figure 7.31). No field emission was observed in the cavity and no defect related heating could be correlated with the breakdown sites. Similar to LE1-21, the equator losses changed following multipacting (Figure 7.32(a)), with significant increases and reductions recorded (see Figure 7.32(b) & (c)). Again, multipacting could be processed fairly easily. However, upon reaching 34 MV/m, we found that breakdown consistently occurred at the same site, as is shown in Figure 7.33. The temperatures recorded at the equator were more than a factor of 20 higher than those observed during regular multipacting.[8] In fact, the values are similar to temperatures recorded during thermal breakdown (see Section 7.2).

extract reliable values for $R_{\rm s}$ based on results from only a few thermometers.

[8]The carbon thermometers are only calibrated up to a ΔT of 2600 mK (for $T_{\rm b} = 1.6$ K). Greater values were obtained from an extrapolation of the thermometer calibrations and are unlikely to be accurate. Nevertheless, it is certain that the ΔT's recorded here exceed those witnessed during regular multipacting by a large amount.

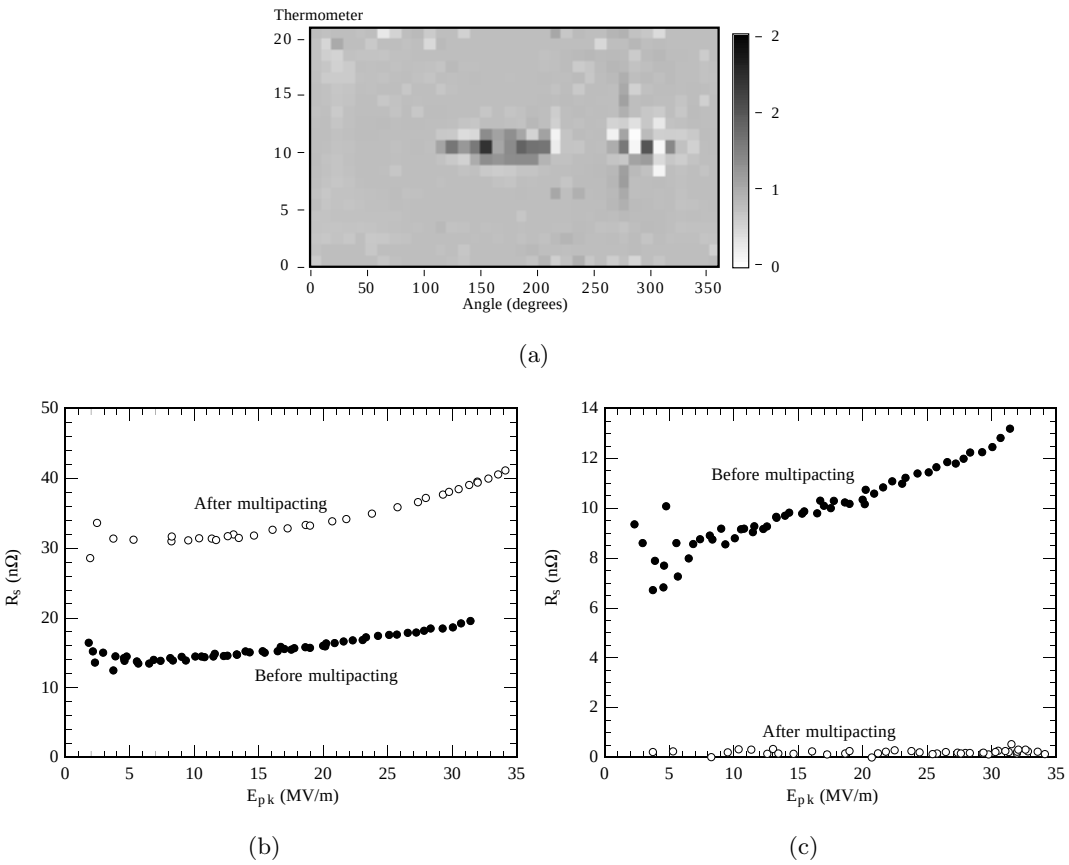

Figure 7.32: (a) Resistance ratio at 31.5 MV/m after and before the first multipacting event in cavity LE1-17. Surface resistance as a function of $E_{\rm pk}$ at (a) 100°, thermometer 10, and (b) 280°, thermometer 11.

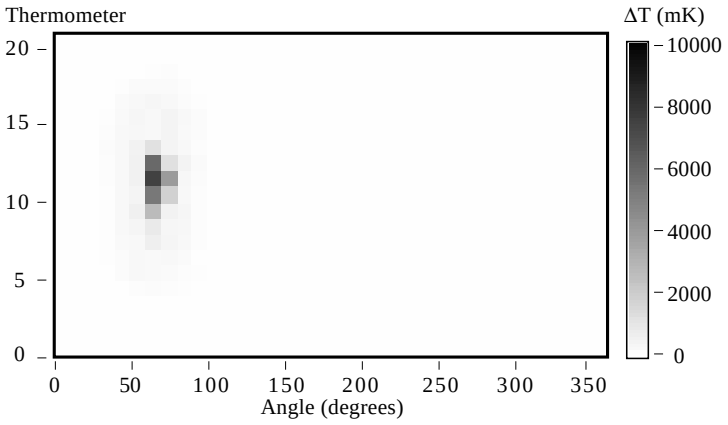

Figure 7.33: Breakdown site in cavity LE1-17 after multipacting was processed and fields were raised to 34 MV/m. At this point, breakdown always occured at the same site, and temperatures were elevated significantly with respect to those in Figure 7.31.

It was not possible to raise the field any further.

From the stable breakdown and the heating pattern we conclude that it was no longer multipacting that caused breakdown, but rather a defect. A search for defect related heating *prior* to the multipacting induced breakdown events did not produce a positive result. An intriguing possibility is that the multipacting induced resistance enhancement along the equator could have been severe enough to pose as a defect. A similar event may have been observed in a TESLA cavity as well. However, since this hypothesis is somewhat speculative, we defer the discussion to Appendix C.

7.3.3.2 Mark II and Mark III cavities

Our trajectory simulations did not predict sustained multipacting in Mark II and Mark III cavities. Correspondingly we did not observe repetitive multipacting induced breakdown (as in cavities LE1-17 and LE1-21) in any of the five Mark II and Mark III cavities that exceeded 30 MV/m. Our simulations show that even very subtle alterations to the cavity shape can have a significant impact on multipacting.

It is interesting to point out, that in all but one of the remaining cavities which reached $E_{\rm pk} = 30$ MV/m, we did observe singular breakdown events that left their "mark" on the low field properties of the cavity.[9] All of these isolated breakdown events occurred at fields close to 30 MV/m. They are suggestive of short lived multipacting activity. A summary of the events is given in Table 7.1.

In many cases the single breakdown event resulted in increased low field losses along the cavity equator. Again, some sites reduced their $R_{\rm s}$ during these events. These observations are very similar to those obtained in Mark I cavities. Figure 7.34, for example, illustrates the changes of $R_{\rm s}$ observed in cavity LE1-20, which broke down at 30 MV/m.[10] The region around 270° showed a marked reduction due to the breakdown event, whereas most of the remainder of the equator increased its surface resistance. The test was followed by a thermal cycle to about 12 K, which removed the increased losses along the equator (Figure 7.35(a)). However, the region around 270° remained unaffected (see Figure 7.35(b)). A complete thermal cycle to room temperature was required to restore the original $R_{\rm s}$.

The fact that only a room temperature cycle restores $R_{\rm s}$ emphasizes that the mechanism resulting in increased losses is not identical with that responsible for the reduction of $R_{\rm s}$ in other regions. Increased losses disappear when the cavity temperature is raised to 12 K, demonstrating that these losses are due to breakdown induced flux trapping (as observed during thermal breakdown). Flux trapping is unlikely to be able to reduce losses in other regions.

Since a temperature cycle to 300 K is required to restore the $R_{\rm s}$ in low loss regions, we suspect that the reduction of losses results from the desorption of gases. Elevated temperatures associated with room temperature cycling are then required to redistribute the gases throughout the cavity and to restore the $R_{\rm s}$. The desorption process can be

[9] In the case of the exception, we observed a breakdown event at 25.3 MV/m following the admission of large amounts of helium to the cavity. However, there is some indication that the breakdown was triggered by field emission rather than by multipacting.

[10] A field emitter had limited the cavity to 20 MV/m, at which point it rf processed. Due to the reduced power dissipation in the cavity, the field rose rapidly to 30 MV/m, and some short-lived self pulsing of the cavity was observed.

Table 7.1: List of LE1 cavities tested, and summary of suspected multipacting (MP) events. The fields (in MV/m) indicate when a particular event was first observed. The column "other events" refers to events that are suspected to be multipacting related. They include, for example, the activation of field emitters which can be due to gases released during multipacting. These are discussed in Chapter 5.

Shape	Cavity name	Repetitive MP observed	Single MP related event	Other MP related event	Maximum field reached
Mark I	LE1-17	32			34
	LE1-21	29.4		29	38
	LE1-Heraeus*				24
Mark II	LE1-20		30	29	32
	LE1-23		31	30	33
	LE1-27*				28
Mark III	LE1-31		25.3†	29	35
	LE1-32*				22
	LE1-33‡			30 – 40	45
	LE1-34		30		38
	LE1-CEBAF*				28

* Cavity failed to reach 30 MV/m.

† It is not certain that breakdown was triggered by multipacting.

‡ No thermometry data available when $E_{\rm pk}$ exceeded 30 MV/m for the first time.

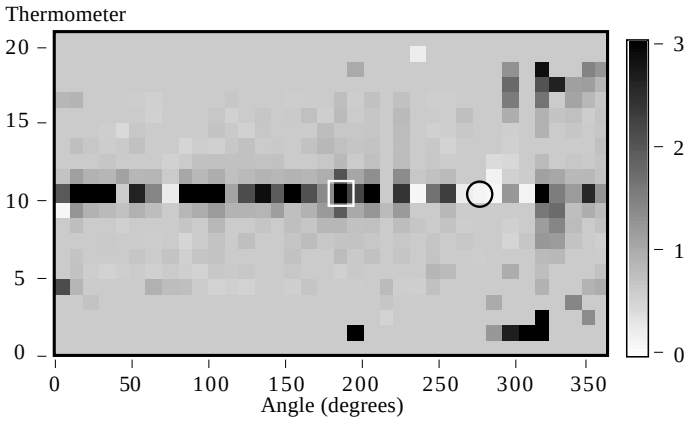

Figure 7.34: Surface resistance ratio map of cavity LE1-20 at 11.3 MV/m after and before a breakdown event was observed at $E_{\rm pk} = 30$ MV/m. The increases recorded near the iris around 310° are field emission related and not due to the breakdown event.

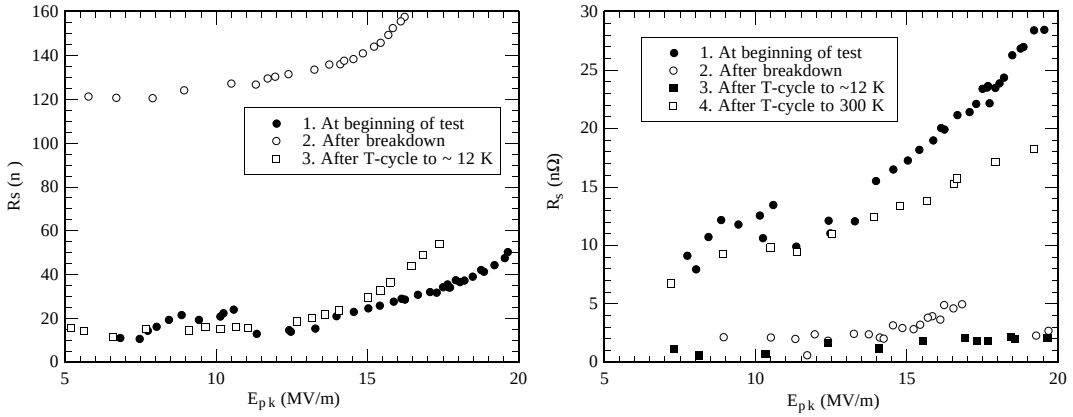

(a) (b)

Figure 7.35: (a) Surface resistance at the framed site in Figure 7.34 as a function of $E_{\rm pk}$. A thermal cycle to ≈ 12 K was sufficient to remove the additional losses due to multipacting. (b) Plot of the surface resistance of the circled site. A complete thermal cycle was required to restore the $R_{\rm s}$ to its initial value.

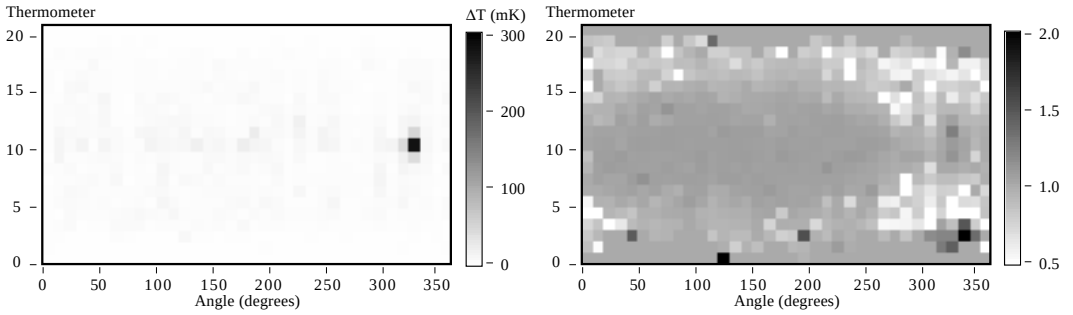

(a) (b)

Figure 7.36: (a) Temperature map of cavity LE1-23 at $E_{\rm pk} = 26.5$ MV/m before any breakdown events. A hot defect is observed on the equator at 320°. (b) Ratio map at 30 MV/m of the surface resistance after and before a single breakdown event at 30 MV/m. Light areas indicate reductions in $R_{\rm s}$.

from the bombardment of the surface by multipacting electrons directly, or due to a gas discharge initiated by the multipacting current [184] and/or the electric field.

On one occasion we observed a singular breakdown event at 30 MV/m which resulted almost exclusively in a reduction of the $R_{\rm s}$. Cavity LE1-23 (Mark II shape) had a hot thermal defect on the equator at 320° (Figure 7.36(a)). Even at $E_{\rm pk} = 30$ MV/m x-rays were not detected, indicating that no field emission was active. At this field, the cavity quenched once, and large areas at intermediate latitudes, centered in ϕ on the hotspot, reduced their surface resistance by as much as a factor of 1/8 (see Figure 7.36(b)). A similar event, although not necessarily multipacting related, was already described in Section 5.5.1. At the same time, a very short burst of x-rays was recorded, indicating that electronic activity took place in the cavity. Since the breakdown occurred at 30 MV/m

(the onset field for multipacting) we assume that it is also multipacting related. If the low loss regions, centered (in azimuth) on the equator defect, were created by ion bombardment during gas discharge, one possible mechanism is that gases evolving from the hot defect were ionized by a short burst of multipacting current. [184] The newly created ions and electrons subsequently spread and impacted the cavity wall, desorbing further gases and reducing the surface resistance (on average from about 17 nΩ to 12 nΩ). At a slightly higher field (31 MV/m), another breakdown event was recorded, and R_s increases as well as reductions were observed between 230° and 50° (similar to the event seen in cavity LE1-20), confirming that multipacting was indeed active. Thermal cycling to room temperature restored all the original losses.

All our observations with Mark II and Mark III cavities[11] show that multipacting in these shapes is very short lived. Only one or two breakdown events are observed in these cavities, and subsecond processing times are sufficient to suppress multipacting altogether. Unlike Mark I cavities, thermal cycling to room temperature does *not* restore multipacting in Mark II and Mark III cavities. The electron impact energies must therefore lie very near the lower crossover of the SEC. The slight differences in shape that do exist between Mark I and Mark II/III cavities must be responsible for shifting the impact energy slightly below 20 eV.

7.3.3.3 Potential Q_0 improvements

The fact that a discharge or multipacting is able to reduce the surface resistance substantially is very interesting. It demonstrates that the Q_0 values of 2×10^{10}, that we routinely achieve, can be improved upon significantly. Although flux trapping of an insufficiently shielded terrestrial magnetic field contributes to the surface resistance (see Section 3.3.1), it appears that adsorbed materials, which can be removed by charged particle bombardment, are responsible for a substantial part of the residual surface resistance in our cavities.[12]

Consider, for example, cavity LE1-23, in particular the event described in Figure 7.36 that led to reduced losses. On average, the affected region reduced its losses from 17 nΩ to 12 nΩ. Individual thermometers registered much greater reductions from a factor of 1/2 to even a factor of 1/8. The low field Q_0 of this cavity was 1.5×10^{10}. If the R_s reductions observed in this test could be achieved with the entire cavity surface, then Q_0 values in excess of 5×10^{10} – 10^{11} should be possible, provided adequate magnetic shielding is used.

7.3.4 Multipacting in other cavity shapes

Multipacting similar to that described here has been observed by researchers in other laboratories as well. In some cases these observations were made indirectly via Q_0 measurements.

[11] Although not presented here, Mark III cavities behaved very similar to Mark II cavities.

[12] Note that BCS losses at 1.6 K are about 2.5 nΩ for RRR = 250 material. Hence Q_0 values in excess of 10^{11} should be possible.

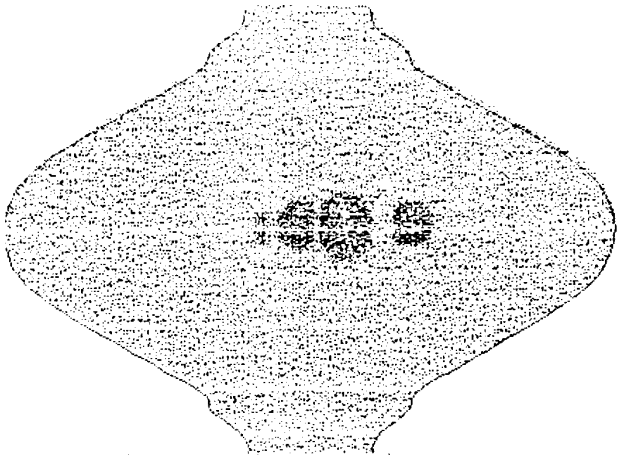

Figure 7.37: Temperature map of a 350 GHz LEP cavity. Dark regions denote high temperatures. The hotspots on opposite sides of the equator reveal two-point multipacting in progress. The peak ΔT was about 1.4 K. [71]

7.3.4.1 CERN LEP cavity

Two point multipacting was first observed in elliptical cavities in the CERN 350 MHz LEP cavities. [71] In this case, multipacting was more persistent than in our LE1 cavities and only disappeared after several hours of rf and helium processing. The cw temperature map in Figure 7.37 shows multipacting in progress and is very similar to our temperature maps. Simulations confirmed the observed multipacting. At 350 MHz, first order, two-point multipacting occurred at an accelerating field of 5.5 MV/m, the corresponding magnetic field being 212 Oe. At 500 MHz, multipacting was detected at $E_{\rm acc} = 8$ MV/m ($H = 303$ Oe). Trajectory calculations showed that the impact energy is only about 30 to 50 eV for a starting energy of 2 to 4 eV (similar to the energies we calculated for our LE1 cavities). This type of multipacting was avoided altogether with special care in cleanliness and drying.

To compare the CERN results with ours, we need to take into account the different cavity frequencies. For first order, two-point multipacting to take place, emitted electrons need to undergo half a cyclotron orbit before they impact the cavity wall. According to Equation 3.18 the threshold magnetic field for multipacting scales linearly with the cavity frequency.[13] Scaling the CERN results from 500 MHz to 1.5 GHz we expect that multipacting should occur at around $H = 910$ Oe in LE1 cavities. For the equator in our cavities $H/E_{\rm pk} = 24.2$ Oe/(MV/m) so that our observed multipacting threshold is about 730 – 770 Oe. This value constitutes good agreement, considering that shape differences between the CERN and LE1 cavities also affect the results.

No changes in the surface resistance due to multipacting were reported by CERN. This is likely due to the fact that their thermometry system lacked the temperature resolution to clearly identify these changes at low field. $R_{\rm s}$ data has to be obtained at low fields because intrinsic features may be masked at high field by field emission and

[13] Although Equation 3.18 applies to one-point multipacting, the same arguments used to derive the equation can be applied to the two-point multipacting described here. The frequency scaling remains unchanged.

other anomalous losses (see, for example, the rapidly rising R_s curves at high fields in Figure 7.35). Most recorded temperature signals at $E_{pk} = 10$ MV/m are on the order of 0.5 mK *or less*. Our temperature mapping system is the first to be able to resolve 0.1 mK temperature signals and simultaneously be able to take a complete map in a short time. Thus we are able to obtain reliable base line data prior to multipacting for comparison with data taken after multipacting.

7.3.4.2 KEK L-band cavities

Less detailed analyses were carried out at KEK with spherical, elliptical, and asymmetric cavities. [185] At 1.3 GHz they frequently found that their Q_0 curves would drop at $E_{pk} = 26.7$ MV/m and recover near 35.6 MV/m after processing (LE1 cavity shape). Multipacting was thought to be responsible for the dip. The severity of multipacting depended on the type of surface treatment the cavity had received prior to the test and on the cavity shape. This is consistent with our calculations that the impact energies are very low, and near the SEC's lower crossover. At KEK, it was found that elliptical cavities were afflicted the most by multipacting. Scaling the KEK multipacting fields to 1.5 GHz, multipacting should be active between $E_{pk} = 30.8$ MV/m and 41 MV/m. The lower bound agrees very well with our observations, and we know from our experiments that multipacting continues up to at least 38 MV/m, in agreement with KEK's upper bound. KEK's bounds also are consistent with the predictions from our multipacting simulations.

7.3.4.3 TESLA cavities

Circumstantial evidence also exists that multipacting occurs in 1.3 GHz TESLA cavities, starting at fields consistent with our observations in the LE1 cavities. At this point, though, this assumption is highly speculative, and we defer the discussion to Appendix D.

7.3.5 Summary

Two point multipacting at the equator has been observed in Mark I, LE1 cavities between $E_{pk} = 29.4$ and 38 MV/m. Repetitive collapse of the cavity fields and associated enhanced heating along the equator are the signature of multipacting.

Trajectory calculations confirm that two point multipacting at the equator is possible above about 32 MV/m. The electron impact energy is very low so that multipacting processes after only a few breakdown events due to the desorption of adsorbates. However, the redistribution of gases following a thermal cycle to room temperature is sufficient to reactivate the multipacting.

Although the multipacting in LE1 cavities itself is quite benign and can readily be processed, it increases the low field losses by trapping magnetic flux along the equator, where the heating by electron bombardment dominates. This effect is similar to that of thermal breakdown. There also is some evidence that these augmented losses can lead to thermal breakdown that might otherwise not take place until higher fields are achieved. Furthermore, we showed in Chapter 5 that gases evolving during multipacting can activated field emission, leading to an additional degradation of the Q_0 at high fields.

Very fleeting multipacting activity was also observed in Mark II and Mark III cavities. Again, these events led to flux trapping. Trajectory calculations do not predict

sustained multipacting when using an SEC that exceeds one between 20 eV and 3000 eV. The slight difference in cavity shape between Mark I and Mark II/III cavities must be responsible for the lowering of the impact energy to 20 eV or below.

Desorption of gases due to multipacting activity and a resultant reduction of the R_s was observed in several cavities. Based on the measured R_s improvements, we estimate that Q_0 values as high as 10^{11} should be attainable, if the discharge "cleaning" procedure could be applied to the entire cavity. Detailed studies to elucidate the cleaning mechanism and to determine its practical potential could therefore prove to be interesting and useful.

Chapter 8

New insights into residual loss mechanisms

8.1 Introduction

This chapter discusses our discoveries on low field residual loss mechanisms. We will give examples of hydride precipitation in cavities (the "Q-virus") and show that precipitation occurs preferentially along the cavity equator weld, resulting in increased losses in this region.

Another, newly discovered, loss mechanism, due to the accumulation of titanium in grain boundaries during heat treatment of cavities, is also discussed. This effect was not mentioned in the introductory chapter on loss mechanisms (Chapter 3), because until now it had never compromised the performance of a cavity. However, we will show that during heat treatment at very high temperatures (> 1500 °C) titanium can diffuse over extraordinarily large distances, resulting in very poor cavity performance.

Furthermore, experimental evidence of the motion of naturally occurring particles during cavity operation is presented for the first time.[1] In many cases, our ability to observe the arrival of particles was reliant on the high sensitivity of our thermometry system.

We identified a fourth residual loss mechanism that results from the generation and trapping of magnetic flux during a cavity quench. However, this mechanism was already covered in Chapter 7, because it is linked to both thermal breakdown and multipacting.

8.2 Hydrogen contamination

As discussed in Section 3.3.3, in the extreme, hydrogen contamination can lead to a severe reduction of the Q_0. Although our experiments were not specifically designed to study cavities afflicted by the "Q-disease", we came across several interesting hydride related cases.

All cavities, except for one, were shown to be free from significant hydride precipitation. However, in one unusual test we did encounter a severe case of Q-degradation, due to changes we made to the cavity etching procedure. 900 °C heat treatment was sufficient

[1] One such event was already discussed in Chapter 5 because it lead to the activation of field emission.

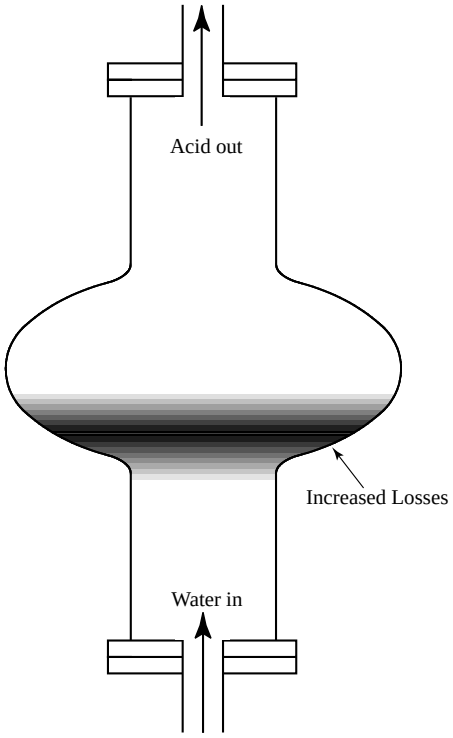

Figure 8.1: Schematic of the cavity isolated from the chem-room environment during its etch and subsequent filtered, deionized water rinse. Increased losses, as indicated in the diagram, were observed in the following rf test.

to "cure" the cavity. In four other cases the surface resistance of the equator was found to be higher than that of the rest of the cavity, leading only to a slight Q-degradation. The observation led us to conclude that the equator weld is more susceptible to hydrogen contamination than the rest of the cavity.

8.2.1 Severe quality degradation

In an attempt to prevent the exposure of freshly etched cavities to dirty chem-room air we modified our etching procedure for a test of cavity LE1-21. Instead of following the usual procedure of immersing the cavity in a bucket filled with acid, we integrated the cavity into a closed loop. Hoses were connected to the top and bottom beam tubes. Acid or filtered, deionized water could then be pumped into the cavity from the bottom and extracted from the top.[2] In this manner, the interior of the cavity was isolated from the chem-room air. For the etch, the cavity was filled completely with acid. Every 10 seconds or so, fresh, cool acid was pumped into the cavity to prevent the temperature from rising above 15 °C. After 3 minutes, water was pumped into the cavity from the bottom to dilute and push out the acid (Figure 8.1). The water flow was continued for over 3 hours to thoroughly rinse the cavity, before moving it to the clean room for draining and drying. Thus the cavity never "saw" dirty air after the etch.

[2]For technical reasons the flow in the reverse direction could not be employed.

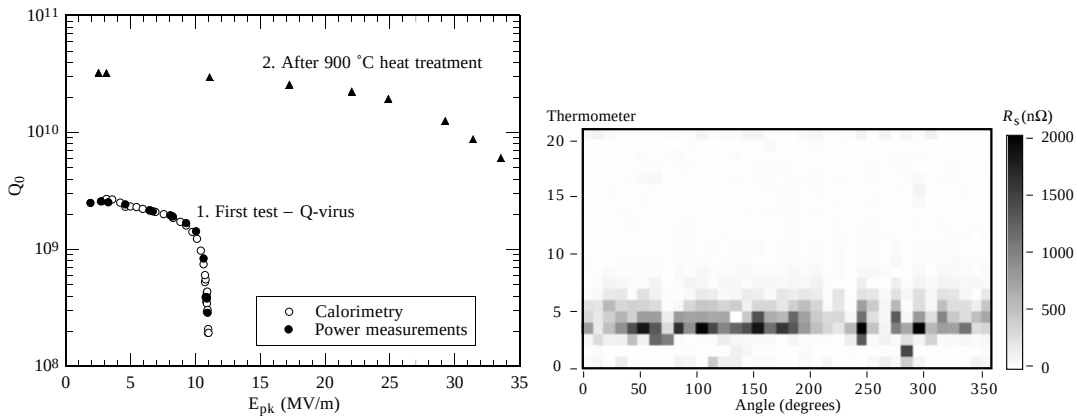

(a) (b)

Figure 8.2: (a) Q_0 versus $E_{\rm pk}$ of cavity LE1-21 after undergoing the modified etch procedure. A Q_0 curve obtained after a 900 °C heat treatment is included for comparison. (b) Map of the cavity surface resistance at 8.3 MV/m.

To our surprise, the Q_0 of this cavity was severely degraded, and a band of *very* lossy material was detected in the bottom half of the cavity (see Figure 8.2). $R_{\rm s}$ values over 1000 nΩ were recorded!

We suspect hydrogen contamination to be the cause of these high losses. It is likely that the acid being diluted by the water heated up due to the acid–water reaction. The very viscous and dense acid mixture will also tend to settle in the bottom half of the cavity, where most of the increased losses were observed.

At a later date, the cavity was heat treated at 900 °C and 10^{-6} torr for two hours. No titanium was used for gettering. Indeed, the cavity recovered it's high Q_0 state of over 3×10^{10}, confirming previous experience that 900 °C heat treatment is sufficient to drive out hydrogen. Anomalous losses could also no longer be detected by thermometry (shown later in Figure 8.5).

Our results therefore clearly demonstrate the need for very rapid rinsing after etching, particularly if large quantities of acid remain in the cavity at the conclusion of the etch. The volume of water used should be significantly greater than the amount of acid remaining, to permit rapid dilution of the acid without significant heating.

8.2.2 Hydride precipitation at the equator

All other cavities tested had Q_0's in excess of 10^{10} and were essentially Q-virus free. However, in four cases we noticed a band of slightly elevated losses along the equator. At low fields this effect was generally not very pronounced, but the equator losses increased more rapidly with $E_{\rm pk}$ than the surface resistance elsewhere, resulting in a very visible lossy band at high fields. An example of these observations is shown in Figure 8.3. Figure 8.4 illustrates the rapid increase of the equator surface resistance by taking the ratio of the site marked "1" in Figure 8.3(b) to that marked "3", a random place in the cavity. For comparison, the same ratio is shown for the site marked "2". In both cases the ratios are normalized to one at low field. Ratios are plotted, rather than true $R_{\rm s}$ values,

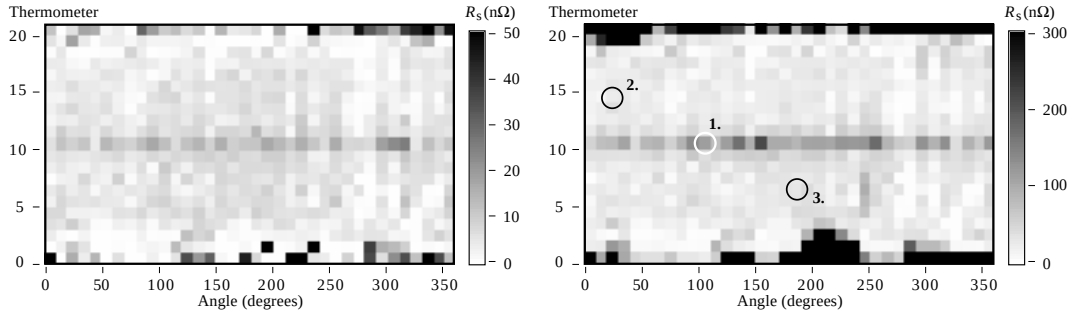

(a) (b)

Figure 8.3: Surface resistance of cavity LE1-20 at (a) $E_{\rm pk} = 15$ MV/m and (b) 30 MV/m. The losses along the equator increase faster with $E_{\rm pk}$ than elsewhere, typical of hydrogen related losses. Dark regions along the irises are either field emission related, or due to noisy signals because the magnetic field is very low in this region.

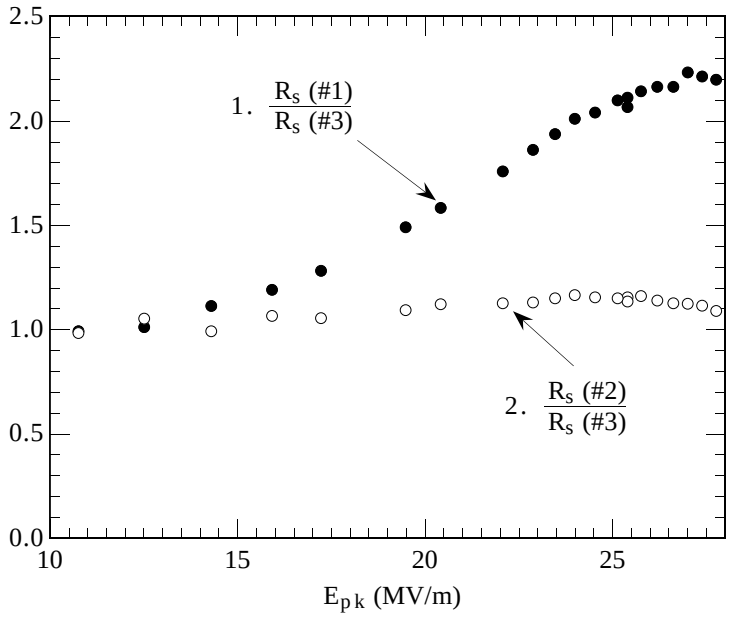

Figure 8.4: Ratio of the surface resistance measured by 1. thermometer "1" in Figure 8.3 to that measured by thermometer "3", and 2. thermometer "2" to that measured by thermometer "3". Both curves are normalized to one at low field.

so that global, non-quadratic losses due to, for example, x-ray bombardment are canceled out. The rapid increase of $R_{\rm s}$ along the equator is very apparent. At 30 MV/m, the mean surface resistance of the equator is 99 nΩ, almost 5 times the resistance measured away from the equator (20 nΩ). The increased losses are responsible for a 20 % drop in the Q_0.

Cavity LE1-21, which had received a 900 °C heat treatment to remove all hydrogen, did not display anomalous equator losses (Figure 8.5). We therefore suspect that the equator is susceptible to hydride precipitation, despite the fact that we always cool

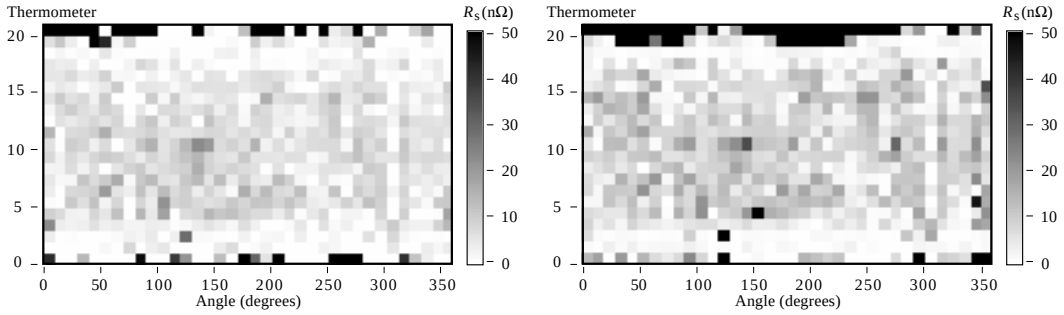

(a) (b)

Figure 8.5: Surface resistance of cavity LE1-21 following a 900 °C heat treatment. (a) At $E_{\rm pk} = 10$ MV/m, and (b) at 27 MV/m. No enhanced losses were observed along the equator. Dark regions along the irises are either field emission related, or due to noisy signals because the magnetic field is very low in this region.

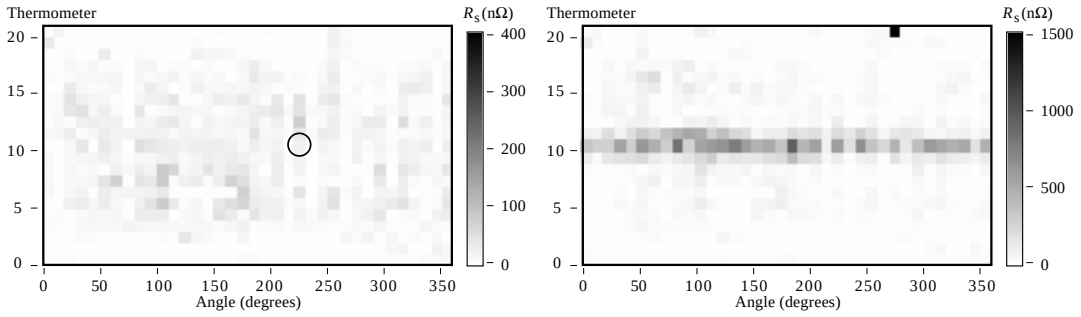

(a) (b)

Figure 8.6: Surface resistance of cavity LE1-34 at 30 MV/m. (a) First test, (b) second test following a temperature cycle to 77 K $< T_{\rm b} <$ 273 K. The losses recorded at the circled site are summarized in Figure 8.8.

cavities rapidly at rates equal to or greater than 5 – 10 K/min.

We obtained confirmation of our hypothesis when we tested cavity LE1-34. In total, this cavity had received a 100 μm etch (inside and outside) with BCP 1:1:2. At no time did the acid temperature exceed 14.5 °C. During the very first test the cavity did *not* have a resistive band along the equator, even at the highest fields (Figure 8.6(a)). The cavity was then permitted to warm to 77 K $< T_{\rm b} <$ 273 K without the cryostat being moved. The exact temperature is not known, but we suspect it was much lower than 273 K because there was significant ice build-up on the top of the cryostat. At that point, liquid helium was retransferred for another test of the cavity.

Immediately it was apparent that a band of very lossy material had appeared along the equator, both at low fields and even more so at high fields (see Figure 8.6(b)). Correspondingly, the cavity Q_0 had degraded by 11 % at the lowest field (2.3 MV/m) and by a factor of 1/2 at 15.3 MV/m. As the fields were increased the Q_0 dropped very rapidly despite the fact that no new field emitters were active when compared to the

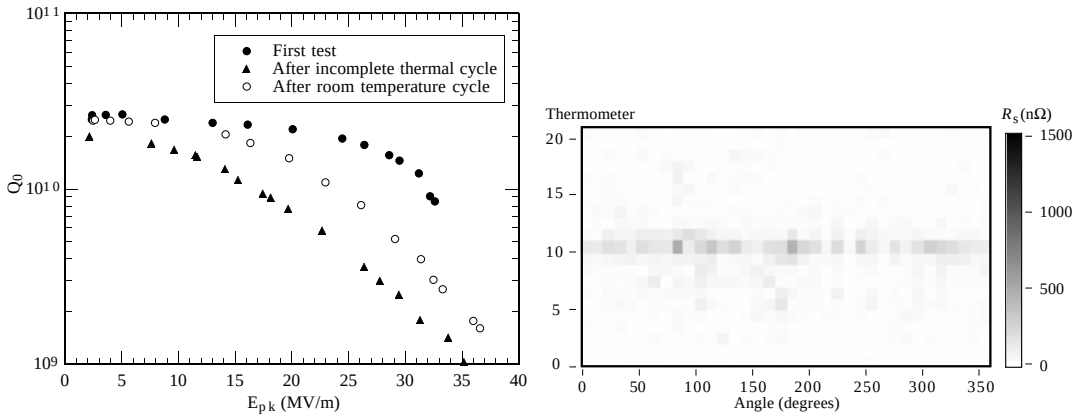

(a) (b)

Figure 8.7: (a) Q_0 results obtained with cavity LE1-34. In all cases, x-rays were only detected at $E_{\rm pk} = 20$ MV/m or higher. (b) Surface resistance of cavity LE1-34 at 30 MV/m, following an incomplete thermal cycle and then a complete cycle to room temperature.

previous test. The first x-rays were not detected until 20 MV/m by which time the Q_0 was only 7×10^9. At 30 MV/m the Q_0 was reduced by over a factor of six with respect to the previous test (Figure 8.7(a)).

To study the new losses, we warmed the cavity once more, this time all the way to room temperature. Helium was then retransferred to the cavity as quickly as possible (it took only 25 min to cool the cavity to 4.2 K). The low field Q_0 recovered completely. At high fields, though, a Q_0 reduction was still observed, albeit to a lesser extent than after the incomplete thermal cycle (Figure 8.7(a)). Not surprisingly we found that the losses along the equator, although significant, were not as severe as before (see Figure 8.7(b)).

The losses observed by the thermometer circled in Figure 8.6(a) are summarized in Figure 8.8. Note the semi-logarithmic scale. The dramatic increase in losses following the incomplete thermal cycle is very apparent. The mean $R_{\rm s}$ recorded by all the equator thermometers during the first test was 28 nΩ at 30 MV/m, which is consistent with a measured cavity Q_0 of over 10^{10}. Following the first temperature cycle, the mean equator resistance increased to a staggering 672 nΩ! If the entire cavity had increased its losses to this value, a Q_0 of only 4×10^8 could be expected. However, since only the equator was afflicted, a Q_0 of 2×10^9 was recorded. A significant improvement following the complete temperature cycle and subsequent fast cooldown was registered. At low field, the original $R_{\rm s}$ was recovered but the losses increased with $E_{\rm pk}$, reaching a mean value of 278 nΩ at 30 MV/m. This value is still a factor of 10 worse than the original losses, and the Q_0 at this point was down by more than a factor of two from the first test.

8.2.3 Discussion

The results obtained with cavity LE1-34 point to an affliction by the Q-disease. The evidence is, that the equator is more susceptible to hydrogen precipitation than the remainder of the cavity. Since the material properties of the weld are different than those of the rest of the cavity, preferential hydride precipitation along the equator is not

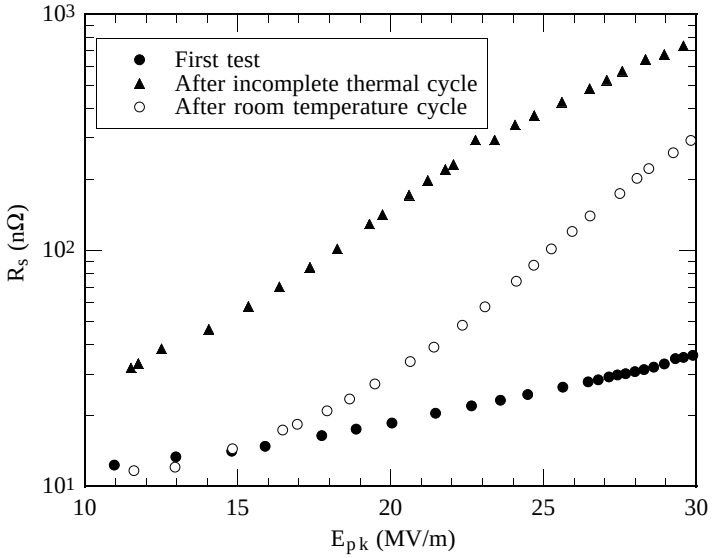

Figure 8.8: Surface resistance recorded at the circled site in Figure 8.6(a) during three different tests. The slight increase in R_s with E_{pk} during the first test was observed throughout the entire cavity and is probably not related to hydrogen contamination.

necessarily surprising. The grain sizes of the weld are quite large (several millimeters), and the impurity concentrations may also differ from the bulk. Past experience has shown that niobium with fewer interstitial impurities (i.e., a higher RRR) is far more susceptible to the Q-virus. [98] The interstitial impurities serve as trapping centers for hydrogen, thereby preventing hydride precipitation. Similarly, vacancies and grain boundaries are also very effective at trapping hydrogen by forming Cottrell clouds. [101, 186–188] It is possible that the welds, because of their large grains, are more susceptible to the Q-virus due to the lack of trapping centers that otherwise prevent hydride precipitation.[3] For confirmation of this assumption, though, a detailed analysis of the weld's material properties is required.

Although a large fraction of LE1-34 was not seriously affected by the hydride precipitation, the losses along the equator were so severe that they lowered the Q_0 substantially. Even a very rapid cooldown, faster than 10 K/min, did not "cure" the cavity completely. (In an accelerator, cooldown rates of 10 K/min are not permitted due to the dangers of stress induced component failures. A "cure" of Q-virus afflicted cavities thus requires a costly disassembly, heat treatment, and reassembly.)

Although cavity LE1-34 was an extreme case, augmented losses along the equator were observed in other cavities as well. In cavity LE1-20 they accounted for a 20 % drop in Q_0. For the highest Q_0 applications it would be advantageous, if welds could be eliminated in high magnetic field regions, to avoid the danger of hydride enhanced losses.

Our results also point to the dangers of repeated temperature cycles of cavities. Hydride precipitation may not occur after the first cooldown, but a second cooldown can cause problems. This effect was also observed with cavities at DESY. [189]

[3] Note that the iris welds do not cause operational problems, since they are in a low magnetic field region.

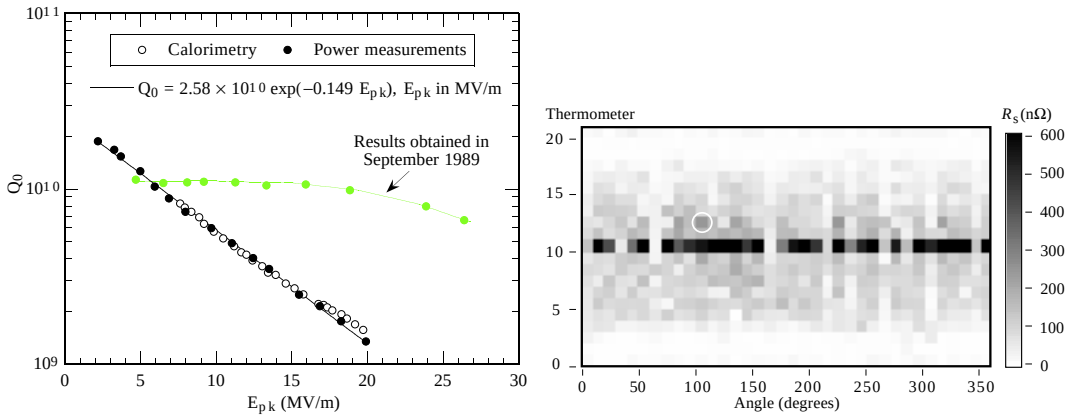

(a) (b)

Figure 8.9: (a) Q_0 versus $E_{\rm pk}$ of cavity LE1-26. Results obtained in 1989 are also included for comparison. (b) Map of the same cavity's surface resistance at 21.7 MV/m.

8.3 Titanium contamination

Two of the cavities we tested (LE1-25 and LE1-26) had unusual losses that were negligible at low fields, but increased *exponentially* with $E_{\rm pk}$. These losses were prevalent throughout the high magnetic field region. Although hydride precipitation was initially believed to be at fault, several observations suggested that a different mechanism was active. We will show in this section that these losses are likely to have been caused by titanium remnants in the grain boundaries from previous high temperature heat treatments in the presence of titanium wrap.

8.3.1 Experimental evidence

Figure 8.9(a) depicts the Q_0 versus $E_{\rm pk}$ curve obtained with cavity LE1-26. Almost identical behavior was observed with cavity LE1-25 as well. The low field $Q_0 \approx 2 \times 10^{10}$ is comparable to values obtained with most cavities. However, despite the fact that there is no field emission (no x-rays were observed), the Q_0 dropped exponentially with $E_{\rm pk}$. At $E_{\rm pk} = 20$ MV/m the Q_0 had already fallen by over a decade. Calorimetry also confirmed the exponentially increasing losses. For comparison, we included the Q_0 results obtained in a 1989 test with the same cavity. The drastically different behavior is clear.

The losses extend over most of the high magnetic field region as shown in Figure 8.9(b). Enhanced losses, reminiscent of those discussed in Section 8.2, are visible along the equator. These losses dominate the landscape at low fields as well (not shown).

Our initial interpretation was, that the cavities had also been contaminated with hydrogen. To investigate this theory, we warmed cavity LE1-25 to room temperature and cooled as rapidly as possible, thereby trying to prevent possible hydride precipitation. However, no improvement in the cavity Q_0 was observed, suggesting that the Q-disease was not responsible for the losses.

We were able to completely rule out hydride precipitation as the loss mechanism, by

heat treating cavity LE1-26 at 900 °C for 2 hours at pressures better than 10^{-6} torr. In the previous section we showed that such a treatment removes all hydrogen from the niobium. This result is also confirmed by calculations (see Equation 3.20). Only a very light etch at 10 °C was performed after the bake to remove surface contaminants, yet to prevent renewed hydrogen contamination. Nevertheless, the heat treatment did *not* change the Q_0 behavior of the cavity.

8.3.2 Discussion

The ineffectiveness of the fast cooldown and the heat treatment essentially rules out hydride precipitation as the dominant loss mechanism. Two other observations are also in agreement with this conclusion.

1. The Q-virus not only reduces the high field Q_0 but also the low field value (see Figure 8.2). In contrast, cavities LE1-25 and LE1-26 both had high Q_0 values at low field, that even exceed previously achieved Q_0's.

2. The Q_0 of heavily hydrogen contaminated cavities drops rapidly at low to intermediate fields, but then stabilizes above $E_{\rm pk} = 10$ MV/m. [96] In our case, however, the Q_0 decline continued unabated.

We therefore expect that another mechanism is responsible for the high losses in Figure 8.9.

8.3.2.1 Intergrain losses

The exponential drop of Q_0 in Figure 8.9 is very reminiscent of the losses observed in sputtered niobium on copper and NbTiN coated cavities. Figure 8.10 shows examples of results obtained with these kinds of cavities. High temperature superconductors also display such behavior.

It is believed that the granularity of the superconducting film is responsible for the losses. [190–192] The grain boundaries form weak Josephson junctions through which the superconducting currents have to tunnel. Excessive power dissipation results, if the critical current density of the junctions is exceeded.

To calculate the surface resistance of the material one has to analyze a lattice of Josephson junctions. Each junction is capable of carrying a maximum current density $j_{\rm max}(T)$ which, near $T = 0$, scales as

$$j_{\rm max} \propto \frac{\Delta/e}{a^2 R_{\rm g}}. \tag{8.1}$$

Here Δ is the superconducting energy gap, and $R_{\rm g}$ is the normal state resistance of a grain boundary of area a^2. [193] For weakly coupled grains, the maximum current density that can be carried by the junction can be significantly less than the critical current density of the bulk superconductor.

An analysis of the lattice of junctions shows that in weak rf fields or for samples with high $j_{\rm max}$ the surface resistance is given by

$$R_{\rm s}^{\rm low} = \frac{\mu_0 \hbar \omega^2}{4\Delta} \frac{\hbar/2eaj_{\rm max}\mu_0}{\sqrt{\lambda_{\rm L}^2 + \hbar/2eaj_{\rm max}\mu_0}}, \tag{8.2}$$

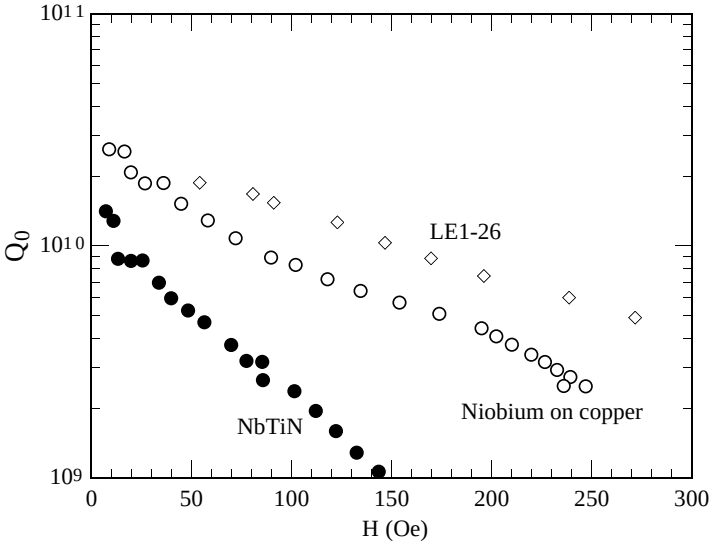

Figure 8.10: Q_0 versus magnetic field measured with (a) niobium sputtered on copper (at 1.5 GHz, $T_\mathrm{b} = 1.7$ K), (b) NbTiN (at 4 GHz, $T_\mathrm{b} = 1.7$ K) [190] and (c) niobium cavity LE1-26 (at 1.5 GHz, $T_\mathrm{b} = 1.67$ K).

λ_L being the London penetration depth of the bulk superconductor. [192] Bulk niobium, as used for our superconducting rf cavities, falls in this category, and the contribution made by the grain boundaries to the total surface resistance is negligible.

However, when the rf fields are increased (or j_max is small) and the current density satisfies $j \gg j_\mathrm{max}$, then the surface resistance is simply given by the normal conducting resistance of the grain boundaries:

$$R_\mathrm{s}^\mathrm{high} = R_\mathrm{g} a/\delta, \tag{8.3}$$

δ being the penetration depth of the fields in the grain boundaries. [190] Since the ratio $\hbar\omega/2\Delta \ll 1$ in the GHz domain, $R_\mathrm{s}^\mathrm{high}$ is significantly larger then $R_\mathrm{s}^\mathrm{low}$.

The transition from $R_\mathrm{s}^\mathrm{low}$ to $R_\mathrm{s}^\mathrm{high}$ in this simple model occurs very abruptly, when the magnetic field in the grain boundary exceeds $H = j_\mathrm{max}\delta$. However, $R_\mathrm{s}^\mathrm{low}$ and $R_\mathrm{s}^\mathrm{high}$ are both field independent.

A more realistic model assumes that there is a spread in j_max values. Thus, even at reasonably low fields a fraction of the grains may be in the high loss state, so that an average of $R_\mathrm{s}^\mathrm{low}$ and $R_\mathrm{s}^\mathrm{high}$ needs to be taken to yield the overall surface resistance R_s. Increasing the field then changes the fraction of grains in the $R_\mathrm{s}^\mathrm{high}$ state and hence R_s.

The behavior of R_s with H depends on the distribution function $p(j_\mathrm{max})\, dj_\mathrm{max}$ describing the fraction of grains that have a critical current density j_max. For example, if $p(j_\mathrm{max})$ is linear with j_max, then R_s increases linearly with H. [190]

8.3.2.2 Diffusion of titanium in niobium

Because of the analogous behavior of Nb/Cu and NbTiN cavities and LE1-25/26 we began considering intergrain losses as a potential explanation for the behavior of our cavities. What caused the grain boundaries to become lossy?

Previously, these two cavities had been the subject of an investigation of high temperature heat treatment in the presence of titanium, to evaluate the benefit on emission reduction. [60][4] Both cavities had been heat treated numerous times at very high temperatures. Cavity LE1-25 was baked for a total of 16 hours at $T < 1450$ °C using titanium *on the outside only* for solid state gettering. [111] In addition, the cavity was also treated at temperatures as high as 1600 – 1700 °C for eight hours. None of the other cavities we tested were baked at such high temperatures. Above 1450 °C the vapor pressure of pure titanium is too high for conventional cavity purification, so NbTi was used instead. *Again, getter material was only applied to the outside of the cavity.* Cavity LE1-26 received a very similar treatment to LE1-25.

Heavy etches were used to remove the getter material from the cavity wall following heat treatment. This step is required because NbTi, that results from extensive diffusion of titanium into the niobium bulk, has a low thermal conductivity and a high resistivity.[5] Subsequent tests confirmed that high Q_0 results could be achieved, as shown in Figure 8.9, and an exponential drop of Q_0 with $E_{\rm pk}$ was not observed until the most recent tests before our studies.

Because of the uniquely high temperature heat treatment received by LE1-25 and LE1-26 we suspected that titanium was responsible for the Q_0 degradation in the last test series. Could it be possible that titanium remained in the cavity wall, even after a 100 μm etch? Reported diffusion rates for titanium in niobium in the range 994 °C $< T <$ 1492 °C are [194]

$$D_{\rm Ti} = 9.9 \times 10^{-6} \ \frac{\rm m^2}{\rm s} \exp\left(-\frac{43750 \ \rm K}{T}\right). \tag{8.4}$$

If we extrapolate this data to 1700 °C then $D_{\rm Ti} = 2.3 \times 10^{-15}$ m^2/s is anticipated. In $t = 8$ hours we expect a maximum diffusion distance of $x = \sqrt{2 D_{\rm Ti} t} \approx 10$ μm, which is much less than the cavity's wall thickness. Volume diffusion therefore cannot account for any presence of titanium on the rf surface.

However, diffusion along grain boundaries can occur at much greater rates than volume diffusion. The 100 μm etches following normal heat treatment (with titanium on the inside and outside), required to restore the Q_0, are indicative of this fact. Measurements show, that the diffusion constant in the grain boundaries of many materials is enhanced by factors as high as $10^5 \rightarrow 10^6$. [195] Thus, distances up to 10 μm $\times \sqrt{10^5 \rightarrow 10^6} =$ 3 mm $\rightarrow$ 10 mm may be possible in 8 hours at 1700 °C.

We suspect that rapid diffusion along the grain boundaries had allowed titanium to move through most of the cavity wall and to segregate between the grains.[6] Repeated etches then uncovered the titanium. The fact that the equator, which is almost 1/16″ (= 1.6 mm) thinner than the rest of the cavity, was much lossier (see Figure 8.9(b)) lends its support to this theory. The NbTi system is either normal conducting or only weakly superconducting at the cavity operating temperature. The Nb-Ti-Nb sandwiches therefore form Josephson junctions that lead to high losses as outlined in the model earlier.

[4]Note that the temperatures quoted in this reference were slightly underestimated at the time.

[5]If titanium is used on the inside surface of a cavity, up to 100 μm need to be removed to restore the low surface resistance of niobium.

[6]Note that the wall had been thinned substantially by the numerous etches the cavity had received in the past.

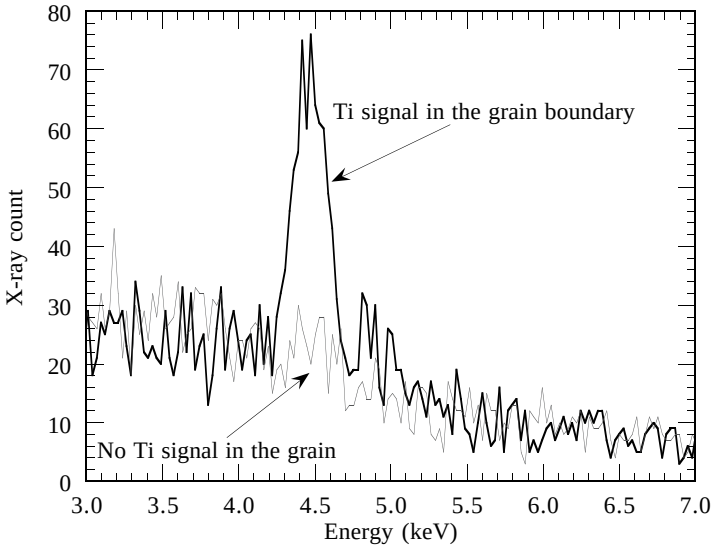

Figure 8.11: PIXE analysis of the rf surface of cavity LE1-25. Results for both a grain and a grain boundary are shown. Titanium was only found in the grain boundary.

Our hypothesis is supported by studies performed at Saclay and the Laboratoire de Süe using proton and deuterium induced x-ray emission (PIXE and DIXE microprobe) analyses of niobium samples heat treated at 1350 °C with titanium. [196] The microprobe has a spatial resolution of 1 μm and is able to detect as little as one monolayer of titanium in a grain boundary. These experiments clearly demonstrated that titanium diffused much further along grain boundaries in the niobium samples than elsewhere. The concentration of titanium in the boundaries was also shown to depend on the orientation of the grains.

To investigate whether titanium was present in cavity LE1-25, we analyzed the rf surface with our EDX system. We failed to detect any titanium in either the grains or the grain boundaries. However, taking into account that the EDX system samples a volume larger than 1 μm^3, and its detection limit is no better than 0.1 at. %, even several monolayers of titanium in a grain boundary will go undetected.[7]

To improve the detection limit, several samples were analyzed at Saclay and the Laboratoire de Süe using the PIXE technique. Very convincingly, large amounts of titanium were detected in the grain boundaries, whereas no titanium was found in the grains themselves. Figure 8.11 shows some of the results obtained. Since the cavity had only been coated with titanium on the outside during heat treatment, titanium must have diffused all the way through the wall to reach very nearly the rf surface.

Samples taken from another cavity heat treated below 1450 °C (LE1-23) were also analyzed, but no titanium was detected. Correspondingly, no Q_0 degradation had been observed. This was despite the fact that the cavity had been thinned to 1.2 mm by repeated etching.

[7]Grain boundaries are no more than a few Angstroms thick.

8.3.3 Summary

We have presented strong evidence that greatly enhanced diffusion of titanium along grain boundaries is possible during heat treatment of cavities. Diffusion over millimeter distances in as little as 24 hours at $T \leq 1700$ °C has been recorded.

Our Q_0 versus $E_{\rm pk}$ and thermometry data suggest that titanium present in the grain boundaries has little or no effect on the losses of a cavity at the lowest fields. However, the losses, which are magnetic in nature, increase exponentially with the applied field by as much as a decade at $E_{\rm pk} = 20$ MV/m! The evidence points to the decoupling of the grains due to weakly superconducting (or normal conducting) titanium contaminated grain boundaries as the source of the enhanced rf losses. Since we are unaware of any means of removing the titanium from the grain boundaries, there does not seem to be a way of salvaging such a cavity.

Titanium related Q_0 degradation has not been observed with any of the other cavities that were heat treated below 1450 °C (for example cavity LE1-23). Good Q_0 values were even achieved when such a cavity was thinned to 1.2 mm with BCP. It therefore appears that conventional heat treatment does not pose a danger of titanium contamination. However, even in this case, diffusion over distances as large as 100 μm in the grain boundaries has been reported. [82] This necessitates the removal of large amounts of niobium following the heat treatment, especially if the cavity interior is coated with titanium for improved gettering during the heat treatment. The danger of hydrogen contamination is thereby greatly enhanced (see Section 8.2). More recently developed low temperature heat treatment with titanium [197], which prevents excessive diffusion, may therefore prove to be more useful.

8.4 Particles

The motion of particles in dc gaps has been reported by several authors (e.g., [198]). Similarly, artificially introduced iron particles in an rf cavity were also shown to move under the influence of electric fields. [64, 67] However, the motion of naturally occurring particles has so far not been observed in rf cavities. Here we present indirect evidence, that indeed such particles can move as well. Our thermometry system is sensitive enough to detect the appearance of new particles on the rf surface.

8.4.1 Example of particle motion

On at least nine occasions in several different cavities we observed abrupt increases in low field ohmic losses in a very localized area of the cavity (i.e., only one thermometer and perhaps its neighbors responded). An example of such a jump is shown in Figure 8.12. Once the transition to the more resistive state was made, the curve marked "3" could be traced out reversibly. The near linear dependence of the curve demonstrates that the losses were ohmic in nature. Since the thermometer was located in the high magnetic field region ($S = -4.7$ cm), we concluded that we had witnessed the arrival of a resistive particle at that site.

Note that a temperature resolution of better than 1 mK is essential to detecting the particle motion. This fact explains, why such events were not previously observed with older thermometry systems.

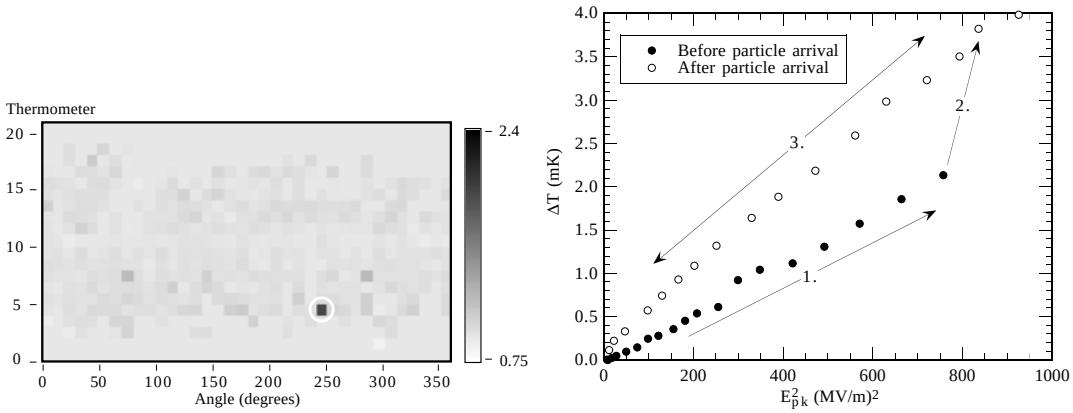

(a) (b)

Figure 8.12: (a) Ratio of the surface resistance of cavity LE1-31 at 16 MV/m after and before a jump in R_s was recorded at the circled site. (b) Temperature data recorded by the circled thermometer. The near linear behavior with E_{pk}^2 both before and after the transition (2) demonstrates that the power dissipation in this area was ohmic in nature.

8.4.2 Estimating the particle size

The information in Figure 8.12 can be used to estimate the size of the arriving particle.

Let us assume that the particle is spherical, radius r_d, and has a surface resistance R_d. To a good approximation, the power $\dot{Q}$ dissipated in the particle then is

$$\dot{Q} = \pi r_d^2 R_d H^2. \tag{8.5}$$

Here we are assuming that the effective area of the particle exposed to the rf field is only one half of the total particle area ($A_d = 2\pi r_d^2$). We are also neglecting the geometric enhancement of the magnetic field. In Section 3.2.2 we showed that this indeed is valid to within less than a factor of 1.5. Since we can only crudely estimate R_d, omission of field enhancement is not a serious problem.

For small temperatures (< 1 K), the theoretical temperature rise ΔT^{theory} at the outside wall is linearly related to the power dissipated in a point defect by $\Delta T^{\text{theory}}/\epsilon_T = \dot{Q}$. The parameter ϵ_T needs to be determined either experimentally or by thermal transport simulations. Since the thermometer efficiency η_T is only about 30 % we can write

$$\dot{Q} = \pi r_d^2 R_d H^2 = \frac{\Delta T}{\epsilon_T \eta_T}, \tag{8.6}$$

where ΔT now is the temperature rise recorded by thermometry *due to the arrival of the particle*. We also have to be able to account for cases where the thermometer is not exactly at the particle location, so we include another correction term $c_d \geq 1$, so that

$$\pi r_d^2 R_d H^2 = \frac{c_d \Delta T}{\epsilon_T \eta_T}. \tag{8.7}$$

The factor c_d depends on the distance between the thermometer and the particle as well as the full-width-at-half-maximum (FWHM) of the temperature distribution at the outside of the cavity.

Table 8.1: Calculated values of the FWHM and $\epsilon_T = \Delta T^{\text{theory}}/\dot{Q}$ for various cavities at a bath temperature of ≈ 1.66 K.

Cavity	FWHM (cm)	ϵ_T (K/W)
LE1-17	1.1	1.66
LE1-20	1.0	1.44
LE1-17	1.0	1.44
LE1-23	0.45	4.12
LE1-27	1.1	1.54
LE1-31	1.1	1.66
LE1-32	1.1	1.66
LE1-31	1.1	1.66
LE1-33	1.1	1.66
LE1-34	1.1	1.66
LE1-CEBAF	1.2	1.42
LE1-Heraeus	1.0	1.27

Solving for r_{d} one finds

$$r_{\text{d}} = \sqrt{\frac{c_{\text{d}}\Delta T}{\pi\epsilon_T\eta_T R_{\text{d}}}}\frac{1}{H}. \tag{8.8}$$

We used the computer code HEAT [119] to simulate the flow of heat from a point source into the niobium wall and the helium bath on the other side. The code takes into account the temperature dependent thermal conductivity of the niobium as well as the temperature dependent Kapitza conductivity of the niobium–helium interface. In this manner, we calculated ϵ_T and FWHM values for all cavities tested. Table 8.1 summaries the results.

Returning to the measured data in Figure 8.12 we are now in a position to estimate the particle size. A priori, we do not know R_{d}. Past experience has shown that most particles encountered in rf cavities are conducting, such as stainless steel, copper, titanium and indium (see also Chapter 5). In many cases, several different impurities are detected in the same particle. For most of these materials, a surface resistance of 10 mΩ at cryogenic temperatures is a reasonable value. Note that r_{d} is proportional to $R_{\text{d}}^{-0.5}$ and therefore fairly insensitive to our guess of R_{d}.

Only thermometer four at 240° recorded a temperature increase. Hence we assume that the thermometer was very close to the particle, and $c_{\text{d}} \approx 1$. At $E_{\text{pk}} = 20$ MV/m ΔT is only 1 mK. The magnetic field H at the particle location ($S = -4.7$ cm) is 450 Oe at 20 MV/m. Thus (8.8) yields

$$r_{\text{d}} = 7\ \mu\text{m}.$$

This particle size is consistent with field emitting particles found in cavities in the SEM (Chapter 5).

In principle, small particles can contaminate the cavity when it is cut apart for examination. Except for emitting particles we are unable to distinguish particles present during cavity tests from those introduced during cutting, and it is fruitless to search for particles whose arrival was detected during tests, unless they melted. However later we will give one example, where we were successful in identifying a particle that had arrived

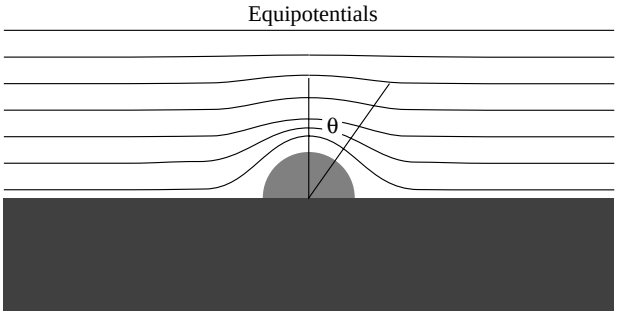

Figure 8.13: Schematic of the equipotentials near a conducting hemisphere sitting on an infinite conducting plane.

during the cavity test. Also, in Chapter 5 we showed a field emitting particle whose arrival was detected by thermometry (see Figure 5.8).

8.4.3 Electric and adhesive forces

The newly arrived particle is subject to two competing forces: the adhesive force and the force exerted by the rf electric field on the particle. We present a simple analysis that permits us to estimate the strengths of these forces.

8.4.3.1 Electric force

The pressure ($P_{\rm e}$) an electric field exerts on a conductor is given by

$$P_{\rm e} = \frac{\sigma E}{2}, \tag{8.9}$$

σ being the charge induced per unit area. Since $\sigma = \epsilon_0 E$, the pressure is

$$P_{\rm e} = \frac{\epsilon_0 E^2}{2}. \tag{8.10}$$

The force is always normal to the surface and outward because of the attractive force between the field and the induced surface charge.

If we consider a conducting hemisphere sitting on the niobium substrate, the equipotentials are distorted as shown schematically in Figure 8.13. The electric field is enhanced at the zenith, and zero at the equator. An analytical treatment of this problem shows that the electric field at the particle surface is [24]

$$E = \hat{r}\, 3E_0 \cos\theta, \tag{8.11}$$

where E_0 is the externally applied field and $\hat{r}$ is the unit vector in the radial direction.[8]

Only a net force on the particle normal to the substrate surface exists. The other component cancels when integrating $P_{\rm e}$ over the hemisphere. The net force $F_{\rm e}$ is

$$\begin{aligned} F_{\rm e} &= \frac{9\epsilon_0 E_0^2}{2} \int_0^{\pi/2} 2\pi r_{\rm d}^2 \cos^3\theta \sin\theta \, d\theta \\ &= \frac{9}{4}\, \pi \epsilon_0 E_0^2 r_{\rm d}^2. \end{aligned} \tag{8.12}$$

[8]Note that the electric field enhancement is greater than the magnetic field enhancement (discussed in Section 3.2.2).

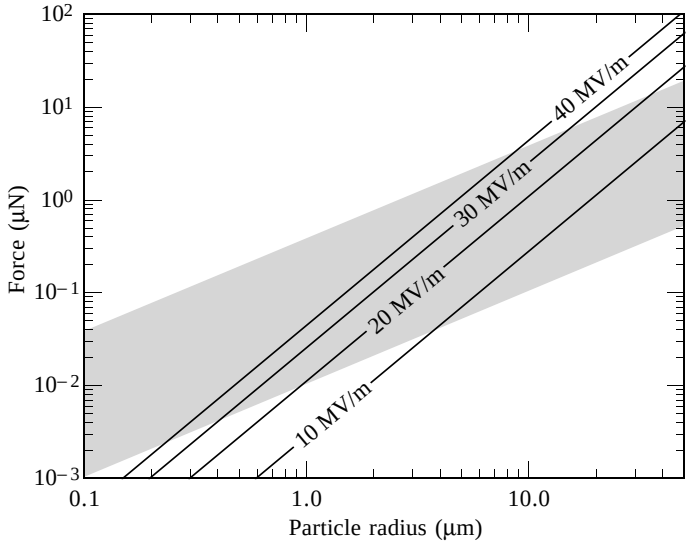

Figure 8.14: Comparison of the adhesive and electric forces acting on micron size conducting particles. The shaded region is the range of the adhesive force applicable to many conducting particles. [199] The parallel lines show the electric force given by (8.13) for a number of fields E_0.

Since we are dealing with rf fields, we multiply by 1/2 to take the time average, so that the effective force acting on the particle is

$$\bar{F}_{\mathrm{e}} = \frac{9}{8}\pi\epsilon_0 E_0^2 r_{\mathrm{d}}^2 \approx \pi\epsilon_0 E_0^2 r_{\mathrm{d}}^2. \tag{8.13}$$

In reality the particle is likely to be more like a sphere than a hemisphere so that the field enhancement is greater. However (8.13) is a good first approximation.

8.4.3.2 Adhesive force

An analysis of the adhesive force (F_{a}) is more involved. In particular, its main components, the van der Waal and electrostatic forces, depend critically on the contact points between the particle and the substrate. The particle's deformation from a perfect sphere and the presence of liquids and surface adsorbates also have a profound impact on the particle's adhesive properties. A theoretical analysis of such factors yields a range for F_{a} that applies to many conducting particles. [199] Figure 8.14 compares the adhesive and electric forces. The lower bound of the adhesive force applies to perfect spheres for which the electrostatic force between the particle and the substrate dominates. The upper bound, on the other hand, applies to spherical particles where the van der Waal force dominates. Significantly greater adhesion is possible for deformed particles and those that had already been present during any wet treatment of the rf surface. [199]

We see, that over a significant range, the electric and adhesive forces are comparable. Particle detachment under the influence of the electric field should therefore be possible. Indeed, this effect has been observed at Saclay in a 1.5 GHz rf cavity at 30 MV/m, when iron particles, 10's of micrometers in size, were sprinkled on a niobium substrate. [64,67]

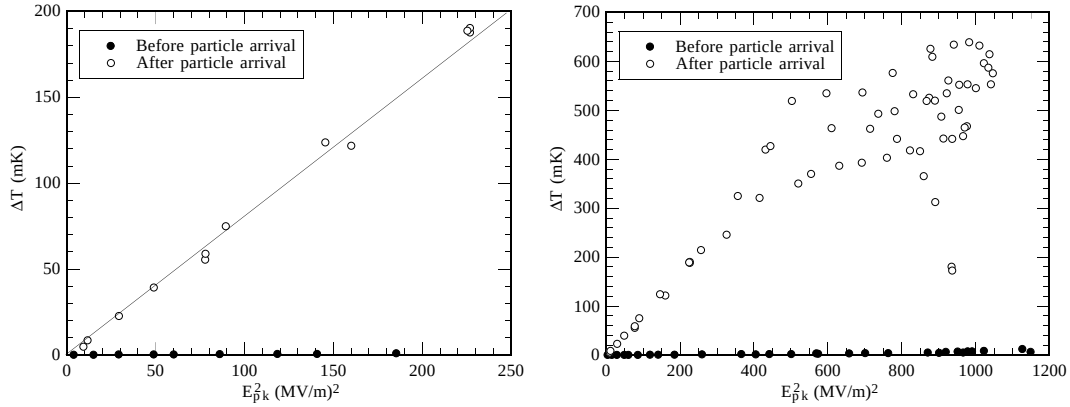

Figure 8.15: Temperature signal recorded in cavity LE1-23 before and after the arrival of a particle. (a) Low field data showing ohmic losses. (b) High field, noisy data. The neighboring thermometers showed a similar, but reduced response.

For the particle discussed in Section 8.4.1, the adhesive force is expected to be

$$0.07\ \mu\text{N} < F_\text{a} < 2.6\ \mu\text{N}.$$

The maximum E_pk achieved in the cavity after the particle arrived was 35 MV/m. At that time the local field at the particle was $E_0 = 17.1$ MV/m. Hence the maximum electric force acting on it was

$$F_\text{e} = 0.4\ \mu\text{N}.$$

Therefore it is reasonable that the particle was not removed by the electric field, thus allowing the thermometry to detect the presence of the particle.

8.4.4 Microscopy results

In many cases the temperature signal following the arrival of a particle was not as well behaved as that shown in Figure 8.12. An example is shown in Figure 8.15.

At low fields, the dissipated power is ohmic and well behaved. The curve in Figure 8.15(a) could be traced out reversibly. However, at high fields the signal becomes very noisy. This behavior was definitely not due to a faulty thermometer or electronic noise, because the neighboring (independent) thermometers showed the same response, albeit with a smaller amplitude (as expected). (This is one example of the benefit of having independent leads for each thermometer.)

The cavity subsequently was thermally cycled to room temperature and then retested. As shown in Figure 8.16, the increased losses at low fields survived the cycle almost unchanged, thereby confirming that they are likely due to the arrival of a particle. At high electric fields, the losses are much better behaved than before, but reduced. Some improvement had already been observed prior to the thermal cycle.

At 10 MV/m, where the losses are still well behaved, a temperature increase of $\Delta T = 70$ mK due to the particle arrival was recorded. By Equation 8.8, the size of the

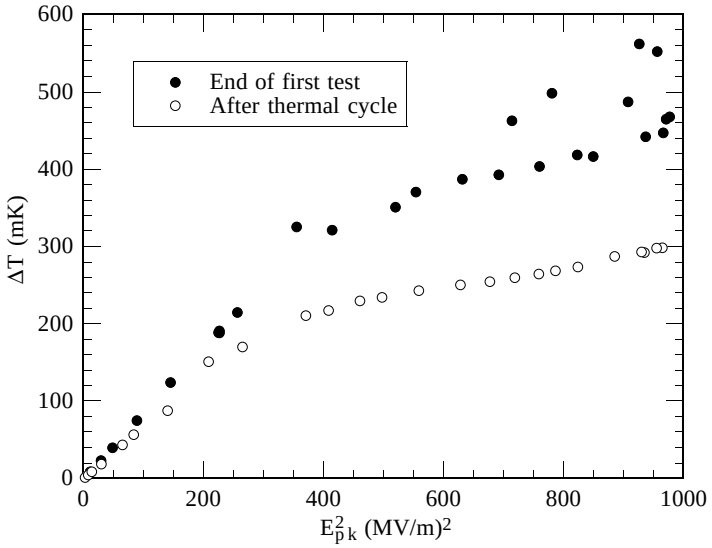

Figure 8.16: Temperature data recorded by the same thermometer as in Figure 8.15 before and after cavity LE1-23 was cycled to room temperature.

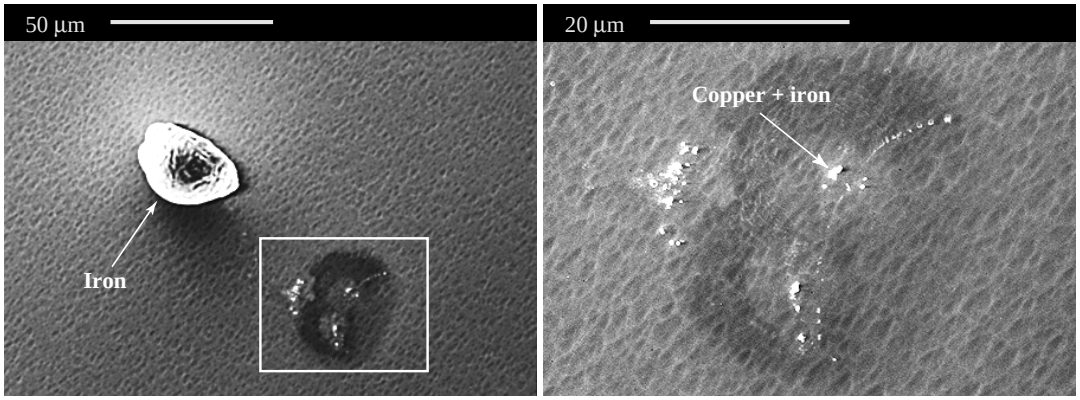

(a) (b)

Figure 8.17: (a) Particle suspected of being responsible for the increase in power dissipation depicted in Figures 8.15 and 8.16. The particle was found within less than 2 mm of the predicted location. (b) Magnified view of the discolored region in (a).

particle must have been about

$$r_{\mathrm{d}} = 70\ \mu\mathrm{m}.$$

In calculating this value we used a thermometer efficiency $\eta_T = 42\ \%$, which was obtained by comparing the Q_0 results from calorimetry with those from power measurements. The magnetic field was 204 Oe (= 16,250 A/m) and $c_{\mathrm{d}} \approx 1$.

A search of the area in the SEM turned up the iron and copper particles shown in Figure 8.17. The large particle could be removed with a 15 psi jet of nitrogen gas. Left behind was a darkened region and some debris very similar in appearance to the discoloration to the bottom right of the particle (see Figure 8.18). We therefore suspect

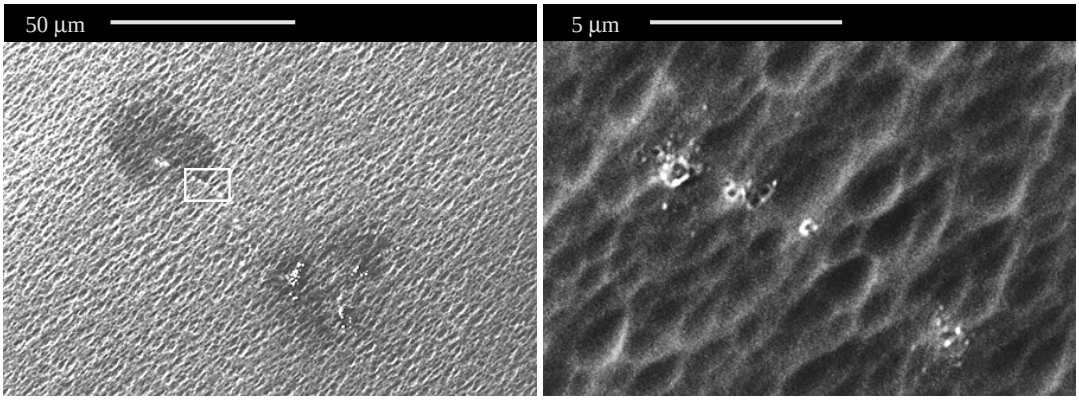

(a) (b)

Figure 8.18: (a) Same region as in Figure 8.17 after the particle had been removed with a 15 psi jet of nitrogen gas. The framed region is enlarged in (b).

that a second particle had originally been present on the rf surface, but became dislodged by the nitrogen used to pressurize the cavity during the cutting process.

There are two reasons to believe that this particle was present in the cavity during the test rather than being introduced by the cutting process. 1. Whenever larger debris is introduced by the cutting process it is very jagged. This particle however has a smooth appearance, almost as if its temperature had approached the melting point. 2. The dark regions under and next to the particle are not observed when debris is introduced by the cutting process.

If we assume that two, roughly equally sized particles were indeed present, then our previous analysis predicts that each particle is of radius

$$r_{\mathrm{d}} = \frac{70\ \mu\mathrm{m}}{\sqrt{2}} = 50\ \mu\mathrm{m}.$$

We observed $r_{\mathrm{d}} \approx 17\ \mu$m, somewhat less than the predictions.

8.4.5 Contact resistance

The discrepancy may be removed if the value of $R_{\mathrm{d}} = 10\ \mathrm{m}\Omega$ that we used is increased to 85 mΩ. This may indeed be necessary if the particle temperature was significantly higher than the bath temperature. At 900 K and above, the surface resistance of high purity iron is 81 mΩ [125], very close to the value required to explain the discrepancy in r_{d}. The question is, why would the particle be so hot?

The answer lies in the poor thermal contact between the substrate and the particle. Little power dissipation by the magnetic field is therefore required to heat the particle. Recall, that in Section 7.2 we presented a particle that had even partially melted.

One can model the particle–substrate system using a contact resistance $\mathcal{R}$ that governs the defect temperature T_{d} by

$$T_{\mathrm{d}} - T_{\mathrm{b}} = \mathcal{R}\dot{Q}. \tag{8.14}$$

Studies at Saclay with microscopic iron particles on a niobium substrate have shown that for *all* particles investigated 10^5 K/W $< \mathcal{R} < 1.4 \times 10^5$ K/W. [130] From our thermometry data we know that each of the two particles in our cavity dissipated

$$\dot{Q} = \frac{\Delta T}{2\epsilon_T \eta_T} = 20 \text{ mW}$$

at 10 MV/m, so that

$$T_\mathrm{d} = \mathcal{R}\dot{Q} \approx 2000 \text{ K!}$$

This temperature is slightly higher than the melting point of iron. However, the Saclay experiments showed that $\mathcal{R}$ drops significantly once the contact between the particle and the substrate melts, thereby preventing a complete melting of the particle. The appearance of particles after the contact resistance began to drop was very similar to the smooth particle in Figure 8.17. We therefore suspect, that the particle had indeed been very hot during the test. The discoloration under the particles is also suggestive of the elevated temperatures. We thus have a correlation with contact resistance measurements performed at Saclay.

It may be possible to trace the noisy temperature signal recorded at high fields back to a high defect temperature as well. Up to 900 °C, iron's surface resistance increases rapidly with temperature from less than 10 mΩ to above 80 mΩ. As the contact resistance changes continuously because of elevated temperatures and melting, T_d fluctuates, and therefore the dissipated power $\dot{Q}$ varies as well.

For consistency with our data, we also checked whether a 17 μm particle is expected to adhere to the rf surface at the maximum cavity field that we achieved ($E_\mathrm{pk} =$ 34 MV/m). At the particle site, the electric field was 21 MV/m so that

$$F_\mathrm{e} = 3.5 \ \mu\mathrm{N}.$$

This force needs to be contrasted with an adhesive force of

$$F_\mathrm{a} = 0.2 \ \mu\mathrm{N} < F_\mathrm{a} < 6 \ \mu\mathrm{N},$$

so that particle adhesion during the test is likely. On the other hand, a 15 psi nitrogen gas jet exerts a force of about

$$F = 10^5 \ \frac{\mathrm{N}}{\mathrm{m}^2} \times \pi r_\mathrm{d}^2 = 91 \ \mu\mathrm{N}$$

on the same particle. This value is in excess of the adhesive force and thus it is not surprising that the particle was removed.

8.4.6 Summary

For the first time, the arrival of particles in rf cavities has been observed.[9] These particles are present in the vacuum environment. Altogether nine cases in six cavity tests were observed where locally the temperature signal increased abruptly, suggesting that a particle had arrived.

[9]The Saclay experiments on particle motion were performed with artificially introduced particles.

In Section 3.3.4 we pointed out that an abundance of particles was found at KEK on silicon [102] and by us on niobium [103], even after employing cleaning procedures similar to those used for cavities. In both cases particle densities between 100 cm^{-2} and 1000 cm^{-2} were recorded. Most of the particles were less than 1 μm in size. At KEK, the density of particles smaller than 1.2 μm was 73 cm^{-2} while 52 particles per cm^{-2} greater than 1.2 μm were found. We expect even higher densities and larger particles to occur in the input coupler region and vacuum tubing of the test stand, because they are not cleaned between tests.

Microscopy results presented in this section (Figure 8.17) and previously discussed in Chapters 5 and 7, demonstrate that thermometry data can be used to predict reasonably accurately the size of particles detected by thermometry. Both here and in Section 7.2.2 we also presented microscopy evidence that particles can be heated close to their melting point by the magnetic field, due to limited thermal conduction from the particle to the niobium substrate. The evidence corroborates contact resistance measurements made at Saclay.

Chapter 9

Summary

We discussed the development of a new, state-of-the-art thermometry system designed to map the temperature distribution of 1.5 GHz superconducting niobium cavities during operation in superfluid helium. Although our new thermometry system is based on previous ones with a proven track record, both its speed and resolution represent significant improvements with respect to existing systems.

Thermometry, in conjunction with another system designed to measure the cavity quality as a function of the electric field, was used to study loss mechanisms in niobium cavities at both low and high accelerating gradients. In many instances, the thermometry data was used to localize the sources of losses, especially field emitters, which subsequently were examined in an electron microscope and EDX system, modified to accommodate a cavity half cell. Besides advancing our basic understanding of cavity losses, our studies also suggest ways to improve cavity performance for future applications.

9.1 Field emission and voltage breakdown

9.1.1 Emission mechanism

Important new insight into rf field emission was gained. We were able to show that field emission in rf cavities occurs primarily from tips on conducting particles, in agreement with research performed at other laboratories. We have witnessed the activation of such emission sites due to the arrival of particles in the high electric field region. Emission by geometric field enhancement is possible for some of the emitters examined, but in other cases smooth emitters were found, so that one has to rely on the metal–insulator–metal (MIM) model or even the metal–insulator–vacuum (MIV) model to explain enhanced emission.

It also appears that the emission from conducting particles, be it by geometric field enhancement or the MIM model, is affected by adsorbed gases. The evolution of gases triggered by unrelated events in the cavity (such as thermal breakdown or multipacting) was documented to lead to the activation of field emission. Such interactions were observed numerous times. In one case we were able to show conclusively, that particles were the source of emission, whose strength changed on several occasions as gases were adsorbed and desorbed. In this case, it would appear that two separate mechanisms, one based on the MIM model and the other on adsorbed gases, cooperated to enhance field emission.

The desorption of gases from field emitters appears to explain the deactivation of a significant number of emitters during rf and helium processing. The renewed adsorption of gases (for example, after a thermal cycle) often reactivates such emitters. For lasting benefits it is therefore important that the emitter be permanently destroyed by melting it completely.

9.1.2 Discharge

A major portion of our study was devoted to understanding the process of voltage breakdown at emission sites and the accompanying destruction of the emitter (explosive processing). Our investigations showed that Joule heating by the emission current alone is insufficient to melt more than just the emission tip (the "microemitter"). Evidence from microscopy and thermometry demonstrates that the production of a plasma is critical to melting an entire particle (the "macroemitter") and/or large parts of the niobium surface (greater than a few microns), as observed after explosive rf processing. This plasma is produced by electron impact ionization of neutral gases evolving from the emitter. A new model was therefore developed to explain the sequence of events leading up to the permanent destruction of emitters. It contains a positive feedback loop for plasma production and the power dissipated in the emitter, which increases dramatically once rf processing is initiated. A discharge results. The observed submicrosecond processing times are also explained by this mechanism. An important conclusion to be drawn from this model is that both a current density *and* a total current threshold must be exceeded before an emitter can rf process. Experimental verification of this prediction was presented as well.

Numerical simulations using a modified version of the program MASK elaborate on our qualitative rf processing model and the important role played by the plasma. The simulations showed, that a dense plasma builds up only a micron (or less) from the emitter, provided a minimum initial gas density is present (i.e., the current density has to exceed a critical value) *and* the ionization rate is high enough (i.e., the total current has to exceed a critical value). The plasma can produce electric fields up to GV/m levels at the rf surface. At this point, mechanisms such as those described by the MIM and tip-on-tip models are no longer necessary for significant current emission. The presence of the plasma allows the entire macroemitter to remain active even if individual microemitters melt. Small sites due to, for example, material ejected from the main emitter also begin to emit with the assistance of the plasma, even if their field enhancement factor is modest. Their explosion leads to the observed satellite craters. Emission continues until the macroemitter melts completely and the energy stored in the cavity is drained. The entire process lasts less than 1 μs.

The initial (critical) gas density required for rf processing, as predicted by the simulations, is consistent with the vapor pressure of metallic emitters at their melting temperature. However, the omission in the simulations of the electric field enhancement by the emitter geometry, as well as the desorption of gas from the heated emitter and by ions bombarding the rf surface, leads us to believe that the true critical gas density is even lower than predicted. More accurate simulations in the future should therefore include such effects.

To further investigate voltage breakdown, helium processed emitters were examined in an electron microscope for the first time. It appears that many helium processing

events can be attributed to the relatively slow desorption of adsorbates by bombarding helium ions or some similar mechanism. However, we identified a distinct class of helium processing that melts and explodes emitters completely. The mechanism differs from rf processing only in that the helium gas artificially enhances the plasma density (either directly or by ion bombardment), to help exceed critical levels needed for processing. This fact underscores the importance of gases to the initiation of discharge. Our experience with helium processing also suggests that high power processing with gases present in the cavity may be useful for improving its performance.

9.2 Other high field loss mechanisms

9.2.1 Thermal breakdown

The thermometry system's high speed capabilities were especially useful during the study of thermal breakdown. We were able to observe breakdown in progress by taking a series of temperature maps in rapid succession, as in a movie. We showed, that statistically a disproportionate number of defect related breakdown sites are on or very near the equator. These are likely to be due to defects introduced during the electron beam welding process. Although continued advances in niobium purification techniques have served to increase the average breakdown field of cavities over the years, it now is important that welding techniques be further improved.

The study of thermal breakdown also led to the discovery of a new loss mechanism. Not only does the breakdown limit the maximum attainable field, but it can also increase the residual resistance in the cavity region directly involved in the breakdown. Increases by over 100 nΩ have been recorded. We believe that magnetic flux, generated by the high temperature gradients during thermal breakdown, is trapped as the cavity wall cools rapidly at the end of the breakdown cycle. A thermal cycle to above the critical temperature T_c is required to release the flux again. We speculate that some of the reports from other laboratories of Q_0 degradation following high peak power processing and breakdown events *may* also be the result of flux trapping. This phenomenon therefore merits further investigation, to determine how common breakdown related flux trapping is in cavities, and whether it contributes to the limitation of their performance.

9.2.2 Multipacting

We also were able to observe two point multipacting in progress, starting at a threshold field of $E_{pk} = 30$ MV/m. Numerical simulations predict multipacting as well, starting at about 32 MV/m. Our results provide a definitive confirmation that two point multipacting takes place in elliptical cavities, as was already suspected by other researchers. Although multipacting was easily processed, it also was responsible for flux trapping that increased the residual resistance (like thermal breakdown). There is limited evidence that the increased losses can lead to premature thermal breakdown which cannot be processed away.

9.3 Residual losses

9.3.1 Discharge cleaning

The observation of a gas discharge initiated by multipacting demonstrated that ion and/or electron bombardment can remove adsorbates from the rf surface, which are responsible for residual losses. On average an improvement of the residual resistance by 30 % was recorded. In some places the residual resistance reduced to values as low as 1/8 of the original surface resistance. If such improvements could be achieved throughout the entire cavity, then Q_0 values of 10^{11} should be possible. Similar discharge cleaning was recorded during thermal breakdown (in limited cases) and also with the aid of helium gas. Investigations into the use of gas discharge to "clean" the rf surface are therefore appropriate and may point the way to improved cavity performance.

9.3.2 Hydrogen precipitation

In many cases the enhanced resolution of the thermometry system permitted us to examine low field residual losses that have gone undetected with other systems. In this manner, we were able to show that equator welds are more susceptible to hydride precipitation and the associated losses than the remainder of the cavity, even if special precautions are taken during cavity etching to keep the temperature below 15 °C. In one instance, a slow cooldown brought about severe losses along the equator that could not be removed completely by a cycle to room temperature and a subsequent rapid cooldown. Such situations may arise with cavities installed in accelerators. It therefore would be useful if the equator weld could be eliminated by using techniques such as hydroforming for cavity manufacturing, rather than deep drawing. Alternatively, 900 °C heat treatment to remove all hydrogen is recommended prior to cavity installation. Cavity etching at temperatures significantly below 15 °C should also be considered.

9.3.3 Quality degradation due to titanium

We also identified a new danger posed by very high temperature heat treatment ($T >$ 1500 °C) used for post purification of cavities. Titanium, which serves as a solid state getter during the heat treatment, diffuses over large distances along grain boundaries, despite the fact that diffusion in the grains is insignificant. For thin-walled cavities the danger exists, that titanium will diffuse all the way from the cavity exterior to the rf surface. The presence of titanium in the boundaries then causes an electrical decoupling of the superconducting niobium grains. The surface resistance of this system increases exponentially with the magnetic field. We recorded a cavity quality degradation by over a factor of 10 at $E_{\mathrm{pk}} = 20$ MV/m. Extended very high temperature heat treatments should thus be avoided for cavity purification. Newly developed low temperature heat treatments may prove to be safer and more useful.

9.3.4 Particles

The high sensitivity of the thermometry system also permitted us to demonstrate for the first time that micron size particles can move in cavities under the influence of the electromagnetic fields. Although their effect on the surface resistance is minimal,

these particles are potential field emitters if they settle in high electric field regions. It is therefore imperative that not only the cavity, but also couplers and probes are thoroughly cleaned to remove particulate matter that otherwise may migrate to high electric field regions in the cavity. The microscopic examination of two particles also demonstrated that particles on the rf surface can be heated to very high temperatures by the magnetic field. In one case even (local) melting was observed, leading to very strong adhesion of the particle to the cavity wall.

Appendix A

Analysis of temperature data

Figure A.1 depicts the user interface of the program developed for analysis of the hundreds of temperature maps generated by each cavity test. The program compiles all the temperature maps of interest and allows the user to examine the data in numerous different ways. The following is a selection of the choices:

1. The option to display the temperature data of a selected thermometer as a function of E_{pk} or U.

2. The option to extract the Fowler-Nordheim parameters of an emitter from the response of a selected thermometer.

3. The option to subtract the ohmic component of the dissipated power in a temperature map. Hence only anomalous losses are displayed.

4. The option to convert a temperature map to an equivalent map of the cavity surface resistance (assuming all losses are quadratic). The surface resistance of a point is given by
$$R_{\mathrm{s}} = \frac{2\Delta T}{K_T H^2}, \tag{A.1}$$
where H is the local surface magnetic field, ΔT is the temperature rise measured by the nearest thermometer and K_T is a calibration constant on the order of 1 $\mathrm{Kcm}^2/\mathrm{W}$.

5. The option to take the ratio of the temperatures or surface resistances of two temperature maps.

6. The option to compile a histogram of the surface resistances in a map or a subregion of a map.

7. The option to extract a Q_0 versus E_{pk} curve from a series of temperature maps.

8. The option to average over a number of temperature maps.

9. The option to average temperature data over nearest (and, if desired, next nearest) neighbors using a user specified weighting function.

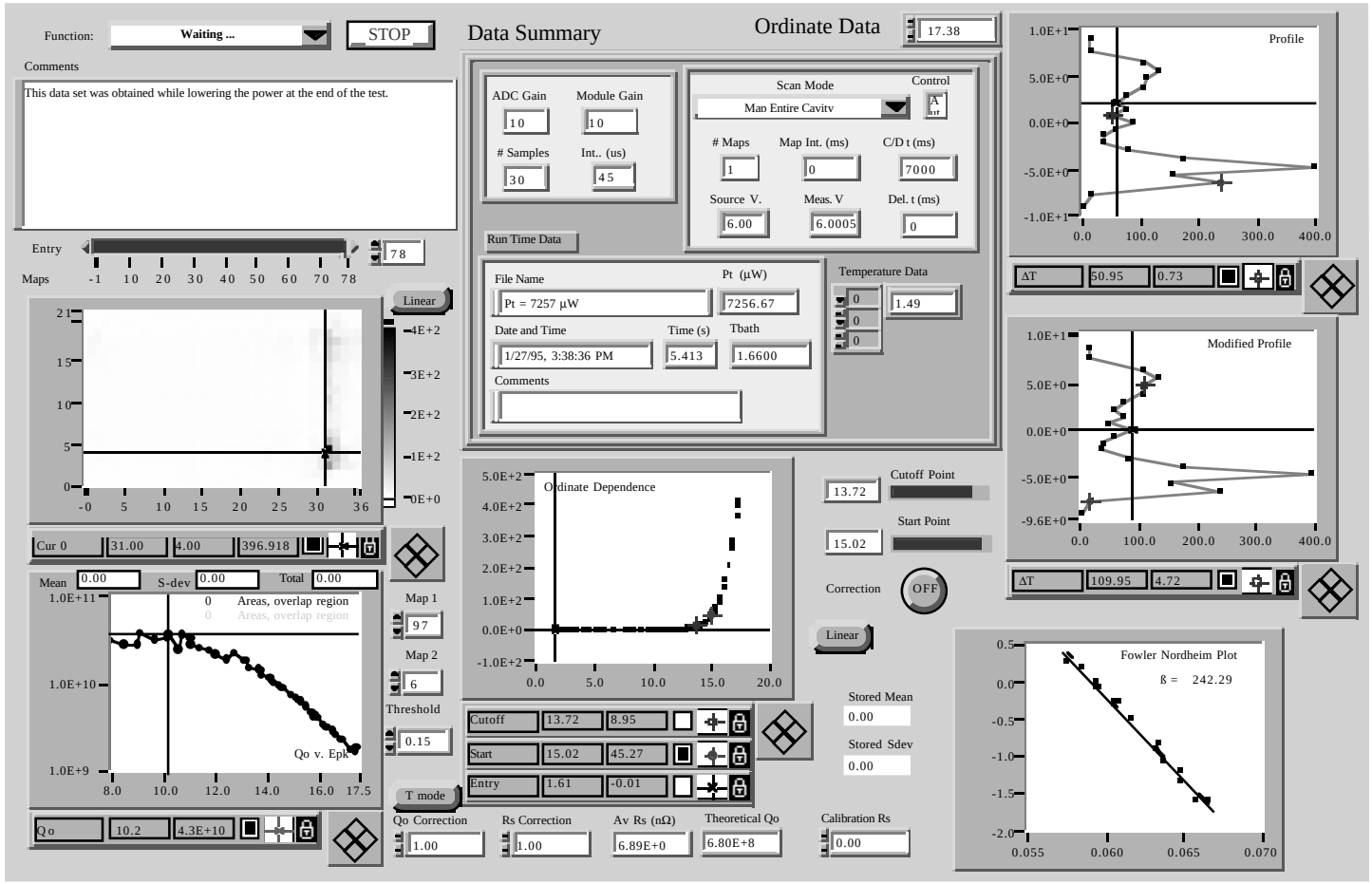

Figure A.1: User interface of the data analysis program.

Appendix B

Starburst formation

As discussed in Chapters 5 and 6, we believe that starburst formation is a direct consequence of plasma activity during rf processing events. The star-shaped and filamentary structure of these features suggest that they are created as a result of some instability. In fact, the self magnetic field of the field emission current, which can rise into the ampere range during processing, may be responsible for this effect. (Note that magnetic fields were not included in our field emission simulations with MASK.)

A current flowing in the $\hat{z}$ direction creates an azimuthal magnetic field in the $\hat{\phi}$ direction. The resultant magnetic force creates a pressure gradient $\boldsymbol{\nabla} p$ in the radial direction, where

$$dp/d\rho = \mu_0 j H. \tag{B.1}$$

This force will pinch the current if the outward plasma pressure is not sufficient to counteract the magnetic force. A simple calculation [200] shows that the plasma pressure and magnetic force are balanced if the beam current satisfies

$$I_{\mathrm{b}}^2 = \frac{4\pi}{\mu_0} \mathcal{N} k_{\mathrm{b}} T, \tag{B.2}$$

where $\mathcal{N}$ is the *linear* plasma density. Equation B.2 for a two ampere current is satisfied when $\mathcal{N} = 5 \times 10^{11}$ m^{-1} (at $T = 5$ eV). For an emission area of $\pi(0.25\ \mu\mathrm{m})^2$, the corresponding plasma density is 2.6×10^{24} m^{-3}. This density is comparable to the densities we expect during the events leading up to rf processing. If the current is greater than the value given by (B.2), then the magnetic force will constrict the emitted beam. In turn, the pinch enhances the magnetic field, causing further constriction. One therefore finds that such a situation is inherently unstable, because any perturbation leading to a slight constriction is amplified. [136] Chaotic electron motion, filamentation and the pinch-off of the beam can result from such an instability, perhaps yielding the starburst patterns we observe. [200] The time scale of this process is limited to one 1/2 rf cycle (since pinching should occur at the peak currents). The maximum distance s traveled by electrons in one 1/2 rf cycle at frequency f is

$$s = \frac{v_{\mathrm{e}}}{2f} \approx \frac{(1 \rightarrow 3) \times 10^6 \text{ m/s}}{2f}, \tag{B.3}$$

for electron energies up to 10's of eV. Hence, at 1.5 GHz, $s = 333 \rightarrow 1000$ μm and at 6 GHz $s = 83 \rightarrow 250$ μm. These distances are close to the starburst sizes observed

in L-band and mushroom cavities respectively. More importantly, we indeed found that starburst sizes scale inversely with frequency (see Figure 5.43), confirming that starburst formation is linked to the length of an rf cycle.

Appendix C

Multipacting induced thermal breakdown

C.1 Cavity LE1-17

Recall, that in Section 7.3.3 we observed multipacting in cavity LE1-17, starting at 32 MV/m (see Figure 7.31). Without difficulty we were able to condition the cavity and raise the fields to 34 MV/m. At that time breakdown events reminiscent of defect induced thermal breakdown were observed at 60° near the equator (see Figure 7.33). We were unable to process through this barrier.

Upon comparison of surface resistance data obtained before and after multipacting, we found that the R_s in the vicinity of the thermal breakdown site had increased (see Figure C.1). The width (in S) of the affected region is greater than the remainder of the equator region affected by multipacting, supporting our suspicions that the breakdown in Figure 7.33 was not caused by multipacting. Similar to other losses in the cavity,

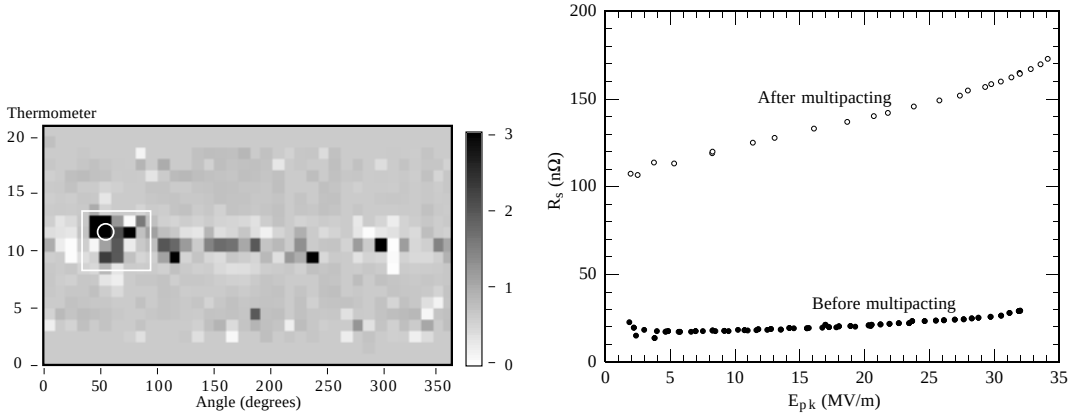

(a) (b)

Figure C.1: (a) Surface resistance ratio after and before multipacting was encountered in cavity LE1-17. The rectangle marks the region affected by the thermal breakdown in Figure 7.33. (b) Surface resistance of the circled site as a function of the peak electric field.

this region reduced its R_s following a temperature cycle. Repeated multipacting events, however, triggered thermal breakdown in this region once more, and the elevated losses reappeared. Hence the arrival of particles can be excluded as the source of losses.

An examination of the temperature data prior to any multipacting failed to reveal any unusual defect related heating at the thermal breakdown location. We therefore consider it possible that the increased resistance due to multipacting was severe enough to pose as a defect.

We cannot completely rule out the possibility, that a small (undetected) defect was present at the thermal breakdown site at the outset of our tests, which would have caused a quench irrespective of multipacting. In that case it would be coincidence that the defect triggered thermal breakdown just above the electric field threshold for multipacting. However, we think it is more likely that thermal breakdown was caused by the increased losses due to multipacting (flux trapping or gas redistribution). Potential thermal breakdown centers may be especially susceptible to increased losses and cause thermal breakdown prematurely. Any flux trapped during the thermal breakdown then only contributes further to the initiation of further breakdown events in this region.

C.2 TESLA cavities

A similar situation may have also been encountered in TESLA cavities tested at DESY. More details are given in Appendix D.

Appendix D

Flux trapping and multipacting in TESLA cavities.

Studies have been performed at DESY (Hamburg) on single cell 1.3 GHz cavities of the TESLA shape using a thermometry system based on the one described here. On numerous occasions, high loss regions were created following field emission induced quenching or emitter processing. Most of these high loss regions were concentrated along the equator. Significant reductions in Q_0 were also observed following these events. [12, 73] At the time, these observations were attributed to the redistribution of gases evolving from hot spots such as field emitters. This explanation was reasonable in view of the fact that thermal cycling was always successful in recovering the original Q_0.

However, we find it unlikely that gases should preferentially adsorb near the equator. Rather, we suspect that these losses are due to the flux trapping mechanism described in Chapter 7. This theory is supported by the fact that high pulsed power processing (up to 1 MW power for 2 ms) in many cases removed or reduced the losses in the affected regions. Especially processing at 4.2 K was effective at eliminating the losses. During these high power processing sessions thermal quenches were always observed. [201] Detailed data on these quenches is not available, but we suspect it is possible that the quenches were of the global thermal instability type (especially when $T_{\rm b}$ was 4.2 K). In this case, strong thermal gradients would be lacking[1], and the quenches could remove flux trapped during previous events.

The fact that newly created high loss regions are primarily concentrated along the equator leads us to suspect that two point multipacting, similar to that discussed in Chapter 7, possibly occurs in TESLA cavities as well and is responsible for some of the observed $R_{\rm s}$ increases.[2] Short lived multipacting may, for example, occur during high power processing sessions. There also is some indication that $E_{\rm acc} \geq 15$ MV/m ($E_{\rm pk} \approx 30$ MV/m) is required for lossy regions to be created (see, for example, Figure 13 in Reference [12]). [201] This threshold agrees well with the multipacting levels observed in the LE1 cavities.

Also of interest is the observation in Reference [12], that a newly created high loss region following a processing event at $E_{\rm acc} = 21$ MV/m subsequently limited the cav-

[1] Similar to the quench we observed due to low liquid helium levels in Figure 7.20.

[2] We wish to emphasize, that at present the notion of multipacting occurring in TESLA cavities is mere speculation, and an in depth analysis would be required for confirmation.

ity to 20 MV/m by thermal breakdown. No defect could be identified by thermometry at the breakdown center prior to the creation of the high loss region. It appears that the increased losses were responsible for precipitating thermal breakdown. This phenomenon is very similar to the observations we made with cavity LE1-17 (described in Appendix C).

Bibliography

[1] R. Peccei, M. E. Zeller, D. G. Cassel, J. A. Bagger, R. N. Cahn, P. D. Grannis, and F. J. Sciulli, editors. *Particle Physics: Perspectives and Opportunities*. World Scientific, Singapore, 1995. Report of the DPF Committe on Long-Term Planning.

[2] H. Padamsee, J. Knobloch, and T. Hays. *RF Superconductivity for Accelerators*. Wiley and Sons, New York, 1998. To be published.

[3] J. R. Delayen and K. W. Shepard. Tests of a superconducting rf quadrupole device. *Applied Physics Letters* **57**, 514–516 (1990).

[4] C. M. Lyneis, M. McAshan, and N. T. Viet. In *Proceedings of the 1972 Proton Linear Accelerator Conference*, p. 98, Los Alamos, NM, 1972.

[5] H. Padamsee, C. Reece, R. Noer, W. Hartung, E. Frick, and R. Kahn. Field emission studies in superconducting cavities. In E. R. Lindstrom and L. S. Taylor, editors, *Proceedings of the 1987 IEEE Particle Accelerator Conference*, pp. 1824–1826, Washington D.C., 1987.

[6] P. Kneisel, G. Müller, and C. Reece. Investigation of the surface resistance of superconducting niobium using thermometry in superfluid helium. *IEEE Transactions on Magnetics* **MAG-23**(2), 1417–1421 (1987). Proceedings of the 1986 Applied Superconductivity Conference.

[7] C. E. Reece. Progress in diagnostic techniques for sc cavities. In K. W. Shepard, editor, *Proceedings of the 3rd Workshop on RF Superconductivity*, pp. 545–563, Argonne, Illinois, 1988. Proceedings also published as internal Argonne report ANL-PHY-88-1.

[8] H. Piel. Superconducting cavities. In S. Turner, editor, *CERN Accelerator School: Superconductivity in Particle Accelerators*, pp. 149–196, Hamburg, Germany, 1988. CERN publication 89–04.

[9] P. Bernard, G. Cavallari, E. Chiaveri, E. Haebel, H. Heinrichs, H. Lengeler, E. Picasso, and V. Picciarelli. First results on a superconducting rf test cavity for LEP. In W. S. Newman, editor, *Proceedings of the 11th International Conference on High-Energy Accelerators*, pp. 878–885, Geneva, Switzerland, 1980.

[10] B. Dwersteg, W. Ebeling, W. Flauger, W.-D. Möller, J. Peters, D. Proch, and J. Susta. Superconducting cavity activities at DESY. In H. Lengeler, editor, *Proceedings of the 2nd Workshop on RF Superconductivity*, pp. 63–73, CERN, Geneva, Switzerland, 1984.

[11] Q. S. Shu, G. Deppe, W.-D. Möller, M. Pekeler, D. Proch, D. Renken, P. Stein, C. Stolzenburg, T. Junquera, A. Caruette, and M. Fouaidy. An advanced rotating T-R mapping and its diagnoses of TESLA 9-cell superconducting cavity. In *Proceedings of the 1995 Particle Accelerator Conference and International Conference on High Energy Accelerators*, pp. 1639–1641, Dallas, TX, 1995.

[12] M. Pekeler, T. Fuljahn, P. Schmüser, H. Padamsee, M. Champion, W.-D. Möller, and D. Proch. Thermometric study of field emission in a 1.3 GHz superconducting cavity. In B. Bonin, editor, *Proceedings of the 7th Workshop on RF Superconductivity*, Gif-sur-Yvette, France, 1995. Proceedings also published as internal Saclay report CEA/Saclay 96 080/1.

[13] G. Müller *et al.* In S. Tazzari, editor, *Proceedings of the 1st European Particle Accelerator Confernece*, p. 1289, Rome, Italy, 1988.

[14] E. Kako, S. Noguchi, M. Ono, T. Shishido, T. Tajima, P. Kneisel, M. Matsuoka, H. Miwa, T. Suzuki, and H. Umezawa. Test results on high gradient L-band superconducting cavities. In R. Sundelin, editor, *Proceedings of the 6th Workshop on RF Superconductivity*, pp. 918–943, Newport News, VA, 1993.

[15] Field emission studies: An owner's manual. Technical report, Cornell University, Laboratory of Nuclear Studies, 1991. SRF/D report 910121-24, edited by W. Hartung.

[16] J. Graber, J. Kirchgessner, D. Moffat, J. Knobloch, H. Padamsee, and D. Rubin. Microscopic investigation of high gradient superconducting cavities after reduction of field emission. *Nuclear Instruments and Methods in Physics Research* **A 350**, 582–594 (1994).

[17] J. H. Graber. *High Power Processing Studies of 3 GHz Niobium Superconducting Accelerator Cavities*. PhD thesis, Cornell University, 1993. Laboratory of Nuclear Studies thesis CLNS 93-1.

[18] R. H. Fowler and L. Nordheim. Electron emission in intense electric fields. *Proceedings of the Royal Society London* **A119**, 173–181 (1928).

[19] Q. S. Shu, K. Gendreau, W. Hartung, J. Kirchgessner, D. Moffat, R. Noer, H. Padamsee, D. L. Rubin, and J. Sears. Influence of condensed gases on field emission and the performance of superconducting rf cavities. *IEEE Transactions on Magnetics: Proceedings of the 14th Applied Superconductivity Conference* **MAG-25**, 1868–1872 (1989).

[20] M. Luong, B. Bonin, H. Long, and H. Safa. Role of adsorbates on current fluctuations in dc field emission. In B. Bonin, editor, *Proceedings of the 7th Workshop on RF Superconductivity*, pp. 509–511, Gif-sur-Yvette, France, 1995. Proceedings also published as internal Saclay report CEA/Saclay 96 080/1.

[21] G. A. Mesyats. Explosive processes on the cathode in a vacuum. *IEEE Transactions on Electrical Insulation* **EI-18**(3), 218–225 (1983).

[22] E. A. Litvinov, G. A. Mesyats, and D. I. Proskurovskii. Field emission and explosive electron emission processes in vacuum discharges. *Soviet Physics Uspekhi* **26**(2), 138–159 (1983).

[23] B. Jüttner. Vacuum breakdown. *Nuclear Intruments and Methods in Physics Research* **A268**, 390–396 (1988).

[24] J. D. Jackson. *Classical Electrodynamics*. Wiley, New York, 2nd edition, 1975.

[25] S. Ramo and J. R. Whinnery. *Fields and Waves in Modern Radio*. Wiley & Sons, New York, 2nd edition, 1959.

[26] K. Halbach and R. F. Holsinger. SUPERFISH — a computer program for evaluation of rf cavities with cylindrical symmetry. *Particle Accelerators* **7**, 213–222 (1976).

[27] D. G. Myakishev and V. P. Yakovlev. An interactive code SUPERLANS for the evaluation of rf cavities and accelerating structures. In *Proceedings of the 1991 IEEE Particle Accelerator Conference*, pp. 3002–3004, San Francisco, CA, 1991.

[28] D. G. Myakishev and V. P. Yakovlev. The new possibilities of SUPERLANS code for evaluation of axis-symmetric cavities. In *Proceedings of the 1995 Particle Accelerator Conference and International Conference on High Energy Accelerators*, pp. 2348–2349, Dallas, TX, 1995.

[29] M. Kuntze, editor. *Proceedings of the Workshop on RF Superconductivity*, Karlsruhe, Germany, 1980. Proceedings also published as internal Kernforschungszentrum Kalsruhe report KFK-3019.

[30] H. Lengeler, editor. *Proceedings of the 2nd Workshop on RF Superconductivity*, CERN, Geneva, Switzerland, 1984.

[31] K. W. Shepard, editor. *Proceedings of the 3rd Workshop on RF Superconductivity*, Argonne, Illinois, 1988. Proceedings also published as internal Argonne report ANL-PHY-88-1.

[32] Y. Kojima, editor. *Proceedings of the 4th Workshop on RF Superconductivity*, Tsukuba, Japan, 1989. Proceedings also published as internal KEK report 89-21.

[33] D. Proch, editor. *Proceedings of the 5th Workshop on RF Superconductivity*, Hamburg, Germany, 1991. Proceedings also published as internal DESY report DESY M-92-01.

[34] R. M. Sundelin, editor. *Proceedings of the 6th Workshop on RF Superconductivity*, Newport News, Virginia, 1993.

[35] B. Bonin, editor. *Proceedings of the 7th Workshop on RF Superconductivity*, Gif-sur-Yvette, France, 1995. Proceedings also published as internal Saclay report CEA/Saclay 96 080/1.

[36] J. Bardeen, L. N. Cooper, and J. R. Schrieffer. Theory of superconductivity. *Physical Review* **108**(5), 1175–1204 (1957).

[37] M. Tinkham. *Introduction to Superconductivity.* Krieger, Malabar, Florida, 1975.

[38] A. C. Rose-Innes and E. H. Rhoderick. *Introduction to Superconductivity.* Pergamon Press, Glasgow, Scotland, 1969.

[39] R. A. French. Intrinsic type-2 superconductivity in pure niobium. *Cryogenics* **8**, 301–308 (1968).

[40] R. B. Flippen. The radial velocity of magnetic field penetration in type II superconductors. *Physics Letters* **17**, 193–194 (1965).

[41] J. Matricon and D. Saint-James. Superheating fields in superconductors. *Physics Letters* **24 A**, 241–242 (1967).

[42] T. Hays and H. Padamsee. Response of superconducting cavities to high peak power. In *Proceedings of the 1995 Particle Accelerator Conference and International Conference on High Energy Accelerators*, pp. 1617–1619, Dallas, TX, 1995.

[43] R. Noer. Electron field emission from broad-area electrodes. *Applied Physics* **A 28**, 1–24 (1982).

[44] E. L. Murphy and R. H. Good, Jr. Thermionic emission, field emission and the transition region. *Physical Review* **102**(6), 1464–1473 (1956).

[45] H. A. Schwettman, J. P. Turneaure, and R. F. Waites. Evidence of surface-state-enhanced field emission in rf superconducting cavities. *Journal of Applied Physics* **45**(2), 914–922 (1974).

[46] N. Pupeter, A. Göhl, T. Habermann, A. Kirschner, E. Mahner, G. Müller, and H. Piel. Influence of surface roughness and preparation, bulk purity and heat treatment on electron field emission from Nb and Nb_3Sn. In B. Bonin, editor, *Proceedings of the 7^{th} Workshop on RF Superconductivity*, pp. 67–77, Gif-sur-Yvette, France, 1995. Proceedings also published as internal Saclay report CEA/Saclay 96 080/1.

[47] M. Jimenez, R. J. Noer, G. Jouve, J. Jodet, and B. Bonin. Electron field emission from large-area cathodes: evidence for the projection model. *Journal of Physics D* **27**, 1038–1045 (1994).

[48] H. H. Race. Effect of small projections on breakdown in air. *General Electric Review* **43**(9), 365–369 (1940).

[49] D. Alpert, D. A. Lee, E. M. Lyman, and H. E. Tomaschke. Initiation of electrical breakdown in ultrahigh vacuum. *Journal of Vacuum Science and Technology* **1**, 35–50 (1964).

[50] G. Vibrans. Technical report, MIT Lincoln Lab, 1964. Report 353.

[51] H. Padamsee. Superconducting rf. In M. Month and M. Dienes, editors, *The Physics of Particle Accelerators*, pp. 1403–1482. American Institute of Physics, 1992. AIP Conference Proceedings 249.

[52] P. Niedermann. *Experiments on Enhanced Field Emission*. PhD thesis, University of Geneva, 1986. Dissertation number 2197.

[53] E. Mahner. Understanding and surpressing field emission using dc. *Particle Accelerators* **46**, 67–82 (1994). Also published in the Proceedings of the 6$^{\text{th}}$ Workshop on RF Superconductivity, Newport News, pp. 252–266, (1993).

[54] N. S. Xu. The physical origin of prebreakdown electron "pin-holes". In R. V. Latham, editor, *High Voltage Vacuum Insulation*, pp. 115–164. Academic Press, London, 1995.

[55] C. S. Athwal, K. H. Bayliss, R. Calder, and R. V. Latham. Field-induced electron emission from artificially produced carbon sites on broad-area copper and niobium electrodes. *IEEE Transactions on Plasma Science* .

[56] C. B. Duke and M. E. Alferieff. Field emission through atoms adsorbed on a metal surface. *Journal of Chemical Physics* **46**, 923–937 (1967).

[57] J. Halbritter. Enhanced electron emission and its reduction by electron and ion impact. *IEEE Transactions on Electrical Insulation* **EI-18**(3), 253–261 (1983).

[58] P. Kneisel, B. Lewis, and L. Turlington. Experience with high pressure ultrapure water rinsing of niobium cavities. In R. M. Sundelin, editor, *Proceedings of the 6th Workshop on RF Superconductivity*, Newport News, Virginia, 1993.

[59] H. Padamsee, K. Gendreau, W. Hartung, J. Kirchgessner, D. Moffat, R. Noer, D. L. Rubin, J. Sears, and Q. S. Shu. Does UHV annealing above 1100C as a final surface treatment reduce field emission loading in superconducting cavities? In *1988 Linear Accelerator Conference Proceedings*, Newport News, VA, 1988. Also published as CEBAF report 89-011.

[60] Q. S. Shu, W. Hartung, A. Leibovich, J. Kirchgessner, D. Moffat, R. Noer, H. Padamsee, D. Rubin, and J. Sears. Reducing field emission in superconducting rf cavities for the next generation of particle accelerators. *IEEE Transactions on Magnetics* **MAG-27**, 1935–1939 (1991). Proceedings of the 1990 Applied Superconductivity Conference, Snowmass, CO.

[61] H. Padamsee, P. Barnes, J. Kirchgessner, D. Moffat, D. Rubin, J. Sears, and Q. S. Shu. Field emission studies of heat treated and chemically treated superconducting cavities. In *Proceedings of the 1991 IEEE Particle Accelerator Conference*, pp. 2420–2422, San Francisco, CA, 1991.

[62] J. Graber, C. Crawford, J. Kirchgessner, H. Padamsee, D. Rubin, and P. Schmüser. Reduction of field emission in superconducting cavities with high power pulsed rf. *Nuclear Instruments and Methods in Physics Research* **A 350**, 572–581 (1994).

[63] D. Moffat, P. Barnes, J. Graber, L. Hand, W. Hartung, T. Hays, J. Kirchgessner, J. Knobloch, R. Noer, H. Padamsee, D. Rubin, and J. Sears. Studies on the nature of field emission sites. *Particle Accelerators* **40**, 85–126 (1992).

[64] R. J. Noer. Microscopic studies of field emission from rf cavity surfaces. In R. Sundelin, editor, *Proceedings of the 6th Workshop on RF Superconductivity*, pp. 236–251, Newport News, VA, 1993.

[65] T. Hays, M. Klauda, J. Knobloch, D. Moffat, H. Padamsee, S. Durbin, and M. Gray. Microscopic examination and elemental analysis of field emission sites in 5.8 GHz superconducting mushroom cavities. In R. Sundelin, editor, *Proceedings of the 6th Workshop on RF Superconductivity*, pp. 750–762, Newport News, VA, 1993.

[66] J. Knobloch and H. Padamsee. Microscopic investigation of field emitters located by thermometry in 1.5 GHz superconducting niobium cavities. *Particle Accelerators* **53**, 53–76 (1996). Also published in the Proceedings of the 7$^{\text{th}}$ Workshop on RF Superconductivity, Gif-sur-Yvette, France, pp. 95–103 (1995).

[67] J. Tan. Field emission studies at Saclay and Orsay. In B. Bonin, editor, *Proceedings of the 7th Workshop on RF Superconductivity*, pp. 105–117, Gif-sur-Yvette, France, 1995. Proceedings also published as internal Saclay report CEA/Saclay 96 080/1.

[68] G. N. Fursey. Field emission and vacuum breakdown. *IEEE Transactions on Electrical Insulation* **EI-20**(4), 659–670 (1985).

[69] E. A. Litvinov. Theory of explosive electron emission. *IEEE Transactions on Electrical Insulation* **EI-20**(4), 683–689 (1985).

[70] F. R. Schwirzke. Vacuum breakdown on metal surfaces. *IEEE Transactions on Plasma Science* **19**(5), 690–696 (1991).

[71] W. Weingarten. Electron loading. In H. Lengeler, editor, *2nd Workshop on RF Superconductivity*, pp. 551–582, CERN, Geneva, Switzerland, 1984.

[72] S. Bajic and R. Latham. A new perspective on the gas conditioning of high-voltage vacuum-insulated electrodes. *Journal of Physics D* **21**, 943–950 (1988).

[73] M. Pekeler. *Untersuchungen der Feldbegrenzenden Mechanismen in Supraleitenden Niob-Resonatoren.* PhD thesis, Deutsches Electronen-Synchrotron (DESY), 1996.

[74] H. Padamsee, D. Proch, P. Kneisel, and J. Mioduszewski. Field strength limitations in superconducting cavities — multipacting and thermal breakdown. *IEEE Transactions on Magnetics* **MAG–17**(1), 947–950 (1981).

[75] H. Padamsee, J. Tückmantel, and W. Weingarten. Characterization of surface defects in Nb microwave cavities. *IEEE Transactions on Magnetics* **MAG–19**(3), 1308–1311 (1983).

[76] F. Kœchlin and B. Bonin. Parameterization of the niobium thermal conductivity in the superconducting state. *Superconductor Science and Technology* **9**, 453–460 (1996).

[77] H. Padamsee. Calculations for breakdown induced by "large defects" in superconducting niobium cavities. *IEEE Transactions on Magnetics* **MAG-19**(3), 1322–1325 (1983).

[78] G. Müller. Superconducting niobium in high rf magnetic fields. In K. W. Shepard, editor, *Proceedings of the 3rd Workshop on RF Superconductivity*, pp. 331–358, Argonne, Illinois, 1988. Proceedings also published as internal Argonne report ANL-PHY-88-1.

[79] R. W. Röth, H.-G. Kürschner, G. Müller, H. Piel, and D. Reschke. Thermal stability of superconducting Nb cavities at 3 GHz. In H. Henke, H. Homeyer, and C. Petit-Jean-Genaz, editors, *Proceedings of the 3rd European Particle Accelerator Conference*, pp. 1325–1327, Berlin, Germany, 1992.

[80] H. Padamsee. A new purification technique for improving the thermal conductivity of superconducting Nb microwave cavities. **MAG-21**(2), 1007–1010 (1985).

[81] H. Padamsee. The technology of Nb production and purification. In H. Lengeler, editor, *Proceedings of the 2nd Workshop on RF Superconductivity*, pp. 339–376, CERN, Geneva, Switzerland, 1984.

[82] C. Crawford, J. Graber, T. Hays, J. Kirchgessner, A. Matheissen, W.-D. Möller, H. Padamsee, M. Pekeler, P. Schmüser, and M. Tigner. High gradients in linear collider superconducting accelerator cavities by high pulsed power to suppress field emission. *Particle Accelerators* **49**, 1–13 (1995).

[83] H. Padamsee. Influence of thermal conductivity on the breakdown field of niobium cavities. *IEEE Transactions on Magnetics* **MAG-21**(2), 149–152 (1985).

[84] H. Padamsee and J. Knobloch. Issues in superconducting rf technology. In S. I. Kurokawa, M. Month, and S. Turner, editors, *Frontiers of Accelerator Technology*. World Scientific, 1996. Proceedings of the joint US-CERN-Japan international school.

[85] A. Woode and J. Petit. Investigations into multipactor breakdown in satellite microwave payloads. *ESA Journal* **14**, 467–478 (1990).

[86] D. Proch and D. Einfeld. Measurement of multipacting currents of metal surfaces in rf fields. In *Proceedings of the 1995 Particle Accelerator Conference and International Conference on High Energy Accelerators*, pp. 1776–1778, Dallas, TX, 1995.

[87] C. M. Lyneis, H. A. Schwettman, and J. P. Turneaure. Elimination of electron multipacting in superconducting structures for electron accelerators. *Applied Physics Letters* **31**(8), 541–543 (1977).

[88] P. Kneisel and H. Padamsee. Modification of the muffin-tin cavity to eliminate multipacting. Technical report, Cornell University, Laboratory of Nuclear Studies, 1979. CLNS report 79/433.

[89] U. Kelin and D. Proch. In *Proceedings of the Conference on Future Possibilities for Electron Accelerators*, volume N1–17, Charlottesville, 1979.

[90] C. Vallet, M. Boloré, B. Bonin, J. P. Charrier, B. Daillant, J. Gratadour, F. Kœchlin, and H. Safa. Flux trapping in superconducting cavities. In H. Henke, H. Homeyer, and C. Petit-Jean-Genaz, editors, *Proceedings of the 1992 European Particle Accelerator Conference*, pp. 1295–1297, Berlin, Germany, 1992.

[91] J. Bardeen and M. J. Stephen. Theory of the motion of vortices in superconductors. *Physical Review* **140**(4A), 1197–1207 (1965).

[92] Y. B. Kim, C. F. Hempstead, and A. R. Strnad. Flux-flow resistance in type II superconductors. *Physical Review* **139**(4A), 1163–1172 (1965).

[93] J. I. Gittleman and B. Rosenblum. The pinning potential and high-frequency studies of type II superconductors. *Journal of Applied Physics* **39**(6), 2617–2621 (1968).

[94] P. Kneisel. Effect of cavity vacuum on performance of superconducting niobium cavities. In B. Bonin, editor, *Proceedings of the 7^{th} Workshop on RF Superconductivity*, pp. 443–447, Gif-sur-Yvette, France, 1995. Proceedings also published as internal Saclay report CEA/Saclay 96 080/1.

[95] W. Weingarten. On electrical breakdown in superconducting accelerating cavities. In *Proceedings of the XIIIth International Symposium on Discharges and Electrical Insulation in Vacuum*, pp. 480–485, Paris, France, 1988.

[96] B. Aune, B. Bonin, J. M. Cavedon, M. Juillard, A. Godin, C. Henriot, P. Leconte, H. Safa, A. Veyssière, and C. Zylberajch. Degradation of niobium superconducting rf cavities during cooling times. In *Proceedings of the 1990 Linac Conference*, pp. 253–255, Albuquerque, NM, 1990.

[97] C. Z. Antoine, B. Aune, B. Bonin, J. M. Cavedon, M. Juillard, A. Godin, C. Henriot, P. Leconte, H. Safa, and A. Veyssière. The role of atomic hydrogen in Q-degradation of niobium superconducting rf cavities: analytical point of view. In D. Proch, editor, *Proceedings of the 5^{th} Workshop on RF Superconductivity*, pp. 616–634, Hamburg, Germany, 1993. Proceedings also published as internal DESY report DESY M-92-01.

[98] B. Bonin and R. W. Röth. Q degradation of niobium cavities due to hydrogen contamination. In D. Proch, editor, *Proceedings of the 5^{th} Workshop on RF Superconductivity*, pp. 210–244, Hamburg, Germany, 1991. Proceedings also published as internal DESY report DESY M-92-01.

[99] J. F. Smith. The H-Nb (hydrogen-niobium) and D-Nb (deuterium-niobium) systems. *Bulletin of Alloy Phase Diagrams* **4**(1), 39–46 (1983).

[100] K. Schulze, O. Bach, D. Lupton, and F. Schreiber. Purification of niobium. In H. Stuart, editor, *Niobium — Proceedings of the International Symposium*, pp. 163–223, San Francisco, CA, 1981.

[101] J. K. Nørskov and F. Besenbacher. Theory of hydrogen interaction with metals. *Journal of the Less-Common Metals* **130**, 475–490 (1987).

[102] K. Saito, H. Miwa, K. Kurosawa, P. Kneisel, S. Noguchi, E. Kako, M. Ono, T. Shishido, and T. Suzuki. Study of ultra-clean surface for niobium sc cavities. In R. Sundelin, editor, *Proceedings of the 6th Workshop on RF Superconductivity*, pp. 1151–1159, Newport News, VA, 1993.

[103] D. Kapner. Surface contaminants of niobium. Technical report, Cornell University, Laboratory of Nuclear Studies, 1997. SRF report 970416-02.

[104] M. Fouaidy, T. Junquera, and S. Bousson. Field emission investigation in a 3.6 GHz srf cavity using x-ray measuring systems. In B. Bonin, editor, *Proceedings of the 7th Workshop on RF Superconductivity*, pp. 373–377, Gif-sur-Yvette, France, 1995. Proceedings also published as internal Saclay report CEA/Saclay 96 080/1.

[105] R. W. Röth, V. G. Kurakin, G. Müller, H. Piel, J. Pouryamout, D. Reschke, and N. Tellmann. Anomalous loss mechanisms in high purity Nb cavities. In D. Proch, editor, *Proceedings of the 5th Workshop on RF Superconductivity*, pp. 599–615, Hamburg, Germany, 1991. Proceedings also published as internal DESY report DESY M-92-01.

[106] T. Junquera, A. Le Goff, B. Bonin, H. Safa, and J. Tan. Field emission in rf cavities: observation of light spots at high electric fields. In R. Sundelin, editor, *Proceedings of the 6th Workshop on RF Superconductivity*, pp. 1014–1019, Newport News, VA, 1993.

[107] T. Junquera, S. Maïssa, M. Fouaidy, A. Le Goff, B. Bonin, M. Luong, H. Safa, and J. Tan. Study of luminous spots observed on metallic surfaces subjected to high rf fields. In *Proceedings of the 1995 Particle Accelerator Conference and International Conference on High Energy Accelerators*, pp. 1632–1635, Dallas, TX, 1995.

[108] H. Piel. Diagnostic methods of superconducting cavities and identification of phenomena. In M. Kuntze, editor, *Proceedings of the Workshop on RF Superconductivity*, pp. 85–118, Karlsruhe, 1980. Proceedings also published as internal Kernforschungszentrum Kalsruhe report KFK-3019.

[109] G. Müller. Diagnostic techniques and defect classification. In H. Lengeler, editor, *Proceedings of the 2nd Workshop on RF Superconductivity*, pp. 377–408, CERN, Geneva, Switzerland, 1984.

[110] J. Knobloch, H. Muller, and H. Padamsee. Design of a high speed, high resolution thermometry system for 1.5 GHz superconducting radio frequency cavities. *Review of Scientific Instruments* **65**(11), 3521–3527 (1994).

[111] H. Padamsee, J. Kirchgessner, D. Moffat, R. Noer, D. Rubin, J. Sears, and Q. S. Shu. New results on rf and dc field emission. In Y. Kojima, editor, *Proceedings of the 4th Workshop on RF Superconductivity*, pp. 207–247, Tsukuba, Japan, 1989. Proceedings also published as internal KEK report 89-21.

[112] M. Kuchnir and J. Knobloch. Pumpdown rate for srf cavities. Technical report, Cornell University, Laboratory of Nuclear Studies, 1992. SRF report 920504-03.

[113] J. Knobloch. Basic concepts of measurements made on superconducting rf cavities. Technical report, Cornell University, Laboratory of Nuclear Studies, 1991. SRF report 910927-07.

[114] D. W. Reschke and R. W. Röth. Fundamentally fastest method measuring $Q_0(E_{\rm acc})$ performance of s.c. cavities. In R. Sundelin, editor, *Proceedings of the 6th Workshop on RF Superconductivity*, pp. 1118–1125, Newport News, VA, 1993.

[115] T. Hays and H. Padamsee. Response of superconducting cavities to high peak power. In *Proceedings of the 1995 Particle Accelerator Conference and International Conference on High Energy Accelerators*, pp. 1617–1619, Dallas, TX, 1995.

[116] G. Müller and P. Kneisel. Development of sensitive thermometers for calibrated surface temperature measurements of niobium cavities immersed in superfluid helium. Technical report, Cornell University, Laboratory of Nuclear Studies, 1985. SRF report 851291 EX.

[117] P. Kneisel. Surface preparation of niobium. In M. Kuntze, editor, *Proceedings of the Workshop on RF Superconductivity*, pp. 27–40, Karlsruhe, 1980. Proceedings also published as internal Kernforschungszentrum Kalsruhe report KFK-3019.

[118] R. Ferraro. Field emission studies: An owner's manual (Part V). Technical report, Cornell University, Laboratory of Nuclear Studies, 1996. SRF/D report 960703-08, edited by W. Hartung.

[119] R. Kahn. Programs to simulate heating of niobium cavities by cavity defects. Technical report, Cornell University, Laboratory of Nuclear Studies, 1991. SRF/D report 910121-20.

[120] W. T. Diamond. High voltage vacuum insulation in crossed magnetic and electric fields. In *Proceedings of the 1993 Particle Accelerator Conference*, pp. 1381–1383, Washington D.C., 1993.

[121] B. Jüttner. Characterization of the cathode spot. *IEEE Transactions on Plasma Science* **PS-15**(5), 474–480 (1987).

[122] G. K. Kartsev, G. A. Mesyats, D. I. Proskurovskii, V. P. Rotshtein, and G. N. Fursei. Investigation of the time characteristics of the transition of field emission to a vacuum arc. *Soviet Physics* **15**(4), 475–477 (1970).

[123] E. Hantzsche and B. Jüttner. Current density in arc spots. *IEEE Transactions on Plasma Science* **PS-13**(5), 230–234 (1985).

[124] G. A. Mesyats and D. I. Proskurovsky. *Pulsed Electric Discharge in Vacuum*. Springer, 1989.

[125] D. E. Gray, editor. *American Institute of Physics Handbook*. McGraw-Hill, New York, 3$^{\rm rd}$ edition, 1972.

[126] Y. Bruysneraede, D. Gorle, D. Leroy, and P. Morignot. Surface resistance measurements in TE_{011} mode cavities of superconducting indium, lead and an indium-lead alloy at low and high rf magnetic fields. *Physica* **54**, 137–159 (1971).

[127] J. Halbritter. Comparison between measured and calculated rf losses in the superconducting state. *Zeitschrift der Physik* **238**, 466–476 (1970).

[128] Table of periodic properties of the elements. Technical report, Sargent-Welch Scientific Company, 1980.

[129] Y. S. Touloukian. *Thermal Conductivity: Metallic Elements and Alloys*, volume 1. Plenum Press, New York, 1970.

[130] J. Tan, H. Safa, and B. Bonin. Thermal contact resistance of a particle on a substrate. In B. Bonin, editor, *Proceedings of the 7^{th} Workshop on RF Superconductivity*, pp. 369–372, Gif-sur-Yvette, France, 1995. Proceedings also published as internal Saclay report CEA/Saclay 96 080/1.

[131] J. Paulini, T. Klein, and G. Simson. Thermo-field emission and the Nottingham effect. *Journal of Physics D* **26**, 1310–1315 (1993).

[132] S. G. Christov. General theory of electron emission from metals. *Physica Status Solidi* **17**(11), 11–25 (1966).

[133] J. Tückmantel and W. Weingarten. On electron loading in superconducting accelerating cavities. Technical report, CERN, 1982. CERN publication CERN/EF/RF 82–4.

[134] P. A. Chatterton. A theoretical study of field emission initiated vacuum breakdown. *Proceedings of the Physical Society London* **88**, 231–245 (1966).

[135] Y. Y. Lau, Y. Liu, and R. K. Parker. Electron emission: from the Fowler-Nordheim relation to the Child-Langmuir law. *Physics of Plasmas* **1**(6), 2082–2085 (1994).

[136] F. F. Chen. *Introduction to Plasma Physics*. Plenum Press, New York, 1974.

[137] A. E. Robson and P. C. Thonemann. An arc maintained on an isolated metal plate exposed to a plasma. *Proceedings of the Physical Society* **73**, 508–512 (1959).

[138] A. I. Bushik, B. Jüttner, and H. Pursch. On the nature and the motion of arc cathode spots in UHV. *Beiträge aus der Plasmaphysik* **19**, 177–188 (1979).

[139] G. Comsa and R. David. Dynamical parameters of desorbing molecules. *Surface Science Reports* **5**, 145–198 (1985).

[140] R. K. Pathria. *Statistical Mechanics*. Pergamon Press, Oxford, 1972.

[141] B. E. Hayden. The dynamics of hydrogen adsorption and desorption on copper surfaces. In C. T. Rettner and M. N. Ashfold, editors, *Dynamics of Gas Surface Interactions*, pp. 137–168. Royal Society of Chemisty, Cambridge, 1991.

[142] Y. Okuno, K. Okuno, Y. Kaneko, and I. Kanomata. Absolute measurement of total ionization cross section of Mg by electron impact. *Journal of the Physical Society Japan* **29**(1), 164 (1970).

[143] R. S. Freund, R. C. Wentzel, R. J. Shul, and T. R. Hayes. Cross-section measurements for electron-impact ionization of atoms. *Physical Review A* **41**(7), 3575–3595 (1990).

[144] M. A. Lennon, K. L. Bell, H. B. Gilbody, J. G. Hughes, A. E. Kingston, M. J. Murray, and F. J. Smith. Recommended data on the electron impact ionization of atoms and ions: fluorine to nickel. *Journal of Physical and Chemical Reference Data* **17**(3), 1285–1363 (1988).

[145] H. C. Straub, B. G. Lindsay, K. A. Smith, and R. F. Stebbings. Absolute partial cross sections for electron-impact ionization of CO_2 from threshold to 1000 eV. *Journal of Chemical Physics* **105**(10), 4015–4022 (1996).

[146] L. B. Loeb. Recombination of ions. In S. Flügge, editor, *Handbuch der Physik*, volume 21, pp. 471–502. Springer Verlag, Berlin, Germany, 1956.

[147] S. C. Brown. *Basic Data of Plasma Physics, 1966.* MIT press, Cambridge, 2nd edition, 1967.

[148] J. D. Cobine. *Gaseous Conductors.* McGraw-Hill, New York, 1941.

[149] D. Wanless. Electron-ion recombination in argon. *Journal of Physics B* **4**, 522–527 (1971).

[150] J. M. Wu, F. T. Wu, and D. T. Shaw. Measurement of electron-ion recombination of a dense high temperature cesium plasma. *Journal of Applied Physics* **44**(7), 3052–3054 (1973).

[151] D. P. Chernin. Computer simulations of low noise states in a high-power crossed field amplifier. *IEEE Transactions on Electron Devices* **43**(11), 2004–2010 (1996).

[152] D. Chernin, A. Drobot, and M. Kress. A model of secondary emission for use in computer simulation of vacuum electronic devices. In *Proceedings of the 1993 International Electron Devices Meeting*, 1993.

[153] D. Q. Posin. The Towsend coefficients and spark discharge. *Physical Review* **50**, 650–658 (1936).

[154] T. L. R. Ayers. The ionization by collisions of hydrogen, nitrogen and argon. *Philosophical Magazine and Journal of Science* **45**, 353–368 (1923).

[155] R. Papoular. *Electrical Phenomena in Gases.* American Elsevier Publishing Company, New York, 1965.

[156] L. B. Loeb. *Fundamental Processes of Electrical Discharge in Gases.* Wiley, New York, 1939.

[157] A. v. Engel. Ionization in gases by electrons in electric fields. In S. Flügge, editor, *Handbuch der Physik*, volume 21, pp. 504–573. Springer Verlag, Berlin, Germany, 1956.

[158] J. S. Towsend. The motion of electrons in gases. *Philosophical Magazine and Journal of Science* **42**, 873–891 (1921).

[159] R. C. Weast. *CRC Handbook of Chemistry and Physics*. CRC Press, Boca Raton, 65^{th} edition, 1984.

[160] J. S. Towsend. Motion of electrons in helium. *Philosophical Magazine and Journal of Science* **46**, 657–664 (1923).

[161] T. Kubono. A theory for the cathode mechanism in low-current vacuum arcs, with application to the calculation of erosion rate. *Journal of Applied Physics* **49**(7), 3863–3869 (1978).

[162] T. Hays. (Cornell University) private communication.

[163] G. M. Kassirov and G. A. Mesyates. Breakdown mechanism of short vacuum gaps. *Soviet Physics — Technical Physics* **9**(8), 1141–1145 (1965).

[164] A. Maitland. New derivation of the vacuum breakdown equation relating breakdown voltage and electrode separation. *Journal of Applied Physics* **32**(11), 2399–2407 (1961).

[165] *Plasma Formulary*, 1987. Naval Research Laboratory publication 0084–4040.

[166] JANAF Thermochemical Tables. Midland, Michigan, 1962–1968.

[167] A. N. Nesmeyanov. *Vapour Pressure of the Elements*. Academic Press, New York, 1963.

[168] H. Jäger, U. Seydel, and H. Wadle. Deviations from Ohm's law for a metal at high current densities. *Physics Letters* **55A**(8), 481–482 (1976).

[169] J. Halbritter. On contamination of electrode surfaces and electric field limitations. *IEEE Transactions on Electrical Insulation* **EI–20**(4), 671–681 (1985).

[170] G. Carter and J. S. Colligon. *Ion Bombardment of Solids*. American Elsevier Publishing, New York, 1968.

[171] N. Laegreid and G. K. Wehner. Sputtering yields of metals for Ar^+ and Ne^+ ions with energies from 50 to 600 eV. *Journal of Applied Physics* **32**(3), 365–369 (1961).

[172] D. Rosenberg and G. K. Wehner. Sputtering yields for low energy He^+, Kr^+, and Xe^+ ion bombardment. *Journal of Applied Physics* **33**(5), 1842–1845 (1962).

[173] S. K. Erents and G. M. McCracken. Desorption of solid hydrogen by energetic protons, deuterons and electrons. *Journal of Applied Physics* **44**(7), 3139–3145 (1973).

[174] G. W. McClure. Plasma expansion as a cause of metal displacement in vacuum-arc cathode spots. *Journal of Applied Physics* **45**(5), 2078–2084 (1974).

[175] C. Reece. Magnetic field enhancement at an inside corner of a cavity: results of SUPERFISH calculations. Technical report, Cornell University, Laboratory of Nuclear Studies, 1996. SRF/D report 840302.

[176] G. Müller, P. Kneisel, D. Mansen, H. Piel, J. Puoryamout, and R. W. Röth. Nb_3Sn layers on high-purity Nb cavities with very high quality factors and accelerating gradients. In S. Myers, A. Pacheco, R. Pascual, C. Petit-Jean-Genaz, and J. Poole, editors, *Proceedings of the 1996 European Particle Accelerator Conference*, pp. 2085–2087, Barcelona, Spain, 1996.

[177] M. Peiniger, M. Hein, N. Klein, G. Müller, H. Piel, and P. Thüns. Work on Nb_3Sn cavities at Wuppertal. In *Proceedings of the 3rd Workshop on RF Superconductivity*, pp. 503–531, Argonne, 1987. Proceedings also published as internal Argonne report ANL-PHY-88-1.

[178] N. Ashcroft and D. Mermin. *Solid State Physics*. W. B. Saunders, 1976.

[179] T. Hays. (Cornell University) private communication.

[180] V. Raag and H. V. Kowger. Thermoelectric properties of niobium in the temperature range 300 – 1200 K. *Journal of Applied Physics* **36**(6), 2045–2048 (1965).

[181] E. R. Rumbo. Transport properties of very pure copper and silver below 8.5 K. *Journal of Physics F* **6**(1), 85–98 (1976).

[182] A. M. Guenault and D. G. Hawksworth. Thermoelectric power of pure noble metals at low temperatures. *Journal of Physics F* **7**(8), L219–L222 (1977).

[183] J.-M. Abraham, C. Tete, and B. Deviot. Résistivité électric d'un niobium de haute pureté de 20 K à la température de fusion. *Journal of the Less Common Metals* **37**, 181–188 (1974).

[184] F. Llewellyn-Jones. *Ionization and Breakdown in Gases*. Wiley, New York, 1957.

[185] K. Saito, T. Higuchi, T. Suzuki, E. Kako, S. Noguchi, M. Ono, and T. Shishido. Water rinsing of the contaminated superconducting rf cavities. In B. Bonin, editor, *Proceedings of the 7th Workshop on RF Superconductivity*, pp. 379–383, Gif-sur-Yvette, France, 1995. Proceedings also published as internal Saclay report CEA/Saclay 96 080/1.

[186] J. A. Rodriguez. More evidence for the formation of a dense Cottrell cloud of hydrogen (hydride) at dislocations in niobium and palladium. *Scripta Metallurgica* **17**, 159–164 (1983).

[187] G. V. Khaldeev and V. K. Gogel. Physcial and corrosion-electrochemical properties of the niobium–hydrogen system. *Russian Chemical Reviews* **56**, 1057–1081 (1987).

[188] K. W. Jacobsen. Bonding in metallic systems: an effective-medium approach. *Comments on Condensed Matter Physics* **15**(3), 129–161 (1988).

[189] G. Enderlein, W. Körber, A. Matheisen, and D. Proch. Investigations on hydrogen contamination of superconducting cavities. In *Proceedings of the 1991 IEEE Particle Accelerator Conference*, pp. 2432–2434, San Francisco, CA, 1991.

[190] B. Bonin and H. Safa. Power dissipation at high fields in granular rf superconductivity. *Superconductor Science and Technology* **4**, 257–261 (1991).

[191] G. Müller. Microwave properties of high-T_c oxide superconductors. In Y. Kojima, editor, *Proceedings of the 4^{th} Workshop on RF Superconductivity*, pp. 267–304, Tsukuba, Japan, 1989. Proceedings also published as internal KEK report 89-21.

[192] T. L. Hylton, A. Kapitulnik, M. R. Beasley, J. P. Carini, L. Drabeck, and G. Grüner. Weakly coupled grain model of high-frequency losses in high T_c superconducting thin films. *Applied Physics Letters* **53**(14), 1343–1345 (1988).

[193] A. M. Portis. Microwaves and superconductivity: Processes in the intergranular medium. In *Earlier and Recent Aspects of Superconductivity*, pp. 278–303. Springer Verlag, Berlin, Germany, 1989. Lectures from the International School, Erice, Italy, July, 1989.

[194] J. Pelleg. Diffusion of ^{44}Ti into niobium single crystals. *Philosophical Magazine* **21**(172), 735–742 (1970).

[195] I. Kaur, Y. Mishin, and W. Gust. *Fundamentals of Grain and Interphase Boundary Diffusion*. Wiley & Sons, Chichester, 3rd edition, 1995.

[196] C. Antoine, B. Bonin, H. Safa, B. Berthier, E. Tessier, O. Trocellier, A. Chevarier, N. Chevarier, and B. Roux. Evidence of preferential diffusion of impurities along grain boundaries in very pure niobium used for radiofrequency cavities. *Journal of Applied Physics* **81**(4), 1677–1682 (1997).

[197] H. Safa, D. Moffat, F. Kœchlin, E. Jacques, and Y. Boudigou. Nb purification by Ti gettering. In B. Bonin, editor, *Proceedings of the 7^{th} Workshop on RF Superconductivity*, pp. 649–652, Gif-sur-Yvette, France, 1995. Proceedings also published as internal Saclay report CEA/Saclay 96 080/1.

[198] R. V. Latham. Microparticle phenomena. In R. V. Latham, editor, *High Voltage Vacuum Insulation*, pp. 229–297. Academic Press, London, 1995.

[199] R. A. Bowling. A theoretical review of particle adhesion. In *Particles on Surfaces I*, pp. 129–142. Plenum Press, New York, 1988.

[200] R. J. Goldstone and P. H. Rutherford. *Introduction to Plasma Physics*. Institute of Physics Publishing, Bristol, 1995.

[201] M. Pekeler. (DESY, Hamburg) private communication.